TAPERED INTAKES ON A SINGLE CYLINDER ENGINE

A Thesis

Presented in Partial Fulfillment of the Requirements for

the Degree Master of Science in the

Graduate School of The Ohio State University

By

Todd Michael Howard, B.S.M.E.

*****

The Ohio State University
2003

Master's Examination Committee:

Dr. Ahmet Selamet, Adviser

Dr. Rajendra Singh

Approved by

A. Selamet

Adviser

Department of Mechanical Engineering

ABSTRACT

The effect of intake runner geometry on the intake and exhaust flow characteristics is studied with a single cylinder engine. Eight different tapered intake runners (or stacks) were placed on this engine and pressure measurements were taken in the intake and exhaust systems, and in the cylinder. The intake stacks maintain the same length, transducer locations, bellmouth radius, and mounting configuration in an attempt to identify the effect of tapered geometry only. The experiments were conducted under both motoring and firing conditions at speeds ranging from 1000 to 5500 rpm at 250 rpm increments. A laminar flow meter was placed in the exhaust system of the motoring engine to measure the mass flow rate, thereby allowing for a comparison of volumetric efficiencies. A finite-difference based engine simulation code was used for predictions, which were compared to actual measurements to assess the ability of the program in capturing the effect of tapered geometries on wave dynamics phenomena.

Dedicated to my family....

ACKNOWLEDGMENTS

I wish to thank my adviser, Dr. Ahmet Selamet, for all the help he has provided over the past few years. His guidance and outstanding technical expertise have been invaluable.

I would also like to thank Ford Motor Company for supporting my research by providing all hardware including the single cylinder engine and the intake stacks and all financial support. In particular, I wish to thank Dr. Rodney Tabaczynski, Dr. Kevin Tallio and Keith Miazgowicz for their assistance in obtaining this support and for guidance concerning the engine simulation code.

Special thanks to Dr. Rajendra Singh for taking his valuable time to serve on my Master's Examination Board.

I would not have been able to complete this course of study and thesis without the extensive knowledge and experimental assistance provided by my research team members at the Center for Automotive Research. Special thanks goes to Adam Christian, Dr. Nolan Dickey, Cam Giang, Iljae Lee, Yale Jones, and Sridevi Rupal Mohan.

On a personal note, I would like to extend my sincere gratitude to my family members who constantly encouraged me through the rough times especially my Mom and Dad. Finally, I would like to thank my wife, Christy, for her support, understanding and wonderful care-giving she gave to our daughter over the past two years.

TABLE OF CONTENTS

Page

LIST OF TABLES

LIST OF FIGURES

CHAPTER 1

INTRODUCTION

The dynamic effects of gas motion on intake and exhaust systems have long been known to influence the volumetric efficiency and therefore the performance of an internal combustion engine. Optimizing engine components to take advantage of the pressure waves is generally referred to as "tuning". Historically, engines were tuned through much experimental iteration with numerous intake and exhaust components in an attempt to achieve peak torque at a specific speed, depending on the application of the engine. A more efficient approach for tuning was needed as internal combustion engines became more complex. Through the mid-1900's, researchers developed a wide range of mathematical approaches beginning with the fairly simple one-dimensional linear frequency-domain approaches to the more complex nonlinear time domain approaches used in current engine simulation codes. The additional variables involved in designing today's internal combustion engines such as multi-valve heads, variable valve events, and variable length intake systems dramatically increase the number of experiments required to optimize a system and quickly becomes both cost and labor prohibitive. Thus the use of engine simulation codes to predict the influence of engine breathing system geometry changes on the overall performance has become extremely important for today's engine designer. With the ever increasing criteria for emissions, performance, noise and drivability in internal combustion engines, there exists a need to further understand and model the complex physics that governs the engine operation and to accurately incorporate it into the engine simulation codes. This thesis concentrates specifically on the impact of tapered intake ducts. A single cylinder engine is used to alleviate all multi-cylinder effects and experiments are conducted over a wide range of operating conditions. The experimental data are then compared to computational results acquired from a finite-difference based engine simulation code to determine its ability to capture the effect of tapered geometries on wave dynamics phenomena.

1.1 Literature Survey

The tuning of intake systems has been of interest to engine designers for many years, with one of the first references to such tuning being made by Koester in 1904. The basic idea of intake tuning is to ensure the return of the initial rarefaction wave in the form of a compression wave before the intake valve closes at a given engine speed. This compression wave produces a small supercharge or ram effect as the valve closes and forces additional air into the cylinder. The additional air that is trapped in the cylinder during intake increases the volumetric efficiency of the engine, defined as

$$\eta_v = \frac{\text{mass of air trapped in cylinder}}{\text{mass of air contained in swept volume of cylinder at inlet air density}}. \quad (1.1)$$

Volumetric efficiency is an important performance measure since, if all other parameters remain constant, the mean effective pressure and therefore torque are proportional to it.

Researchers have investigated and developed a wide range of mathematical methods to calculate the effect of intake tuning on internal combustion engines. Initially, simple one-dimensional linear frequency-domain approaches were used and found to provide adequate information about resonance frequencies and the engine speed at which maximum tuning would occur. Morse *et al.* (1938) employed an organ pipe analysis for the intake duct, which was then modified by Engelman and his coworkers who coupled the intake duct and the cylinder volume to resemble Helmholtz resonators. This approach is based on an idealized lumped parameter system where the gas in the pipe is regarded as a lumped mass with no compressibility, and the gas in the cylinder is regarded as a spring with no inertia [Fig. 1.1 (a)]. They postulated that when the intake valve is open, tuning occurs when the engine speed is such that the induction process is matched to the natural frequency of the combined intake pipe and cylinder system. This approach has been widely used since and does provide reasonable results for engine speeds. An engine designer, knowing the target speed for an engine's peak performance can use this equation and vary the length dimensions of the intake runners to get the proper tuning effect. The simplicity of this approach makes it useful for practicing engineers towards rough estimates during the initial design stage. Driels (1975) extended the Helmholtz approach in the frequency domain by incorporating a valve model between the cylinder volume and the intake pipe to approximate a realistic engine breathing process. Selamet *et al.* (1995) examined the effect of a distributed analysis on the resonance frequencies by comparing with the classical lumped approach. Another simplistic approach based on distributed parameters was described by Winterbone and Yoshitomi (1990). This approach: (1) considers the system as two connected pipes of different geometric dimensions with the larger area pipe having a closed end, and (2) allows for the gas in both the pipe and cylinder to have compressibility and inertia [Fig. 1.1 (c)]. Winterbone and Pearson (1999) also describe a simplified version of this approach where only the intake is regarded as a distributed element and the cylinder is considered a lumped element [Fig. 1.1(b)].

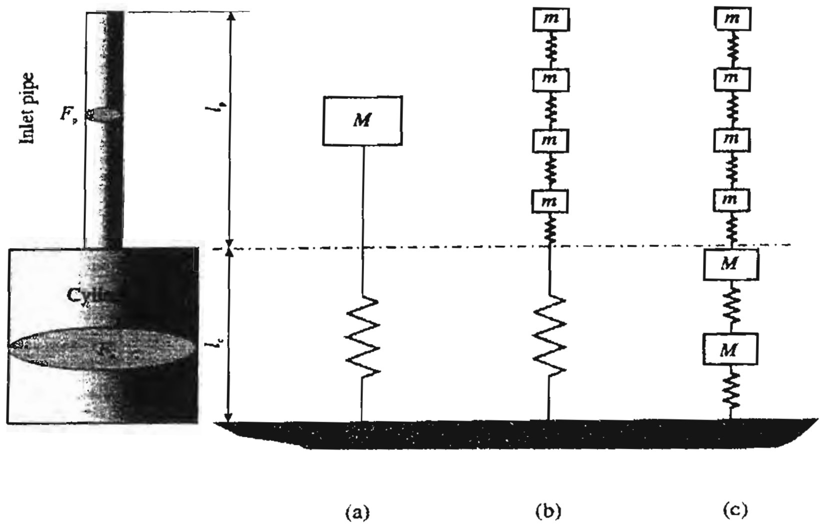

Figure 1.1: Methods of simulating a Helmholtz resonator:
(a) Engleman's lumped model, (b) distributed mass-lumped spring method, and (c) distributed parameter model

These methods were simple for the practicing engineer to use but did not provide any information about the overall amount of performance improvement and had no way of accounting for losses or being used in conjunction with combustion models. To overcome this deficiency, while retaining some of the simplicity of the frequency domain approach, Chapman *et al.* (1983) developed an innovative approach that is based on the linearized conservation equations in the intake and exhaust ducts combined with in-cylinder thermodynamics. The method consisted of three sub-models: (1) a series of coupled nonlinear Helmholtz resonators used to describe the flow in ducts; (2) an in-cylinder thermodynamic model, and (3) valve port boundaries that drive the system of Helmholtz resonators. Although the fluid compressibility in the ducts and the inertia in the volumes were assumed negligible, a reasonable correlation was obtained between the computational and experimental results for the single-cylinder and four-cylinder engines analyzed. While this method simplifies the duct calculations in a manner similar to linearized acoustics, it is capable of predicting the absolute magnitudes of performance parameters such as volumetric efficiency, as well as the time resolution of pressure, velocity, and density in the ducts.

More complex time-domain nonlinear approaches have been developed to allow for more accurate predictions by taking into account nonlinearities, flow losses, and heat transfer. This approach, to treat the unsteady conservation equations was first proposed by Benson *et al.* (1964) who employed the method of characteristics. Laksminarayanan *et al.* (1979) present a finite difference approach based on centered spatial differences and a Runge-Kutta temporal integration. Takizawa *et al.* (1982) use a two-step Lax-Wendroff finite differencing procedure to model the gas exchange process. The finite difference approach of Chapman *et al.* (1982) for engine simulation is based on a FRAM algorithm. With the rapid improvement in computing times, these numerical techniques are now widely used in the automotive industry for designing complex intake and exhaust systems.

1.2 Objective

The objective of the present experimental and computational study is to examine the effect of tapered geometry intake stacks on overall engine performance. This is achieved by performing motoring experiments over a wide range of operating speeds on a single cylinder engine with eight different tapered intake stacks. In order to isolate the effects of the tapered geometry, the experiments are conducted with no throttle body, identical bellmouthed and flanged openings and identical overall intake system lengths. Comparing the volumetric efficiency and the crank-angle resolved pressure at a number of locations in the intake, exhaust and in-cylinder reveals the effect of the geometry change. The study provides the experimental findings for: (1) the crank-angle resolved gas pressure at two locations in the intake system, one location in the exhaust manifold and in cylinder at speeds ranging from 1000 to 5500 rpm at 250 rpm increments; and (2) the volumetric efficiency of the engine at the same speeds for eight different intake stacks.

In view of the cost, the need for hardware, and the time frame associated with engine dynamometer experiments, a predictive tool is desirable to study the trends, narrow the options, and thereby accelerate the development process of engines and intake/exhaust systems. The ultimate objective of the work is to validate a finite difference approach for the prediction flow performance based on the work of Chapman *et al.* (1982) which solves the one-dimensional, variable cross-sectional area, nonlinear balance equations of mass, momentum and internal energy coupled with the equation of state for compressible flows. The model predictions for the volumetric efficiencies and pressures at a number of locations in the intake and exhaust system are then compared to the experimental results.

Following this introduction, Chapter 2 describes the dynamometer experimental setup, time-domain pressure and mass flow rate data acquisition, and the computational engine simulation code. Chapter 3 examines the results of the motoring single cylinder engine experiments. The calibration of the engine simulation code is discussed in Chapter 4, along with the comparison of predictions to experiments. The results from two simple linear frequency domain approaches are also provided. The study concludes with some final remarks in Chapter 5.

CHAPTER 2

EXPERIMENTAL SETUP AND COMPUTATIONAL APPROACH

The motoring dynamometer experiments are conducted on The Ohio State Unversity single cylinder engine. Eight different tapered intake stacks are used on the engine. The present study focuses on the motoring experiments and the computational results from a finite difference engine simulation code described later in this chapter.

2.1 Intake Geometries and Manufacturing

The complete induction system consists of dual intake valves, oval intake port, injector block, adapter section and the eight intake stacks (Figure 2.1). The eight intake stacks are connected to the engines using the same 12.05 cm long adapter section that provides a smooth transition from the round opening of the stacks that has a cross-sectional area of 13.8 cm^2 to the oval opening of the injector block and head face with a cross-sectional area of 12.37 cm^2. Once inside the head, the cross-sectional area of the intake system remains 12.37 cm^2 for approximately 2 cm and then splits into the two divided intake ports with cross-sectional areas of 5.95 cm^2. All the intake stacks maintain the same overall length of 26.45 cm and the same pressure transducer locations (Figure 2.1). The two intake pressure transducer locations, e11 and e12, are the same distance from the intake valves for each of the eight intake setups. Transducer locations e11 and

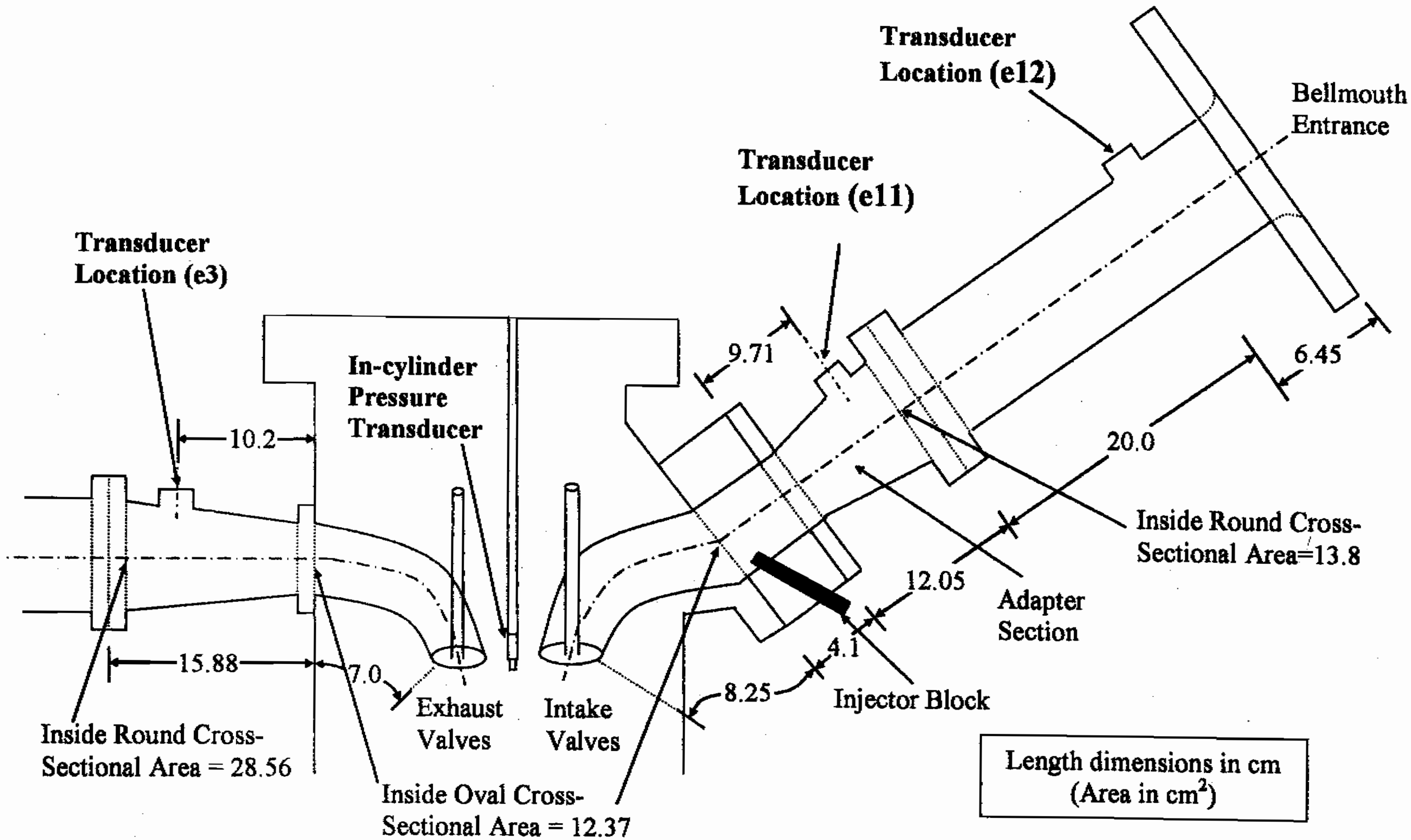

Figure 2.1: Schematic of Experimental Setup
OSU Single Cylinder Engine

e12 are 22.06 cm and 44.44 cm, respectively, from the intake valves. The overall length of the intake from bellmouthed entrance to valves is 50.85 cm. The 1 cm bellmouth radius at the intake opening is the same for each stack and smoothly transitions into a large flanged termination to ensure a hemispherical acoustic pattern for the pressure waves as they exit the bellmouthed entrance of each intake stack.

The physical dimensions of each intake stack are given in Table 2.1. The diameter (D_1) and area (A_1) at the bellmouthed entrance of the stacks is measured at the inner surface of the duct after the 1 cm radius. Intake #1 is a constant cross-sectional area or non-tapered piece and is used as a baseline for the rest of the comparisons [Figure 2.2 (a)]. Intakes #2 through #8 have different tapered geometries over different lengths of the intake stacks (L_t) as represented in Figure 2.2 (b). Intake #2 has a taper area ratio of 1.5 over 100% of the length of the intake stack. Intakes #3 and #4 also have a taper area ratio of 1.5 but L_t is only 50% and 25% respectively. Intake #5 has a taper area ratio of

<table>
<tr><th>Intake</th><th>L_t (cm)</th><th>D_1 (cm)</th><th>D_2 (cm)</th><th>Taper Area Ratio (A_1/A_2)</th></tr>
<tr><td>#1</td><td>No Taper</td><td>4.19</td><td rowspan="8">4.19</td><td>1</td></tr>
<tr><td>#2</td><td>26.45</td><td rowspan="3">5.13</td><td rowspan="3">1.5</td></tr>
<tr><td>#3</td><td>13.23</td></tr>
<tr><td>#4</td><td>6.613</td></tr>
<tr><td>#5</td><td>26.45</td><td rowspan="2">5.93</td><td rowspan="2">2</td></tr>
<tr><td>#6</td><td>13.23</td></tr>
<tr><td>#7</td><td rowspan="2">26.45</td><td>6.62</td><td>2.5</td></tr>
<tr><td>#8</td><td>7.26</td><td>3</td></tr>
</table>

Table 2.1: Intake Stack Dimensions

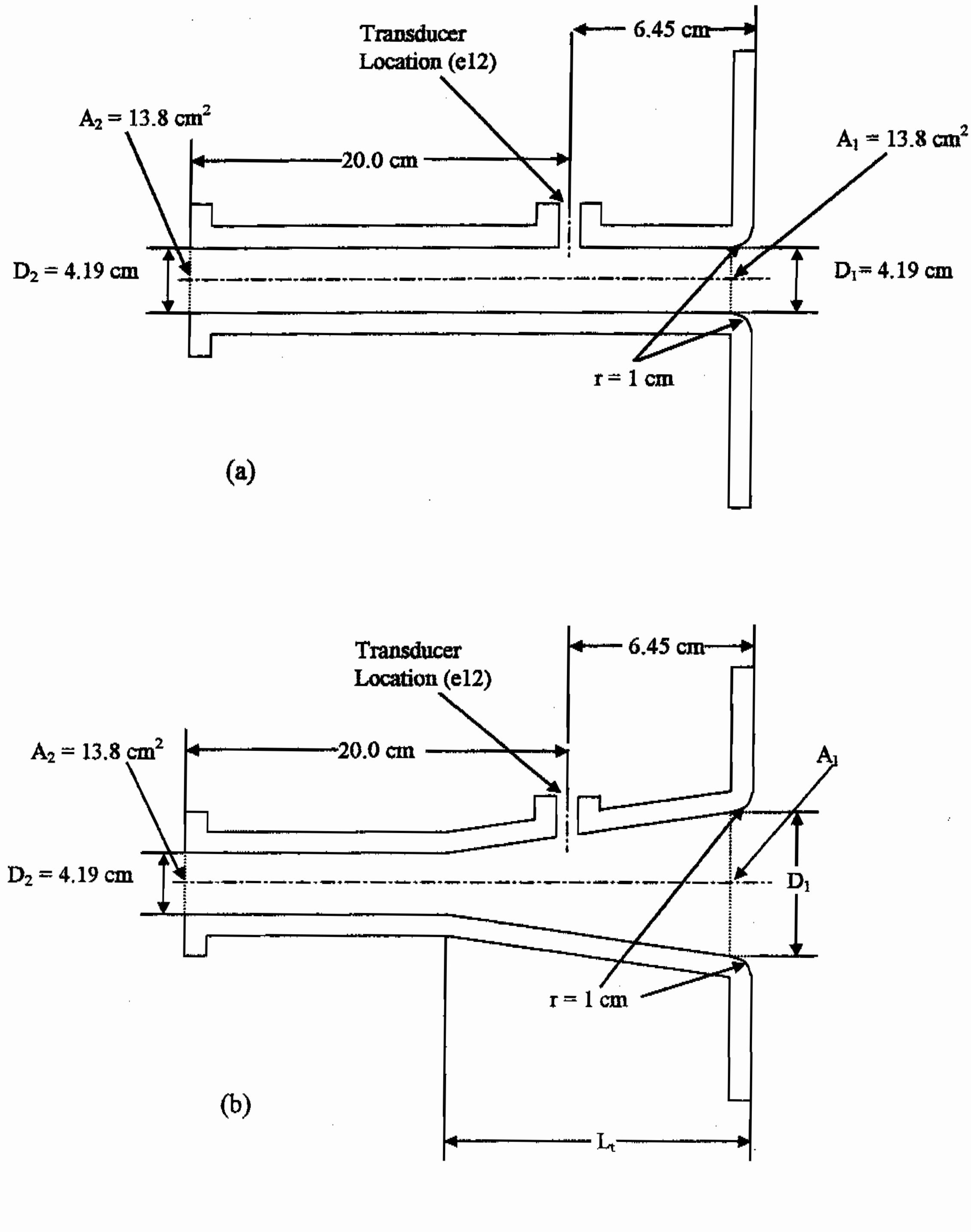

Figure 2.2: Intake Stack Schematic
(a) Intake #1 - Baseline (b) Intake #2 - #8 - Tapered

2.0 over 100% of its length. Intake #6 has a taper area ratio of 2.0 over only 50% of its length. Intake #7 has a taper area ratio of 2.5 over 100% of its length. Finally, Intake #8 has the largest taper area ratio of 3.0 and it is over 100% of its length.

The intake stacks and the adapter section are rapid prototype plastic pieces built by the stereo-lithography method. They were created in a computer aided design program and transferred to the stereo-lithography machine via a direct program conversion interface. The stereo-lithography machine can then read the converted file, which is made up of many thin 2-D cross sections. The stereo-lithography machine is made up of a laser, bin of photocurable liquid acrylate resin, and an elevator in the bin. The laser traces the current 2-D cross section onto the surface of the liquid resin, which solidifies when struck by the intense UV light. The elevator then lowers the hardened cross section below the surface of the liquid resin and the next cross section is traced on top with the laser. This cycle repeats until the part is completed and then the part is removed from the bin for a final UV light post cure. This rapid prototyping process has provided quality pieces with good dimensional accuracy for all of the intake stacks.

2.2 OSU Single Cylinder Engine Description

The single cylinder engine located at The Ohio State University's Center for Automotive Research was used to conduct all motoring experiments and is setup with components from a 2.5L Ford V-6 engine. This engine is solely used for the purpose of research but maintains the overall engine specifications of the Ford 2.5L engine, which are listed in Table 2.2. The engine has dual overhead cams with direct acting lobes and a dry oil sump. Its only external accessory is a belt-driven Peterson racing oil pump to provide the engine oil from the six-gallon external oil sump. The engine block and oil are cooled with water supplied from a large external cooling tower and circulated with electric pumps. These two cooling systems are computer and thermostatically controlled to maintain constant engine operating temperatures. For the experiments in the study, the water and oil temperatures were maintained at 70°F.

Bore	8.153 cm
Stroke	7.95 cm
Clearance Volume	41.4 cm^3
Rod Length	13.81 cm
Compression Ratio	10.0:1
Maximum Valve Lift	
Intake	0.8382 cm
Exhaust	0.94234 cm
Valve Timing	
Intake Open	45° BTDC
Intake Duration	320°
Exhaust Open	105° BBDC
Exhaust Duration	335°

Table 2.2: OSU Single Cylinder Overall Engine Specifications

The engine exhausts through a 15.88 cm long adapter section similar to that of the intake (Figure 2.1). It allows for a smooth transition from the oval port exit at the head face to the round cross sectional area of the exhaust piping. The exhaust system consists of several sections of straight pipe, three 90° mandrel bent elbows and one 45° mandrel bent elbow as illustrated in Figure 2.3. A 24 cm long flexible coupling was installed in the exhaust system to help reduce the vibrations. The exhaust system terminates approximately 15 cm inside an 80-gallon expansion tank. The motoring dynamometer power sweeps were initially conducted from 1000 to 5000 rpm. Some additional data

Dimensions	
L_1	15.88
L_2	17.73
L_3	30.03
L_4	46.07
L_5	183.92
L_6	140.31
θ_1	90°
θ_2	45°

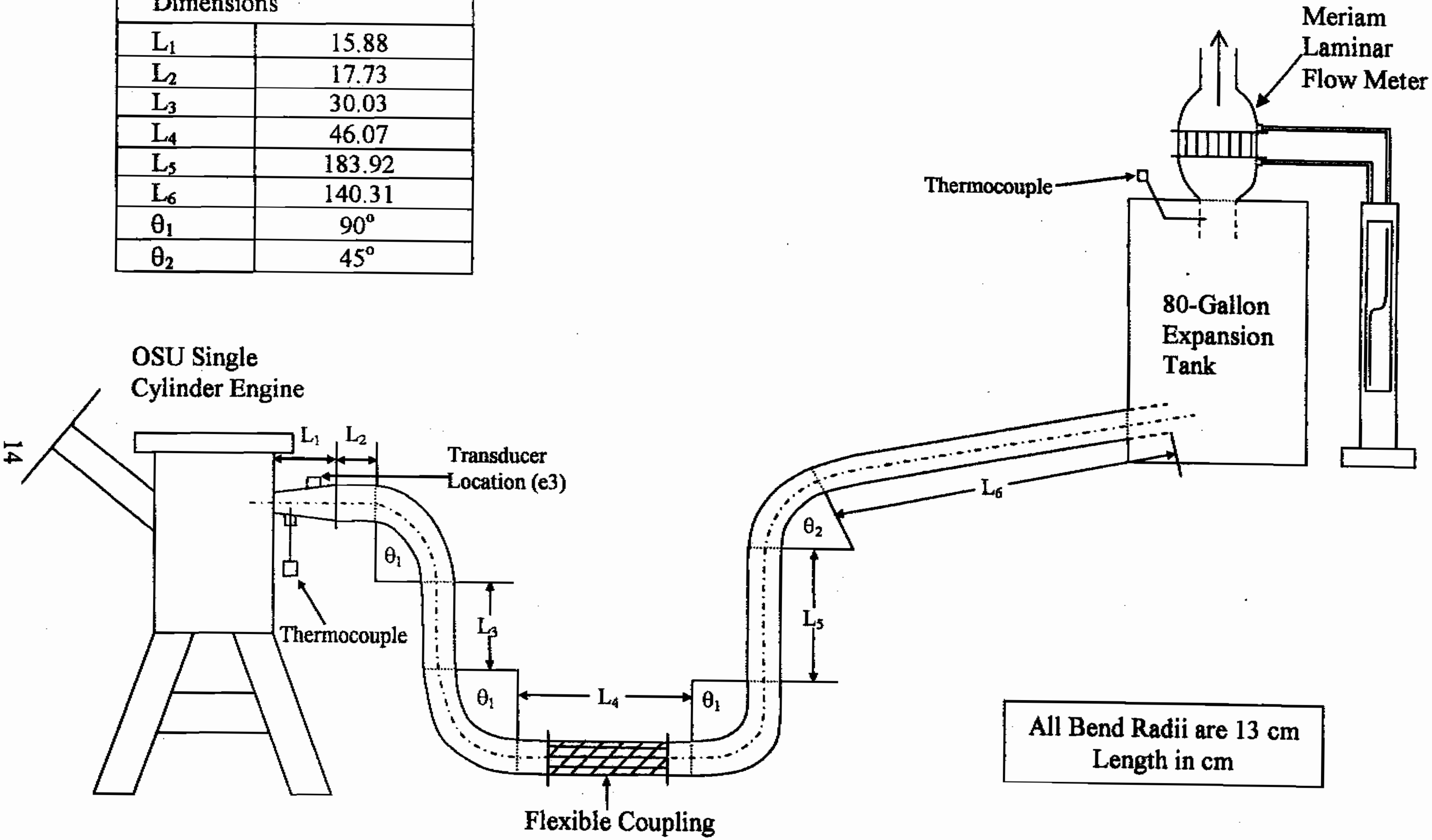

Figure 2.3: Exhaust System Schematic

was obtained at 5250 and 5500 rpm to ensure that the peak volumetric efficiency had been reached for particular intake stacks showing higher rpm trends. The engine is rotated by a General Electric direct current dynamometer Model #426403AE with a maximum motoring speed of 6300 rpm. The dynamometer is controlled by a Dynesystems Dyn-Loc IV and a Horiba computer system.

2.3 Pressure and Volumetric Efficiency Measurements

The crank-angle resolved pressures are measured at both intake system locations and in the exhaust system using Kistler 4045A2 piezoresistive pressure transducers. The signal is amplified by Kistler model #4603A piezoresistive amplifiers. All the amplified signals are recorded using a Concurrent Masscomp model #7250 high-speed data acquisition computer. This computer is coupled to a Concurrent CPU model #MC68040 running a RTU based operating system. This system is capable of acquiring data simultaneously from 32 channels at a sampling rate of 2 MHz and has a 12 bit A/D converter. The raw intake and exhaust pressure data are collected for 64 cycles, and averaged per crank-angle degree (CAD) to determine an average time-dependent pressure profile at every location for a given engine speed. The average intake and exhaust pressure traces are then corrected to the ambient atmospheric conditions measured near the intake during the experiments.

The intake pressure transducers are installed into the pressure tap locations (e11 and e12) using a brass insert. The brass insert slides into the tap locations and is sealed using vacuum grease. The center of the insert is drilled and tapped to the transducer dimensions so that it may be securely threaded in. This installation ensures that the transducer is sealed and that its height is always maintained flush with the inner intake stack wall. The bottom of the brass inserts for tap location e12 is machined to the same radius as the inside of the intake stacks to provide a smooth transition from the rounded inner surface of the intake stack to the flat surface of the transducer face. The exhaust pressure transducer is installed in much the same way except that it is threaded directly into a welded on bung in the first section of exhaust piping (Figures 2.1 and 2.4). During initial installation, the transducer height was adjusted flush with the inner wall of the exhaust piping and then used at this height for all experiments.

The in-cylinder pressure is measured using a PCB piezoelectric transducer model #145A07 connected to a PCB model #462A charge amplifier. The crank-angle resolved pressure is acquired for a total of 256 consecutive cycles. The voltage output from the amplifier is sent to the high-speed data acquisition system and is averaged per crank-angle. The in-cylinder pressure transducer is installed through the cylinder head into the top center section of the combustion chamber between the intake and exhaust valves and next to the spark plug. The output of the piezoelectric transducer has a bias voltage. Thus, the measured pressure is relative and needs to be corrected (pegged) to absolute. Averaging the pressure measurements from the intake piezoresistive transducer at location e11 at one degree before bdc, at bdc, and one degree after bdc after the intake stroke is a reasonable approximation to the actual in-cylinder pressure. This averaged intake pressure at e11 combined with the average of the same three CAD of the relative in-cylinder pressure measurements gives the correction factor for pegging. The correction factor is then added to all crank-angle resolved data to obtain the absolute in-cylinder pressure trace for the entire cycle.

To determine the volumetric efficiency of the motoring engine, a laminar flow meter is placed in the exhaust system as shown in Figure 2.4 and the exhaust gas flow rate is determined by measuring the pressure drop across a calibrated flow element. A Meriam Laminar Flow Meter model #50MC2-4SF is used with a maximum flow capacity of 400 cfm. The exhaust piping from the engine to the expansion tank is completely sealed using flanged connections, gaskets, and silicone sealant to ensure the flow measurement accuracy. The flexible coupling was sealed by wrapping it with a plastic sheet and sealing the ends with an elastic tape.

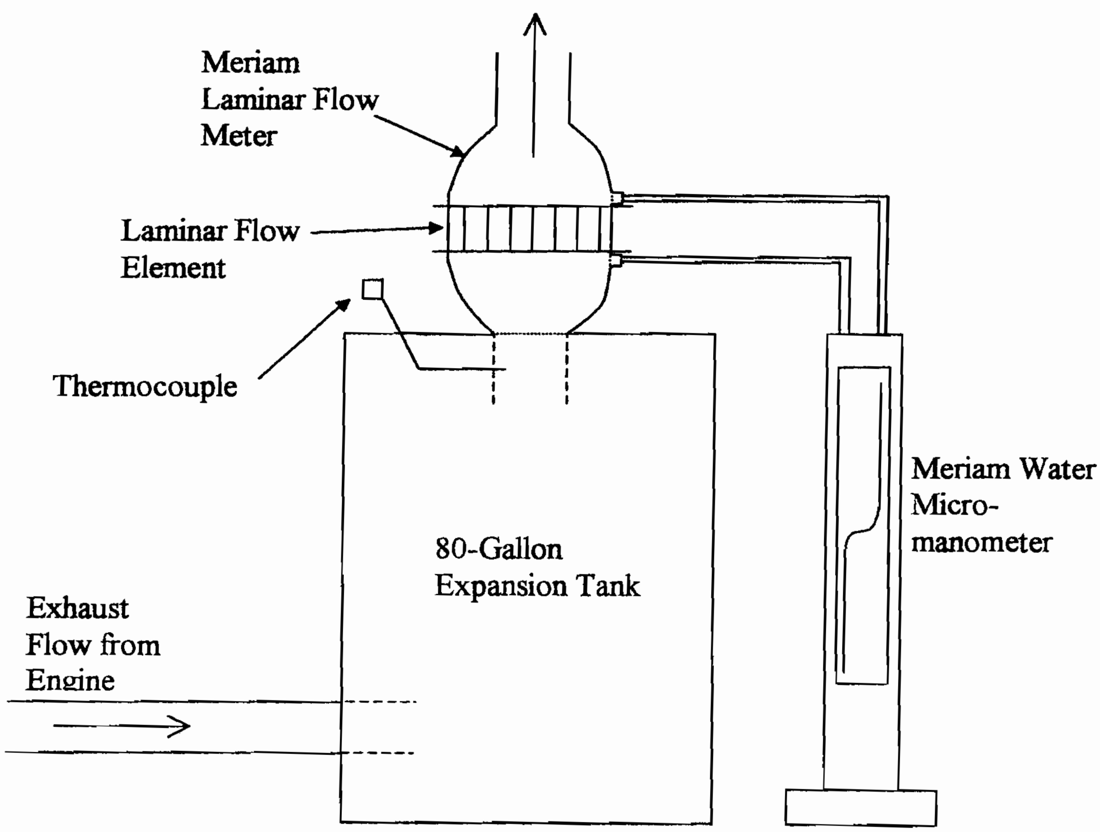

Figure 2.4: Laminar Flow Meter Schematic

The exhaust pipe is routed into a sealed opening at the bottom of the 80-gallon expansion tank. The large expansion tank allows the exhaust gases to both expand and cool prior to entering the flow meter and suppresses the pulses in the gas flow, thereby allowing a more accurate flow measurement. The flow meter was calibrated at OSU using the Ford Scientific Laboratories flowbench, which is capable of flowing 1150 cfm at up to 35 in H_2O or 350 cfm at 90 in H_2O across the test piece. The ambient pressure and temperature was 29.92 in Hg and 70°F respectively during the flowlab calibrations. The flow meter accuracy is dependent on both of these atmospheric conditions, thus any variation from these conditions must be accounted for with correction factors. Tables were supplied from the manufacturer of the flow meter with correction factors for both temperature and pressure variations. To ensure accurate temperature measurements, a thermocouple is inserted through the expansion tank and into the flow meter just upstream of the flow element (Figure 2.4). The range of temperatures at the flow meter during the engine experiments was only from 60°F to 80°F thus producing only minor corrections. The ambient pressure is measured in the dynamometer cell and then the pressure drop across the flow element is subtracted from ambient to get the exact pressure upstream of the element. The pressures at the flow meter entrance ranged only from 29.5 in Hg to 29.7 in Hg.

A pressure tap is located both upstream and downstream of the calibrated laminar flow element and the pressure difference across it can be read directly from the connected Meriam water micro-manometer (Figure 2.4). The water micro-manometer is manually operated with a range of 0 to 6 in H_2O and an accuracy of 0.001 in H_2O. This pressure difference is then converted to a volumetric flow rate (in cfm) by using the flowbench calibration graph. The volumetric flow rate is corrected, if needed, for both temperature and pressure as described earlier using the supplied tables. The corrected volumetric flow rate is then converted to the metric units of m^3/s and used to get the mass flow rate:

$$\dot{m}_a = \rho_{a,i}\dot{V}, \tag{2.2}$$

where $\dot{m}_a$ is the mass flow rate (kg/s), $\dot{V}$ the volumetric flow rate (m^3/s), and $\rho_{a,i}$ the air inlet density. A value of $\rho_{a,i}$ =1.20 kg/m^3 was used based on atmospheric conditions of 70° F and 29.92 in Hg. The volumetric efficiency can then be directly determined using the mass flow rate, the engine speed and the engine specifications as

$$\eta_v = \frac{2\dot{m}_a}{\rho_{a,i}V_d N}, \tag{2.3}$$

where η_v is the volumetric efficiency, V_d the volume displaced by cylinder (m^3), and N the engine speed (rev/s).

2.4 Computational Approach - Formulation

Ford Motor Company's MANDY (MANifold flow DYnamics) engine intake/exhaust flow dynamics simulation program used in this study is an extension of the nonlinear, one-dimensional finite difference scheme presented by Chapman *et al.* (1982). The code was originally developed to aid in the design of intake and exhaust manifolds and cam/lift profiles of automobile engines to obtain improved wide open throttle torque and horsepower. This finite difference scheme is based on a FRAM algorithm that allows for the use of a higher order finite difference scheme in regions where the flow is smooth and introduces a minimal amount of dissipation only in those regions where a higher order algorithm would produce non-physical oscillations. It is a second order accurate technique where the truncation error is third order in the spatial discretization of cell sizes. It is a numerical technique that solves the mass, momentum, and energy balance equations for compressible, unsteady, gasflow throughout the intake and exhaust flow passages. For one-dimensional flow in ducts of variable cross section with neglected axial conduction, the governing equations may be expressed as,

$$\frac{\partial}{\partial t}(\rho A)+\frac{\partial}{\partial t}(\rho A U)=0, \tag{2.3}$$

$$\frac{\partial}{\partial t}(\rho A U)+\frac{\partial}{\partial t}\left(\rho A U^{2}\right)+\frac{\partial}{\partial x}(p A)-\tau_{w} P=0, \tag{2.4}$$

$$\frac{\partial}{\partial t}(\rho A e)+\frac{\partial}{\partial t}(\rho A U e)+p \frac{\partial}{\partial x}(U A)-\tau_{w} P U+q P=0, \tag{2.5}$$

where ρ is the density, A the cross-sectional area, U the velocity, p the pressure, τ_w the wall shear stress, P the perimeter, e the internal energy, and q the wall heat transfer per unit area. The ideal gas equation of state,

$$p=(\gamma-1)\rho e, \tag{2.6}$$

is used to relate the thermodynamic variables and close the system of equations with γ being the ratio of specific heats. Atmospheric pressure and temperature provide the boundary conditions at the air inlet and the exhaust pipe outlets. The staggered mesh used in the discretization of the balance equations divides a duct into cells with vector quantities located at node points, denoted by spatial index j, and scalar quantities at cell midpoints, denoted by j +/-1/2 (Fig. 2.5).

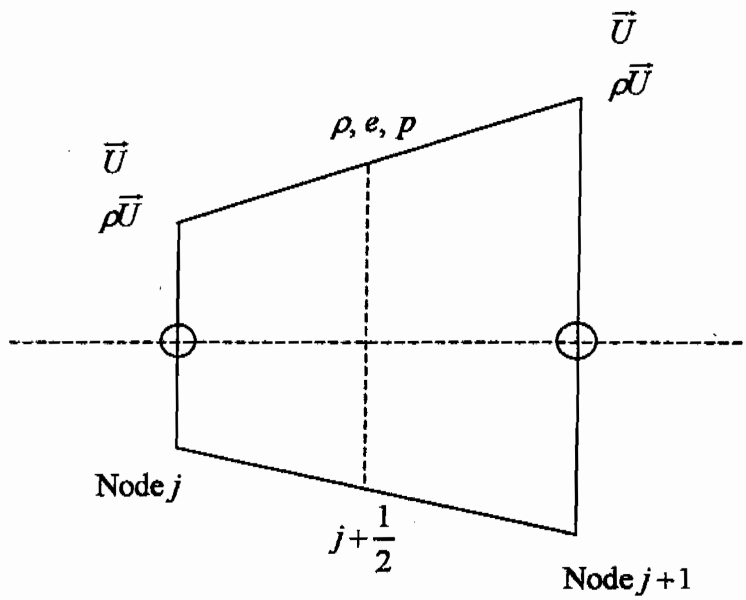

Figure 2.5: Duct Discretization and Variable Centering in Numerical Scheme.

The key sub-models within the code include: (1) The in-cylinder thermodynamic variation of pressure, specific internal energy, and temperature as functions of the piston motion, heat transfer to and from the cylinder walls, and combustion energy release schedule; (2) The mass flow rate of air and exhaust gases across the valves as functions of the valve lift profiles; (3) The rate of heat transfer to the port and manifold walls; (4) The thermodynamic properties of the gases within the cylinder and flow passages; and (5) Flow losses due to bends, junctions, abrupt area changes, and other transition geometries such as throttle orifices. For further details, the reader is referred to earlier publications by Chapman *et al.* (1982) and Selamet *et al.* (1994).

CHAPTER 3

MOTORING ENGINE: EXPERIMENTAL RESULTS AND DISCUSSION

3.1 Introduction

To improve the understanding of tapered intake runners on engine performance, dynamometer experiments are conducted with eight different tapered intake stacks (Table 2.1) on a single cylinder engine. This chapter focuses on the results obtained from the motored single cylinder engine at OSU. Experiments are conducted with each stack at speeds ranging from 1000 to 5500 rpm at 250 rpm increments. The geometry, setup, and data acquisition for all eight intake stacks are described in Chapter 2 (Refer to Figures 2.1 and 2.2 for the measurement locations and intake dimensions.) Pressures are acquired at two locations (e11 and e12) in the intake, in the cylinder, and at one location in the exhaust (e3). The mass flow rate is also measured to determine the volumetric efficiency as described in Section 2.4. All other variables such as overall intake length, mounting configuration and measurement locations are maintained for each experiment to isolate the effect of the tapered geometry.

Following a brief Introduction, Section 3.2 discusses the impact of different tapers on the volumetric efficiency of the engine. Section 3.3 examines the measured pressure traces from the intake system at locations e11 and e12 for the eight intake stacks and relates them to the measured volumetric efficiency. Section 3.4 discusses the in-cylinder pressure results using the pumping loop section from the log p-log V diagram. Finally Section 3.5 reports and evaluates the exhaust pressure traces.

3.2 Volumetric Efficiency

Volumetric efficiency is an overall measure of the effectiveness of an internal combustion engine and its breathing system as an air pumping device. If all other variables remain the same, volumetric efficiency is proportional to the mean effective pressure and torque and thus provides valuable information about an engine's performance capabilities. The volumetric efficiency of the motoring engine is determined in this study by measuring the exhaust flow rate using a laminar flow meter (Fig. 2.4) and then converting it to volumetric efficiency using Eqs. (2.2) and (2.3) as described in Section 2.4.

The measured volumetric efficiency is shown in Figs. 3.1 - 3.10. Figures 3.1 - 3.7 retains the straight Intake #1 as a baseline in comparison with each of the seven tapered intakes. Figure 3.8 compares the three 50% tapered intake stacks (Intake #2, #3 and #4) and Fig. 3.9 compares the two 100% tapered intake stacks (Intake #5 and #6). These groupings isolate the effect of the different length of tapers on the volumetric efficiency. Figure 3.10 compares the four full length tapered intakes (Intake #2, #5, #7, and #8) to show the effect of increasing taper size only. All curves cover a range of 1500 rpm to 5500 rpm, where the repeatability was satisfactory and estimated error was less than 2%. Speeds lower than 1500 rpm were excluded due to the magnitude of error introduced by the laminar flow meter, as discussed in Section 2.4.

Figure 3.1 shows the volumetric efficiency comparison of Intake #1 and #2. Most notable is the shift of the two high speed peaks at 3750 and 4750 rpm for Intake #1 to 4250 and 5000 rpm, respectively, for Intake #2. From 2500 rpm and higher, the volumetric efficiency for the two intakes is similar in magnitude, including the high speed peaks. An rpm shift for the peak locations of volumetric efficiency is expected as the tapered intakes are going to have a larger cross-sectional area, A_p. A simple method to explain this trend would be to use the classical lumped parameter approach which models the intake system as a Helmholtz resonator first proposed by Thompson and Engleman (1969). This approach gives the resonance frequency of the system, f_R, as

$$f_R = \frac{c_o}{2\pi}\sqrt{\frac{A_p}{l_p V_c}}\,, \tag{3.1}$$

where c_o is the speed of sound, l_p the length of intake pipe, and V_c is ½ the swept volume of cylinder plus clearance volume. This equation shows directly that an increase in area leads to an increase in the system natural frequency. Thus, as the cross-sectional areas increase, a higher engine speed will be expected before the system hits resonance and provides the peak beneficial ramming effect. This behavior of high speed peak shifting is evident in the experimental results as the percentage of taper increases for Intake #5, #7, and #8.

Figure 3.2 compares Intake #1 and #3 and shows a smaller shift in the two high-speed peaks. Intake #3 has its two dominant peaks at 4000 and 4750 rpm and maintains nearly the same volumetric efficiency magnitudes as Intake #1. Figure 3.3 compares Intake #1 and #4, which shows basically the same shift in high-speed peaks as Intake #3. Intake #4 does, however, show the highest peak volumetric efficiency of all the intakes at

4750 rpm and shows a reasonable improvement at 3250 rpm as well as maintaining nearly the same magnitudes or better at most other speeds.

Figure 3.4 compares Intake #1 with #5, which is the second full length taper at 100%. This figure shows the two high speed peaks for Intake #1 at 3750 and 4750 rpm have now shifted up to 4500 and 5250 rpm for Intake #5. As discussed earlier, this trend is expected, showing an increase of an additional 250 rpm at both peaks over Intake #2. The tapered geometry negatively affects the magnitude of the volumetric efficiency for the most part, particularly at the peak locations. As the taper area ratio gets larger and the diameter increases at the intake inlet, the inertia effect at the natural frequency is less because the reflection coefficient at the ambient junction is reduced (Selamet *et al.* 2001). This reduces the tuning effect because the compression wave coming back to the intake valve is weaker. This trend continues as the tapers get larger (Figs. 3.6 and 3.7) and is also seen as an amplitude loss in the intake pressures for the larger tapered intakes (Figs.3.14 – 3.17). Figure 3.5 compares Intake #1 and #6 and shows the high speed peak shift from 3750 and 4750 rpm to 4250 and 5000 rpm, respectively. The peak volumetric efficiency and the overall magnitude throughout the speed range are similar to those of Intake #1. Figure 3.6 compares Intake #1 and #7 and shows the shift in high speed peak and reduction in both peak and overall volumetric efficiency. Intake #7 shows its first high speed peak at 4500 rpm with a second peak expected at 5500 rpm based on earlier intake experiments and the code predictions to be discussed in Chapter 4 (Fig. 4.11). From approximately 3000 rpm and above the overall volumetric efficiency is also lower when compared to Intake #5 (Fig 3.4) confirming the trend that larger taper diminishes the inertia effect. Figure 3.7 compares Intake #1 to #8 which is the largest tapered duct at

200%. The visible high speed peak has now moved from 3750 rpm for Intake #1 to 4750 rpm for #8 and a second high speed peak is expected near 5500 rpm. This is confirmed by the engine simulation code in the next chapter (Fig. 4.12). Intake #8 shows the lowest peak and most overall loss of volumetric efficiency following the discussed trends.

Figure 3.8 compares the three 50% tapered intake stacks #2, #3, and #4. The full length tapered stack (Intake #2) shows a 250 rpm increase in both high speed peaks over the other two partial length tapered stacks (Note even the shift at the 3500 rpm peak.). Intake #4, tapered for only 25% of its length, shows the highest peak magnitude of the three at 4750 rpm. Figure 3.9 compares the two 100% tapered intake stacks #5 and #6. This figure displays similar trends as the 50% tapered stacks (Fig 3.8) with the full length tapered stack (Intake #5) having peaks 250 rpm higher and having a lower peak magnitude than the partial length stack (Intake #6). Intake #6 shows identical engine speeds for both high speed peaks at 4250 and 5000 rpm and very similar volumetric efficiency magnitudes as Intake #2. As intake #6 has twice as much taper but only half the tapered length of Intake #2, this appears to show that similar volumetric efficiency trends can be obtained by either one size taper over the full length of the stack or doubling the taper size over only half of the length. Figure 3.10 shows the four full length tapered intakes #2, #5, #7 and #8. This figure clearly shows both trends of the high speed peak shifts and the volumetric efficiency reduction as the taper is increased over the full length of the stack.

3.3 Intake Pressure Traces

The crank-angle resolved pressure in the intake is measured at two locations (e11 and e12) as shown in Fig. 2.1 and described in Section 2.3. Location e11 is significantly closer to the intake valve and thus shows greater magnitude variations for all speeds. The significant trends for phasing of major peaks and valleys and relative magnitudes are however captured well at e12. For brevity, the following discussion for the comparison of intake pressures is limited to pressures at e11 corresponding to the peak volumetric efficiency speeds of a representative set of intake stacks (Intake #1, #2, #5, and #7). This set of intakes was chosen due to its wide range of tapers and the fact that experimental data were acquired at or near both high speed volumetric peaks. The highest speed peak for Intake #7 is actually expected between 5250 and 5500 rpm based on Chapter 4 computational results. The discussion will also focus on the portion of the cycle between intake valve opening (IVO) and intake valve closing (IVC). Table 3.1 lists the engine speeds discussed in this section for each of the four intakes involved. All experimental data acquired at both e11 and e12 with each of the eight intake stacks at every engine speed can be found in Figs. A.1 – A.74 of Appendix A.

Intake	High Speed Volumetric Efficiency Peaks	
#1	3750 rpm	4750 rpm
#2	4250 rpm	5000 rpm
#5	4500 rpm	5250 rpm
#7	4500 rpm	5250 rpm

Table 3.1: Engine Speeds for High Speed Volumetric Efficiency Peaks

Figure 3.11 shows pressure traces only for Intake #1 in the vicinity of both high speed volumetric peaks of 3750 and 4750 rpm. This figure attempts to demonstrate the pressure trends in the intake leading up to and just after the volumetric peaks. Figure

3.11 shows that the pressure peak in the intake just before IVC is highest at the volumetric efficiency peak speeds of 3750 rpm and 4750 rpm. This trend is seen in all other intake stack pressures for the first high speed peak. For the second high speed volumetric peak, several of the intakes (Intake #2, #3, #4, and #6) have larger magnitude pressure peaks before IVC at higher engine speeds. These higher pressure peaks are shifted later in the cycle and occur to close to IVC and thus do not provide any additional positive tuning effect. Thus, the results support the idea discussed in the Introduction that tuning would occur if the initial rarefaction wave returns to the valve in the form of a compression wave before the intake valve closes.

Figures 3.12 – 3.17 compare the intake pressures for Intake #1 to those of Intake #2, # 5 and #7 at the engine speeds listed in Table 3.1. These figures show how the pressure traces for different intake stacks vary, sometimes significantly, at the same engine speeds. Figure 3.12 compares Intake #1 and #2 at the first high speed volumetric peak for each intake. Figure 3.12 (a) (3750 rpm) shows that the pressure peak before IVC is much greater for Intake #1. At 4250 rpm [Fig.3.12 (b)], however, the pressure peak before IVC for Intake #2 has increased and becomes larger than Intake #1 thus improving the volumetric efficiency. Note that Fig. 3.1 clearly shows an approximately 8% higher efficiency for Intake #1 at 3750 rpm and a 1% higher efficiency for Intake #2 at 4250 rpm.

Figure 3.13 also compares Intake #1 and #2 but at the second high speed peak for each intake. Again, the peak pressure for Intake #1 is significantly greater than Intake #2 in Fig. 3.13 (a) (4750 rpm). Figure 3.13 (b) (5000 rpm) shows noticeable increase in the peak pressure for Intake #2 but it is still lower than Intake #1. The pressure peak for

Intake #1 is, however, 10 CAD later, which appears to be sufficient to negate any additional tuning effect. This result illustrates that the magnitude of the pressure peak before IVC is not the only factor influencing the volumetric efficiency. Other factors such as in-cylinder pressure and the phasing of the pressure peak in relation to IVC are also important for determining volumetric efficiency magnitudes. Intake #1, with its higher peak intake pressure before IVC, has approximately 8% lower volumetric efficiency than Intake #2 at 5000 rpm (Fig. 3.1).

Figure 3.14 compares Intake #1 and #5 at the first high speed peak for each intake. Figure 3.14 (a) (3750 rpm) shows that Intake #1 has a greater pressure peak before IVC. The pressure peak occurs approximately 25 CAD closer to IVC but not so close to reduce the tuning effect as seen in Fig. 3.13 (b) for Intake #1. At 4500 rpm, the pressure peak for Intake #5 has increased and shifted toward IVC to match the phasing of Intake #1. The magnitude of the pressure peak for Intake #1 is still larger. The volumetric efficiency curve comparing these two intakes (Fig. 3.4) shows that even though 4500 rpm is a peak for Intake #5, it actually has a lower efficiency by about 4% than Intake #1.

Figure 3.15 compares Intake #1 and #5 at the second high speed peak for each intake. At 4750 rpm, Fig. 3.15 (a) shows that Intake #1 once again has a higher peak pressure before IVC. At 5250 rpm [Fig. 3.15(b)], Intake #1 still has a higher peak pressure but the peak occurs 8 CAD later in the cycle and, similar to the comparison involving Intake #2, does not provide any additional positive tuning effect.

Figure 3.16 compares Intake #1 and #7 at the first high speed peak for each intake. Fig 3.16 (a) shows that Intake #1 has significantly higher pressure peak before

IVC at nearly the same CAD. The magnitude difference and the phasing are similar to those in Fig 3.12 (a) for Intake #2. The volumetric efficiency curves for Intake #7 (Fig. 3.6) and Intake #2 (Fig. 3.1) support this magnitude difference by showing that both intakes have substantially less (8 - 9%) volumetric efficiency at 3750 rpm. Figure 3.16 (b) (4500 rpm) shows that the peak pressure for Intake #7 increased but is still lower than Intake #1, while maintaining the same phase. The volumetric efficiency curve for Intake #7 (Fig. 3.6) reveals that the efficiency has increased for Intake #7, when compared to Intake #1, but is still approximately 5% lower.

Figure 3.17 compares Intake #1 and #7 at or near the second high speed peak for each intake. At 4750 rpm [Fig 3.17(a)], Intake #1 shows the greatest magnitude difference in peak pressure before IVC. This correlates with Fig. 3.6, which also shows the greatest efficiency difference of approximately 7% at this speed for the foregoing intakes. Figure 3.17 (b) (5250 rpm) shows that the pressure peak has increased for Intake #7 but remains well below the peak for Intake #1. Due to the 8 CAD shift of the pressure peak for Intake #1 and the extra area under curve for Intake #7 leading up to the peak, the volumetric efficiency for these two intakes is nearly identical at this engine speed.

3.4 In-Cylinder Pressure Traces

The crank-angle resolved pressure in the cylinder is acquired with one piezoelectric transducer as described in Section 2.3. Due to the overall range of this pressure transducer, its accuracy is significantly less than the intake and exhaust transducers used in the study. With motoring experiments, the pumping loop portion of the engine cycle (the exhaust and intake strokes) is of most interest. The pressure in the cylinder during this during the pumping loop remains near 1 bar [Fig. 3.18(a)]. With the error range of the transducer and careful analysis of the experimental data, it was determined that the in-cylinder pressure data was not of sufficient quality for extensive comparisons. All experimental data acquired from the in-cylinder transducer are presented in Figs. A.75 – A.98 of Appendix A. The reader is cautioned that the accuracy is significantly reduced from the intake and exhaust data. Figure 3.18 is presented as the only typical example. Figure 3.18 (a) shows the Intake #1 p-v loop for three engine speeds and does show a low pressure period just before top dead center of the intake stroke for the engine speed where peak volumetric efficiency occurs. This trend of lowest pressure in the cylinder during the intake stroke at the highest speed volumetric efficiency peak is noted in Intake #1 - #6. Experimental data was not acquired at high enough engine speeds to determine the highest speed volumetric efficiency peak for Intake #7 and #8. Figure 3.18 (a), also, illustrates some of the inconsistencies discovered in the data including the small loop seen near top dead center before the exhaust stroke most notably for 2000 rpm and the narrowing of the pumping loop near bottom dead center for the higher speeds. Figure 3.18 (b) shows how the in-cylinder and intake pressure at e11 differ in both amplitude and phasing during the intake portion of the cycle and how jagged the in-cylinder trace is even though it is averaged over 256 cycles from a motoring engine.

3.5 Exhaust Pressure Traces

The crank-angle resolved pressure in the exhaust is acquired as described in Section 2.3 at one location identified as e3 (Fig. 2.1). The geometry changes in the intake system with the eight intake stacks had only a minimal effect on the exhaust pressures. The discussion in this section is therefore limited to comparisons of the exhaust traces for Intake #1 and #8 at engine speeds ranging from 1500 rpm to 5000 rpm at 500 rpm increments. These two intakes have the largest geometric difference and produce the largest variation in pressure traces. The variation is also not significantly different at each engine speed so 500 rpm increments are used for brevity. All experimental data acquired at e3 with each of the eight intake stacks at every engine speed can be found in Figs. A.99 – A.122 of Appendix A.

Figures 3.19 - 3.22 show the comparison of experimental exhaust pressure results for Intake #1 and #8. The general shape of the pressure traces changes significantly for every engine speed, yet the results in the exhaust are quite similar even for these two largely geometrically different intakes. One noticeable difference in the results is that Intake #8 leads Intake #1 for all engine speeds from 1500 rpm to 4500 rpm by approximately 10 CAD at most locations. The lead becomes smaller as the engine speed increases with the traces becoming basically identical at 5000 rpm. Intake #8 also shows slightly smaller amplitudes at the peaks and valleys, along with some peak smoothing at lower engine speeds. By 3500 rpm, the amplitudes become very similar and remain so throughout the rest of the speed range.

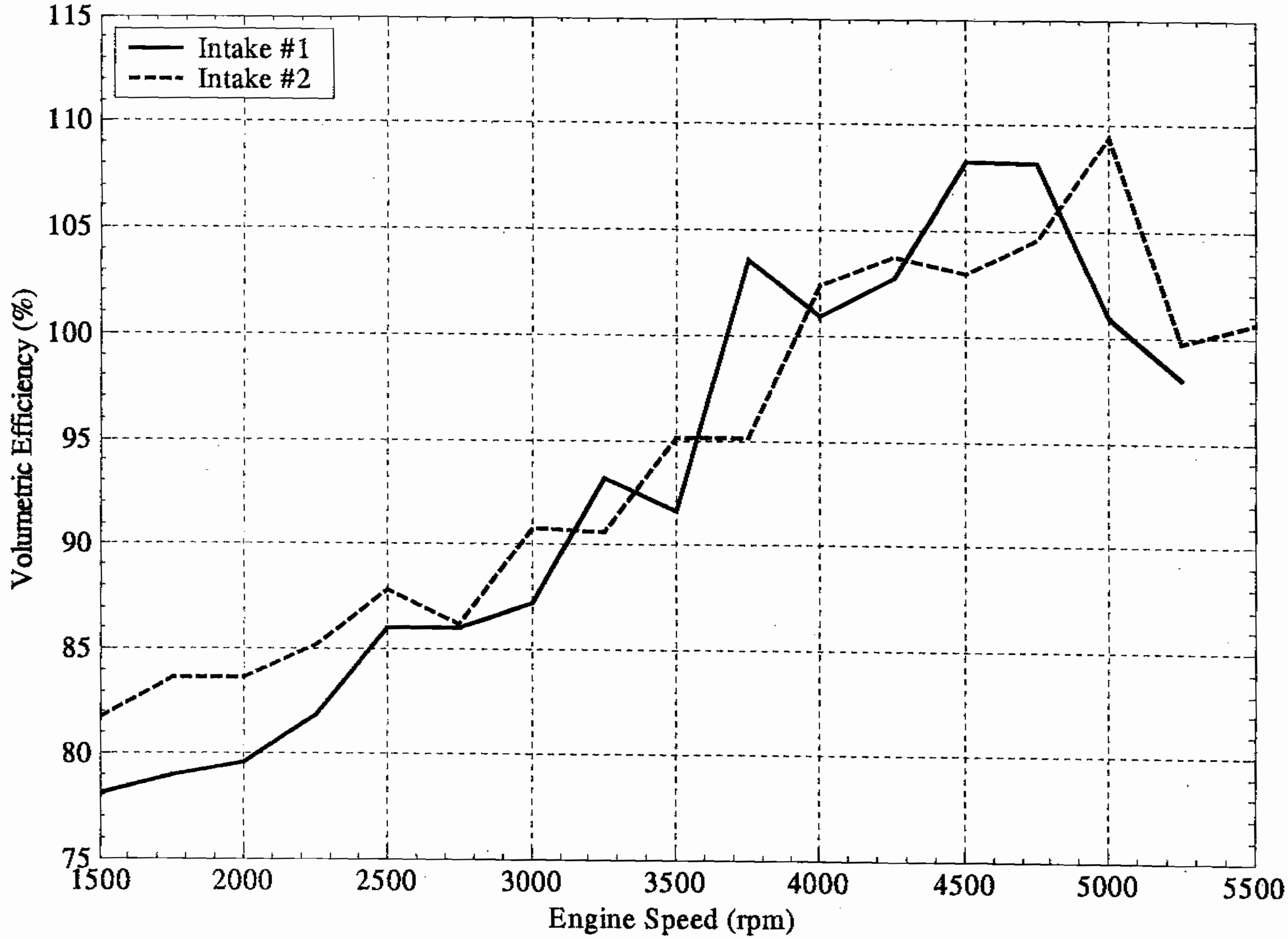

Figure 3.1: Single Cylinder Motoring Experiment:
Volumetric Efficiency for Intake #1 and Intake #2

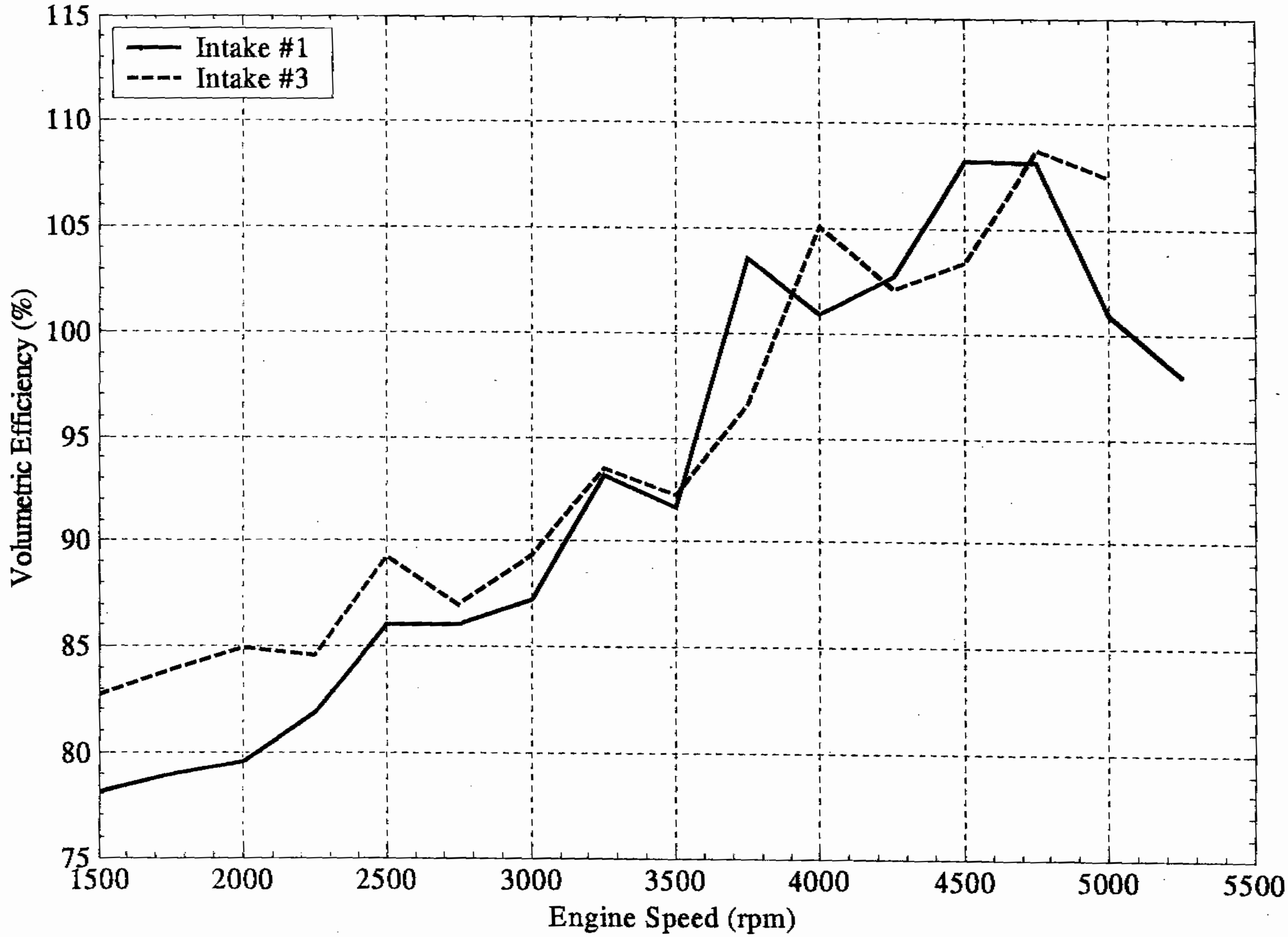

Figure 3.2: Single Cylinder Motoring Experiment:
Volumetric Efficiency for Intake #1 and Intake #3

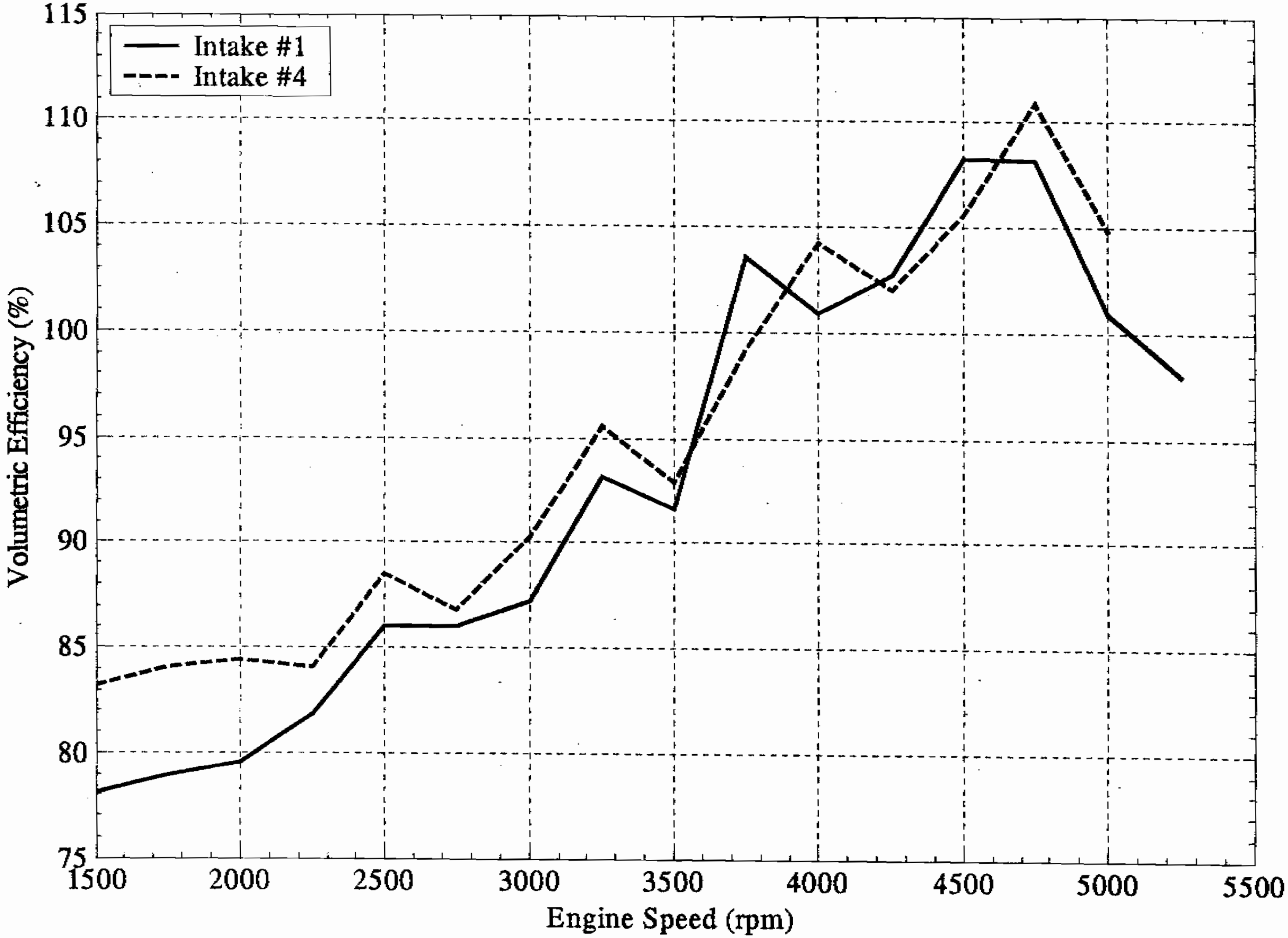

Figure 3.3: Single Cylinder Motoring Experiment:
Volumetric Efficiency for Intake #1 and Intake #4

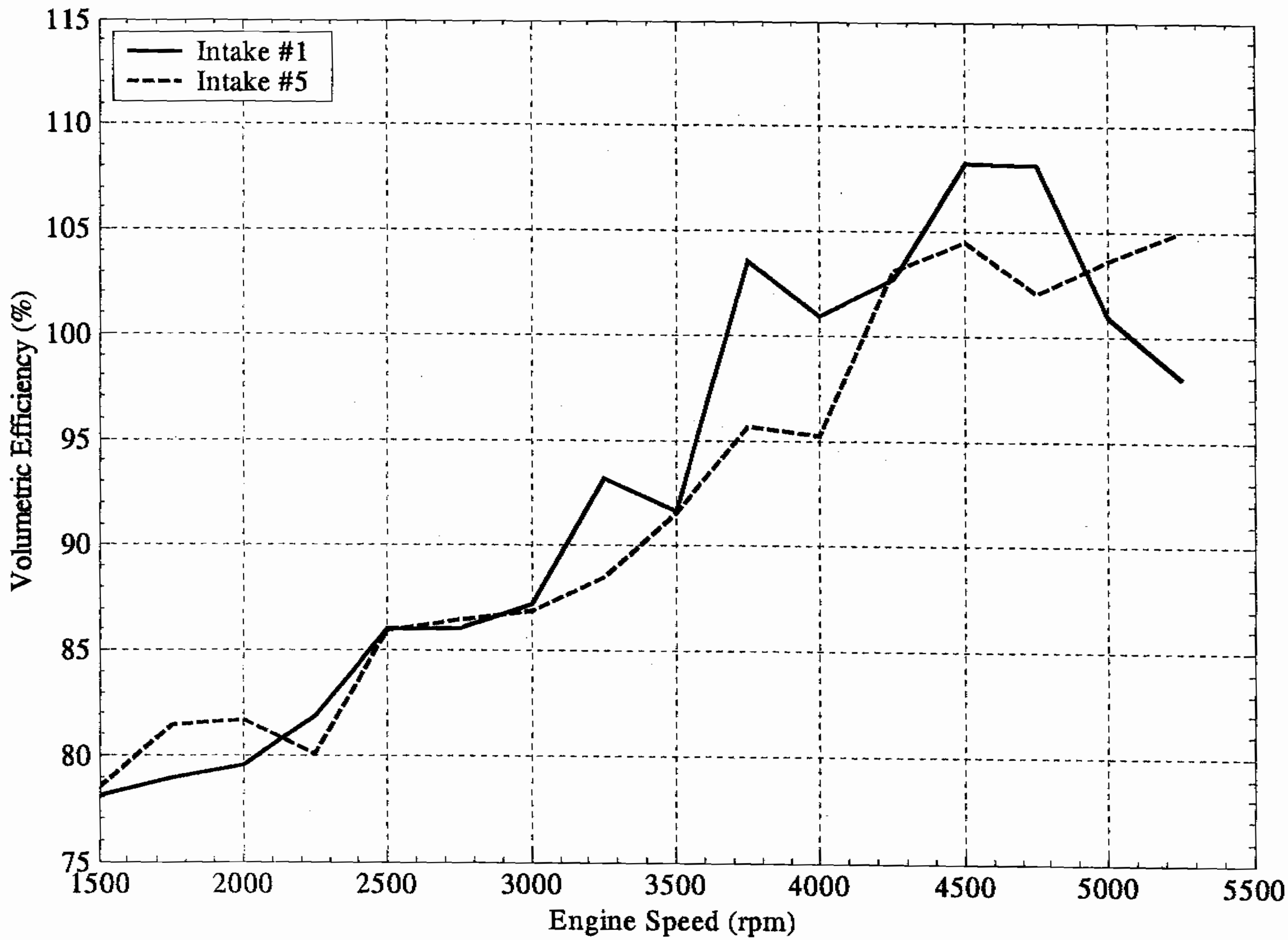

Figure 3.4: Single Cylinder Motoring Experiment:
Volumetric Efficiency for Intake #1 and Intake #5

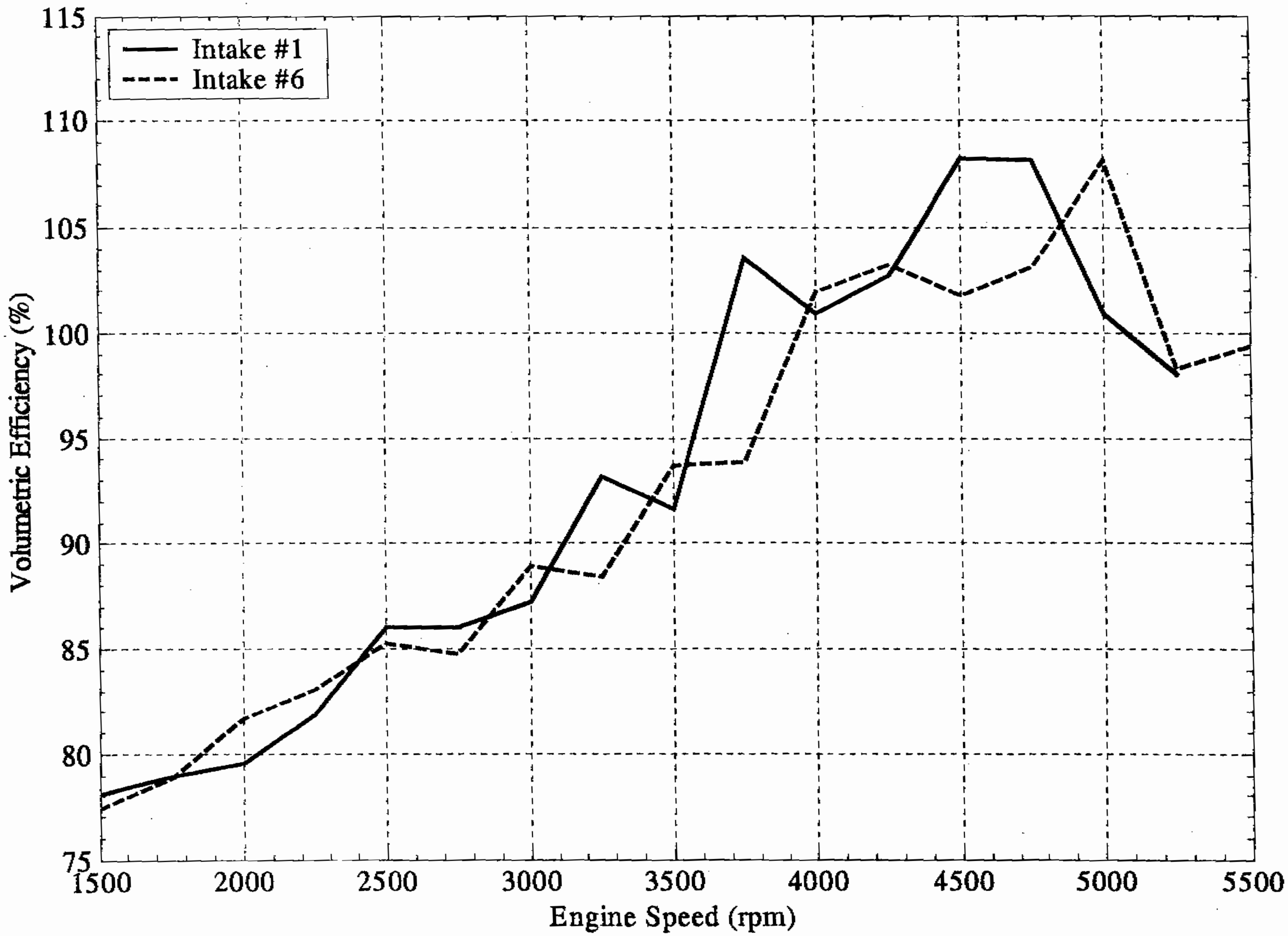

Figure 3.5: Single Cylinder Motoring Experiment:
Volumetric Efficiency for Intake #1 and Intake #6

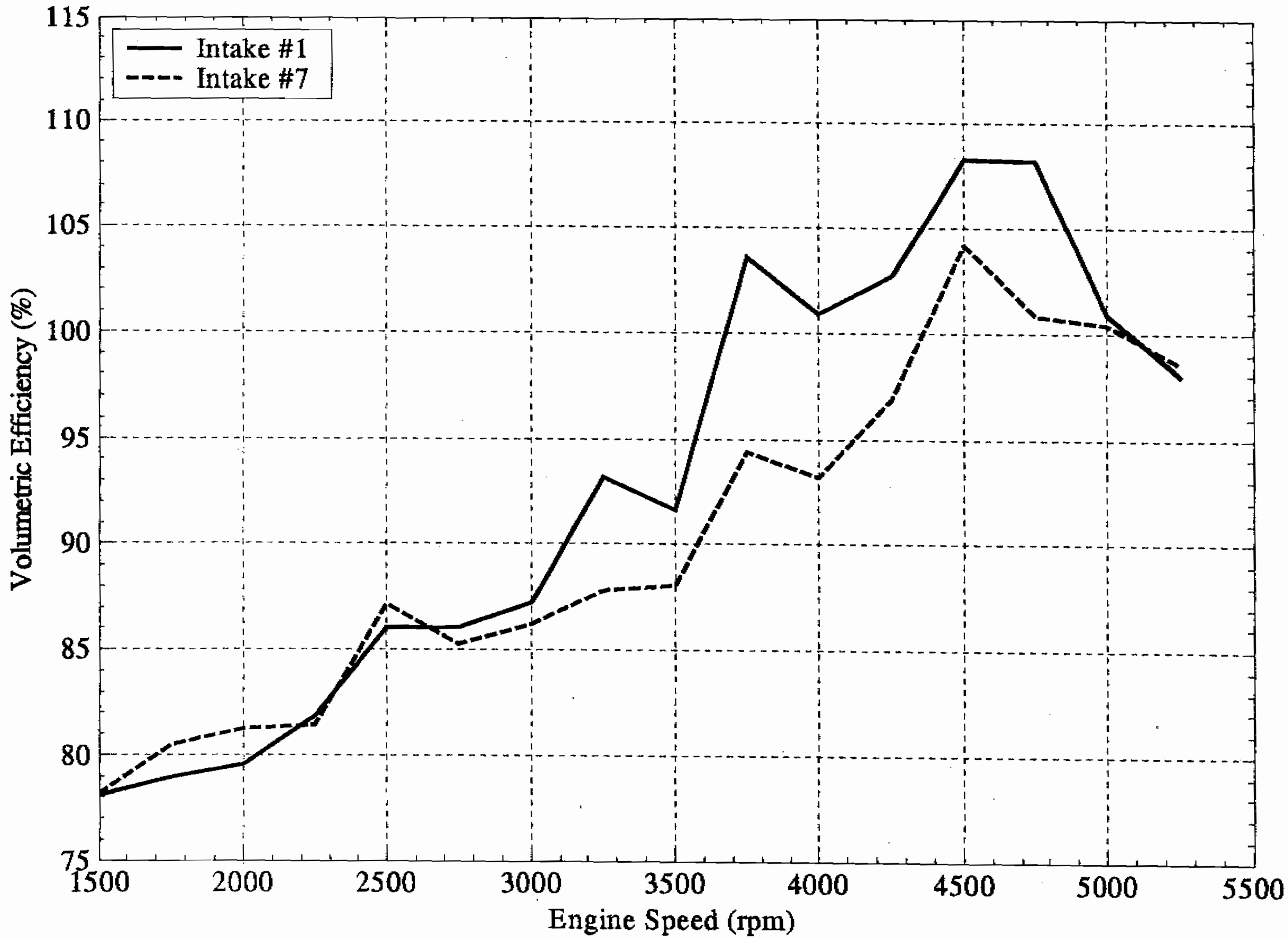

Figure 3.6: Single Cylinder Motoring Experiment:
Volumetric Efficiency for Intake #1 and Intake #7

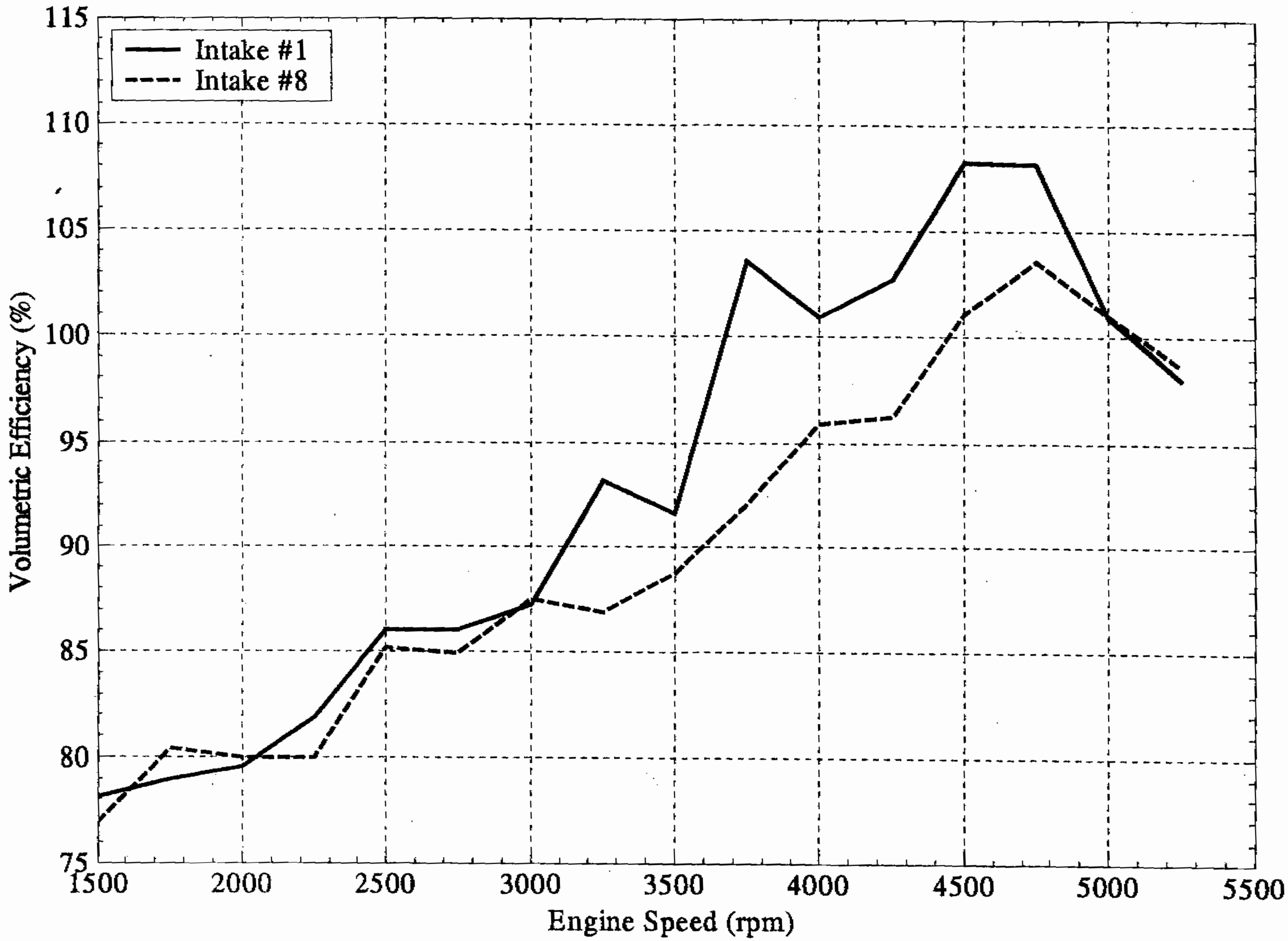

Figure 3.7: Single Cylinder Motoring Experiment:
Volumetric Efficiency for Intake #1 and Intake #8

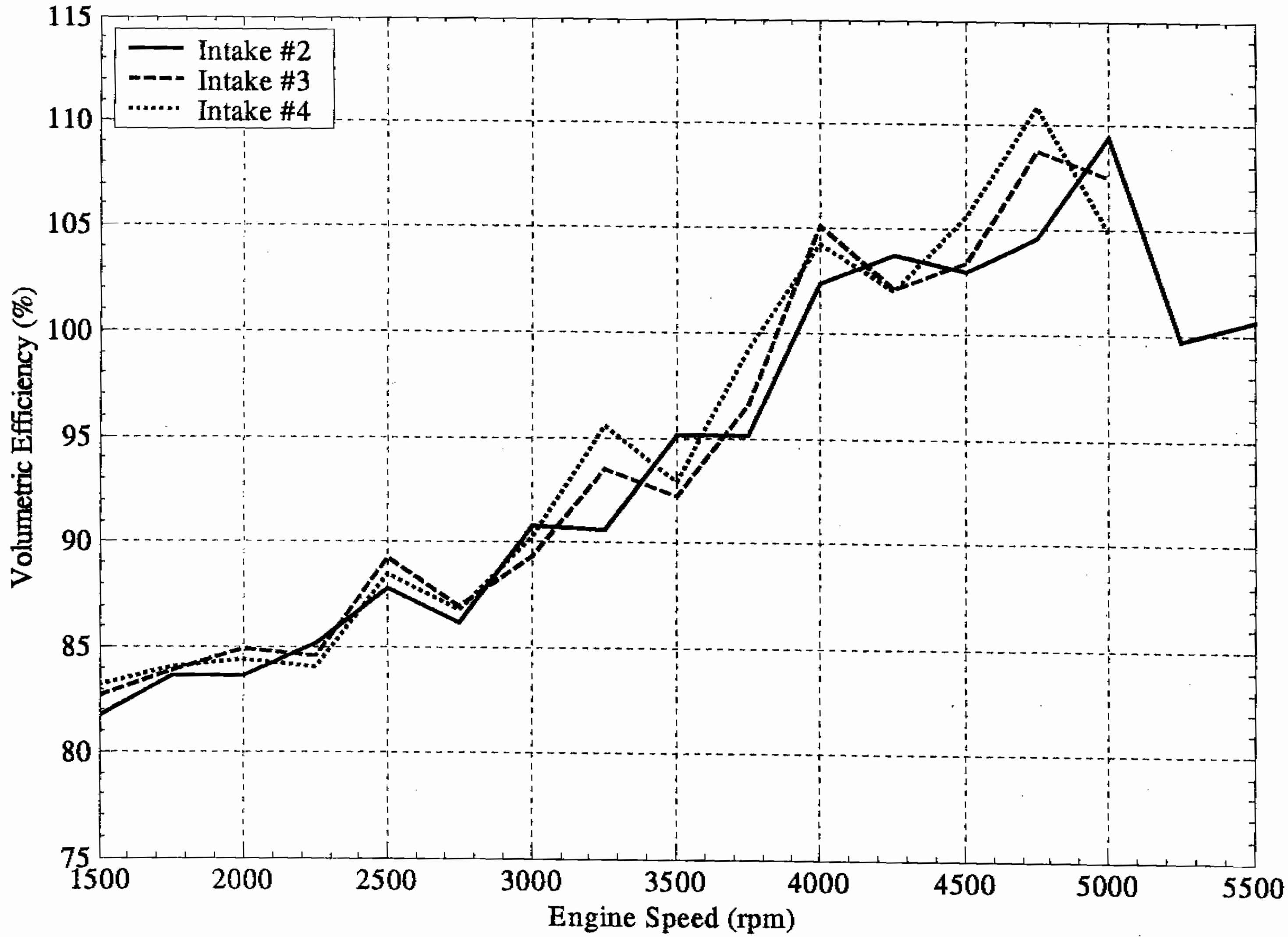

Figure 3.8: Single Cylinder Motoring Experiment: Volumetric Efficiency for 50% Tapers - Intake #2, Intake #3 and Intake #4

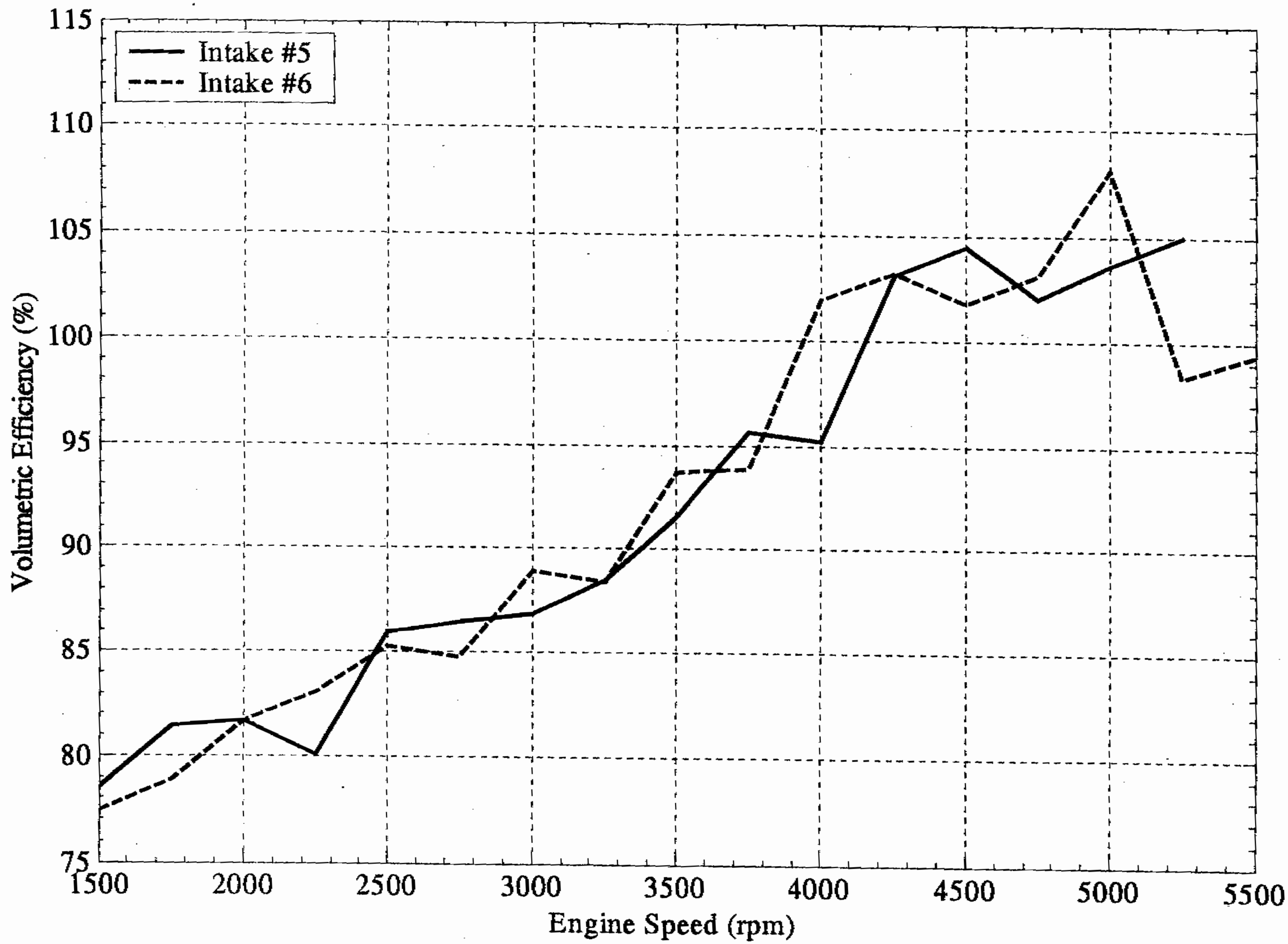

Figure 3.9: Single Cylinder Motoring Experiment: Volumetric Efficiency for 100% Tapers - Intake #5 and Intake #6

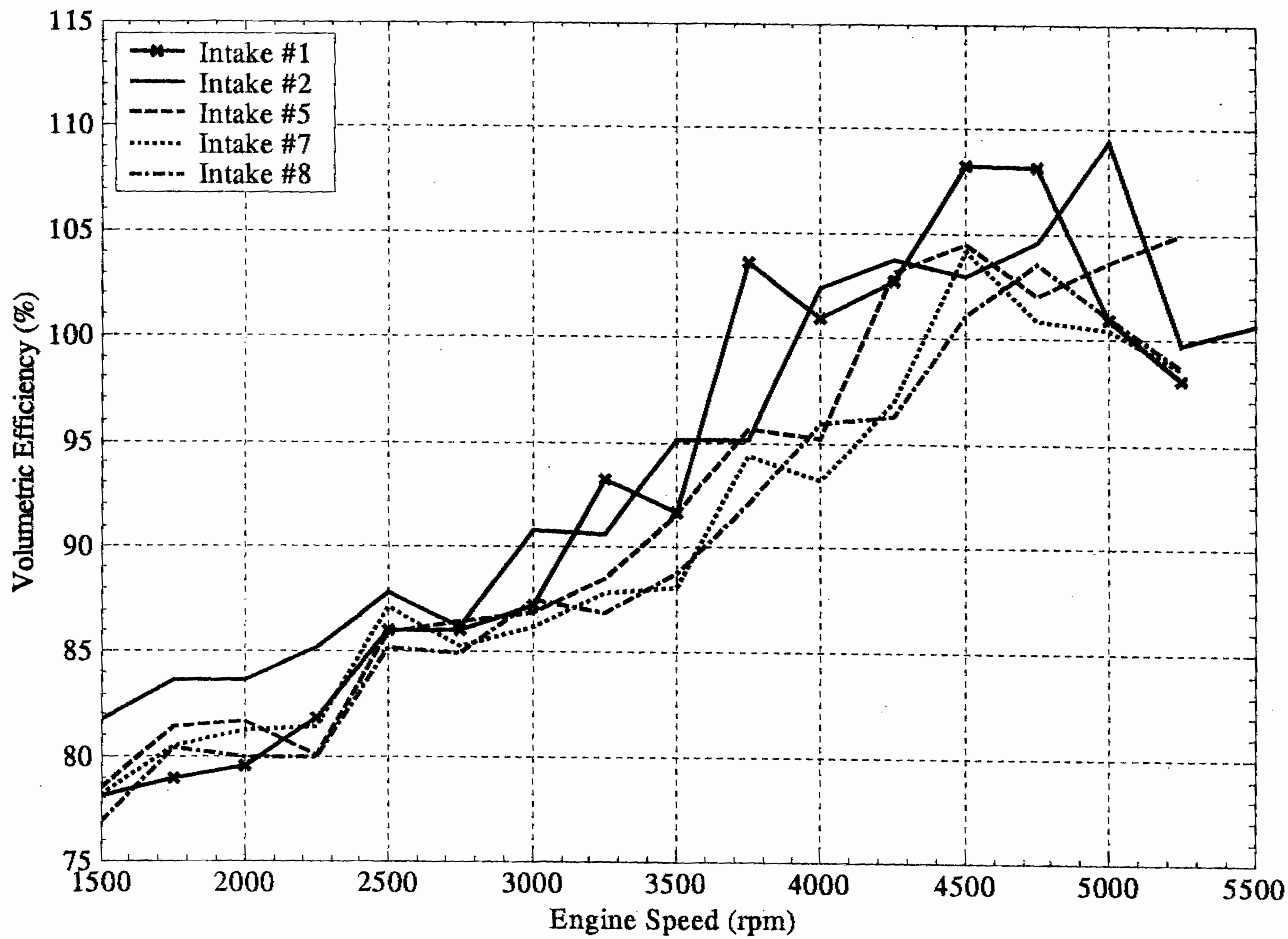

Figure 3.10: Single Cylinder Motoring Experiment: Volumetric Efficiency for Full Length Tapers - Intake #1, Intake #2, Intake #5, Intake #7, and Intake #8

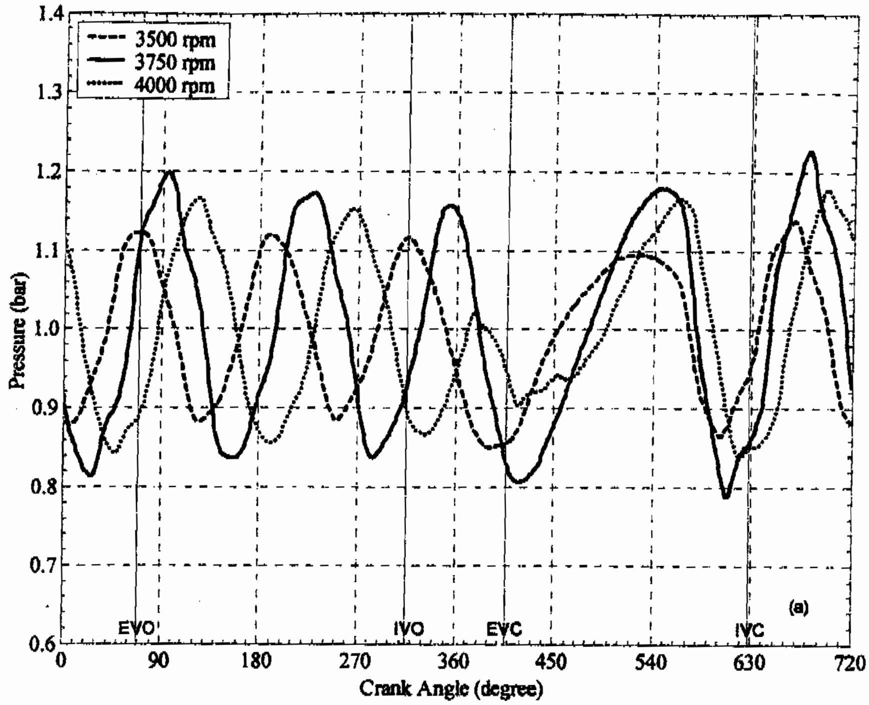

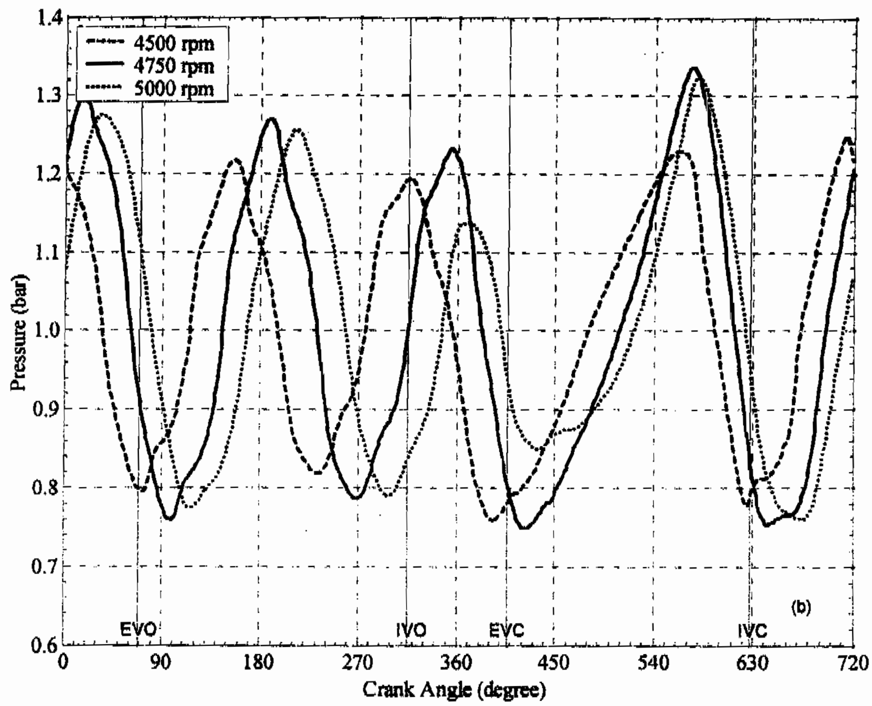

Figure 3.11: Single Cylinder Motoring Experiment: Intake Pressure (e11) for Intake #1 at Volumetric Efficiency Peaks of (a) 3750 rpm and (b) 4750 rpm

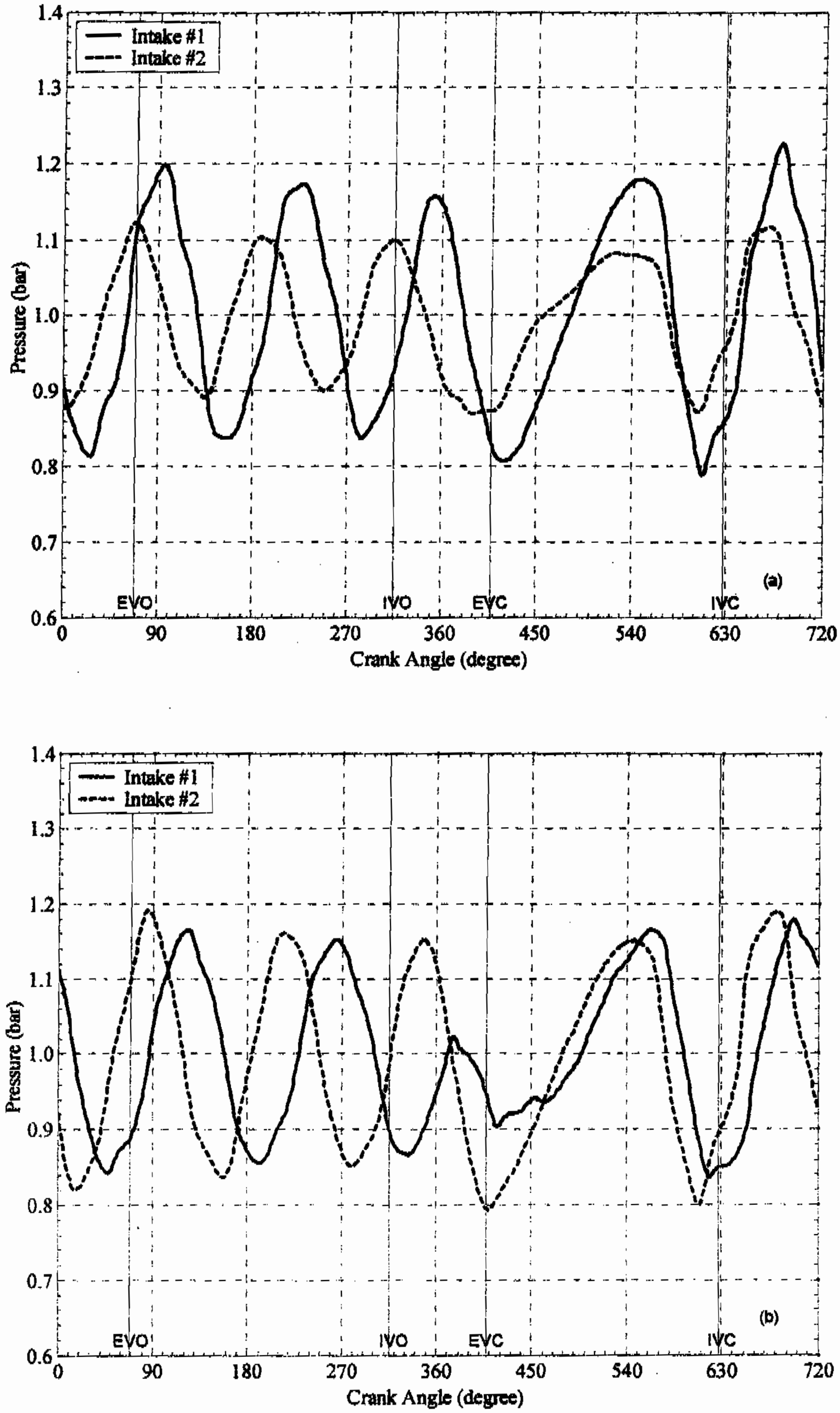

Figure 3.12: Single Cylinder Motoring Experiment: Intake Pressure (e11) for Intake #1 and Intake #2 at (a) 3750 rpm and (b) 4250 rpm

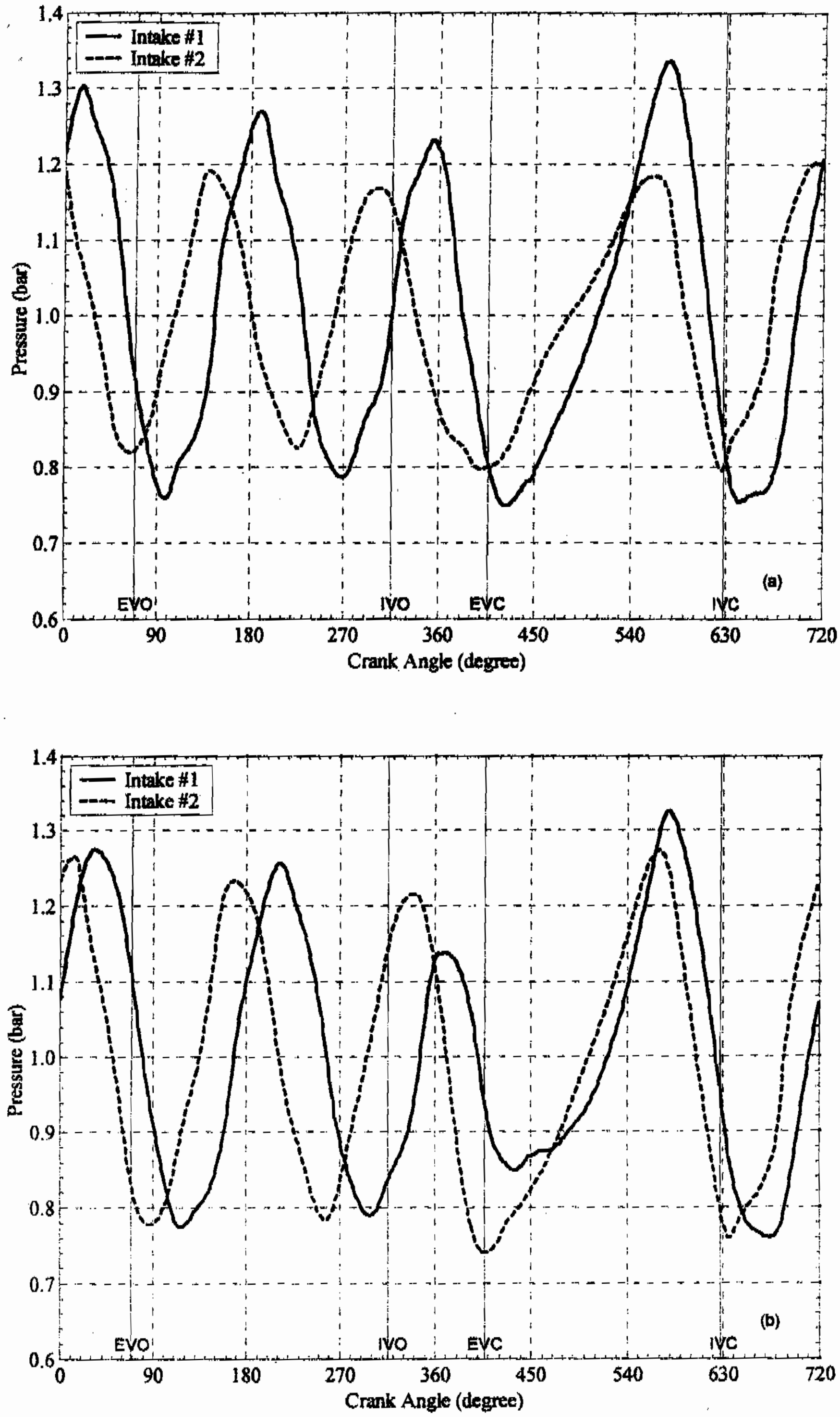

Figure 3.13: Single Cylinder Motoring Experiment: Intake Pressure (e11) for Intake #1 and Intake #2 at (a) 4750 rpm and (b) 5000 rpm

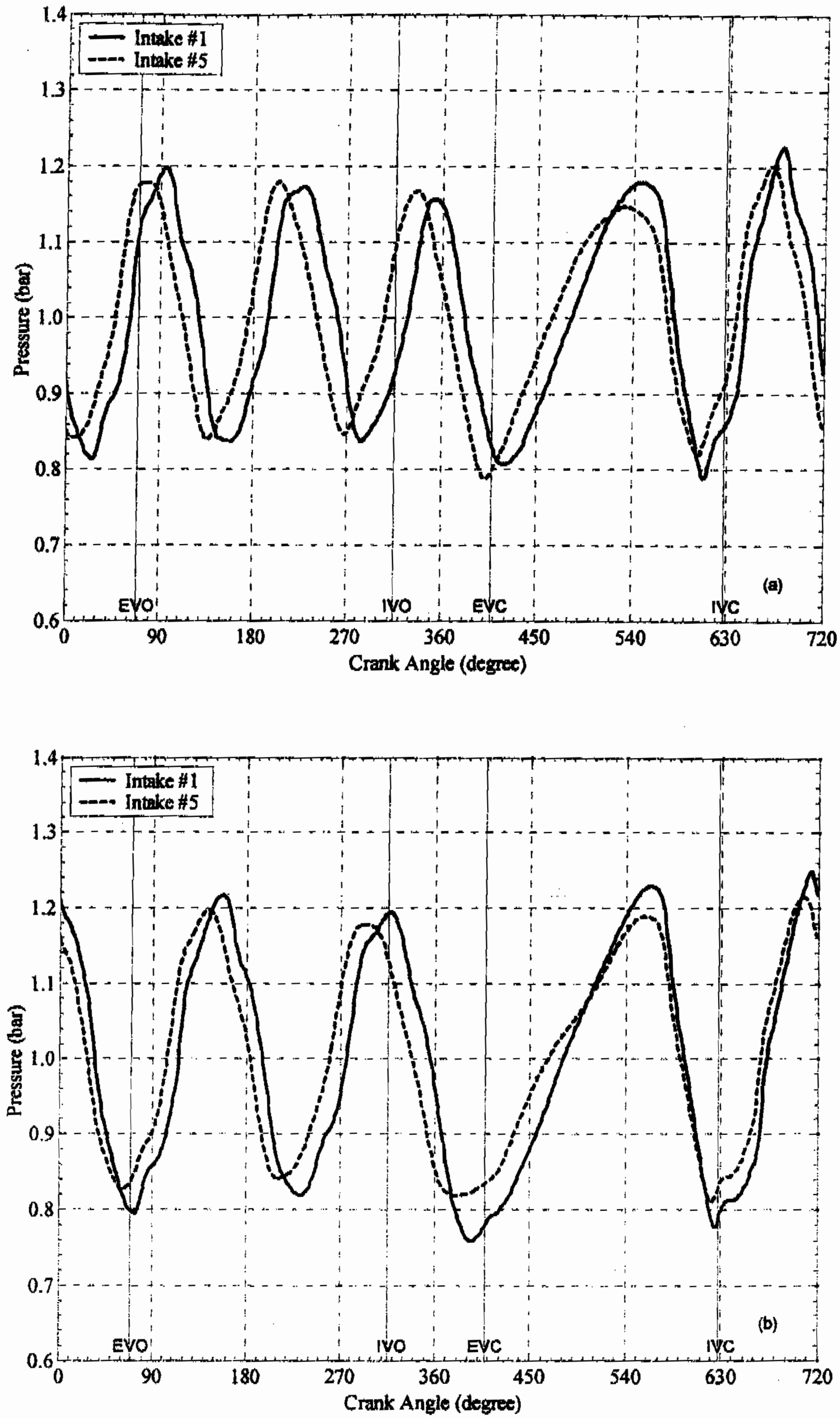

Figure 3.14: Single Cylinder Motoring Experiment: Intake Pressure (e11) for Intake #1 and Intake #5 at (a) 3750 rpm and (b) 4500 rpm

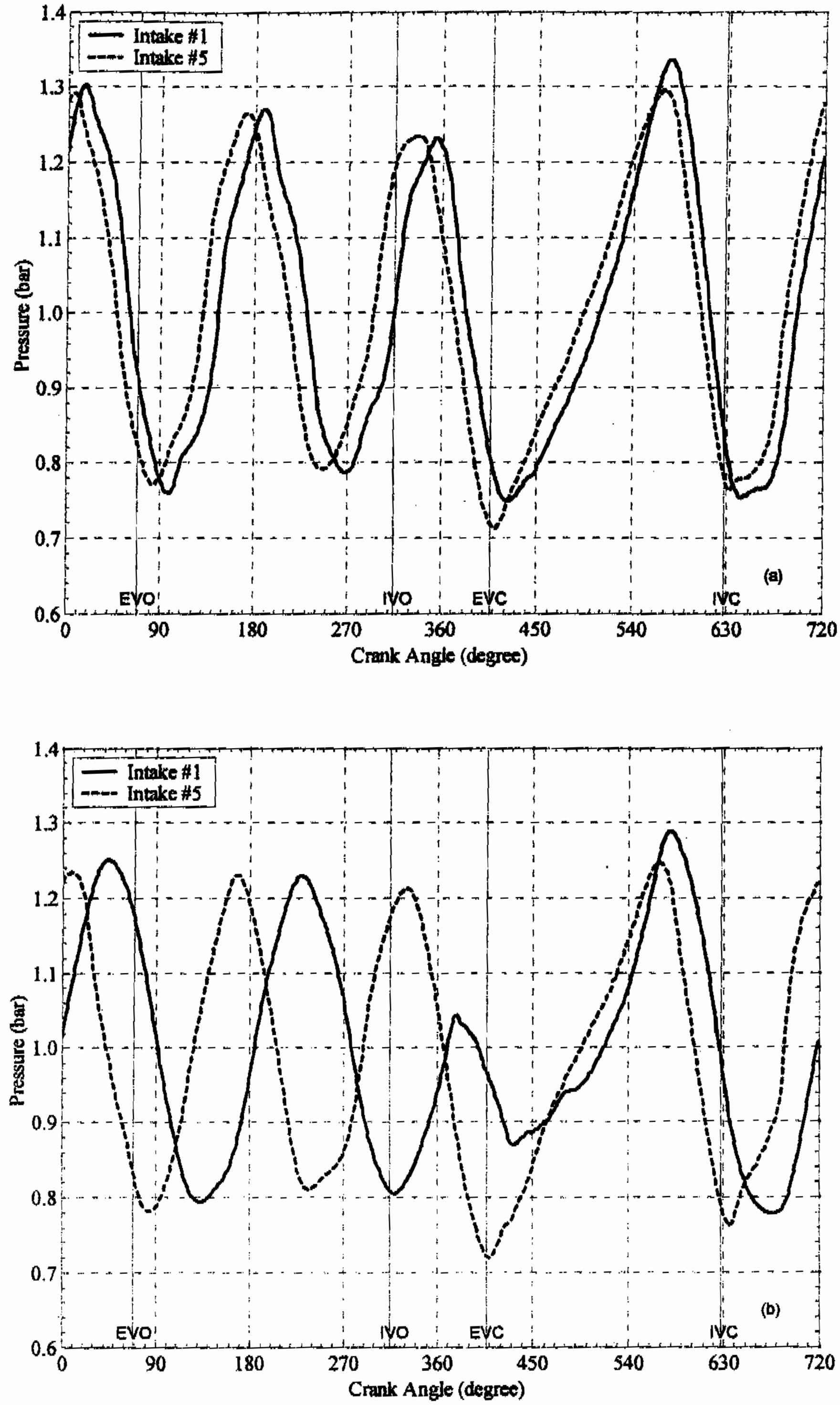

Figure 3.15: Single Cylinder Motoring Experiment: Intake Pressure (e11) for Intake #1 and Intake #5 at (a) 4750 rpm and (b) 5250 rpm

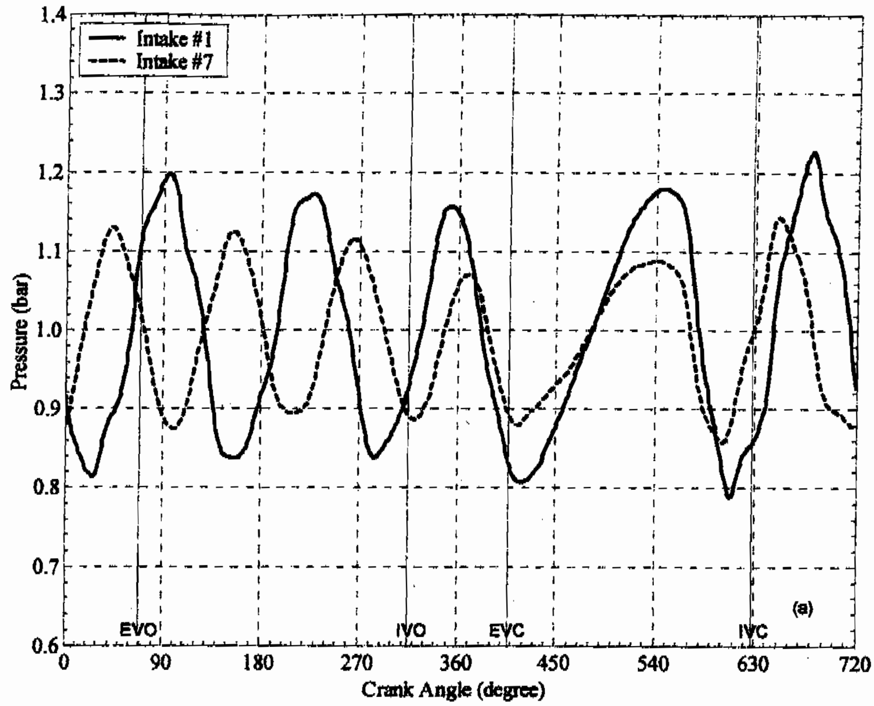

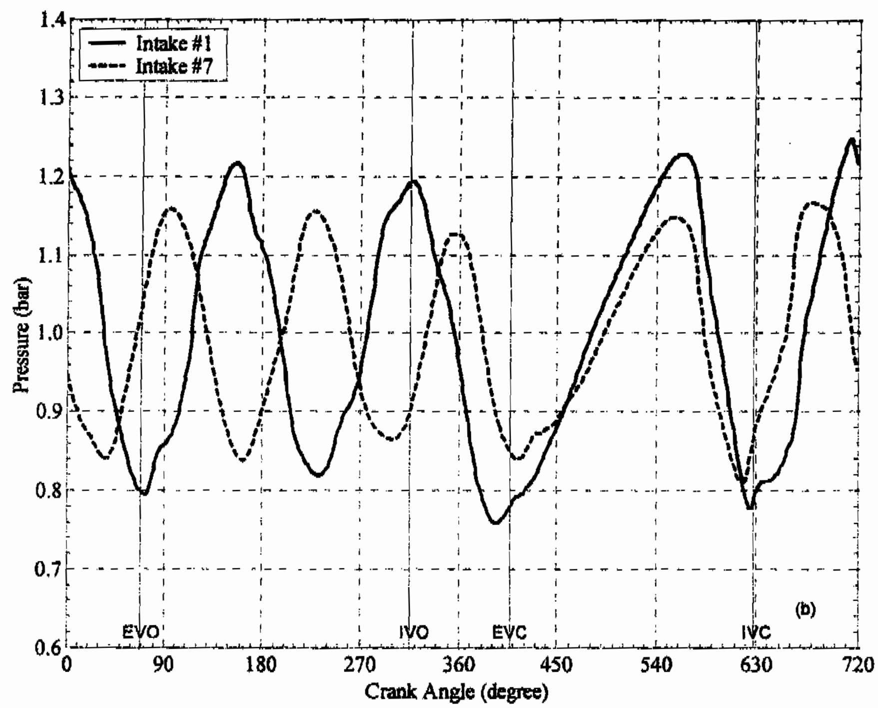

Figure 3.16: Single Cylinder Motoring Experiment: Intake Pressure (e11) for Intake #1 and Intake #7 at (a) 3750 rpm and (b) 4500 rpm

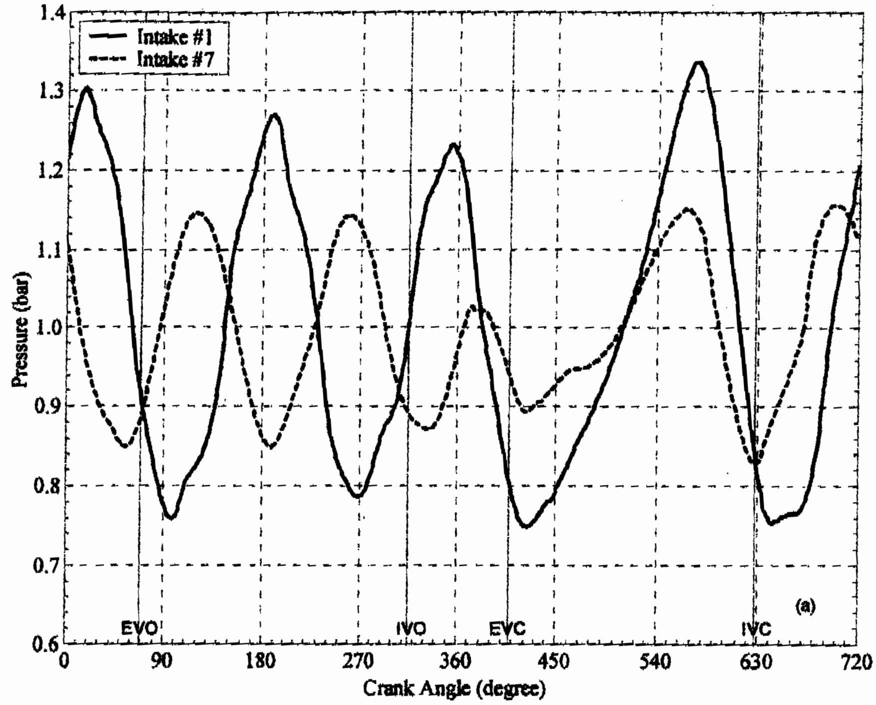

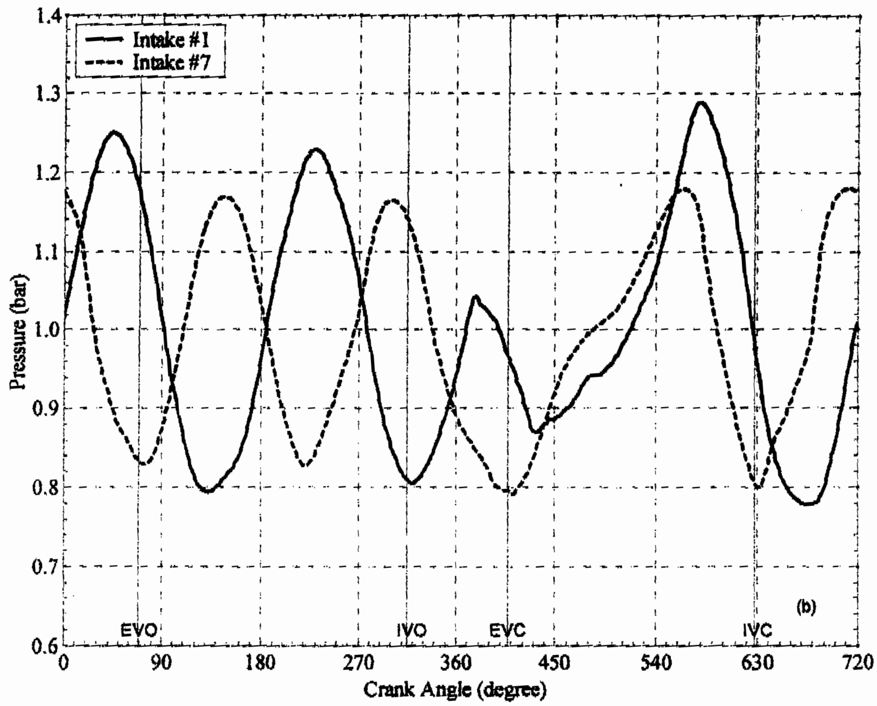

Figure 3.17: Single Cylinder Motoring Experiment: Intake Pressure (e11) for Intake #1 and Intake #7 at (a) 4750 rpm and (b) 5250 rpm

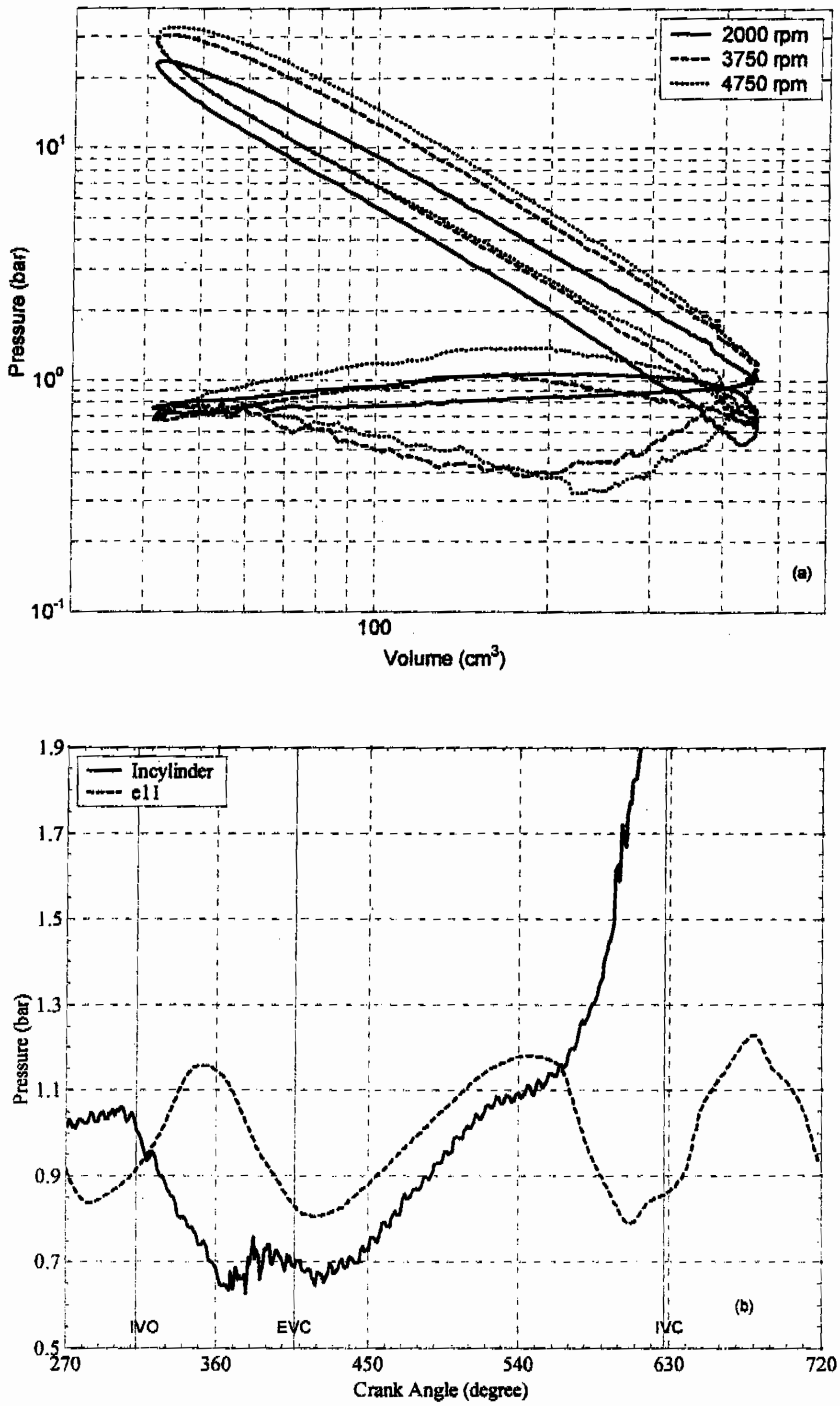

Figure 3.18: Single Cylinder Motoring Experiment: In-Cylinder Pressure for Intake #1: (a) P-V Loop (2000, 3750, and 4750 rpm) and (b) vs. Intake Pressure (e11) at 3750 rpm

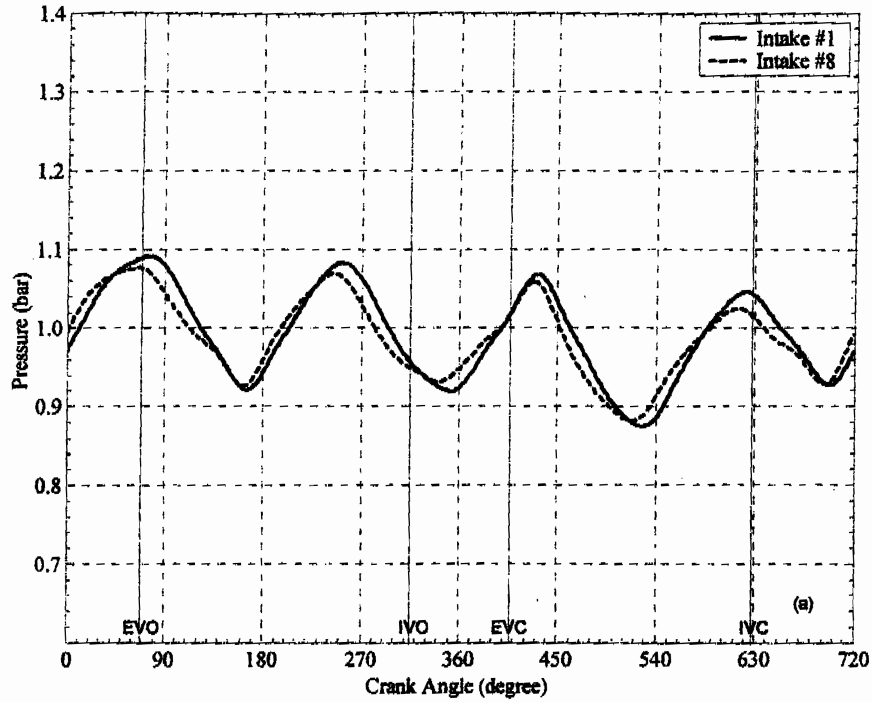

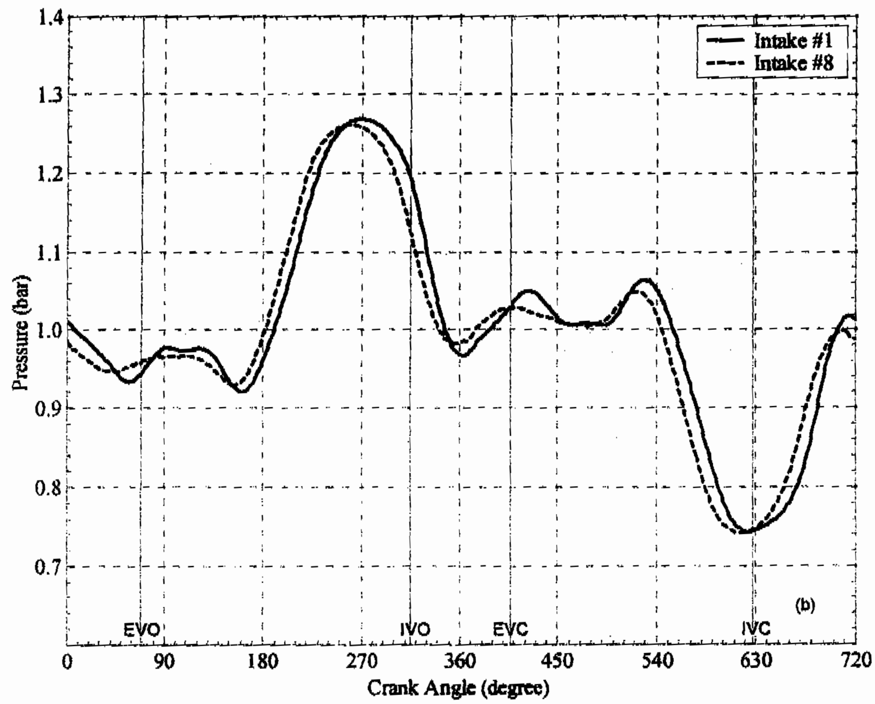

Figure 3.19: Single Cylinder Motoring Experiment: Exhaust Pressure (e3) for Intake #1 and Intake #8 at (a) 1500 rpm and (b) 2000 rpm

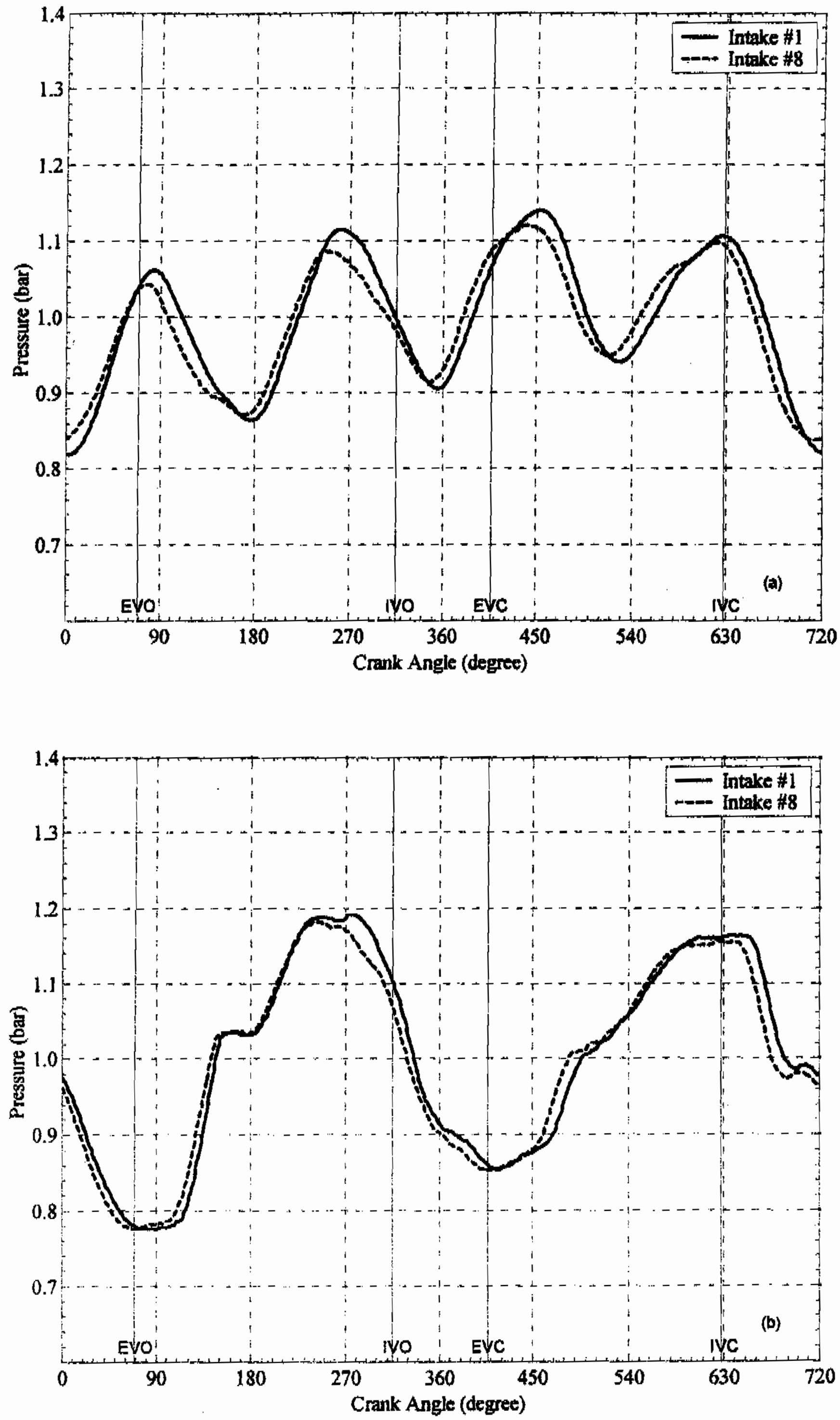

Figure 3.20: Single Cylinder Motoring Experiment: Exhaust Pressure (e3) for Intake #1 and Intake #8 at (a) 2500 rpm and (b) 3000 rpm

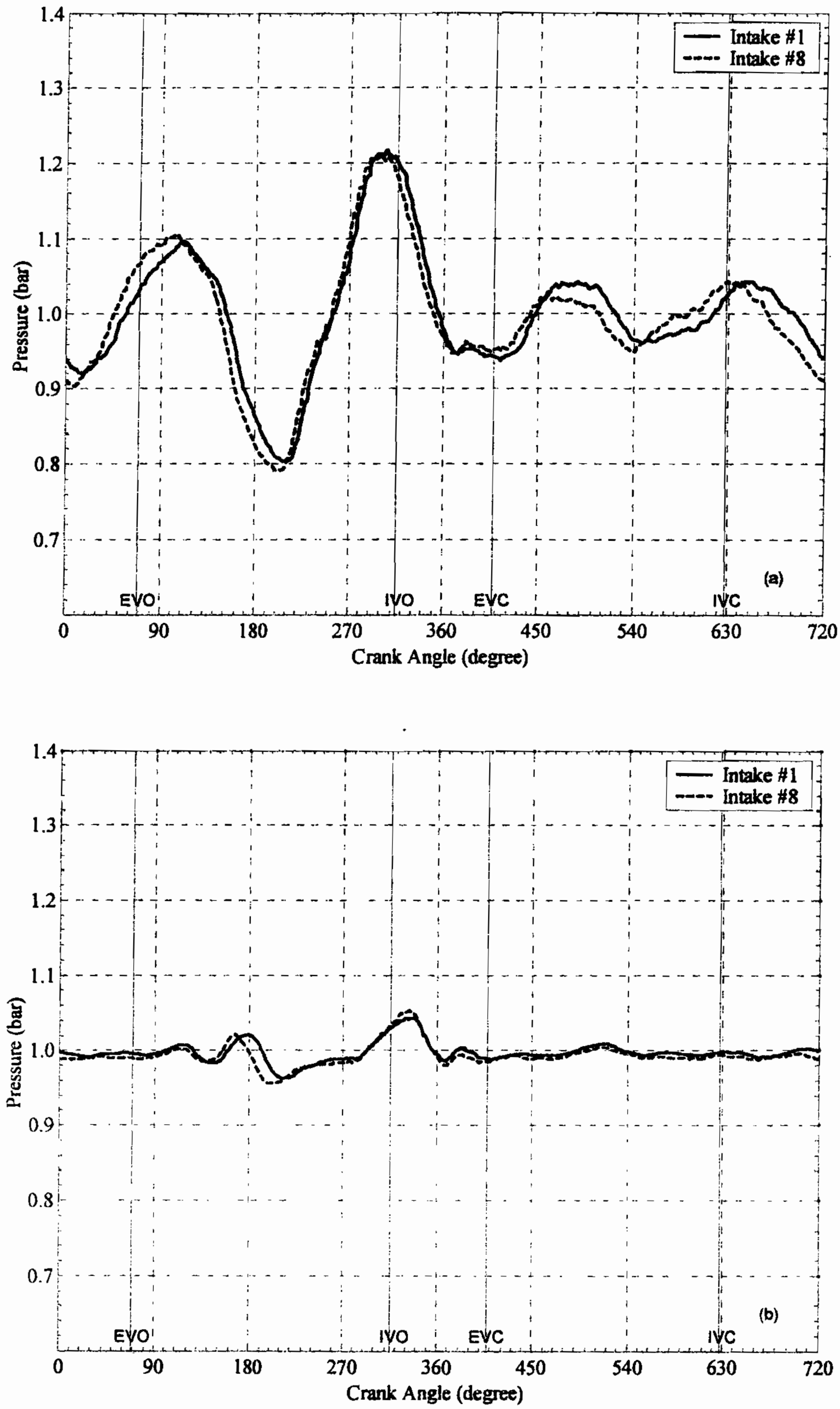

Figure 3.21: Single Cylinder Motoring Experiment: Exhaust Pressure (e3) for Intake #1 and Intake #8 at (a) 3500 rpm and (b) 4000 rpm

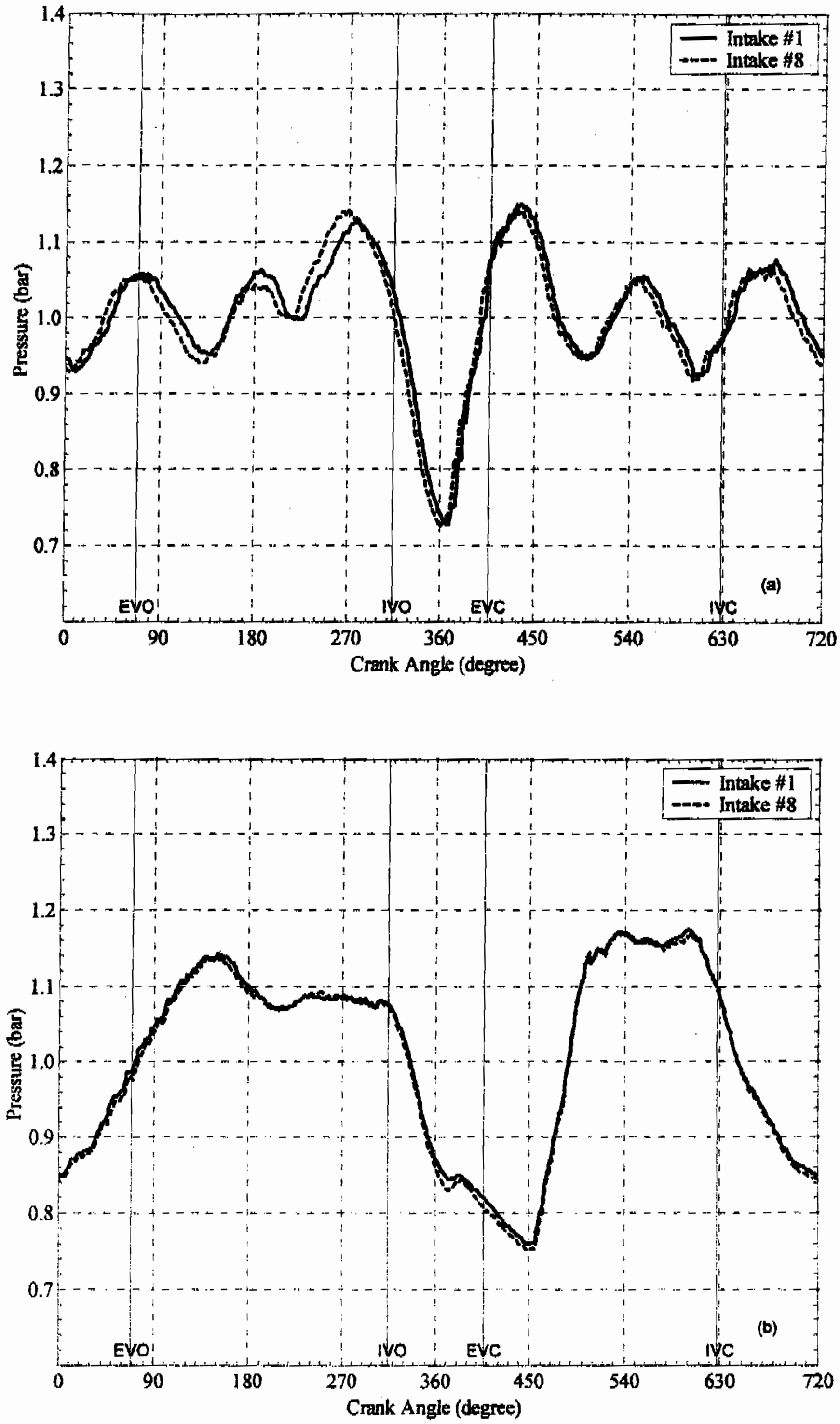

Figure 3.22: Single Cylinder Motoring Experiment: Exhaust Pressure (e3) for Intake #1 and Intake #8 at (a) 4500 rpm and (b) 5000 rpm

CHAPTER 4

COMPUTATIONAL RESULTS AND DISCUSSION

The predictions from two simple one-dimensional linear frequency-domain approaches and a finite difference engine simulation code are compared with experimental data from engine dynamometer in this chapter. The motoring results from the OSU single cylinder engine with the eight different tapered intakes are used in these comparisons. Section 4.1 compares results from two simple approaches, Engelman's Helmholtz analogy and the distributed parameters, in estimating the speed of the peak volumetric efficiency. Section 4.2 describes the results obtained from the finite difference engine simulation code, MANDY. Section 4.2.1 discusses the calibration of the code through several variables that can be modified to improve the prediction. Sections 4.2.2 and 4.2.3 compare the predictions from the calibrated engine simulation code to the motored experimental results, including volumetric efficiency and crank-angle resolved pressures in both intake and exhaust systems.

4.1 One-dimensional Linear Frequency-Domain Approaches

Thompson and Engleman (1969) at the Ohio State University developed one of the first linear empirical approaches for intake tuning that could be used to help evaluate the effects of different intake geometries on engine performance. This approach is based on a Helmholtz resonator analogy as introduced earlier in Section 1.1. The natural frequency of this type of single degree of freedom system is given by Eq. (3.1). They have postulated that the tuning occurs at an engine speed where the induction process is matched to the natural frequency of the combined intake pipe and cylinder system during the intake valve open period. Thompson and Engleman (1969) proposed a simple relationship based on Eq. (3.1) to determine the engine speed, N [rpm], for the intake tuning peak

$$N = \frac{1348}{k} c_o \sqrt{\frac{A_p}{l_p V_c}} \sqrt{\frac{R-1}{R+1}} \,, \tag{4.1}$$

where k is the valve timing correction factor, V_D the piston displacement and R the compression ratio. They also proposed that the exact relationship between the engine speed and the natural frequency of the resonating system was dependent on the engine valve timing, leading to k that varied from 2 to 2.5 to account for different engine valve open periods. Since the exact value of this factor has to be generally verified with actual engine test data, the overall usefulness of this approach is limited.

In this study, Eq (4.1) is calculated using an average value of 2.25 for the correction factor. Comparisons are made by using all applicable geometric dimensions from the OSU single cylinder intake system with the straight and the four full length tapered intake stacks (Intake #1, #2, #5, #7, and #8). However, due to the changing cross sectional area of the experimental intake systems an approximation must be made for the value of A_p. The method proposed by Engelman (1973), which uses a ratio of length, l_p, to cross-sectional area, A_p, is used. The composite pipe is treated on the basis that

$$\left(\frac{l_p}{A_p}\right)_{eff} = \frac{l_1}{A_1} + \frac{l_2}{A_2} + \ldots\ldots + \frac{l_n}{A_n}, \tag{4.2}$$

where the subscripts refer to the individual sections. To calculate Eq. (4.2), an average cross-sectional area is used here as an approximation for the tapered section. The tapered section average area is determined based on the known volume of each intake stack and the constant length of each piece. This method with an average A_p for the entire intake system provided excellent results as listed in Table 4.1.

Intake Stack	Helmholtz Approach	Experiment or Computational Results
#1	4730 rpm	4750 rpm
#2	4942 rpm	5000 rpm
#5	5156 rpm	5250 rpm
#7	5318 rpm	5500 rpm
#8	5454 rpm	5500 rpm

Table 4.1: Helmholtz Resonator Approach Predictions for Engine Speed for Peak Tuning

Engleman's small amplitude frequency-domain approach was later improved by other studies. One such approach, described by Winterbone and Yoshitomi (1990), is based on distributed parameters, and considers the system as two connected pipes of different geometric dimensions with the larger area pipe having a closed end. The natural frequency of this system is given by

$$\frac{A_c}{A_p}\tan\left(\frac{\omega \cdot l_c}{c_o}\right)\tan\left(\frac{\omega \cdot l_p}{c_o}\right) = 1, \tag{4.3}$$

where ω is the system angular frequency, A_c the cross-sectional area of the cylinder, and l_c is ½ the length of the cylinder. This approach uses distributed analysis to represent the column of air moving in the runner and cylinder and thus gives an infinite series of natural frequencies, while Eq. (4.1) provides only the fundamental frequency. Equation (4.3) is solved for the resonance frequency with the same dimensions used for Eq. (4.1), including the averaged A_p determined from Eq. (4.2), and the results are listed in Table 4.2.

Intake Stack	Distributed Parameters	Experiment or Computational Results
#1	3930 rpm	4750 rpm
#2	3960 rpm	5000 rpm
#5	4050 rpm	5250 rpm
#7	4095 rpm	5500 rpm
#8	4110 rpm	5500 rpm

Table 4.2: Distributed Parameters Approach Predictions for Frequency of Tuning Peak

The results from this approach do not compare well with the experimental results. This approach does capture the trend of increased engine speed for increased taper, but the engine speed for peak tuning is consistently low and does not show the 250 rpm increase with each intake stack.

4.2 Engine Simulation Code

The engine simulation code, MANDY, used in this study is based on the finite difference approximation of the balance equations in the time domain for mass, momentum, and internal energy. The numerical technique is an extension of the work first presented by Chapman, Novak and Stein (1982) as briefly discussed in Section 2.5.

4.2.1 Engine Simulation Code Calibration

All physical dimensions and measurable quantities were verified and entered into a simulation file to best represent the actual single cylinder engine at OSU. The engine was taken apart and all dimensions such as piston bore, stroke, clearance volume and valve size were measured. The cylinder head was flow tested using the Ford Scientific Laboratories flowbench discussed in Section 2.4. Both intake and exhaust camshaft lifts were measured and the dynamic profile is used to determine the valve position at any crank-angle. A parametric study was also conducted to determine the effect of various code parameters on the predictions. The most influential of these variables for motoring conditions include the cylinder wall heat transfer constant, HFACT, the temperature range for the cylinder wall, TWCYL, and the duct wall friction multiplier, WF. A reference range was given as HFACT = 2-3, TWCYL = 300 to 400 K and WF = 0.07 to 0.12. Simulation runs were conducted to determine the effect of changes to these values in order to help calibrate the engine input file. All runs for the parametric study were conducted with the physical dimensions of the reference stack, Intake #1, where the most accurate predictions would be expected from this simplest intake design.

Figure 4.1 shows the effect of HFACT ranging from 1.0 to 3.0. This variable controls the amount of heat transfer from the cylinder to the cooling water. Figure 4.1 clearly shows a fairly linear downward trend across the entire engine speed range as the value of HFACT is increased. The magnitude of the decrease is also quite similar across the speed range with an average decrease of about 2% and a maximum of about 4%. In view of the fairly even effect that it has on the volumetric efficiency over the speed range, HFACT = 2.5 (midpoint) was chosen in this study.

Figure 4.2 shows the effect of TWCYL. This variable is input as one wall temperature for the lowest engine speed and another for the highest speed. The engine simulation code uses linear interpolation to determine values for all other speeds. The parametric experiments are conducted with values ranging from 300 to 350 K for 1500 rpm and 325 to 375 K for 6000 rpm at 25 K increments. During the motoring experiments on the dynamometer the exhaust gas temperature was measured near pressure transducer location e3 and varied approximately 25 K from 290 to 315 K. Thus temperature variations across the entire engine speed range of 25 K are used for all parametric runs. Figure 4.2 shows an overall downward trend as the TWCYL values are increased. The air entering the cylinder will warm up as a result of heat transfer from the cylinder walls, resulting in a decrease in mass flow rate, therefore volumetric efficiency. The magnitude of the reduction for increasing TWCYL does, however, vary with engine speed. The low speed end is more affected by temperature variations showing about 5% reduction, while the high-speed end above 4750 rpm has 1% or less reduction with the same temperature increase. This effect can be explained by the fact that the air will spend more time in the cylinder at low speeds and thus will have more time to warm up and cause a greater decrease in volumetric efficiency. During the motoring experiments, both the oil and cooling water were maintained at temperatures near 293 K. This combined with the measured exhaust gas temperatures led approximately to TWCYL = 325 and 350 K.

Figure 4.3 compares the predictions for values of WF ranging from 0.07 to 0.11. This variable is a multiplier of the Blasius formula for the turbulent wall friction factor. WF is used to account for flow losses not specified and any differences between unsteady flow losses and those assuming steady fully developed flow. This variable is input as one value for the intake system and another for the exhaust. The exhaust system piping is generally considered to be smooth, thus WF is set to 0.04 for all experiments.

The intake system, however, involves in general more flow development and component-to-component interactions leading to a higher value for WF. Figure 4.3 shows that increasing WF results in loss of volumetric efficiency at higher engine speeds. As the engine speed increases so does the flow rate in the intake system and with higher wall friction the resulting losses are higher and causing a reduction in efficiency. A maximum loss of approximately 2% is seen at the volumetric efficiency peaks. A value of 0.09 was chosen for WF based on these results and the Ford engineer's recommendation.

Another important parameter that must be accounted for is the inertia end correction for the intake system at the ambient junction. This correction is needed because a segment of the ambient air at the mouth of the intake stack has a significant velocity and therefore acts as though it were a part of the intake system length. The rarefaction wave coming from the cylinder will actually travel outside the bellmouthed entrance of the intake for a short distance before reflecting back as a compression wave. Depending on the overall intake length and the size of the intake piping this additional length can have a significant impact on the speed at which the volumetric peaks occur. Extensive work has been conducted to determine end corrections for various duct terminations. One such computational study by Selamet *et al.* (2001) investigated numerous duct terminations, including a bellmouthed inlet with an attached large flange, which is similar to those on the intake stacks in this study. From figures provided in Selamet's study end correction estimations can be made, with the measured dimensions of the bellmouthed radius and inside duct diameter at the ambient junction (Fig. 2.2 – D_1

and r). Based on the dimensions of the intake stacks, end corrections should range from 2 cm for Intake #1 to 3 cm for Intake #8.

Figure 4.4 compares the predictions with the end correction ranging from 0 to 2.5cm for Intake #1. Unlike the other variables discussed where only magnitudes are changed, variations in end correction actually affect the shape of the curve. The figure shows that a 2.5 cm addition of length effectively shifts the high speed peaks back 250 rpm, while overall magnitude remains relatively similar across the engine speed range. This trend can be explained by once again using a classical lumped parameter analysis as discussed in Section 3.2. The length of the intake system, l_p, is in the denominator of Eq. (3.1) thus an increase in intake length will directly reduce the system frequency and engine speed for the peak inertia tuning. As the end correction is based on the size of the pipe at the ambient interface, its value in this study changes for different tapered intake stacks. Several parametric experiments were conducted for each intake stack dimensions until satisfactory results were achieved for the high speed peaks when compared to the experiments. The final end corrections used for this study are listed in Table 4.3.

Intake Stack	End Correction (cm)
#1	1.25
#2	2.0
#3	1.5
#4	1.5
#5	2.5
#6	2.0
#7	3.0
#8	3.5

Table 4.3: MANDY Prediction End Corrections

Once values were determined for all of these variables, they were implemented into the engine input files and maintained for the remaining runs to ensure as much accuracy and consistency as possible in order to provide a fair comparison base for all eight intake stacks.

4.2.2 Volumetric Efficiency Predictions

The volumetric efficiency is measured by using a laminar flow element in the exhaust system as described in Section 2.4, with the results being fully described in Section 3.2. The predictions from MANDY for volumetric efficiency for all eight intake stacks are compared with the experimental results as shown in Figs. 4.5 - 4.12, revealing a good agreement. The predictions generally show less than 2% deviation from the experiments for all intakes above 3000 rpm. The code accurately predicts the engine speed for peak volumetric efficiency for every intake and is generally within 1% of the magnitude. This is exceptional when considering the error encountered with the laminar flow meter of approximately 1% at these speeds. Nearly all of the other peaks above 3000 rpm are also accurately predicted both in phasing and magnitude. Below 3000 rpm the predictions show a higher overall trend for Figs. 4.5 and 4.9 - 4.12. The maximum deviation of approximately 7% is seen at 1500 rpm but with the increasing error from the laminar flow meter at these slower speeds even these predictions would still be useable as the overall shape of the curve is still fairly accurate.

4.2.3 Intake Pressure Predictions

The following discussion for the comparison of crank-angle resolved pressure in the intake system is limited to the first high speed volumetric efficiency peak for each intake stack. This ensures that experimental data is available for comparison for all of the stacks at a specific point. The second volumetric peak cannot be used, as experimental data was not obtained at engine speeds high enough to produce a second peak for Intake #7 and #8.

The intake pressure is measured at two locations (e11 and e12) as shown in Fig. 2.1 and discussed in Section 2.4. Figures 4.13 – 4.16 show the predictions for e11 and Figs. 4.17 – 4.20 show the predictions for e12. Figure 4.13 (a) is for Intake #1 and shows a good agreement for both phasing and magnitude. Slight over-prediction is seen at the peak (540 CAD) and valley (410 CAD) during the intake portion of the cycle. Nearly identical trends for phasing and magnitudes can be seen in both predictions for Intake #3 and #4 [Fig 4.14 (a) and (b)]. The predictions for the other five stacks (Intake #2, #5, #6, #7, and #8) also provide reasonable agreement with the experiments. These five intake predictions do show a noticeable phase shift of about 5 to 10 CAD from the experimental results. Some additional over-prediction in the magnitudes can also be seen in the peaks and valleys for Intake #2, #7, and #8 [Fig. 4.13 (b), 4.16 (a) and (b)]. When comparing the three 50% tapered intakes (Intake #2, #3, and #4), the phase shift seen in the Intake #2 prediction completely disappears in the predictions for Intake #3 and #4. An improvement can also be seen when comparing the two 100% taper intakes #5 and #6 [Fig. 4.15 (a) to (b)] with the only difference being that the shift does not completely disappear. This shows that the engine simulation code performs slightly better in predicting the intake pressures when the tapered length is minimized. Although minor, the foregoing discrepancies may possibly be attributed to the additional multi-dimensional effects in the full length tapers that are not accounted for in the inherently one-dimensional simulation code.

4.2.4 Exhaust Pressure Predictions

The following comparisons of crank-angle resolved pressures in the exhaust system are limited to three engine speeds from only two intake stacks. The distinguishable differences between the exhaust pressures for the different intake stacks are minimal, thus comparisons are made only for Intake #1 and Intake #8 at 2000 rpm, 3750 rpm, and 4750 rpm.

The exhaust pressure is measured at one location (e3) in the exhaust manifold (Fig 2.1). Figures 4.21 – 4.23 compare the predictions and experimental results for (a) Intake #1 and (b) Intake #8 at three engine speeds. The experimental results for even these two intakes with the greatest dimensional difference are very similar as can be observed in the comparison of (a) to (b) for each engine speed. The engine simulation code predicts this similarity as well and shows nearly identical traces for both intakes. The predictions for 2000 rpm (Figure 4.21 (a) and (b)) compare reasonably well with the experiments for both intakes. The most noticeable trend for the phasing of the major peak and valley is captured well, however, the amplitudes are over-predicted at both points. Figure 4.22 shows that the predictions for 3750 rpm compare reasonably well with the experiments for both intakes. The predictions for phasing of the significant peaks and valleys compare well with the experiments and the magnitudes are reasonable. Some over-prediction of amplitude is observed for Intake #1, while Intake #8 is more accurate. The smaller amplitude wave oscillations, however, are not captured well. The major peaks and valleys are noticeable in the predictions for 4750 rpm, however, the phasing appears to lead the experiment and the amplitudes are under-predicted. Again, the smaller oscillations are not captured. Due to the size and length of the exhaust system, additional issues such as numerical dissipation at higher frequencies or multi-dimensional effects may influence these predictions, as discussed by Dickey *et al.* (2003).

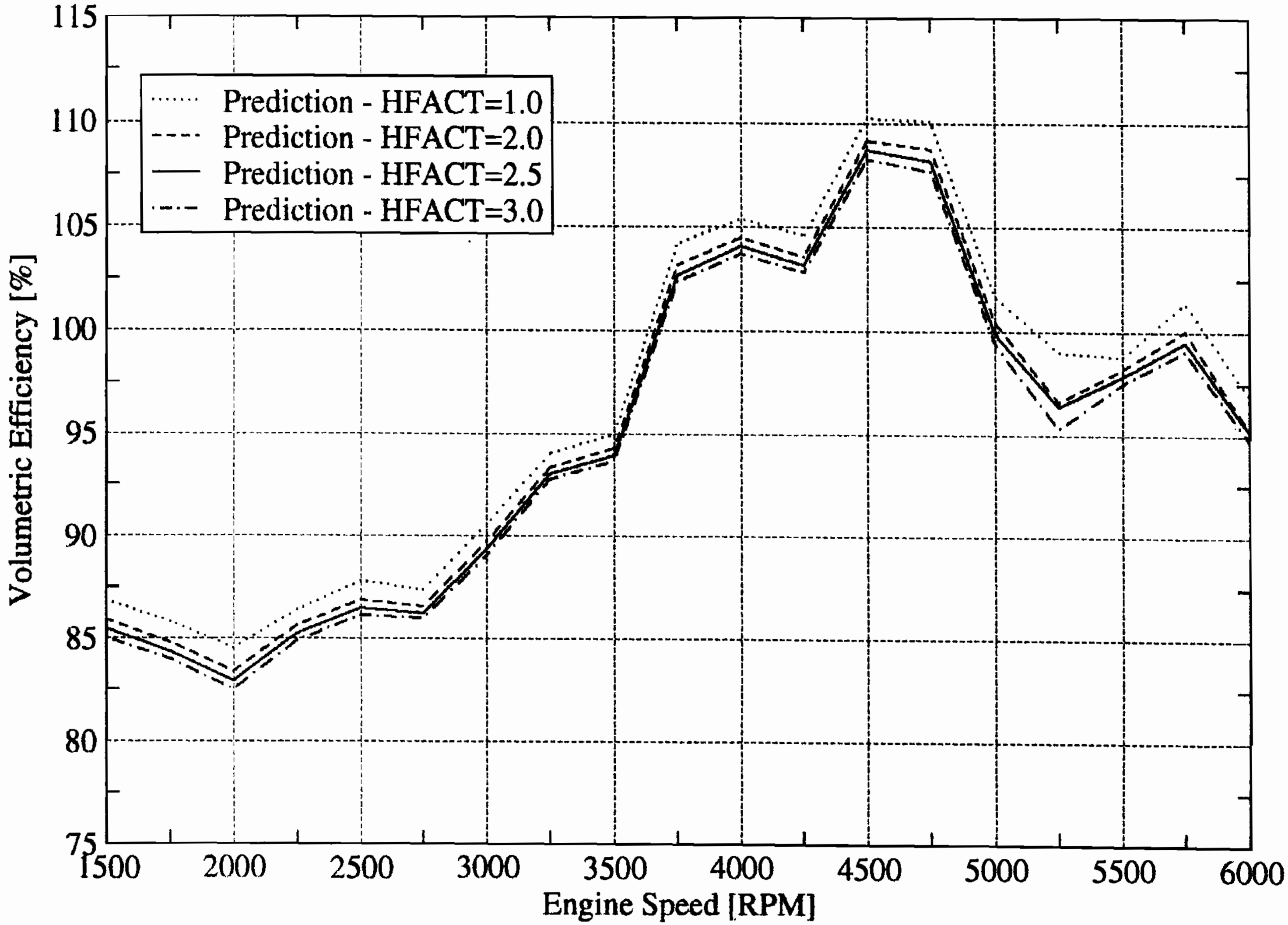

Figure 4.1: Comparison of Predictions with Different Values of HFACT for Intake #1

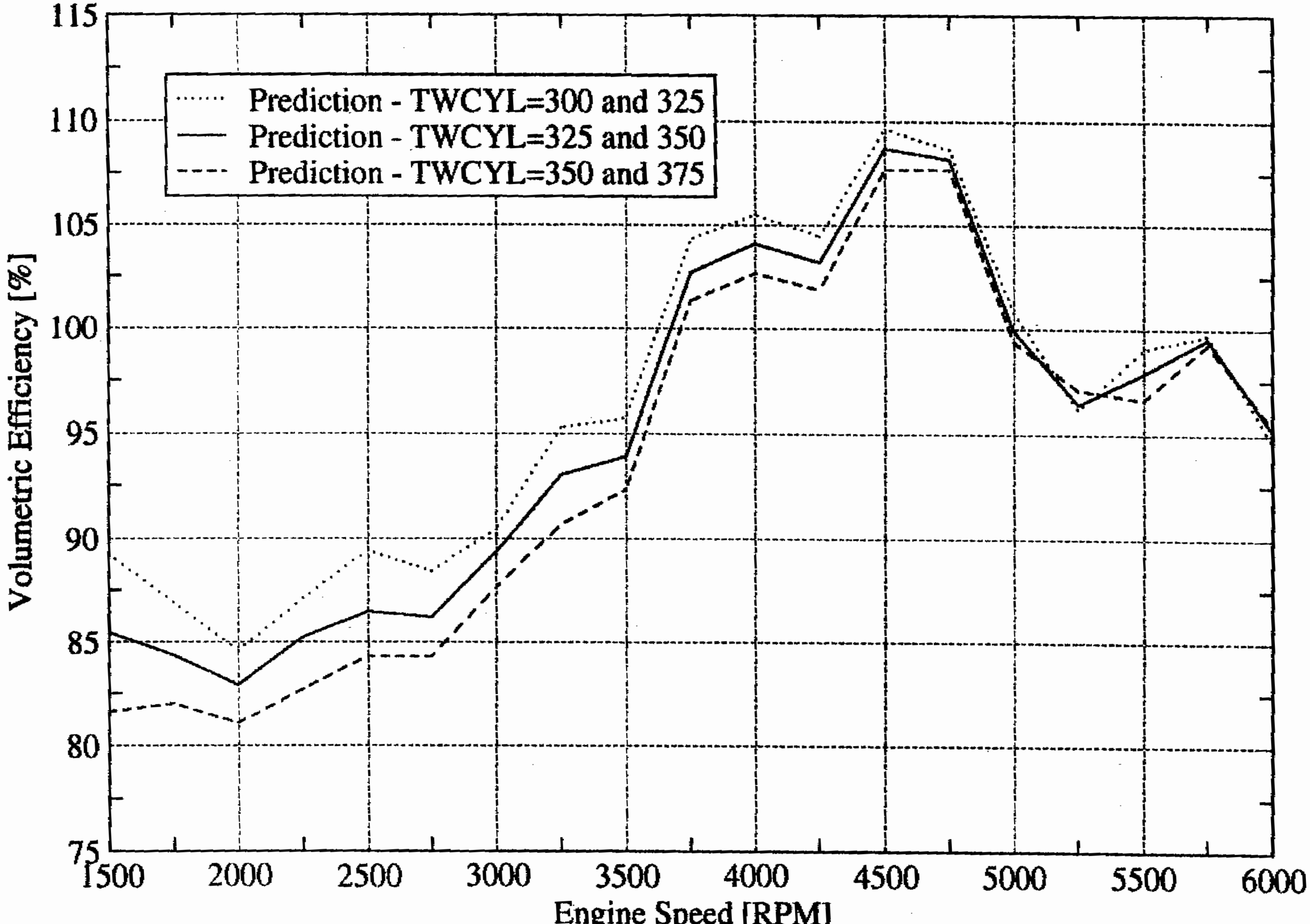

Figure 4.2: Comparison of Predictions with Different Values of TWCYL for Intake #1

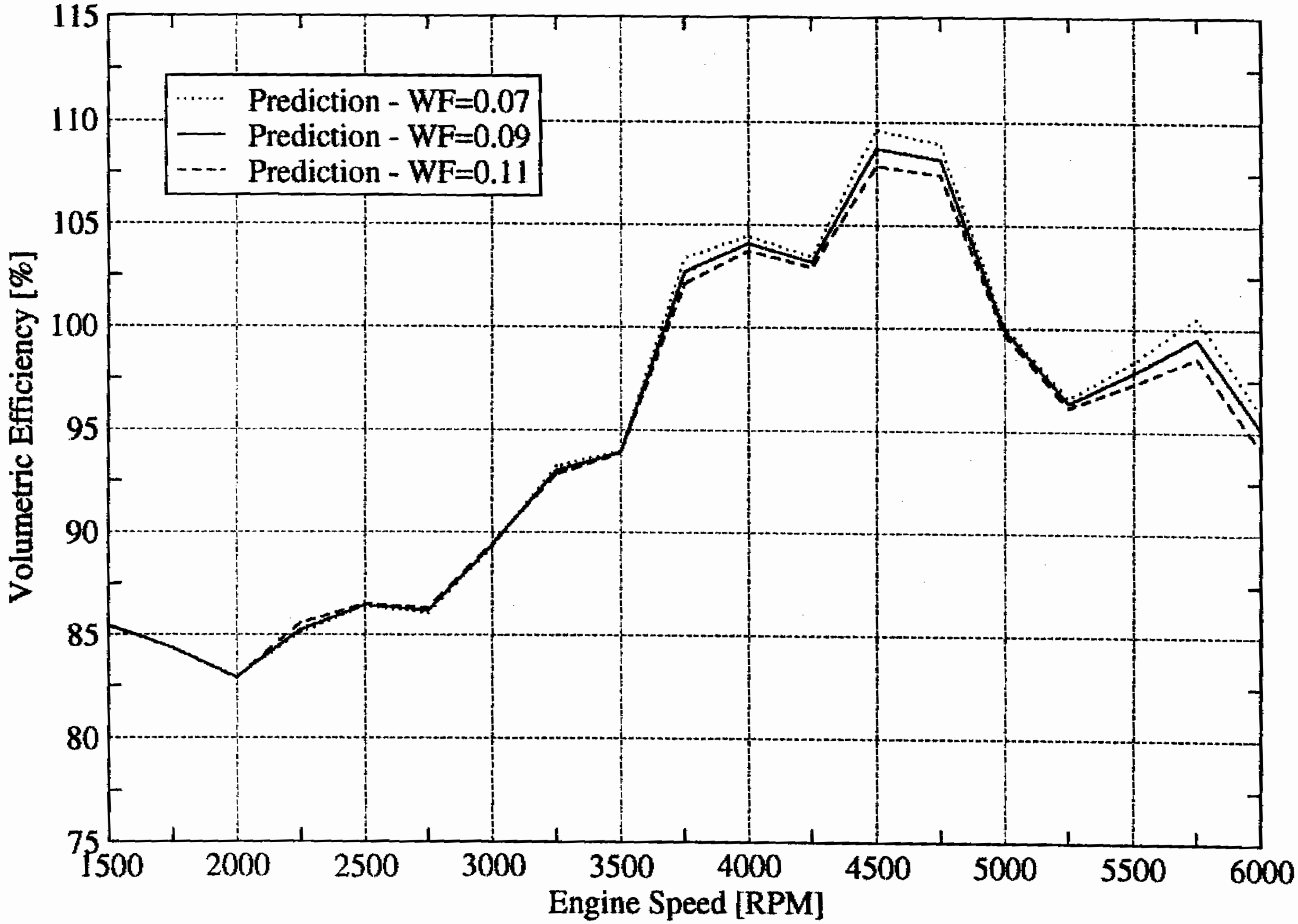

Figure 4.3: Comparison of Predictions with Different Values of WF for Intake #1

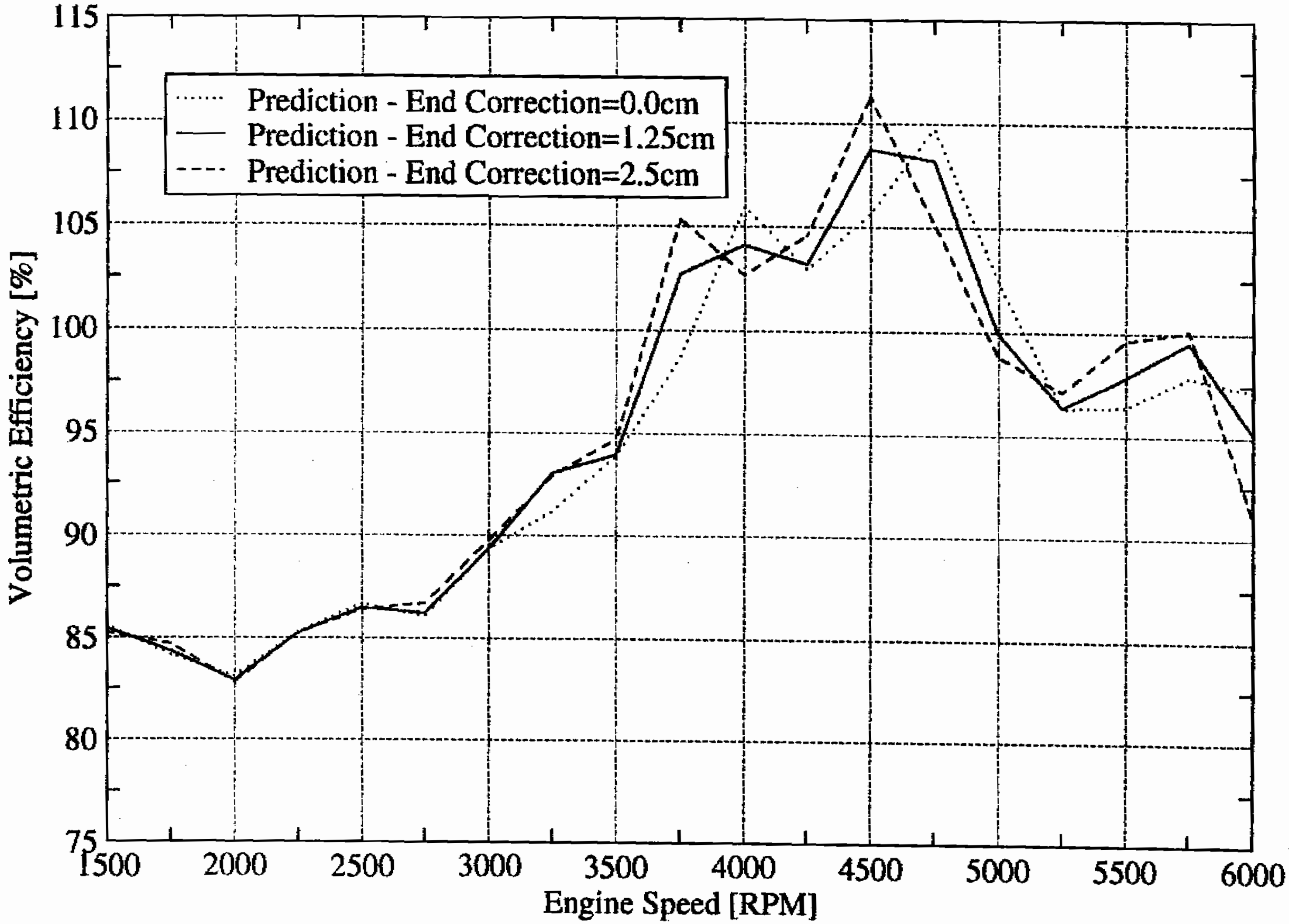

Figure 4.4: Comparison of Predictions with Different Values of End Corrections for Intake #1

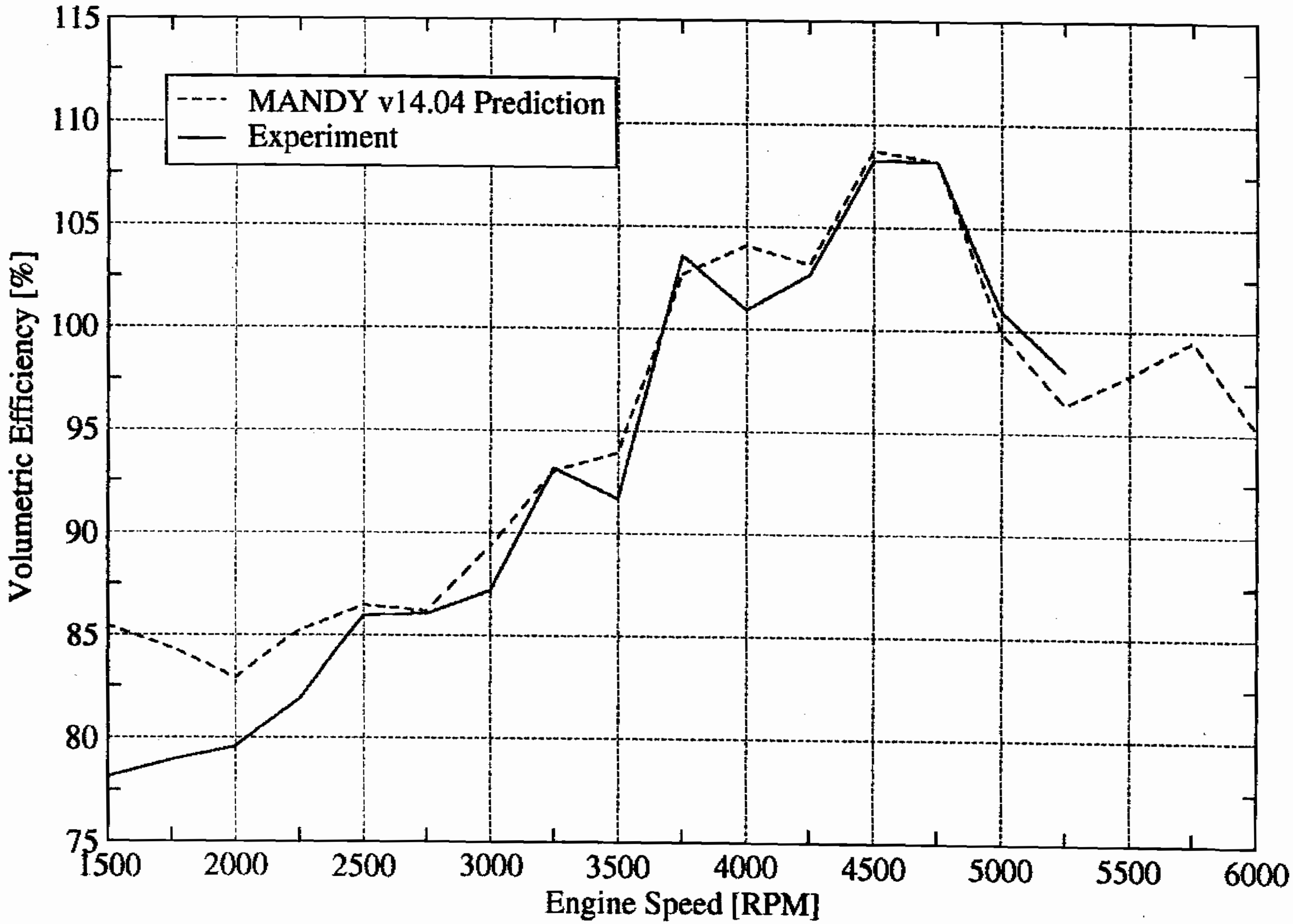

Figure 4.5: Comparison of Predicted and Measured (with Motored Engine) Volumetric Efficiency for Intake #1

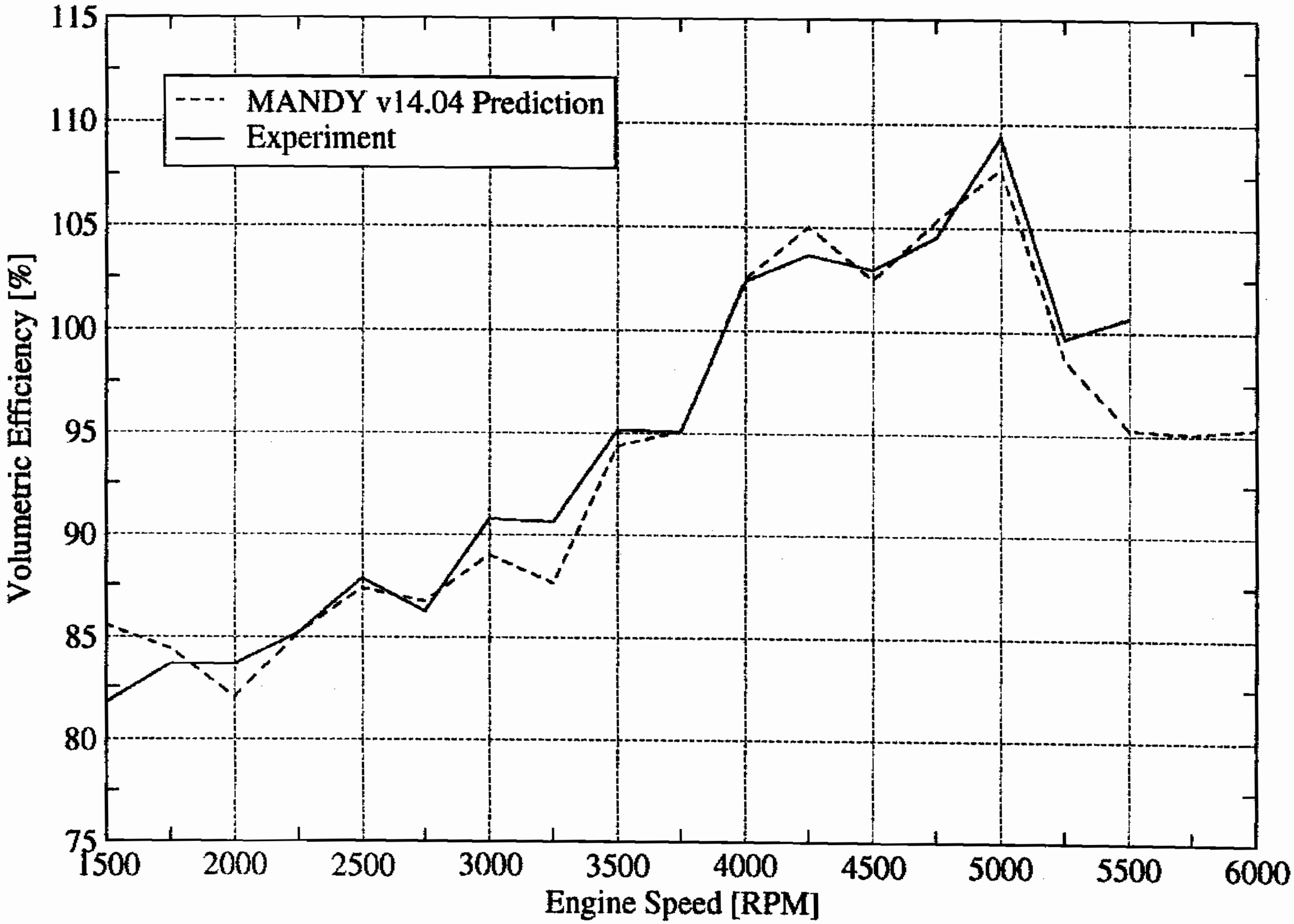

Figure 4.6: Comparison of Predicted and Measured (with Motored Engine) Volumetric Efficiency for Intake #2

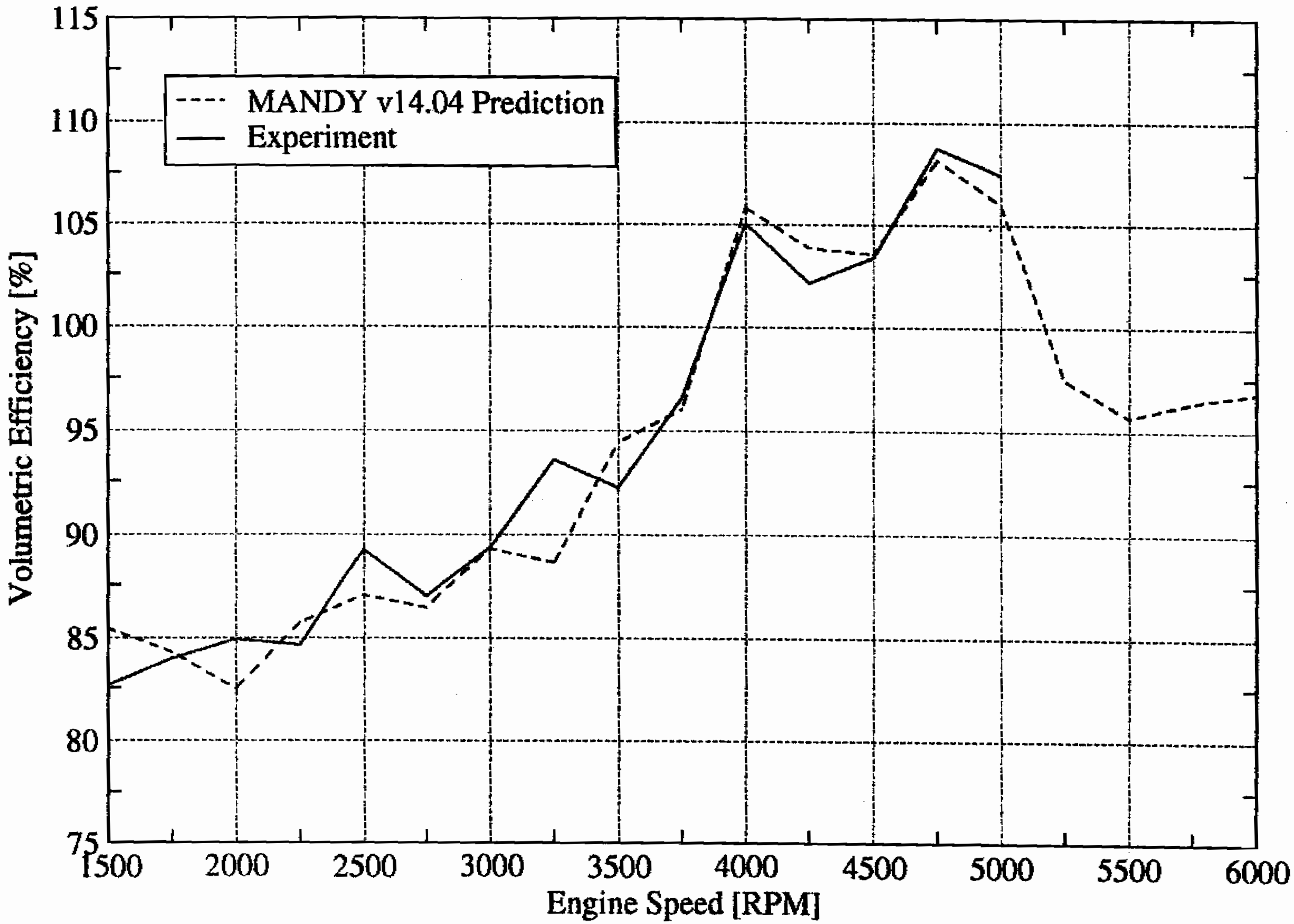

Figure 4.7: Comparison of Predicted and Measured (with Motored Engine) Volumetric Efficiency for Intake #3

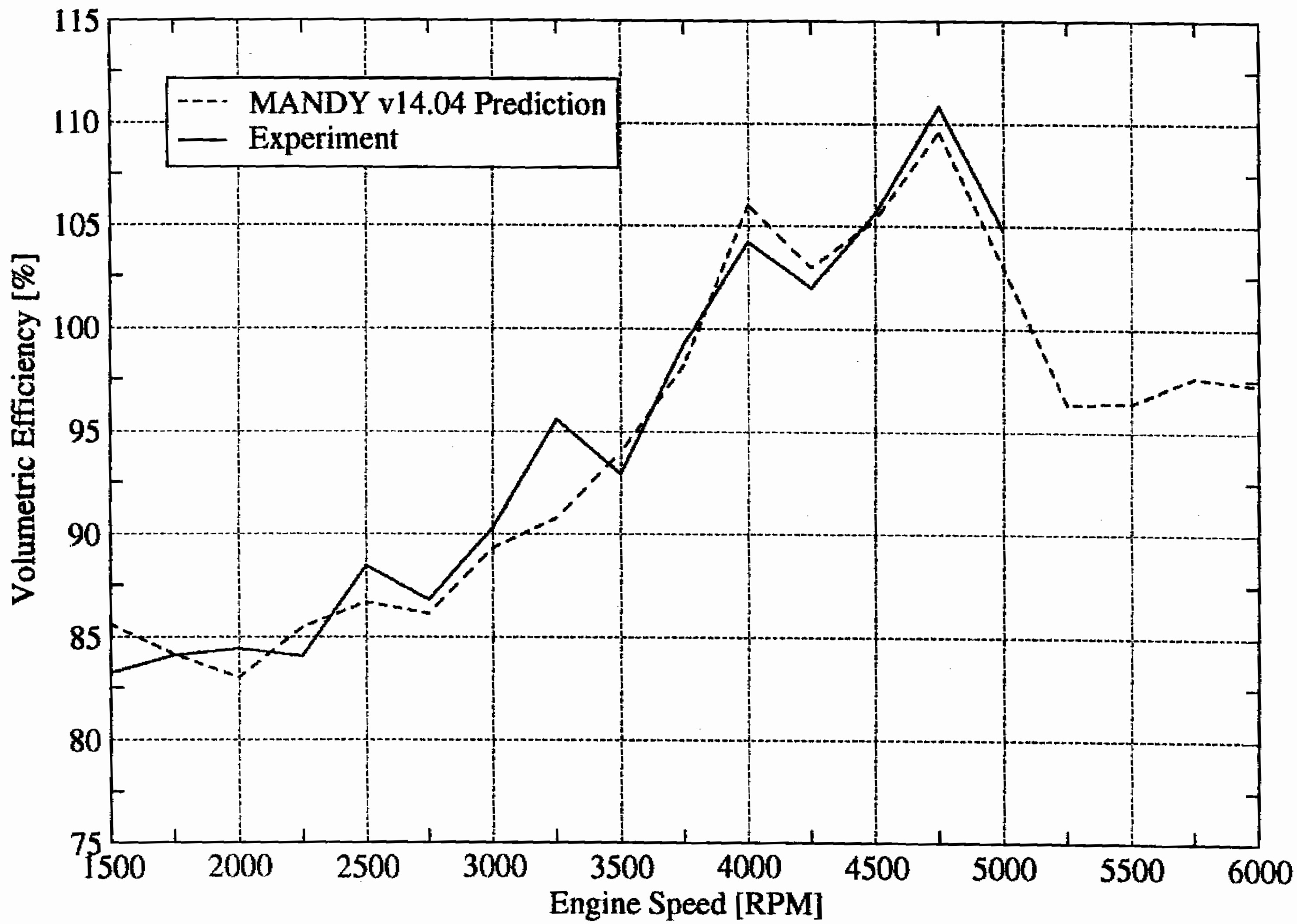

Figure 4.8: Comparison of Predicted and Measured (with Motored Engine) Volumetric Efficiency for Intake #4

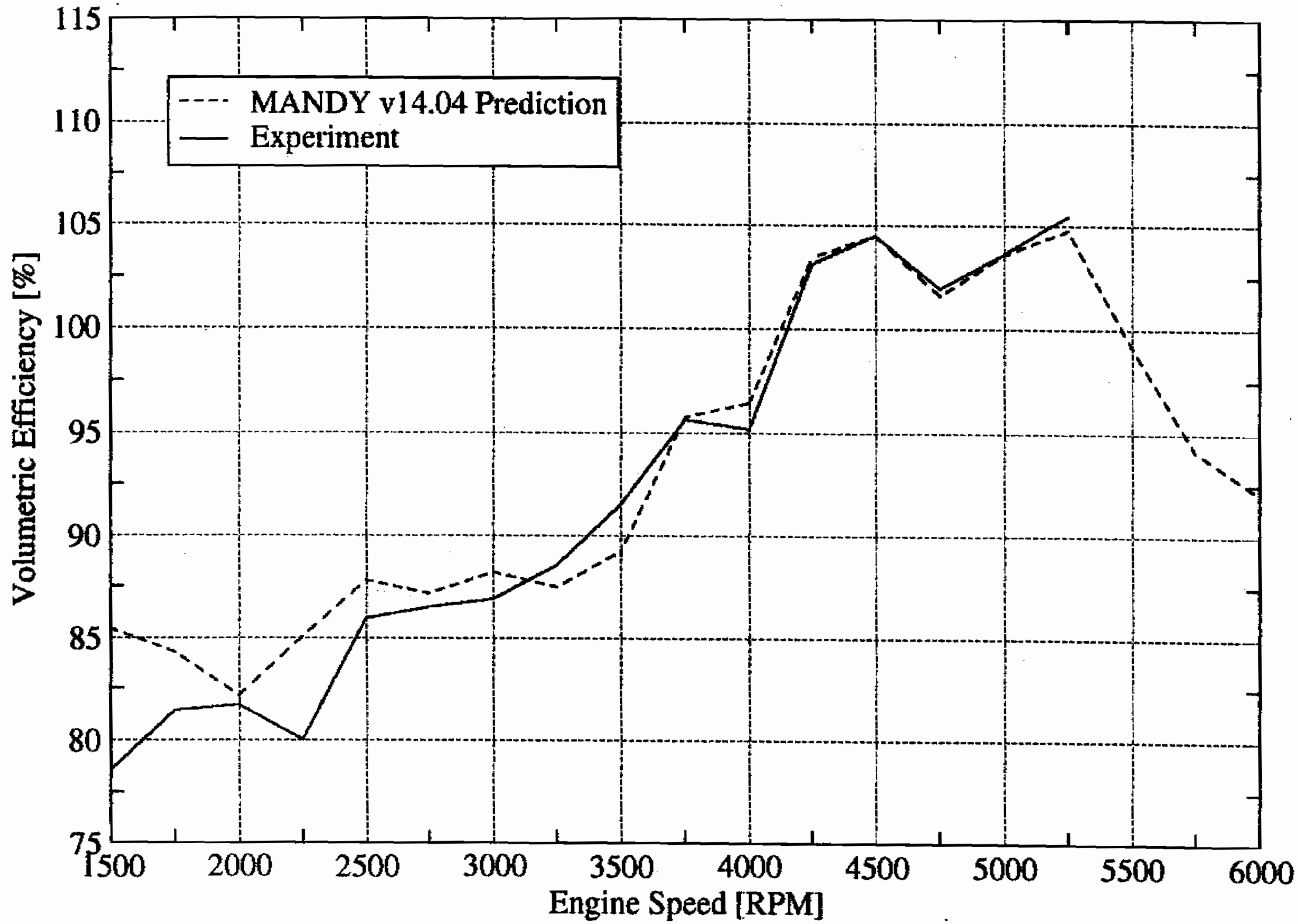

Figure 4.9: Comparison of Predicted and Measured (with Motored Engine) Volumetric Efficiency for Intake #5

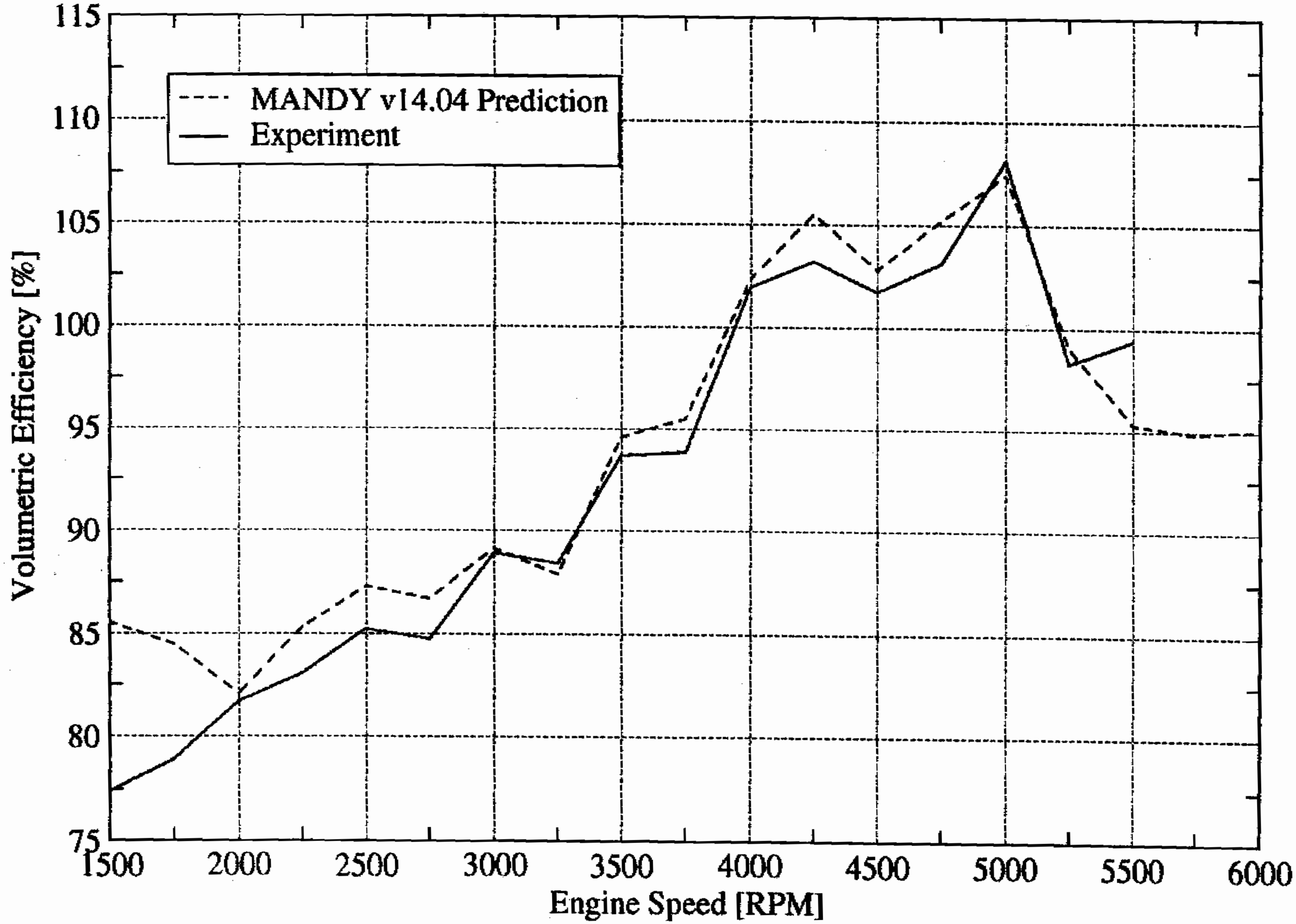

Figure 4.10: Comparison of Predicted and Measured (with Motored Engine) Volumetric Efficiency for Intake #6

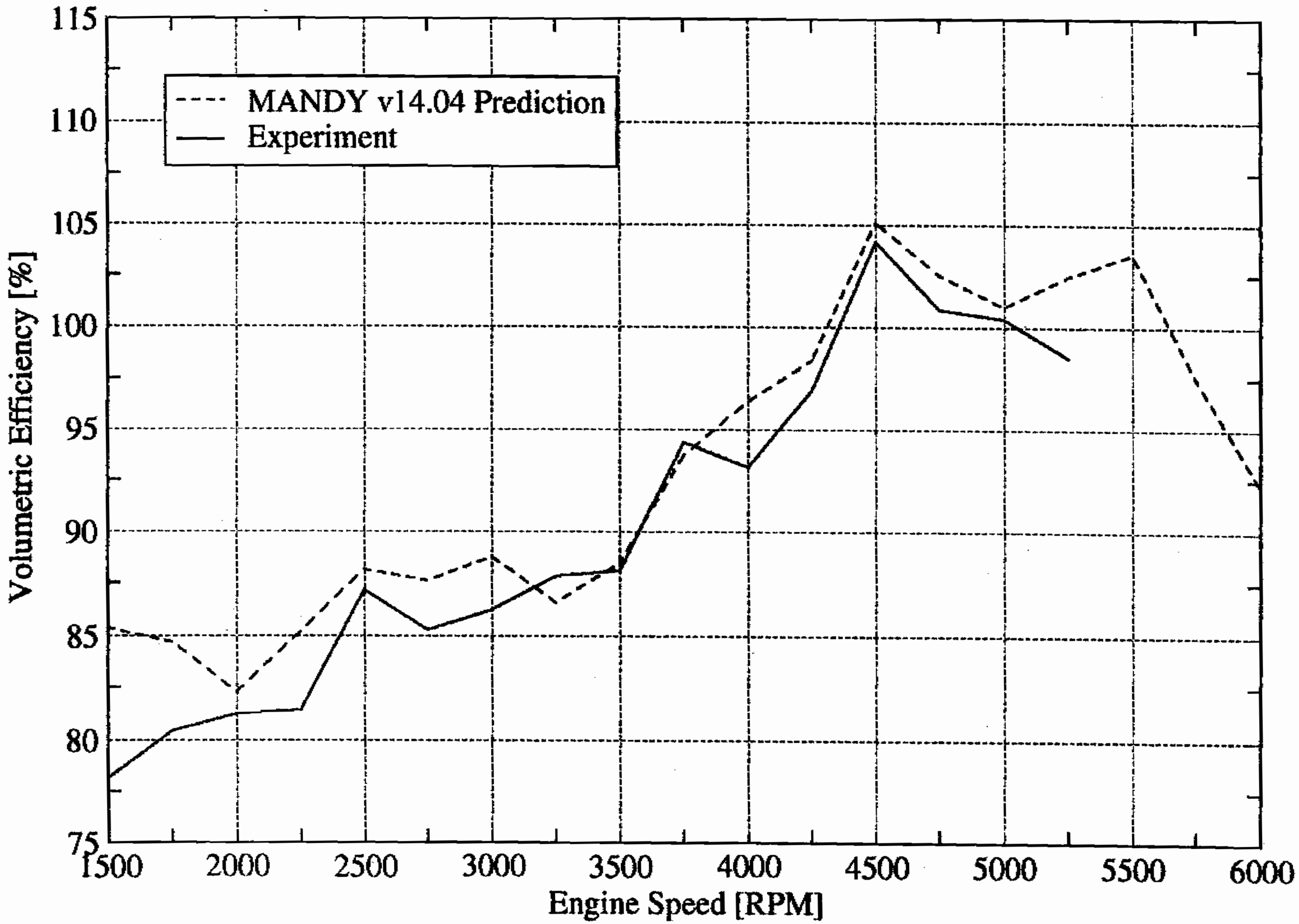

Figure 4.11: Comparison of Predicted and Measured (with Motored Engine) Volumetric Efficiency for Intake #7

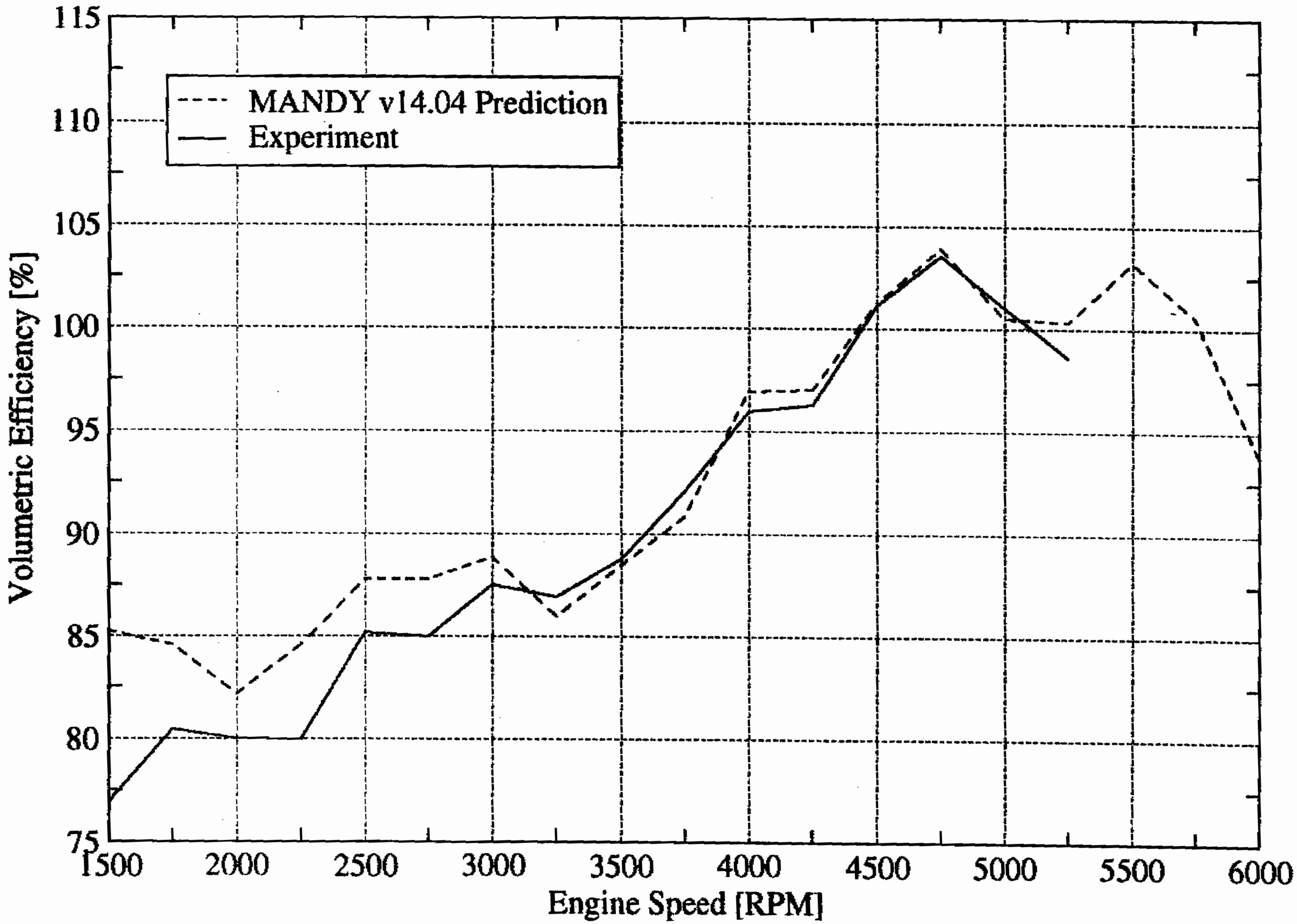

Figure 4.12: Comparison of Predicted and Measured (with Motored Engine) Volumetric Efficiency for Intake #8

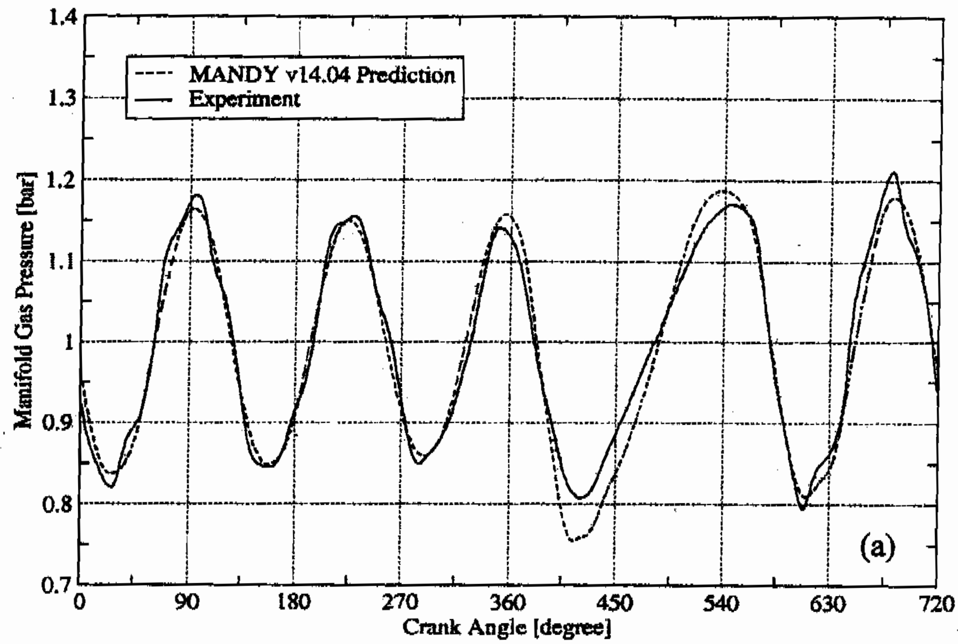

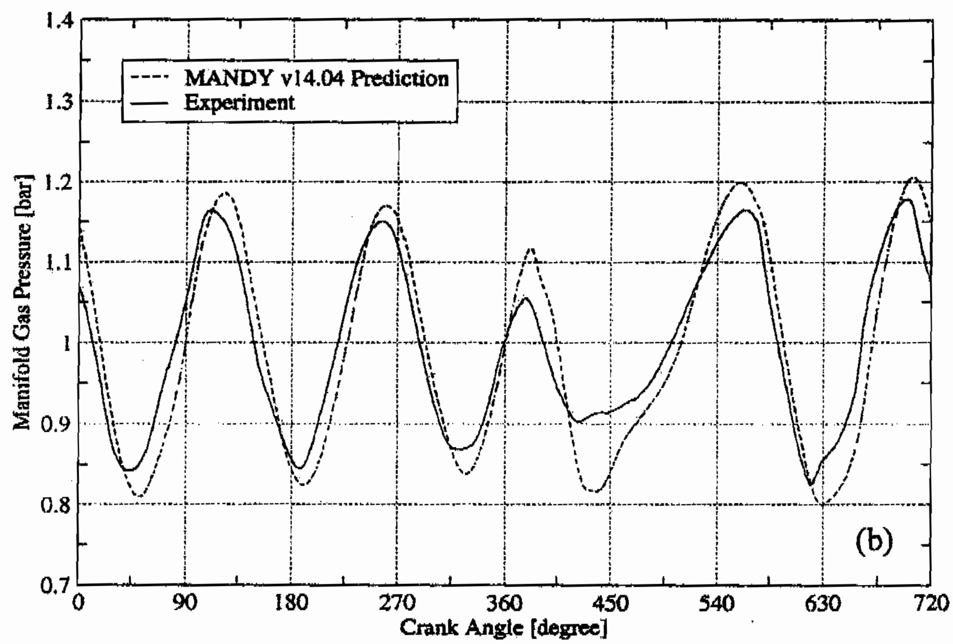

Figure 4.13: Comparison of Predicted and Measured (with Motored Engine) Intake Pressure at e11 for (a) Intake #1 (3750 rpm) and (b) Intake #2 (4250 rpm)

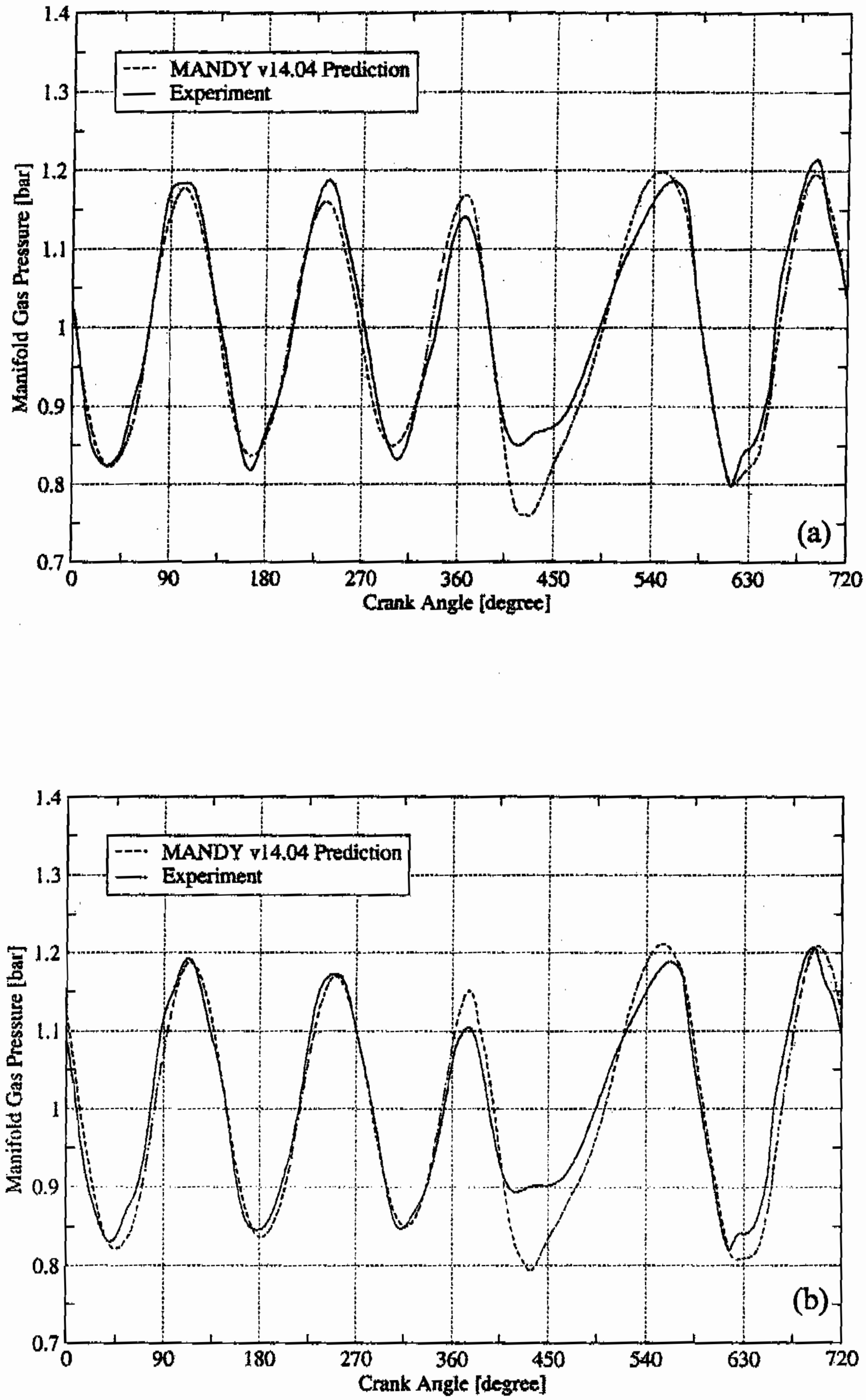

Figure 4.14: Comparison of Predicted and Measured (with Motored Engine) Intake Pressure at e11, 4000 rpm, for (a) Intake #3 and (b) Intake #4

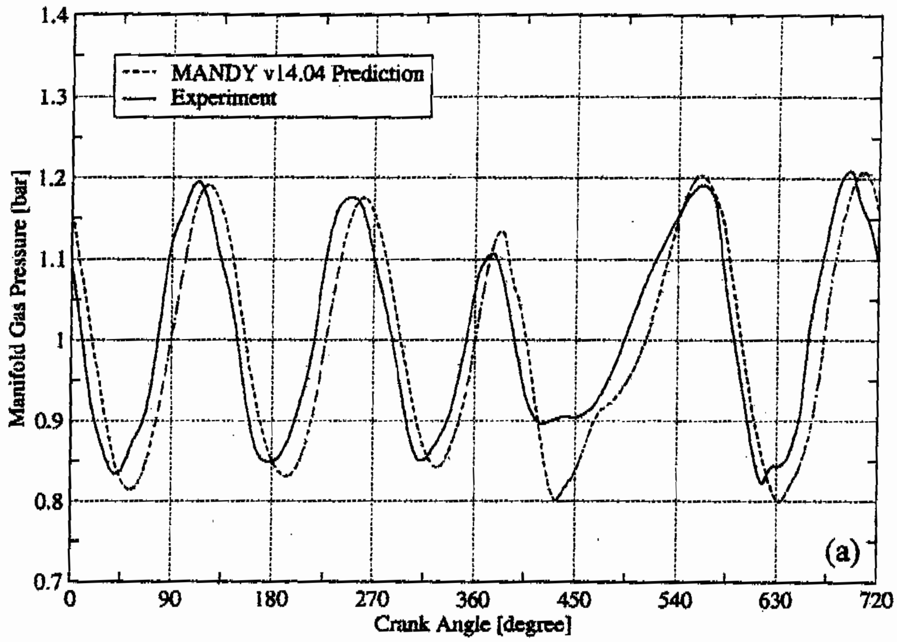

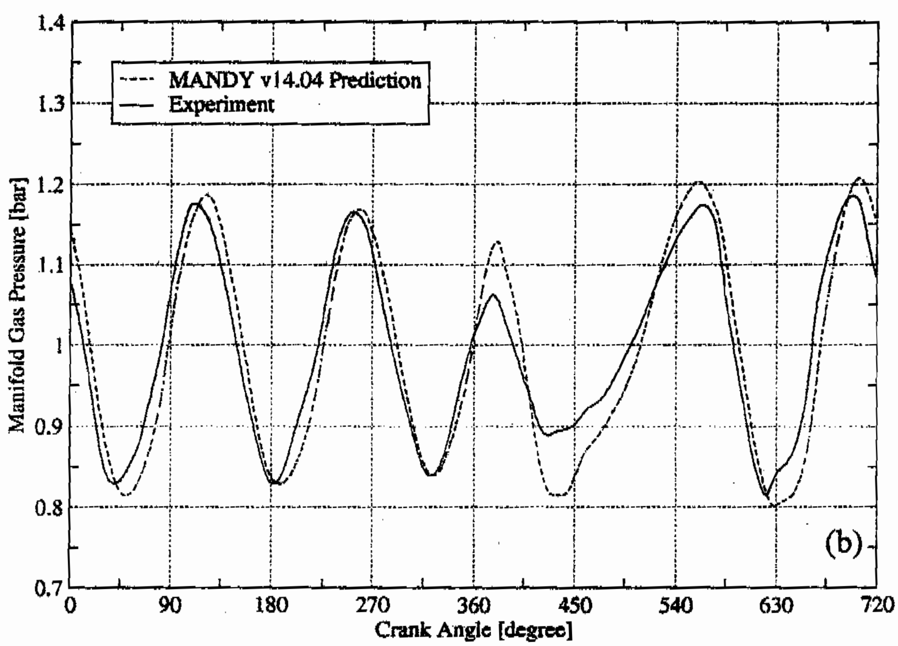

Figure 4.15: Comparison of Predicted and Measured (with Motored Engine) Intake Pressure at e11 for (a) Intake #5 (4500 rpm) and (b) Intake #6 (4250 rpm)

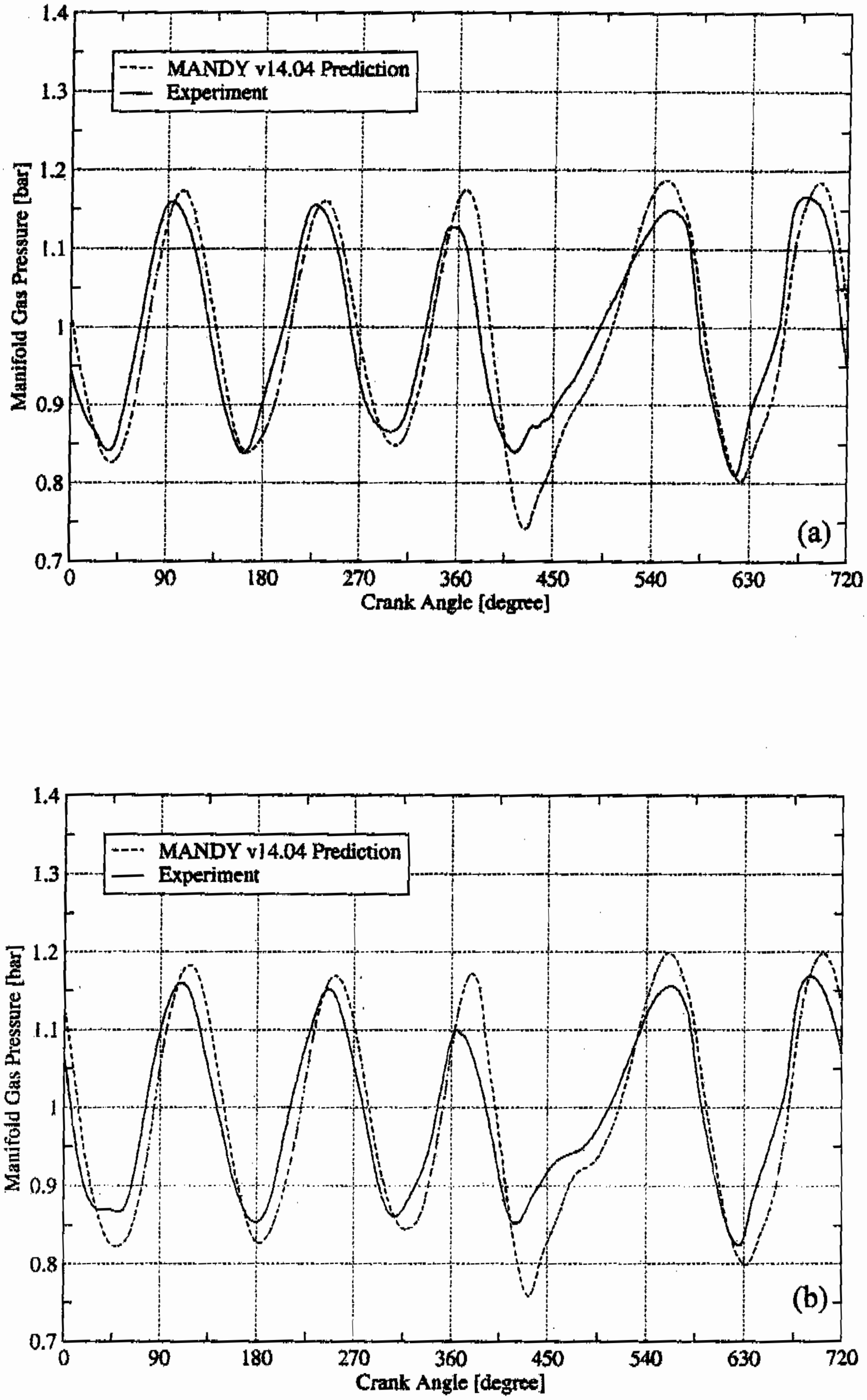

Figure 4.16: Comparison of Predicted and Measured (with Motored Engine) Intake Pressure at e11 for (a) Intake #7 (4500 rpm) and (b) Intake #8 (4750 rpm)

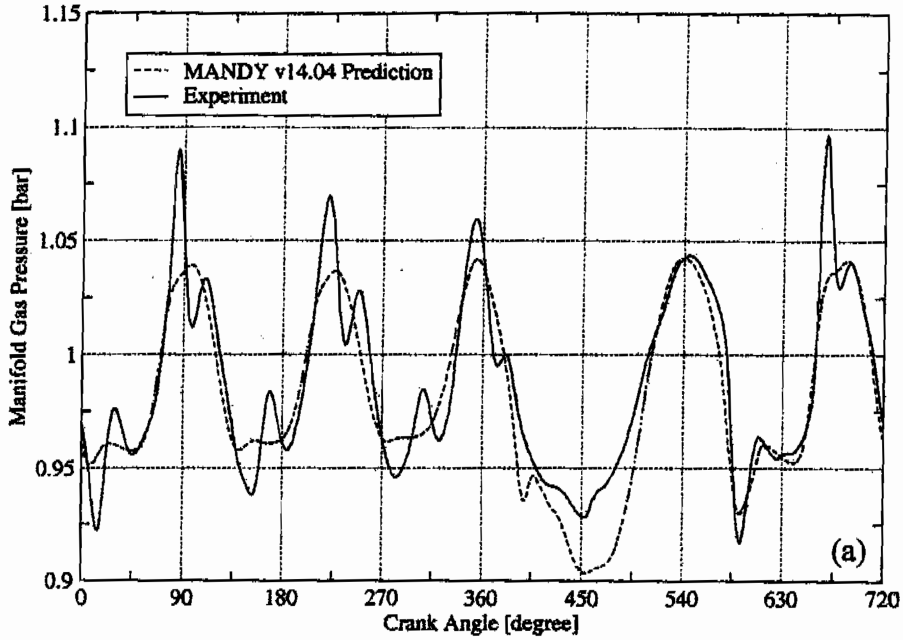

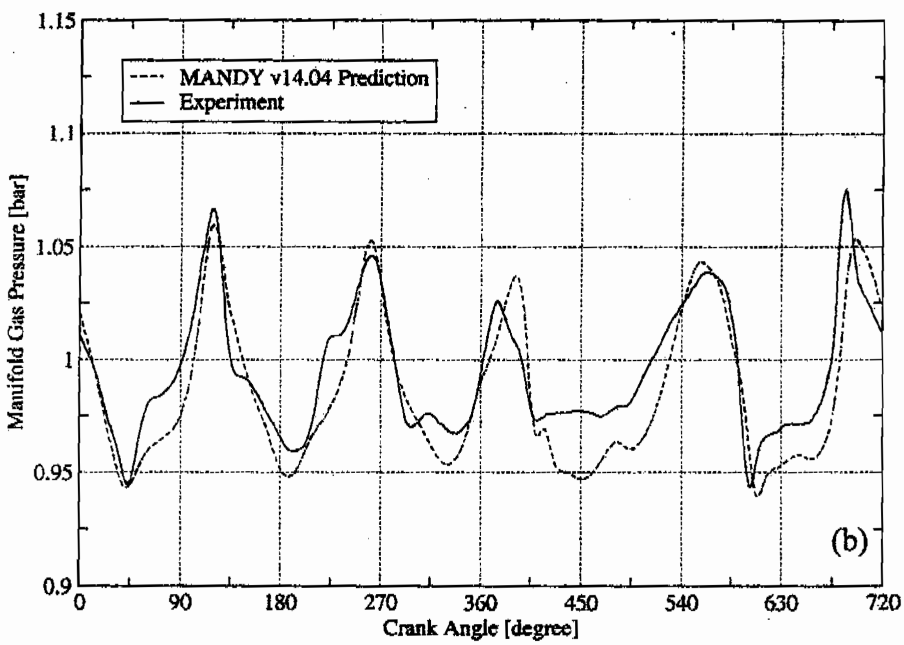

Figure 4.17: Comparison of Predicted and Measured (with Motored Engine) Intake Pressure at e12 for (a) Intake #1 (3750 rpm) and (b) Intake #2 (4250 rpm)

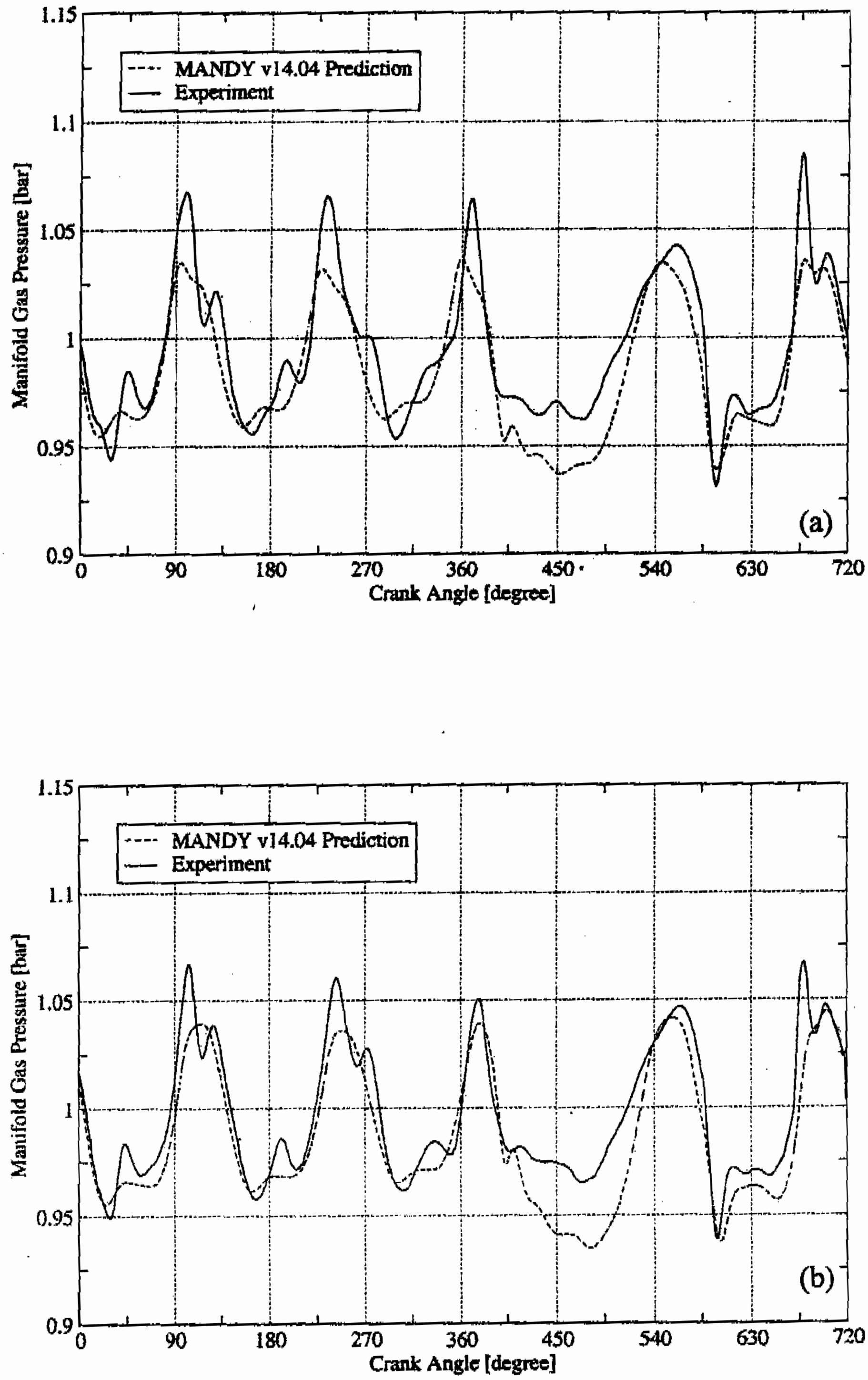

Figure 4.18: Comparison of Predicted and Measured (with Motored Engine) Intake Pressure at e12, 4000 rpm, for (a) Intake #3 and (b) Intake #4

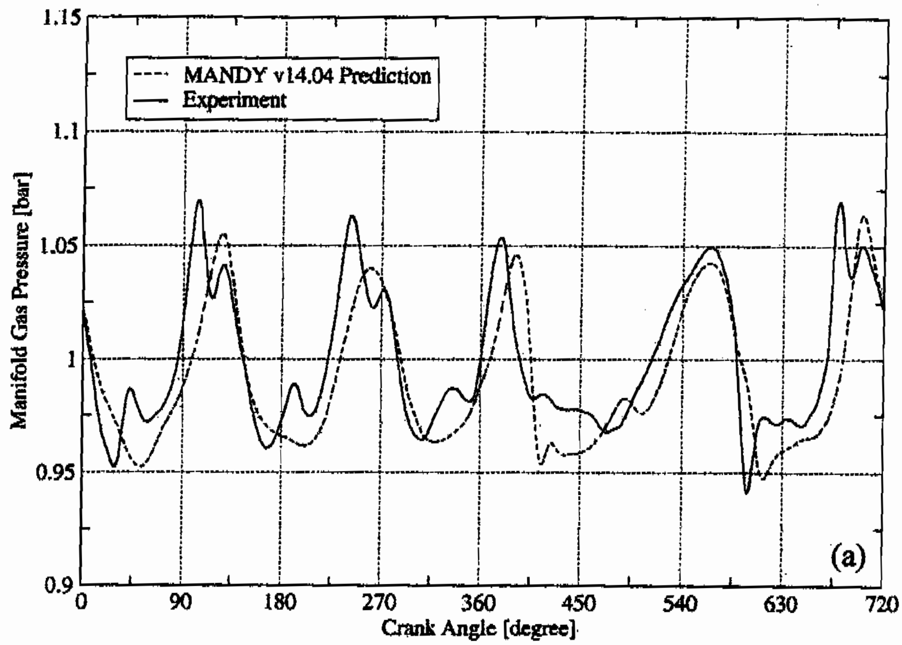

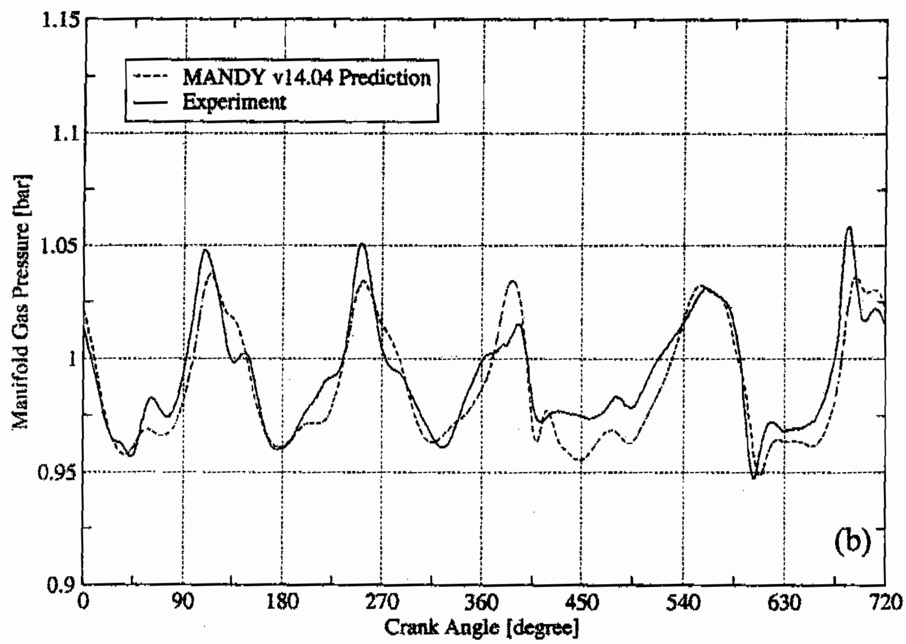

Figure 4.19: Comparison of Predicted and Measured (with Motored Engine) Intake Pressure at e12 for (a) Intake #5 (4500 rpm) and (b) Intake #6 (4250 rpm)

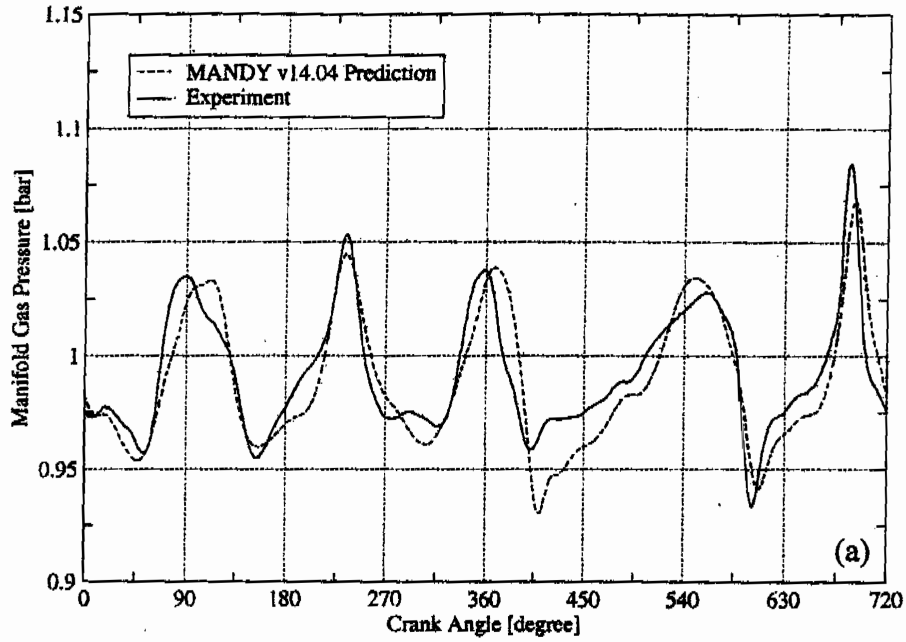

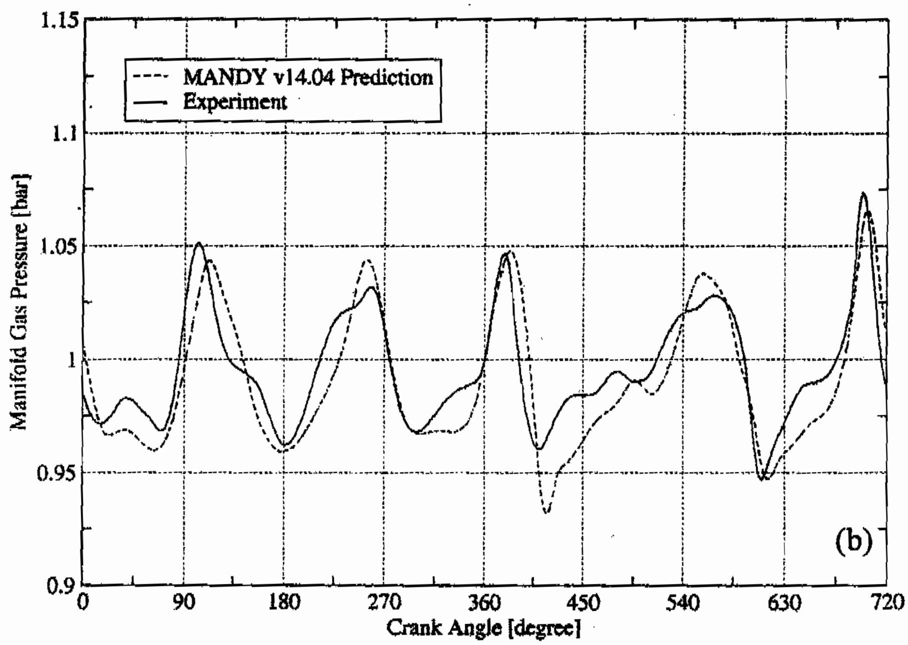

Figure 4.20: Comparison of Predicted and Measured (with Motored Engine) Intake Pressure at e12 for (a) Intake #7 (4500 rpm) and (b) Intake #8 (4750 rpm)

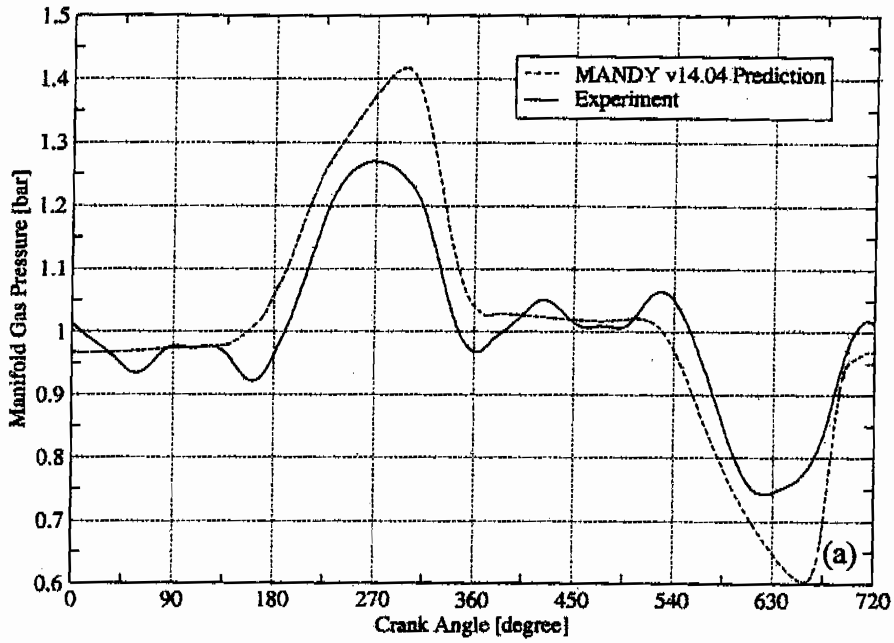

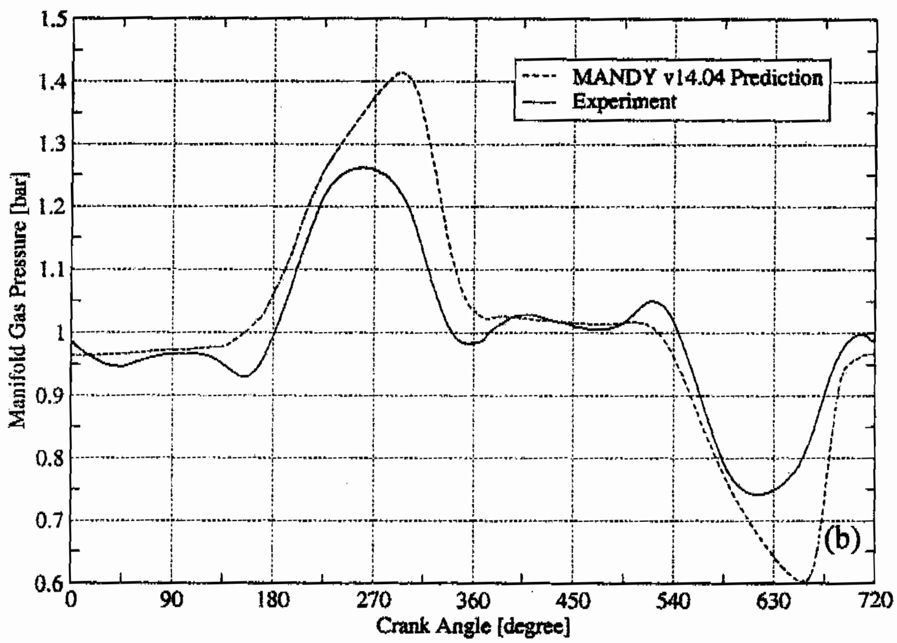

Figure 4.21: Comparison of Predicted and Measured (with Motored Engine) Exhaust Pressure at e3, 2000 rpm, for (a) Intake #1 and (b) Intake #8

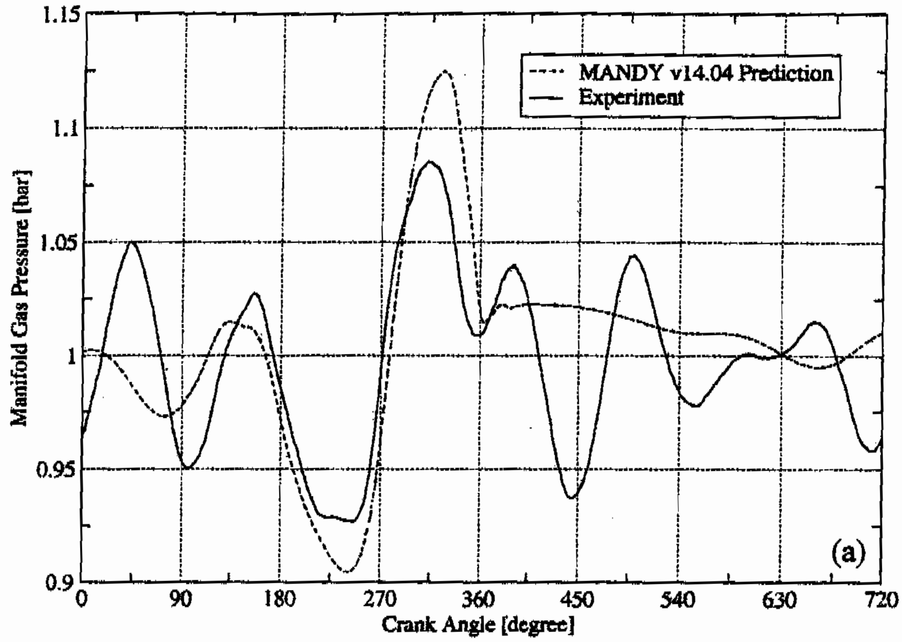

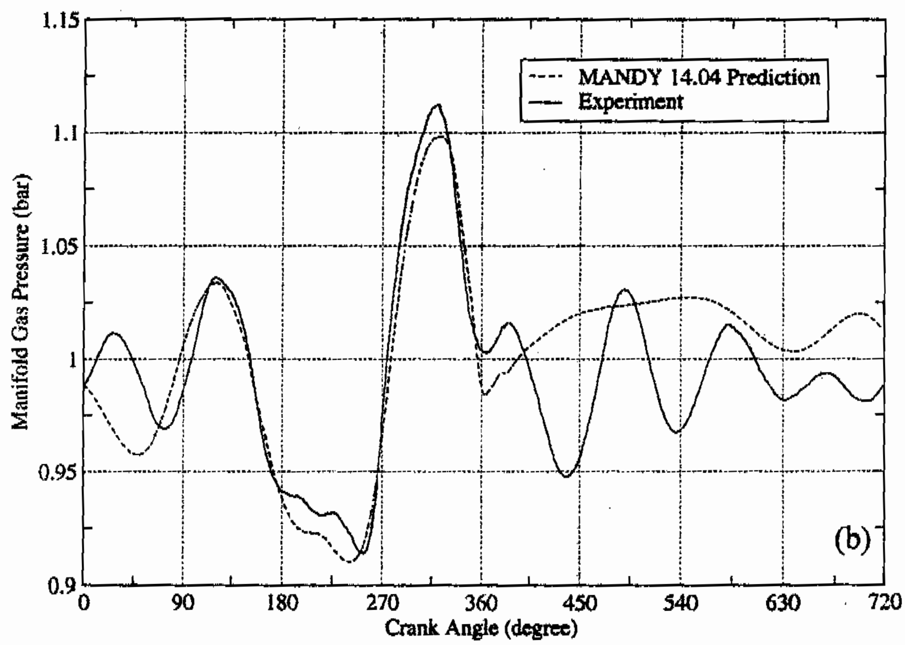

Figure 4.22: Comparison of Predicted and Measured (with Motored Engine) Exhaust Pressure at e3, 3750 rpm, for (a) Intake #1 and (b) Intake #8

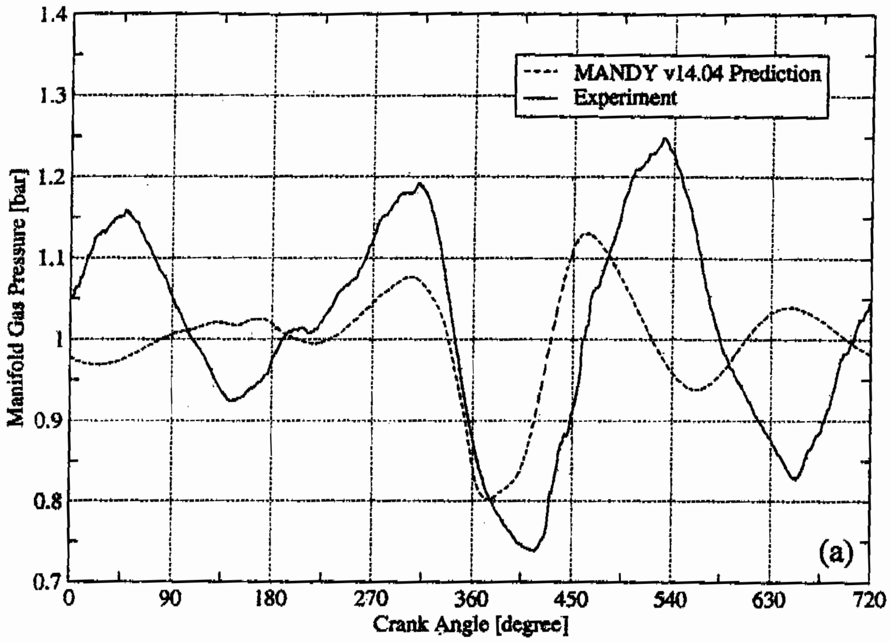

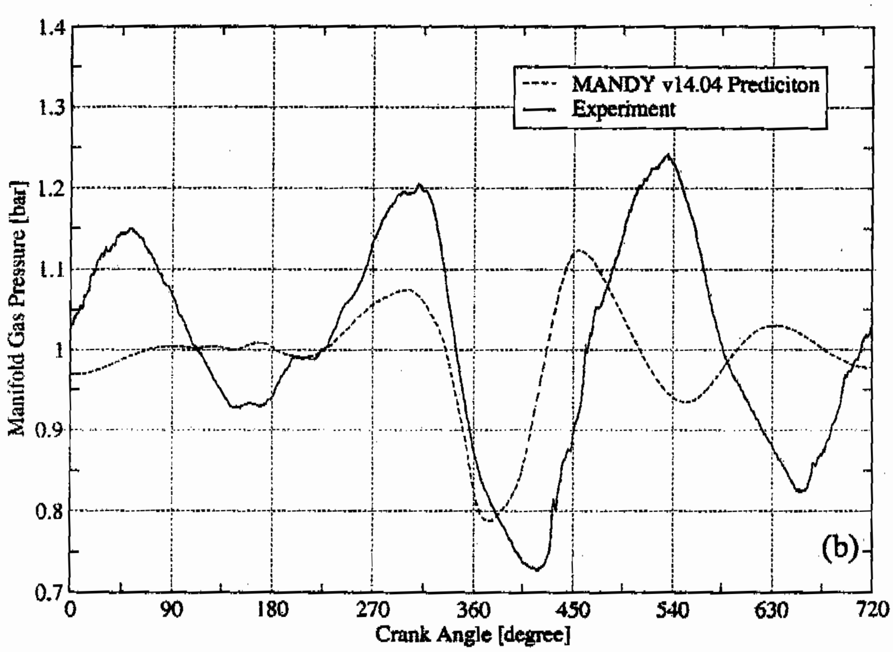

Figure 4.23: Comparison of Predicted and Measured (with Motored Engine) Exhaust Pressure at e3, 4750 rpm, for (a) Intake #1 and (b) Intake #8

CHAPTER 5

CONCLUDING REMARKS

The effects of tapered intake stacks on overall engine performance are examined in this study. The experiments are performed on a motoring single cylinder engine over a wide range of operating speeds with eight different tapered intake configurations. The eight intake stacks evaluated have cross-sectional area changes with taper area ratios ranging from 1 (no taper) to 3 (200% increase in area at the entrance). Crank-angle resolved intake, exhaust, and in-cylinder pressure data and the exhaust mass flow rate are acquired from the motoring engine to quantify the impact on overall engine performance. A time-domain flow dynamics computer code is used to simulate the breathing system behavior. The predicted results are compared with the experimental data for model validation. The present chapter summarizes the results of this study.

5.1 Experimental Results

In order to isolate the effects of the tapered geometry, the experiments are conducted while retaining all other geometric features the same, including the bellmouth entry, large flanged openings, and overall intake system lengths. The influence of the tapered geometry in the induction system is demonstrated by using time-domain pressure measured in the intake and exhaust at key locations and volumetric efficiency inferred from exhaust mass flow rates at speeds ranging from 1000 – 5500 rpm at 250 rpm increments.

The experimental volumetric efficiency results show that the tapered geometry produces significant variations in the engine performance. Engine speeds for peak volumetric efficiency show a regular increase of approximately 250 rpm for each increase of taper area ratio. The length of the taper also produces a noticeable trend, in that the engine speed for peak efficiency was reduced by 250 rpm when compared to the same taper area ratio intake stack with full length taper. These trends in engine speed shifts are shown to be qualitatively captured by the classical lumped parameter approach for intake tuning proposed earlier by Engelman and his coworkers. The experimental data also illustrated that, as the taper size gets larger than 50%, the peak magnitude of volumetric efficiency drops with each succeeding taper area ratio increase. Conversely, reducing the length of the taper increases the peak volumetric efficiency magnitude similar to the level of a one-step smaller taper area ratio intake stack.

The crank-angle resolved data acquired in the intake system demonstrated that the tapered geometry also had a significant impact on the pressures at both locations in the intake duct. At the same engine speed and transducer location, the magnitude and phasing of the pressure are significantly different for even two intakes just one-step different in taper area ratio. The pressure peak before IVC, is in general, an indicator of the trend for the magnitude of volumetric efficiency. Volumetric efficiency peaks usually correlate with the intake pressure trace that displays the highest peak pressure before intake valve closing. This correlation is, however, very sensitive to the CAD where it occurs. With only a relatively small shift of approximately 10 CAD, a higher peak pressure shows no additional benefit on the volumetric efficiency. This is noted for several intakes with significantly less peak pressure but similar or better volumetric efficiency. The in-cylinder pressure traces showed substantial variations for each intake at different engine speeds during the pumping loop portion of the engine cycle. Based on the percentage of error for this type of transducers and a comparison of results with the engine simulation code predictions, these experimental results were not emphasized or fully evaluated in this study.

The exhaust pressures were found to be relatively insensitive to the presence of the tapered geometry intake stacks, as expected. While these pressures showed dramatically different magnitude and phasing with engine speed, they were nearly identical for all eight intake stacks. A trend evident from the exhaust pressures is that at 4000 rpm the trace shows nearly no magnitude variation across the entire cycle. Simple calculations based on the classical lumped approach using temperatures measured in the exhaust system combined with the length of the exhaust pipe support the idea that this is the natural frequency of the system.

5.2 Time-Domain Computational Model

Although the simple lumped parameter approach produced reasonable results in determining the engine speed for peak efficiency, it has no means for predicting the magnitude of engine parameters such as power, torque or volumetric efficiency. Such a prediction needs a more complex time-domain nonlinear approach that has been developed and widely used over the last three decades. The predictions from one such finite difference engine simulation code are compared with the experimental data from a single cylinder engine for volumetric efficiency, and intake and exhaust pressures. The nonlinear fluid dynamic model predictions compared, in general, well with the experiments. The agreement between the model and experiment for volumetric efficiency is excellent for all eight intake stacks, capturing both the engine speed shift for peak efficiency and the magnitude reduction as taper increased. The predictions for both transducer locations in the intake are also found to match well for amplitude and phasing. The pressure wave forms in the exhaust are found to match reasonably with the experiments by predicting the phasing of the major peaks and the overall shape of extremely diverse traces. However, additional exhaust system modeling changes should be considered to possibly improve these predictions.

The completed parametric study for model input file calibration shows that the predictions are sensitive to several variables that are not readily attainable. Such variables as wall heat transfer, temperature of the cylinder wall, and the duct wall friction could not be measured during the course of this study. Knowledge of these variables and care must be used when setting their values in the input files of the model as predictions can be significantly influenced.

The time-domain computational model based on the finite difference approach is thus, a useful tool to study both the overall engine performance parameters and the pressure variation in the intake and exhaust in terms of amplitudes and phasing. With the level of agreement attained in this study, this computational model would reduce the number of alternatives and accelerate the development process of intake/exhaust systems at the design stage. While the present work considered tapered intake stacks, further work is being conducted on other intake geometries including, different radius bellmouths at the stack opening, 135° bends, and 135° S-shaped bends. Firing engine data will also become available for all intakes to investigate the nature of variations from the motored engine data.

Appendix A – Experimental Data

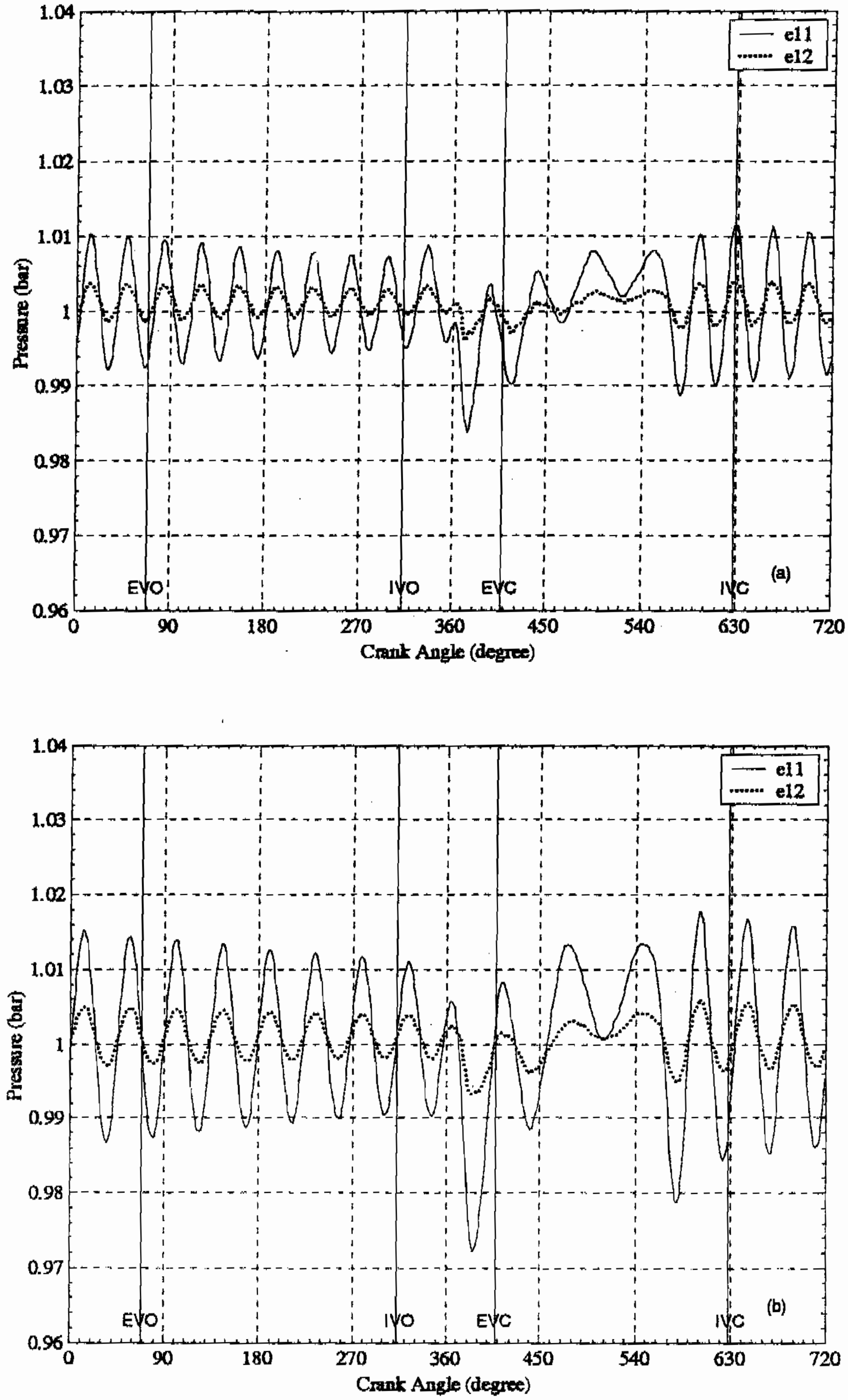

Figure A.1: OSU Dynamometer Experiment: Intake #1 – Pressure versus CAD for Intake Pressure Transducers at (a) 1000 rpm and (b) 1250 rpm

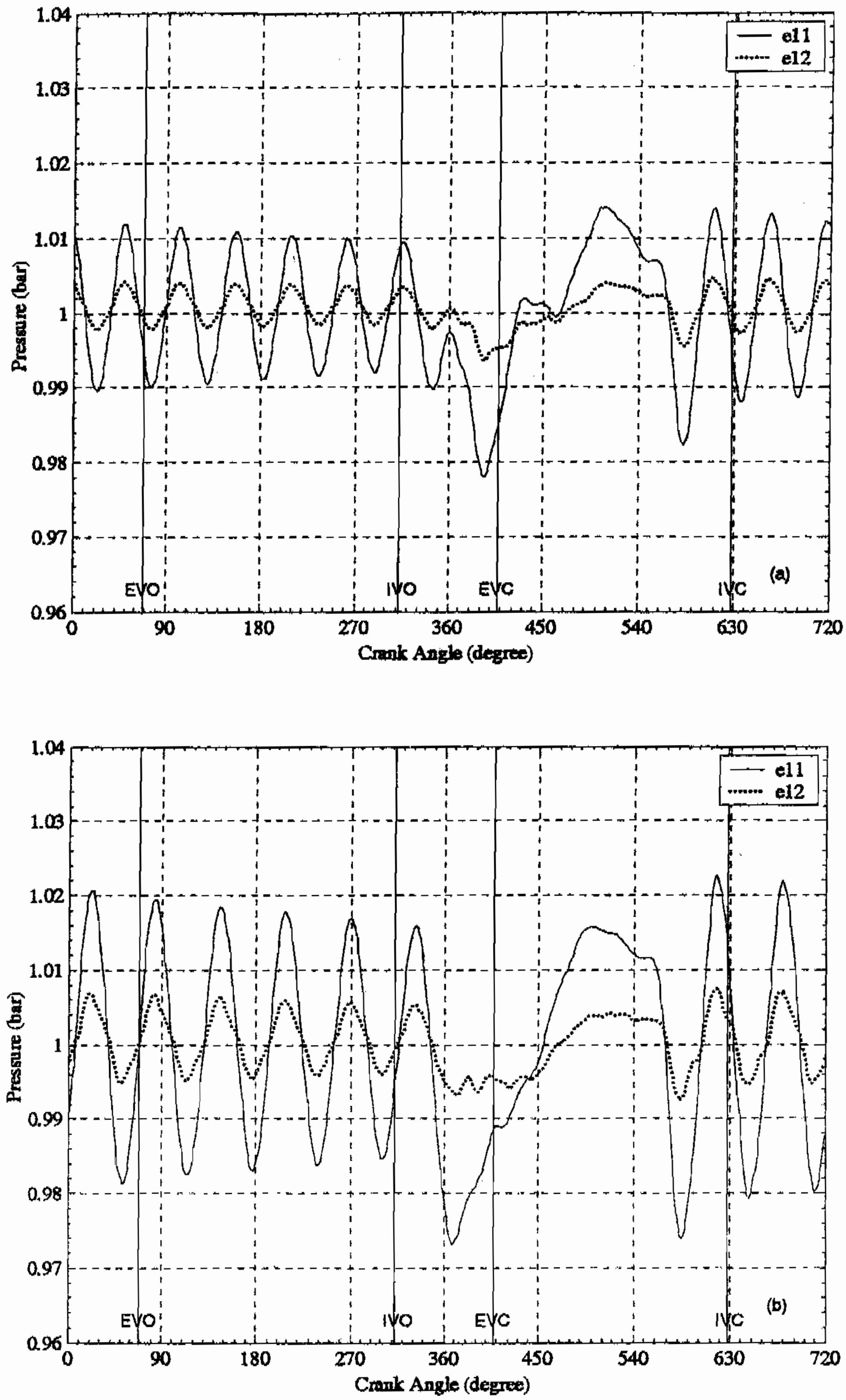

Figure A.2: OSU Dynamometer Experiment: Intake #1 – Pressure versus CAD for Intake Pressure Transducers at (a) 1500 rpm and (b) 1750 rpm

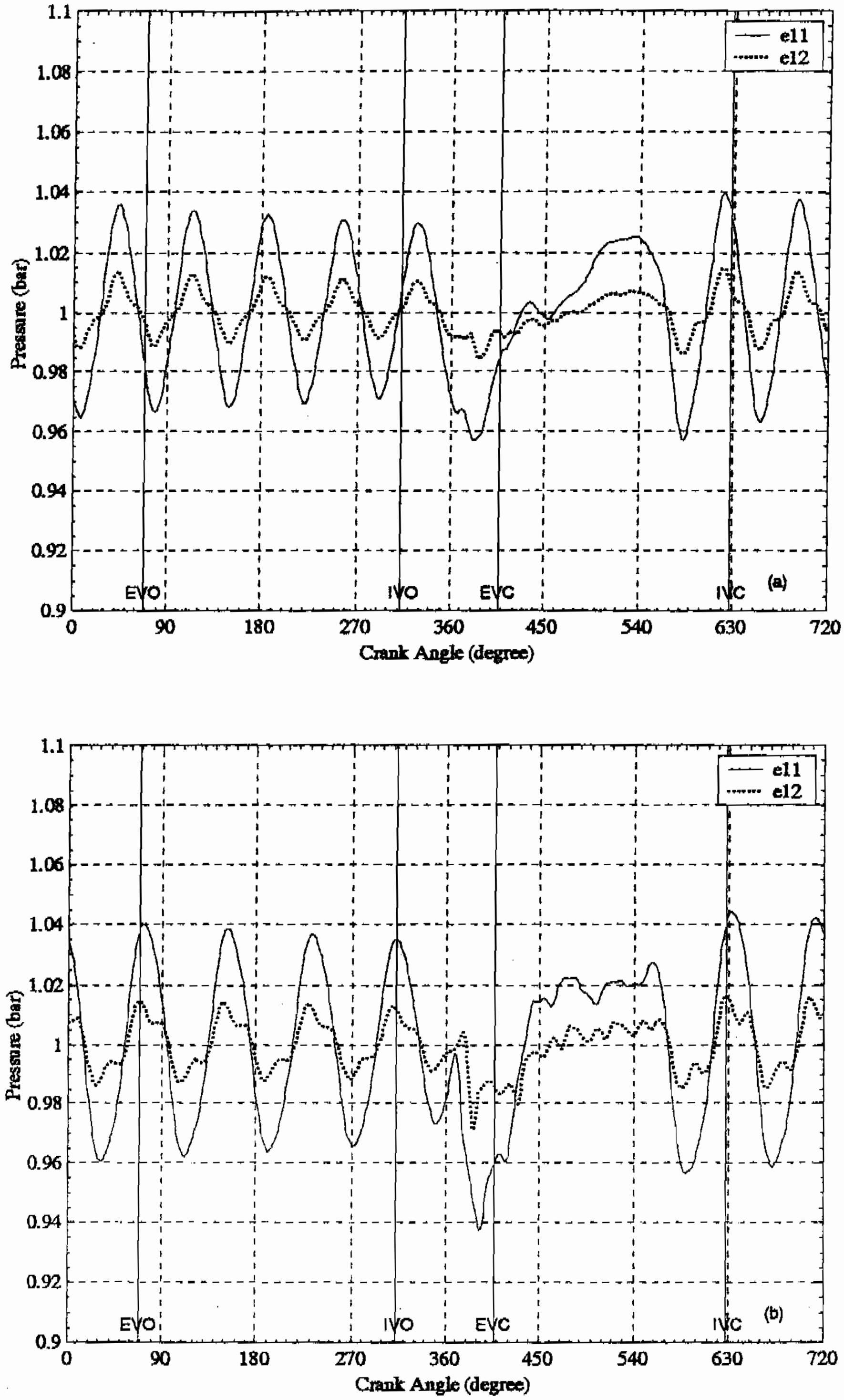

Figure A.3: OSU Dynamometer Experiment: Intake #1 – Pressure versus CAD for Intake Pressure Transducers at (a) 2000 rpm and (b) 2250 rpm

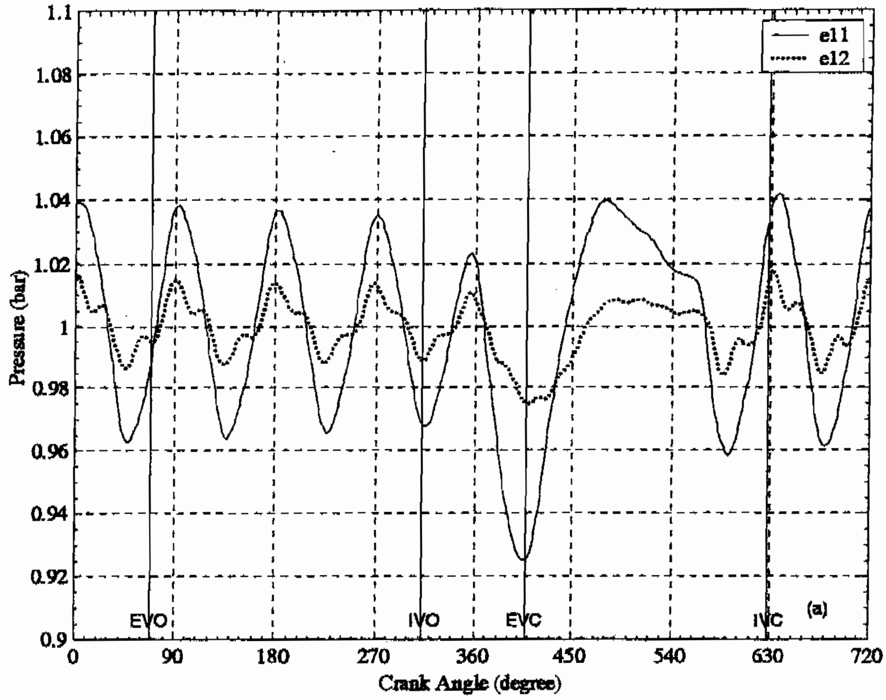

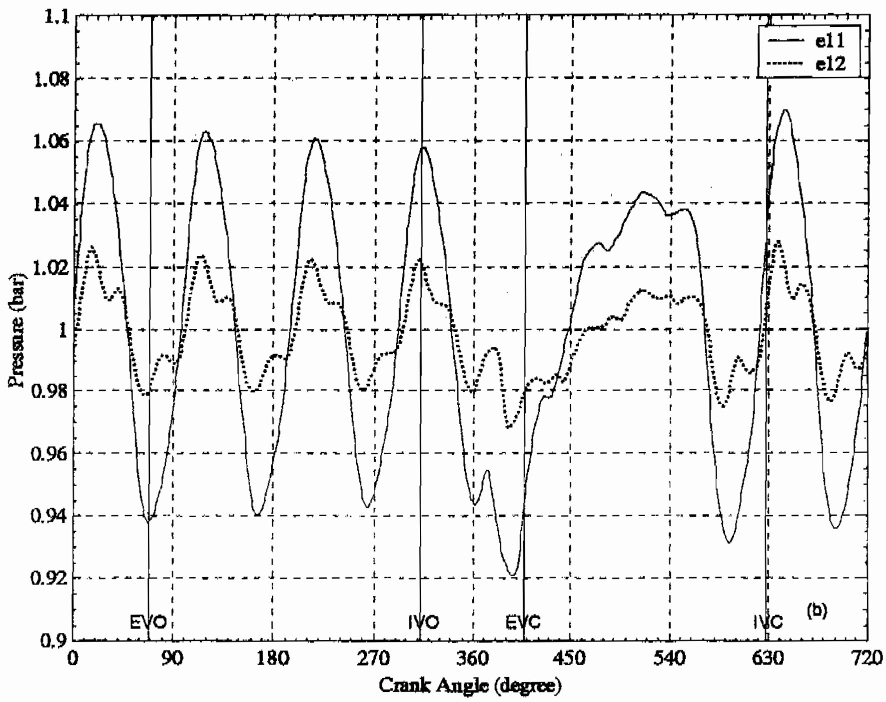

Figure A.4: OSU Dynamometer Experiment: Intake #1 – Pressure versus CAD for Intake Pressure Transducers at (a) 2500 rpm and (b) 2750 rpm

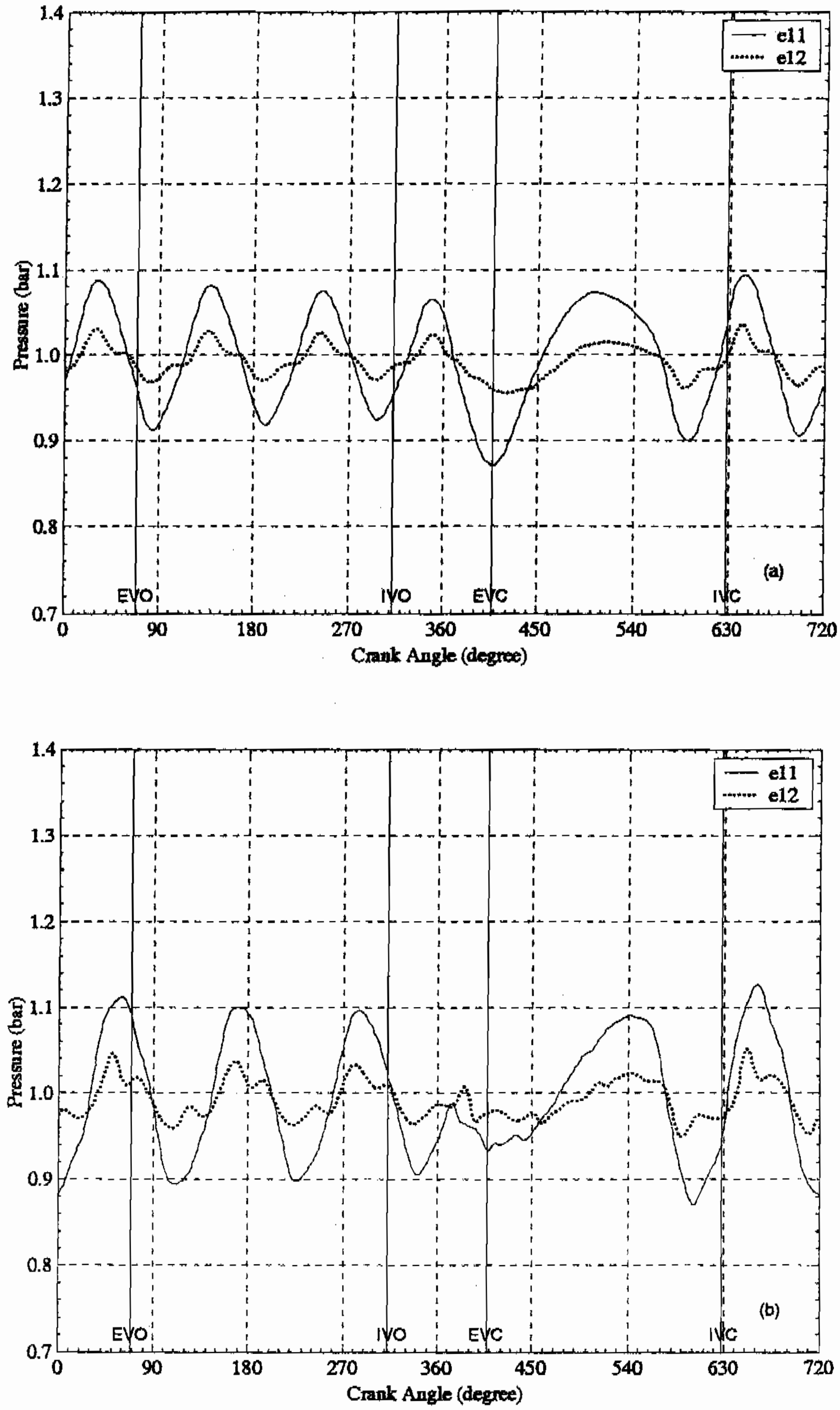

Figure A.5: OSU Dynamometer Experiment: Intake #1 – Pressure versus CAD for Intake Pressure Transducers at (a) 3000 rpm and (b) 3250 rpm

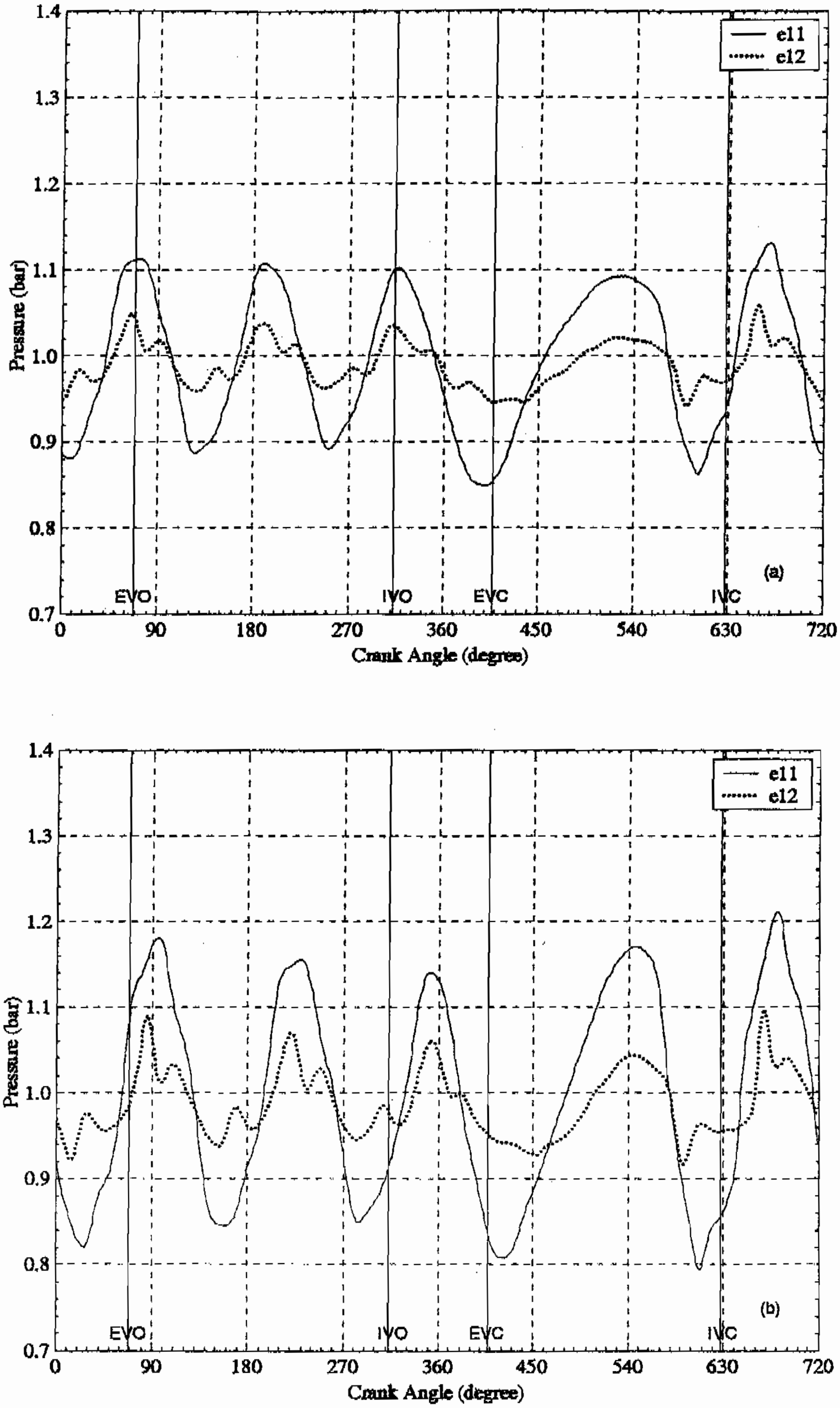

Figure A.6: OSU Dynamometer Experiment: Intake #1 – Pressure versus CAD for Intake Pressure Transducers at (a) 3500 rpm and (b) 3750 rpm

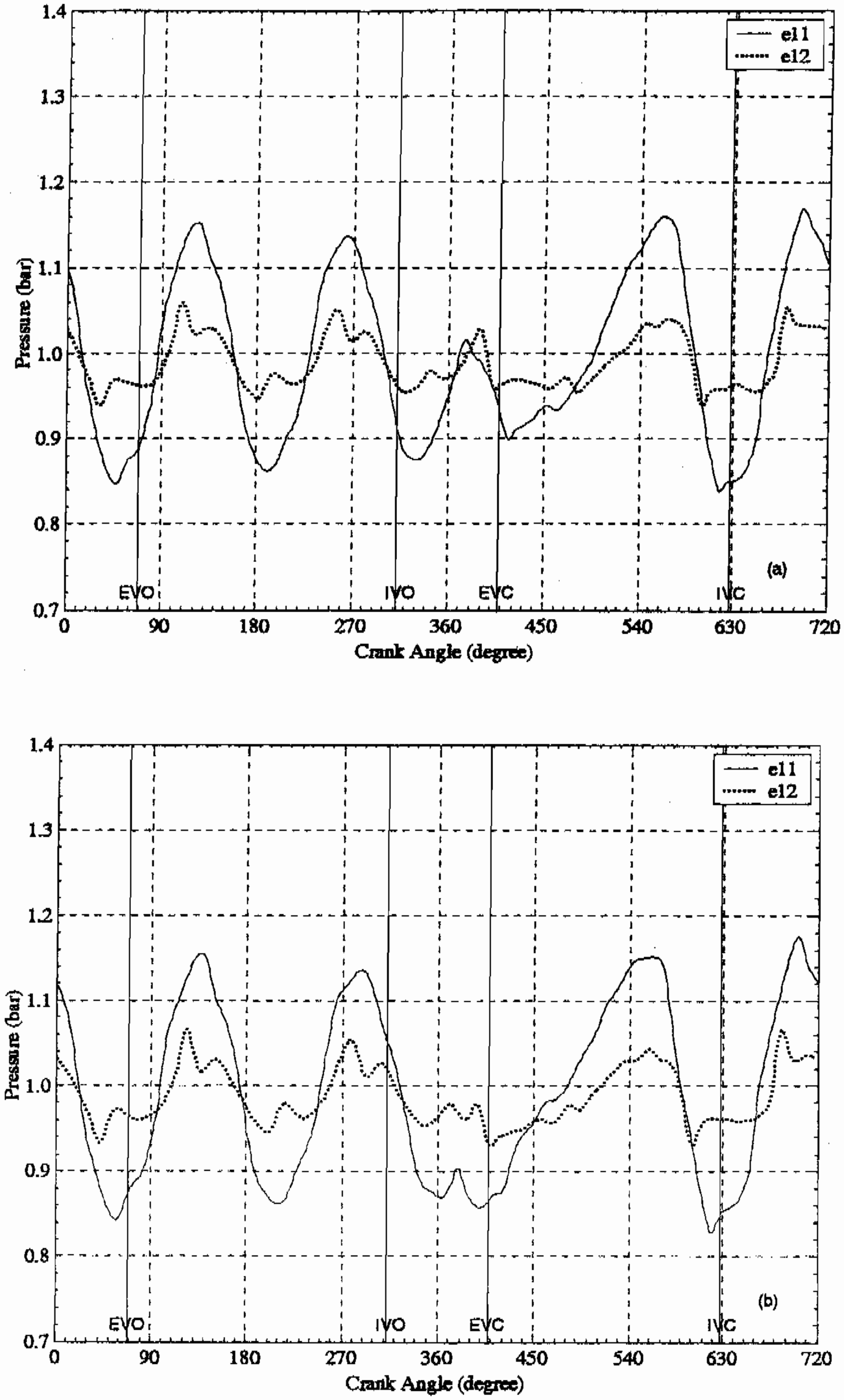

Figure A.7: OSU Dynamometer Experiment: Intake #1 – Pressure versus CAD for Intake Pressure Transducers at (a) 4000 rpm and (b) 4250 rpm

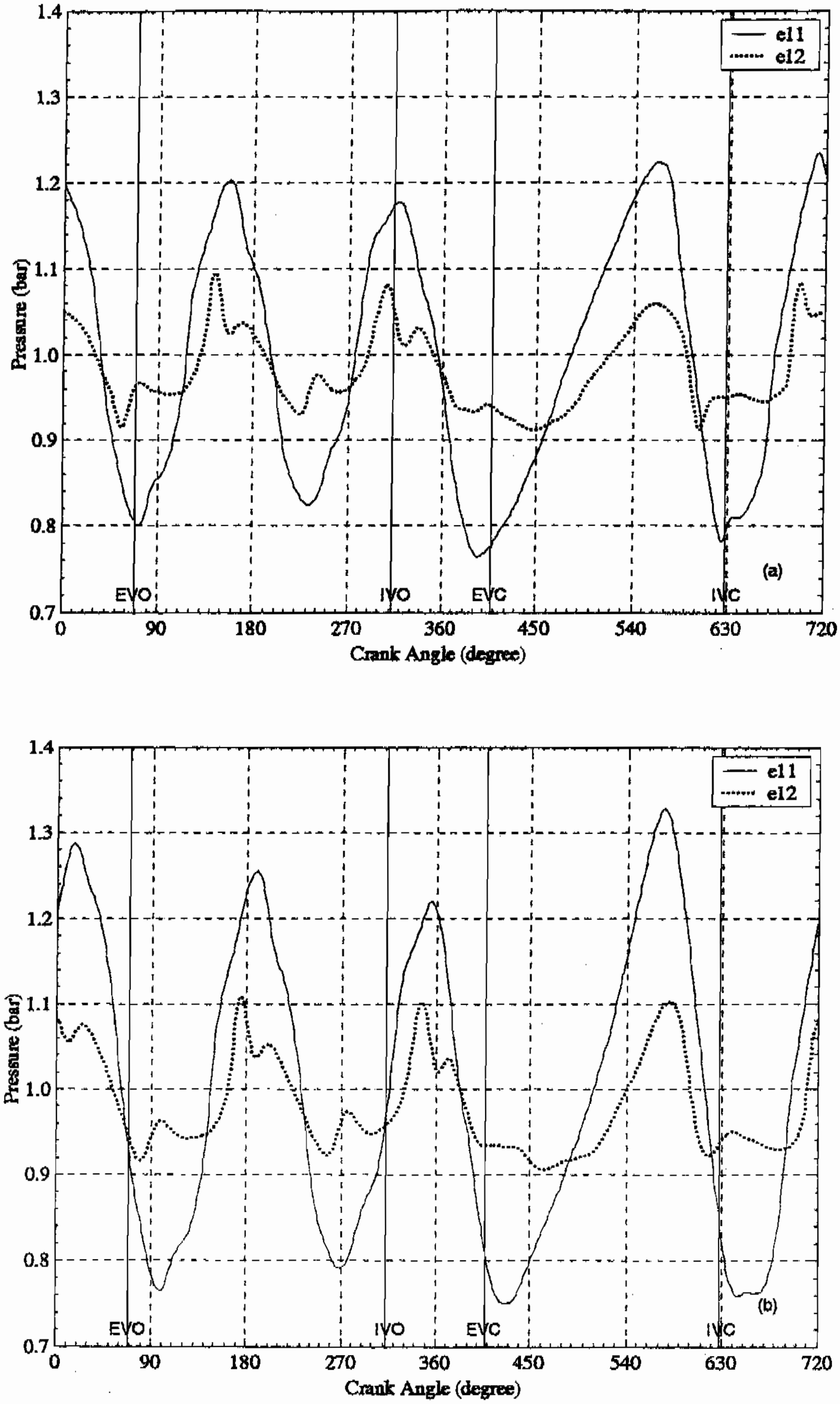

Figure A.8: OSU Dynamometer Experiment: Intake #1 – Pressure versus CAD for Intake Pressure Transducers at (a) 4500 rpm and (b) 4750 rpm

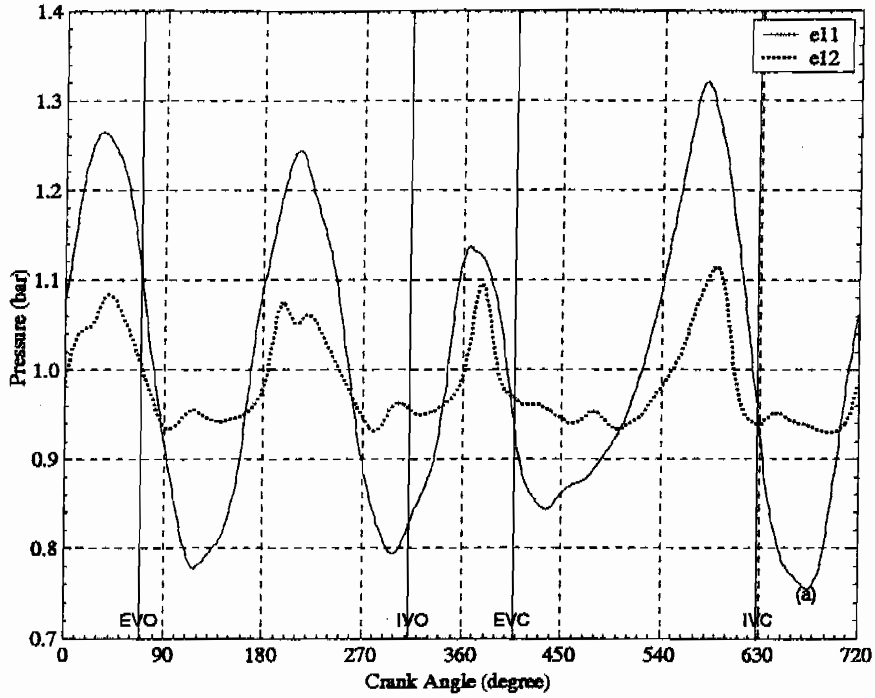

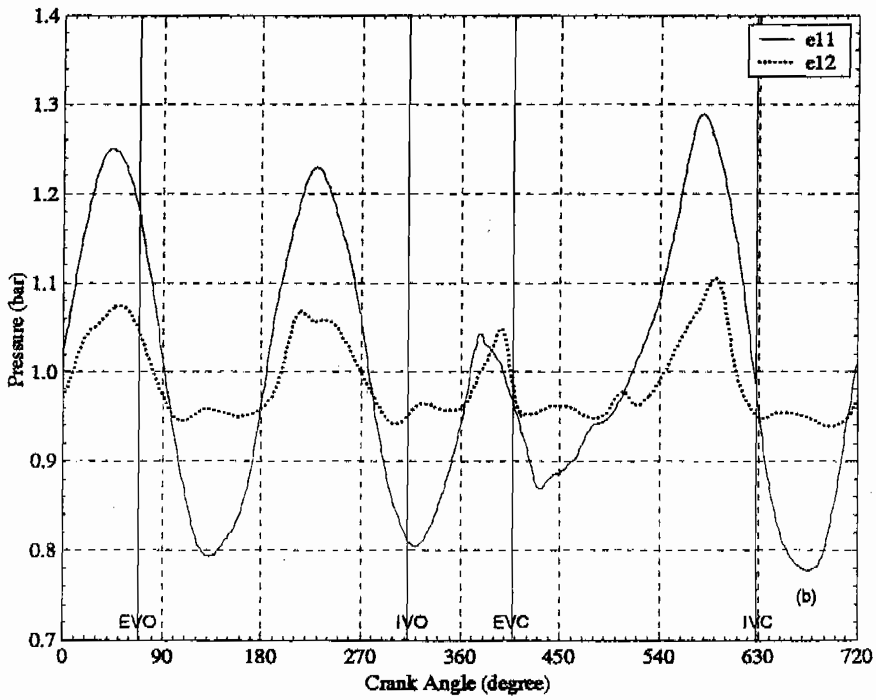

Figure A.9: OSU Dynamometer Experiment: Intake #1 – Pressure versus CAD for Intake Pressure Transducers at (a) 5000 rpm and (b) 5250 rpm

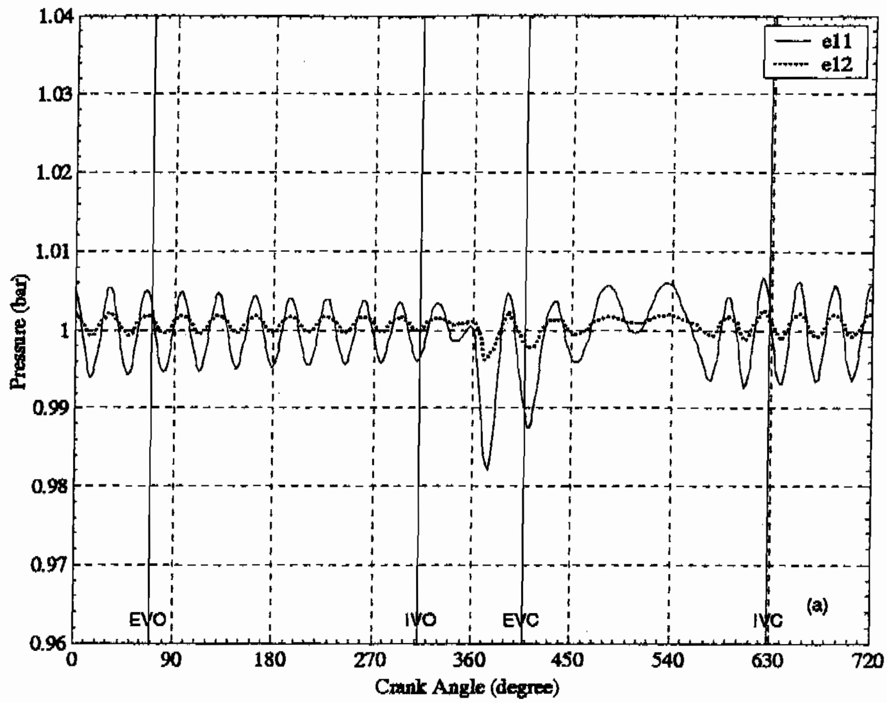

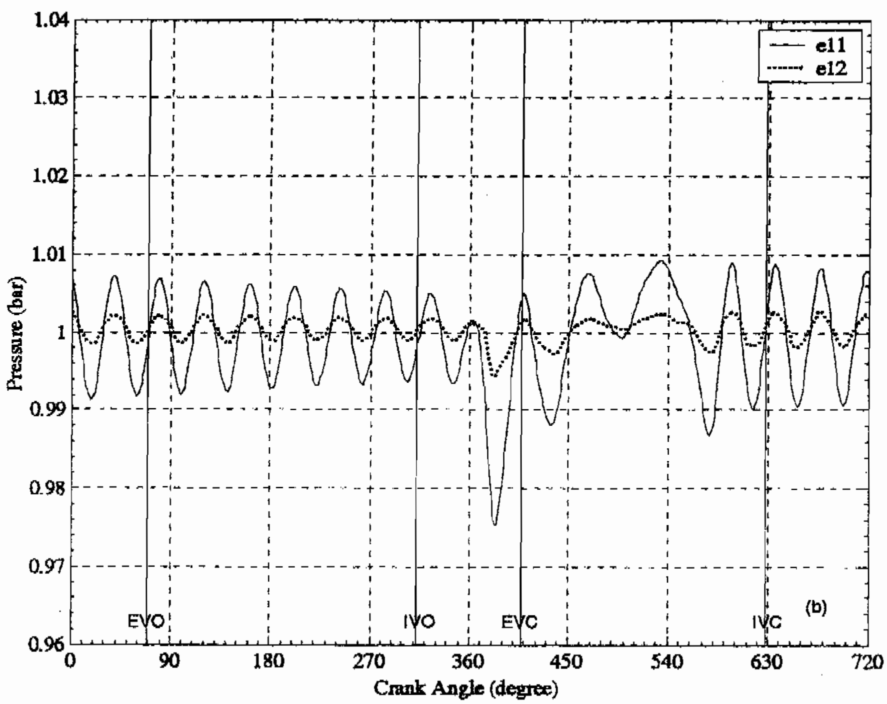

Figure A.10: OSU Dynamometer Experiment: Intake #2 – Pressure versus CAD for Intake Pressure Transducers at (a) 1000 rpm and (b) 1250 rpm

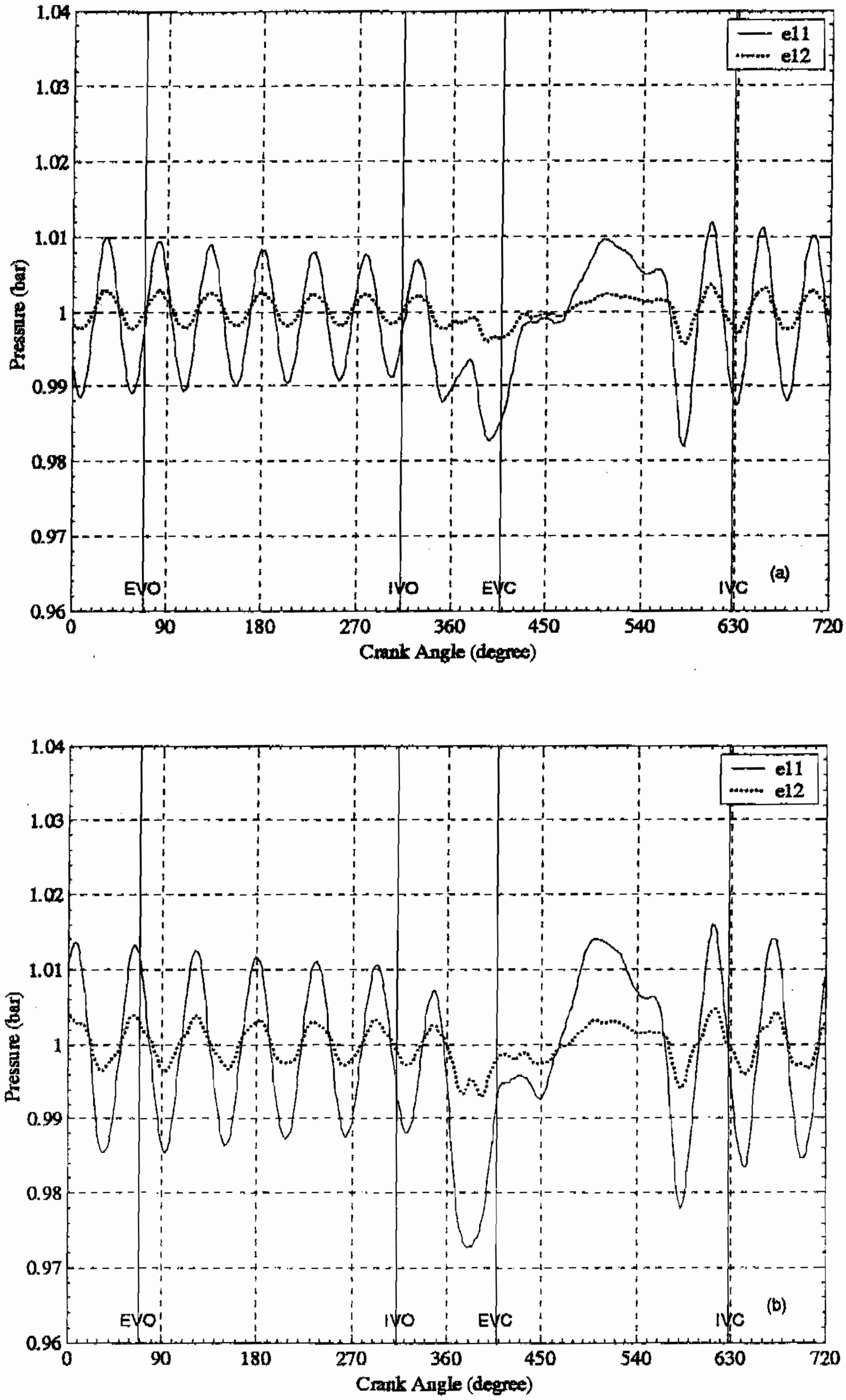

Figure A.11: OSU Dynamometer Experiment: Intake #2 – Pressure versus CAD for Intake Pressure Transducers at (a) 1500 rpm and (b) 1750 rpm

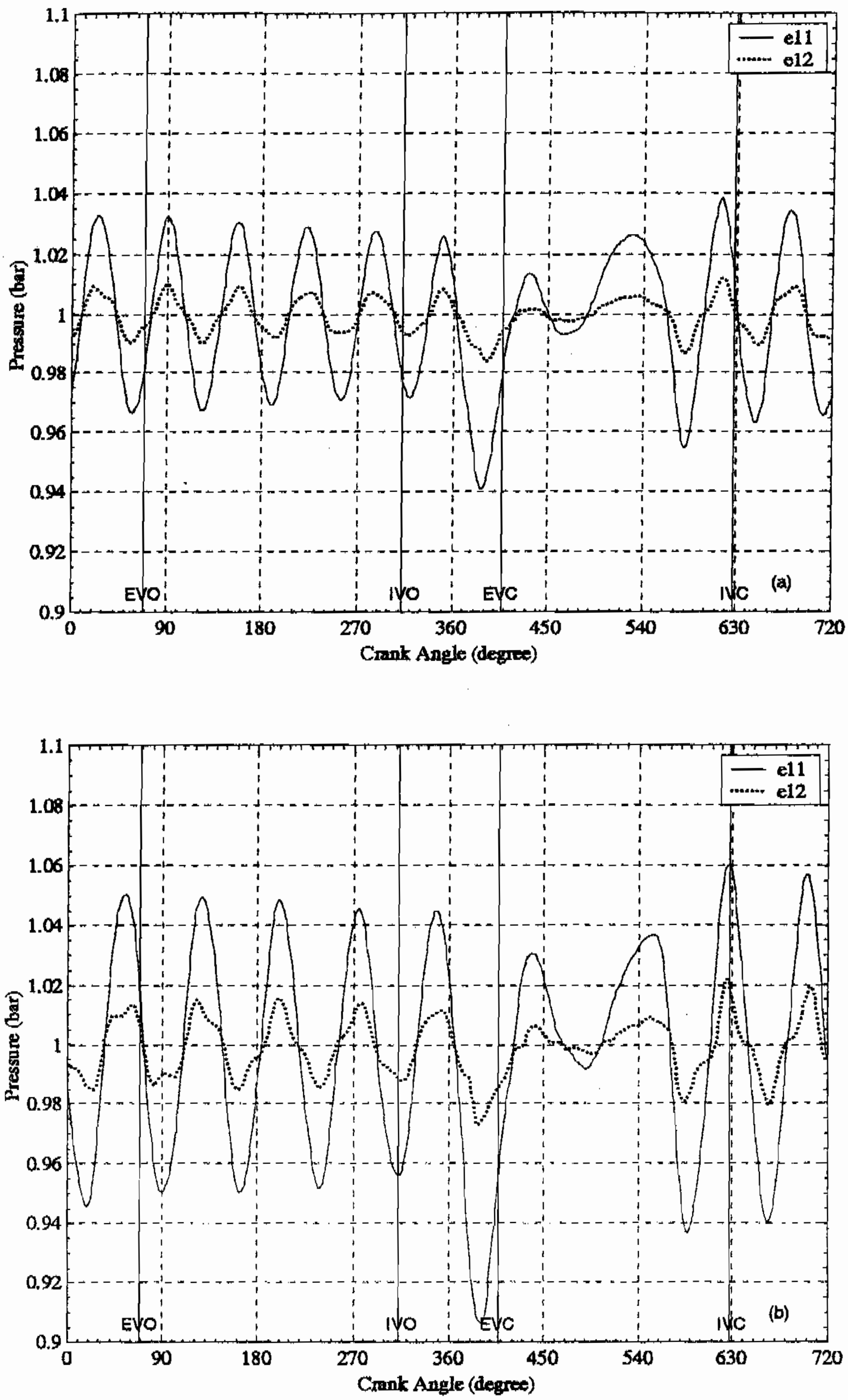

Figure A.12: OSU Dynamometer Experiment: Intake #2 – Pressure versus CAD for Intake Pressure Transducers at (a) 2000 rpm and (b) 2250 rpm

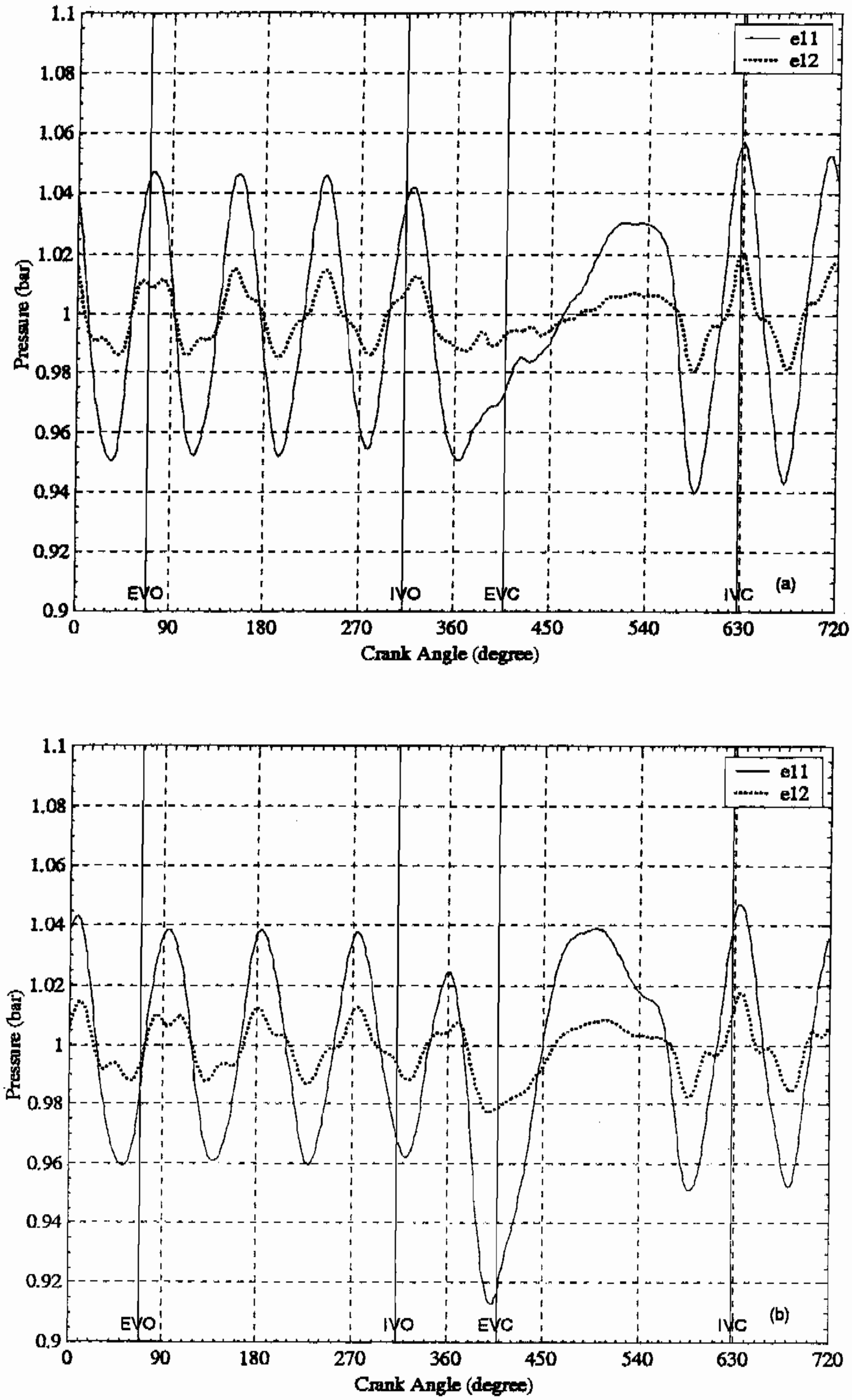

Figure A.13 OSU Dynamometer Experiment: Intake #2 – Pressure versus CAD for Intake Pressure Transducers at (a) 2500 rpm and (b) 2750 rpm

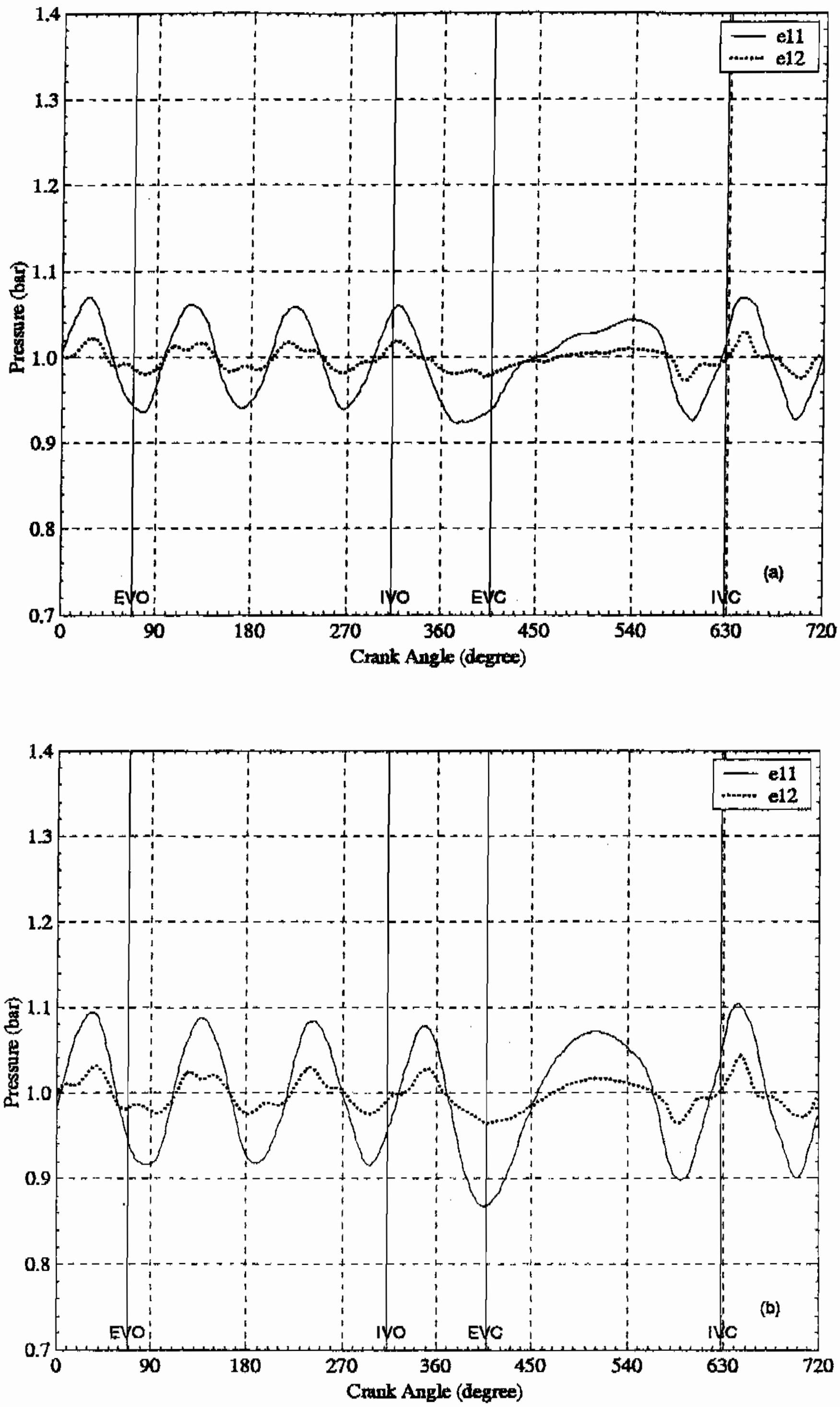

Figure A.14: OSU Dynamometer Experiment: Intake #2 – Pressure versus CAD for Intake Pressure Transducers at (a) 3000 rpm and (b) 3250 rpm

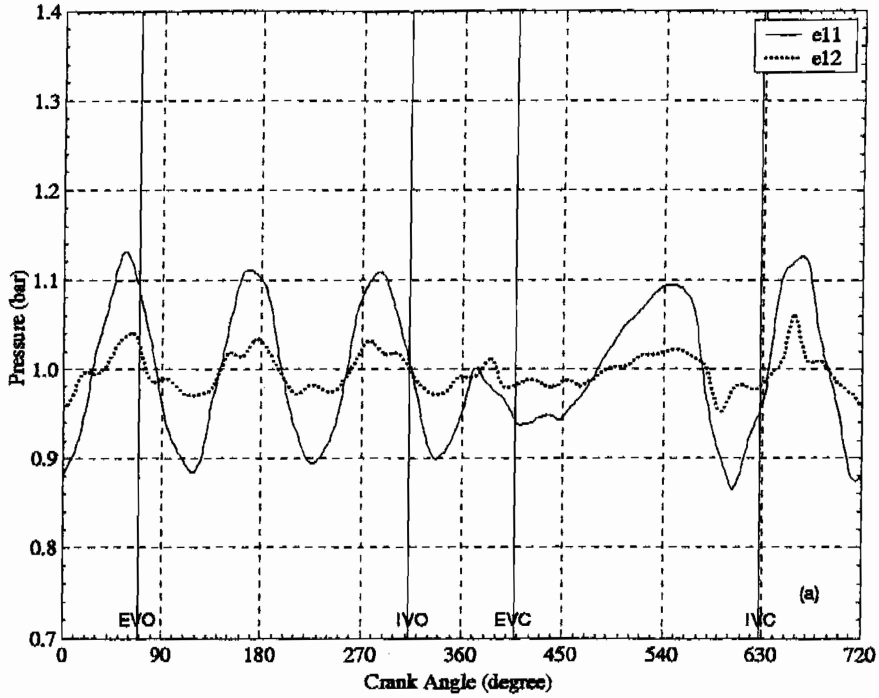

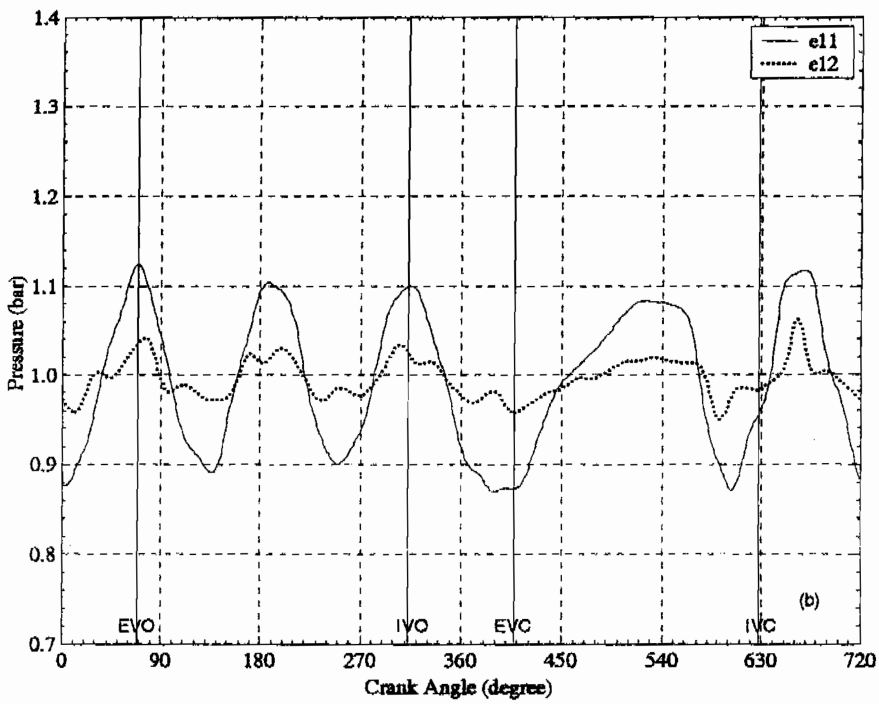

Figure A.15 OSU Dynamometer Experiment: Intake #2 – Pressure versus CAD for Intake Pressure Transducers at (a) 3500 rpm and (b) 3750 rpm

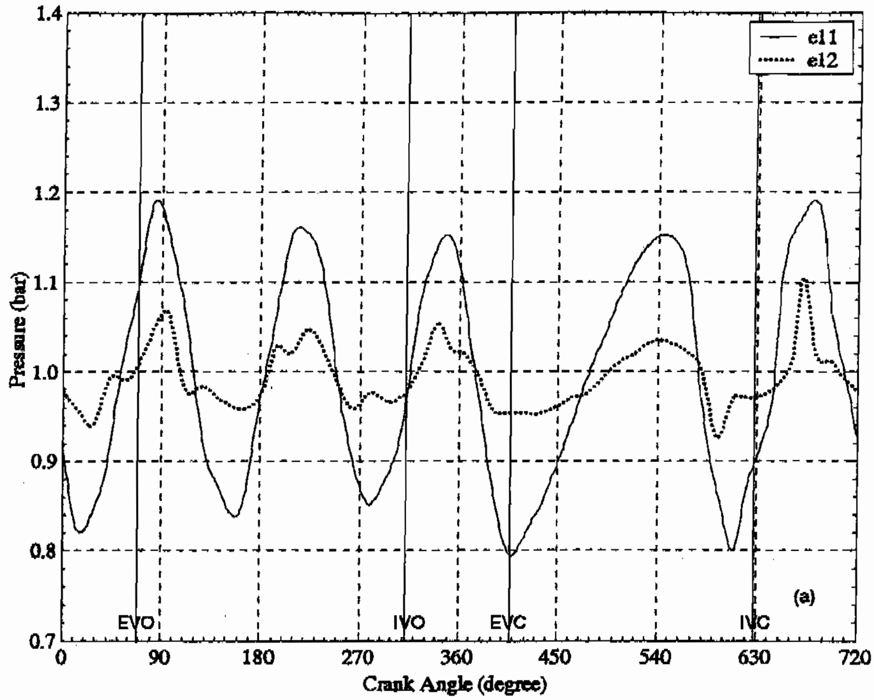

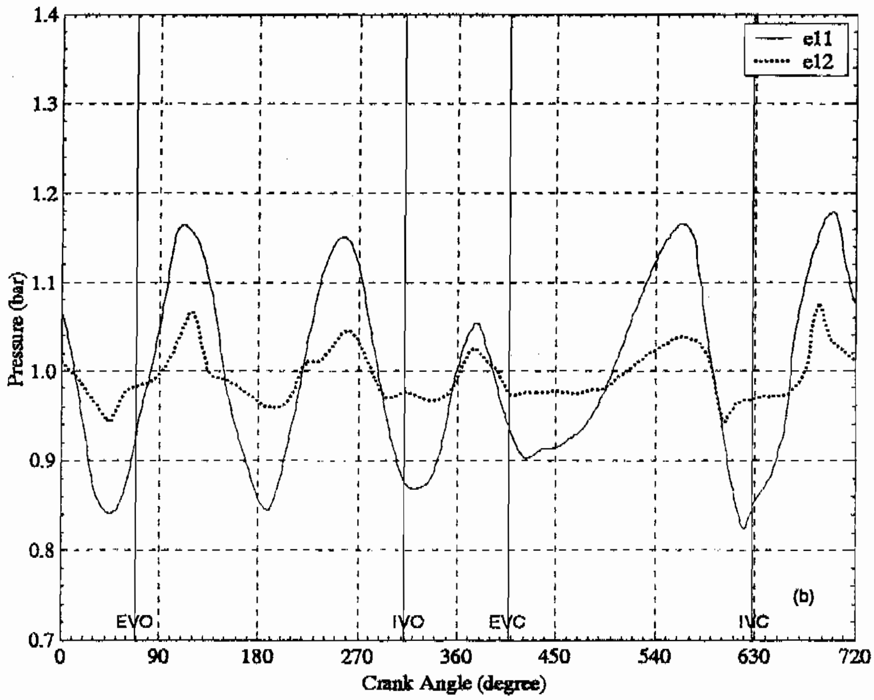

Figure A.16 OSU Dynamometer Experiment: Intake #2 – Pressure versus CAD for Intake Pressure Transducers at (a) 4000 rpm and (b) 4250 rpm

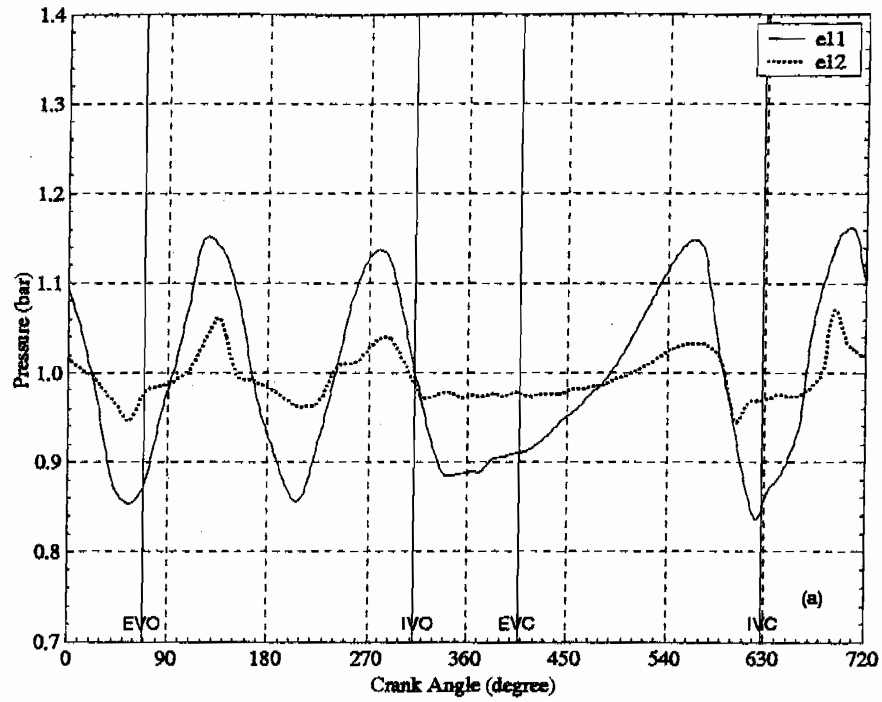

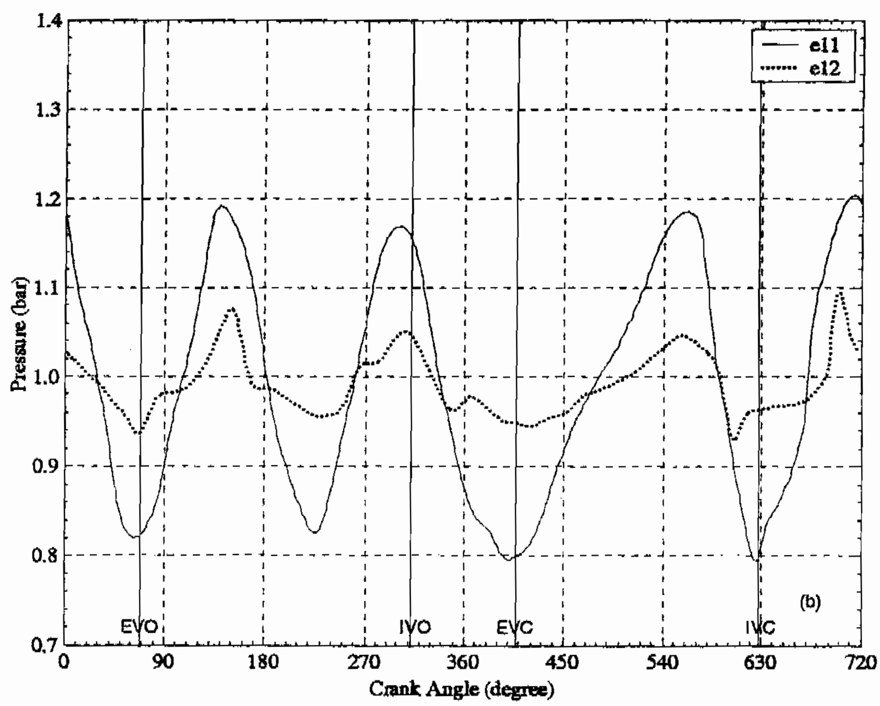

Figure A.17: OSU Dynamometer Experiment: Intake #2 – Pressure versus CAD for Intake Pressure Transducers at (a) 4500 rpm and (b) 4750 rpm

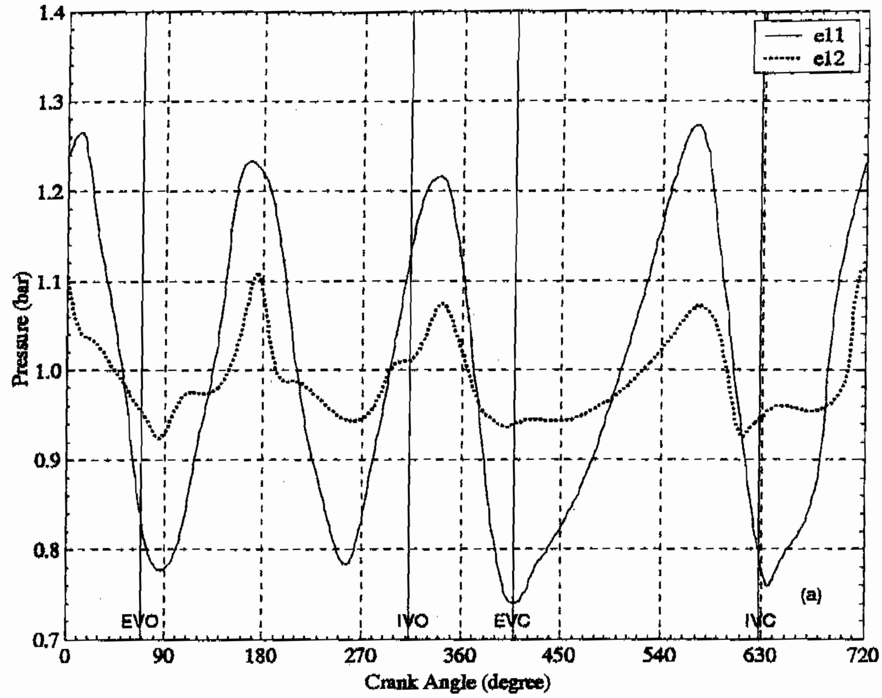

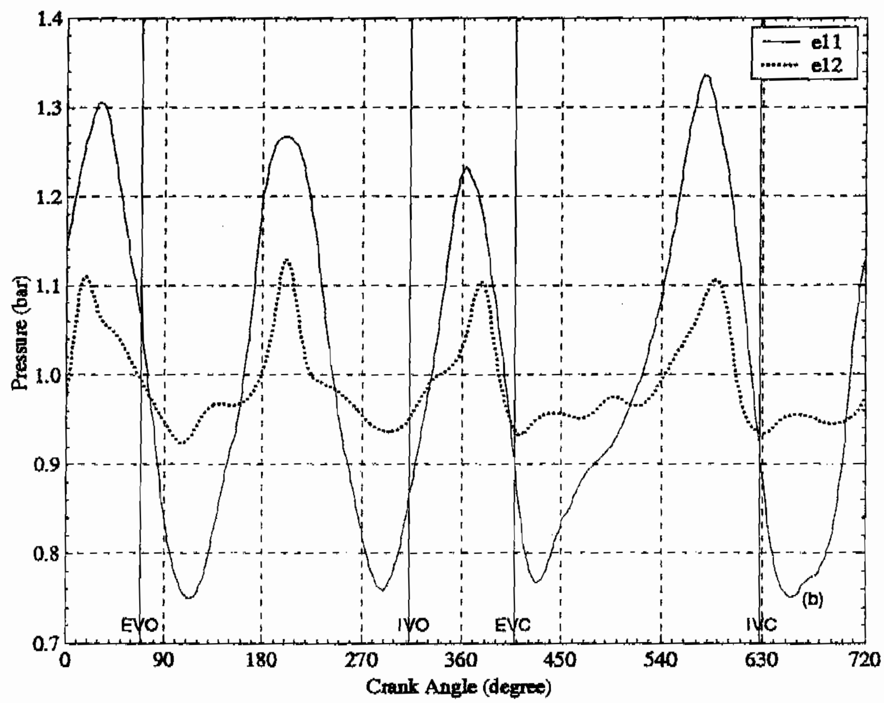

Figure A.18: OSU Dynamometer Experiment: Intake #2 – Pressure versus CAD for Intake Pressure Transducers at (a) 5000 rpm and (b) 5250 rpm

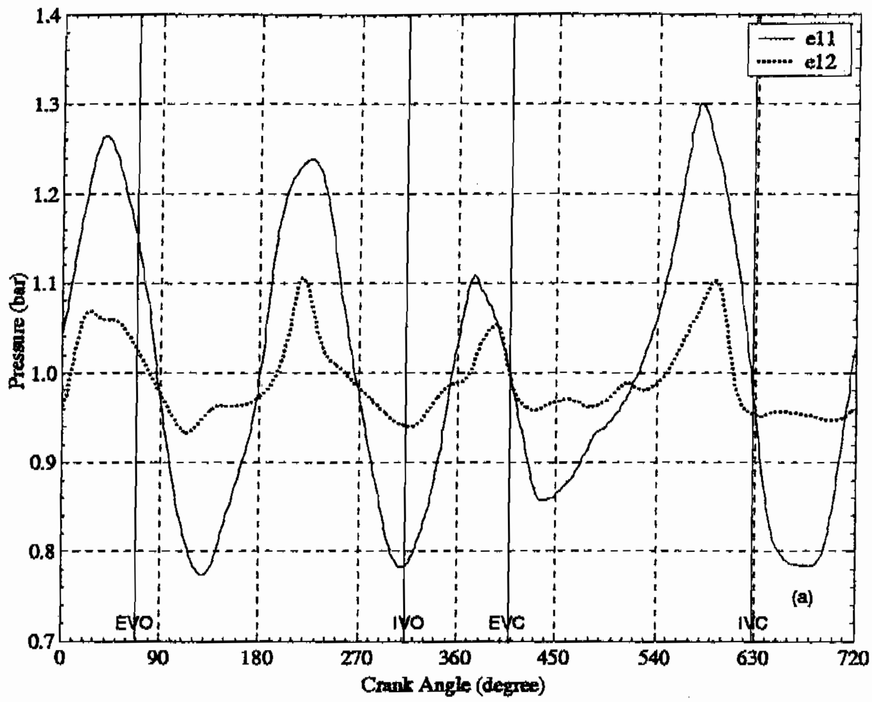

Figure A.19: OSU Dynamometer Experiment: Intake #2 – Pressure versus CAD
for Intake Pressure Transducers at (a) 5500 rpm

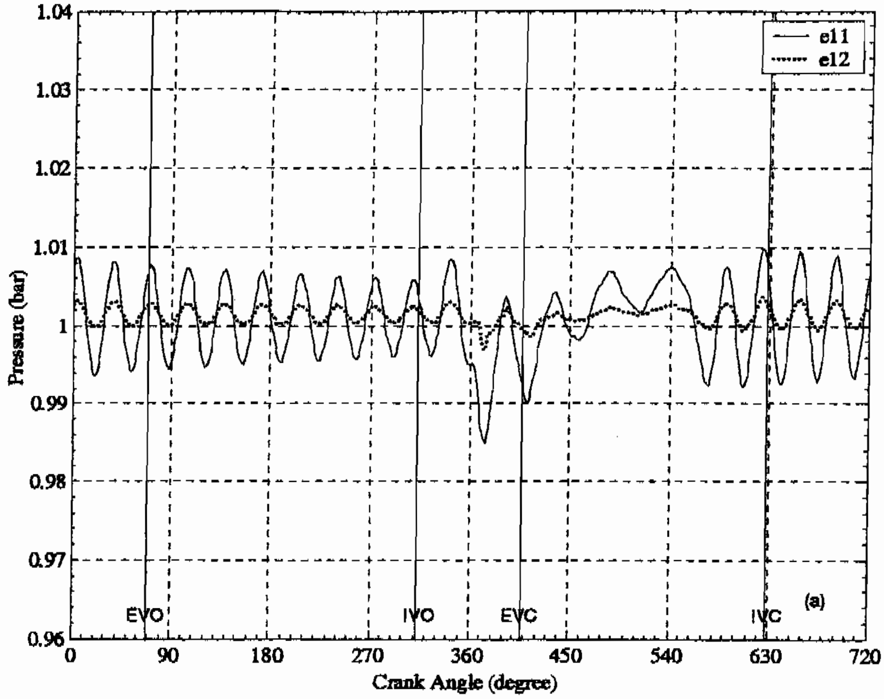

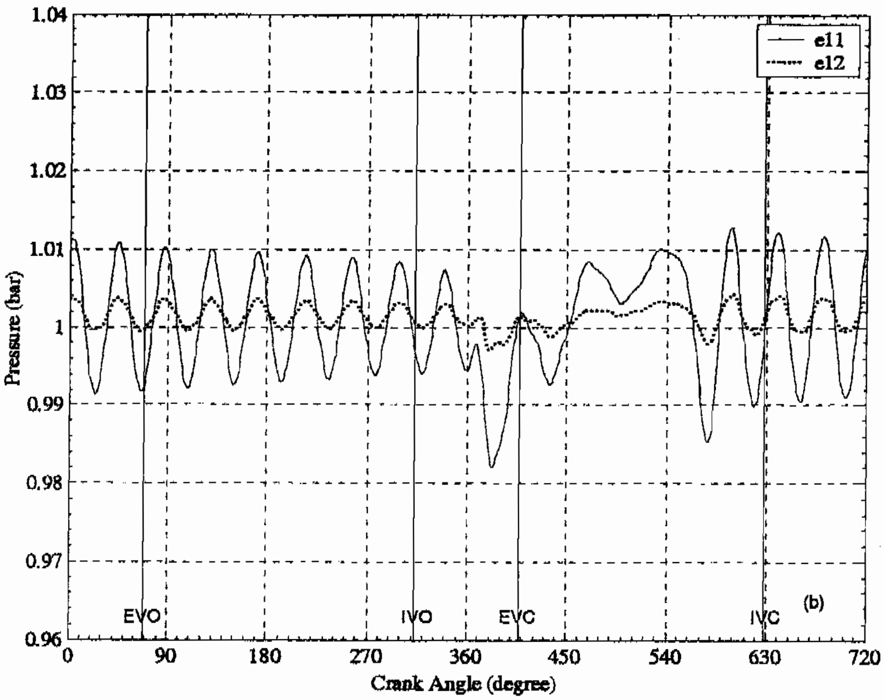

Figure A.20: OSU Dynamometer Experiment: Intake #3 – Pressure versus CAD for Intake Pressure Transducers at (a) 1000 rpm and (b) 1250 rpm

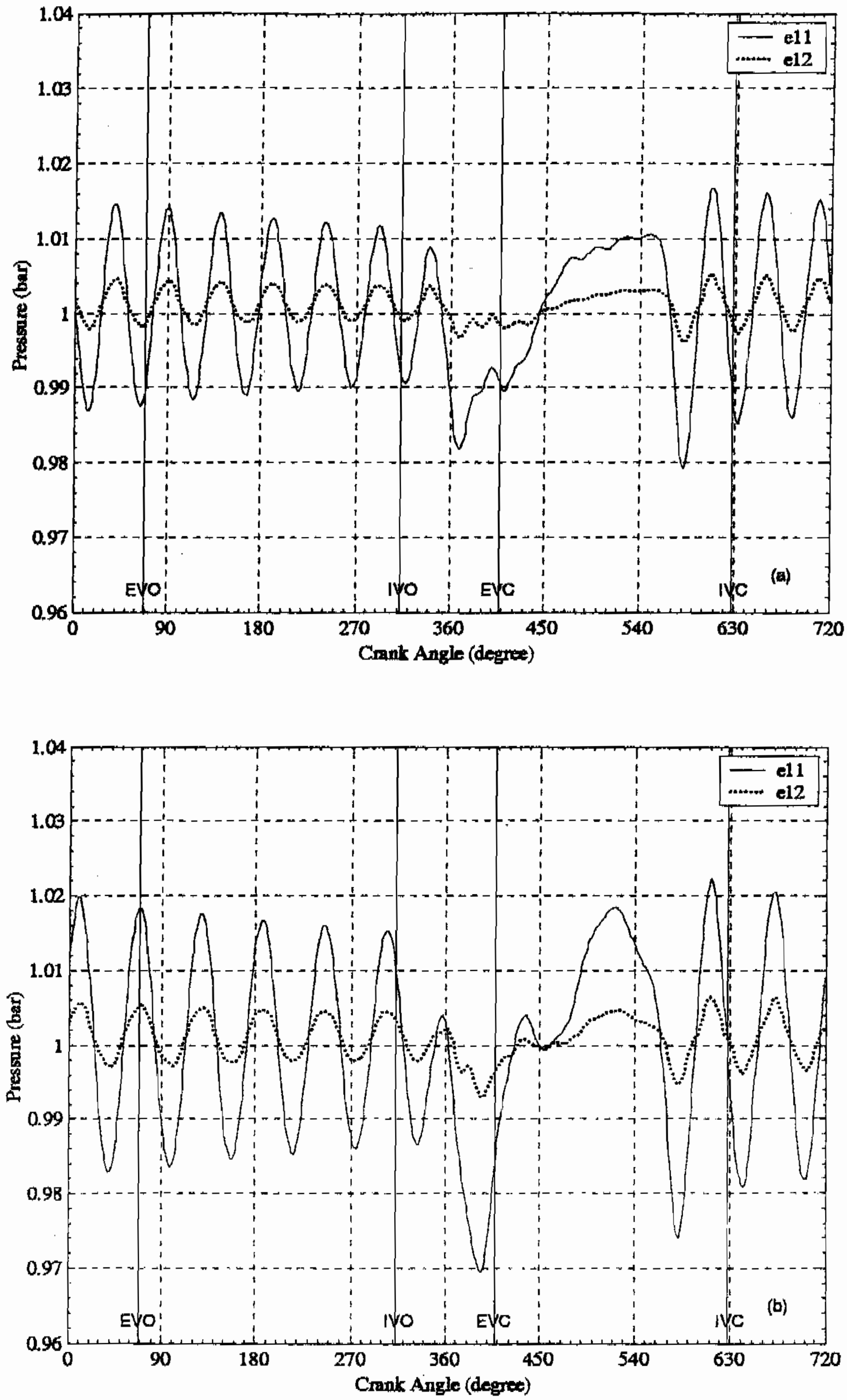

Figure A.21: OSU Dynamometer Experiment: Intake #3 – Pressure versus CAD for Intake Pressure Transducers at (a) 1500 rpm and (b) 1750 rpm

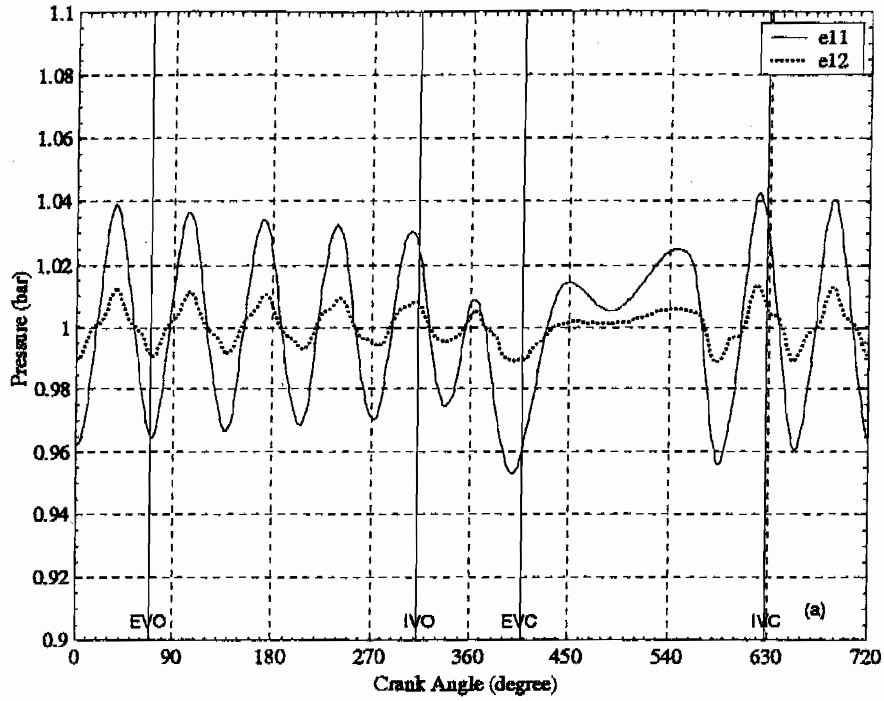

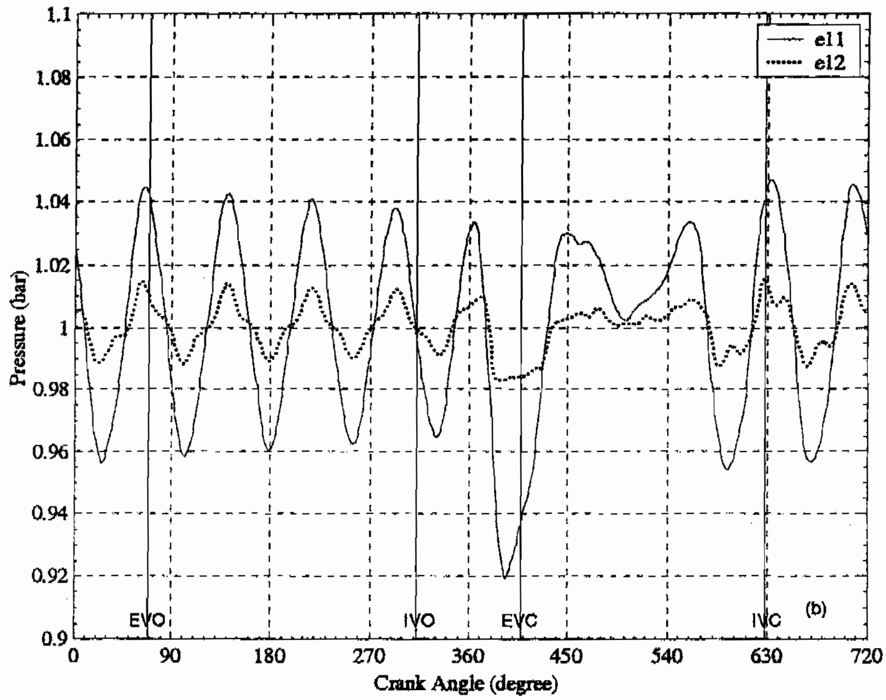

Figure A.22: OSU Dynamometer Experiment: Intake #3 – Pressure versus CAD for Intake Pressure Transducers at (a) 2000 rpm and (b) 2250 rpm

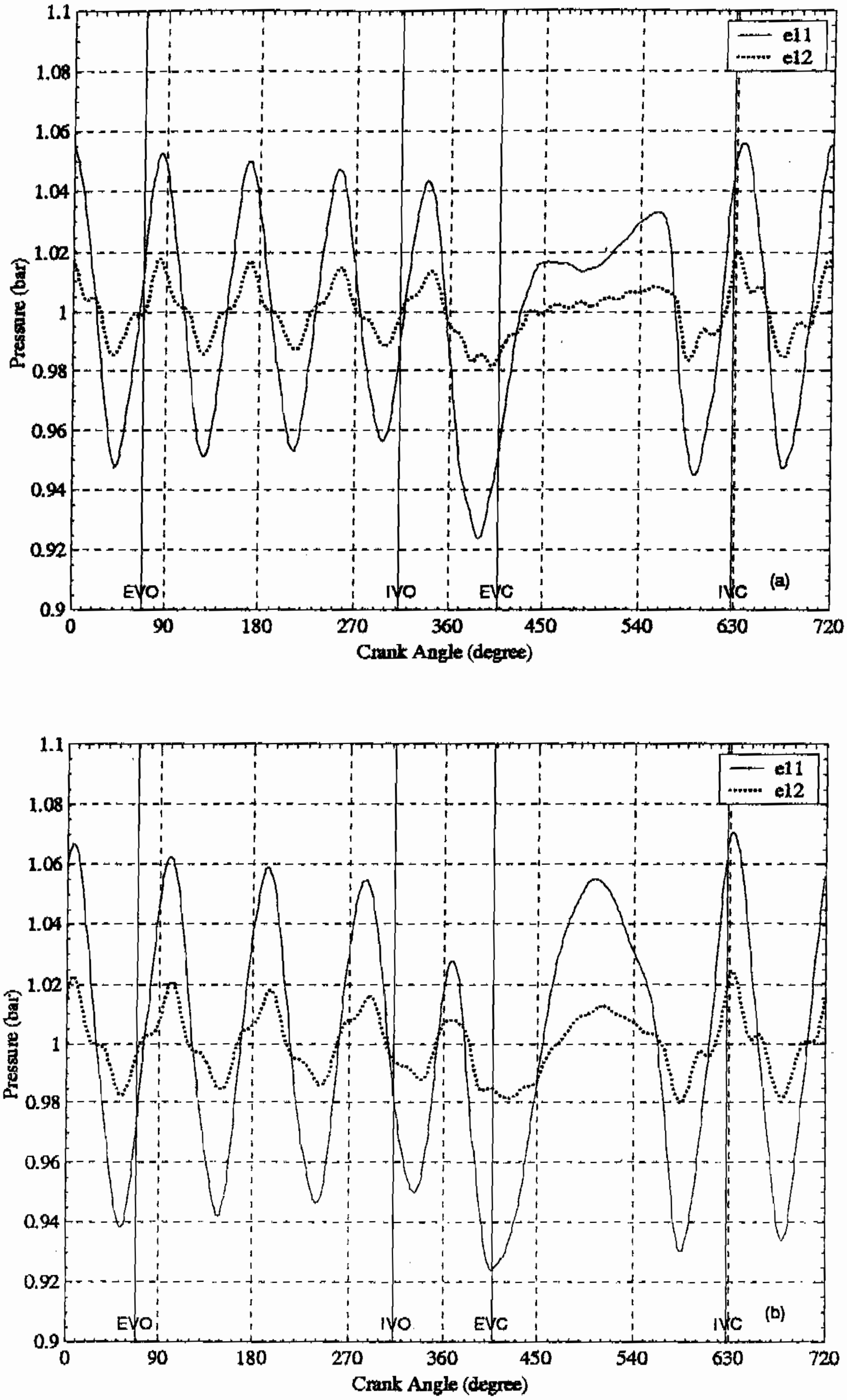

Figure A.23: OSU Dynamometer Experiment: Intake #3 – Pressure versus CAD for Intake Pressure Transducers at (a) 2500 rpm and (b) 2750 rpm

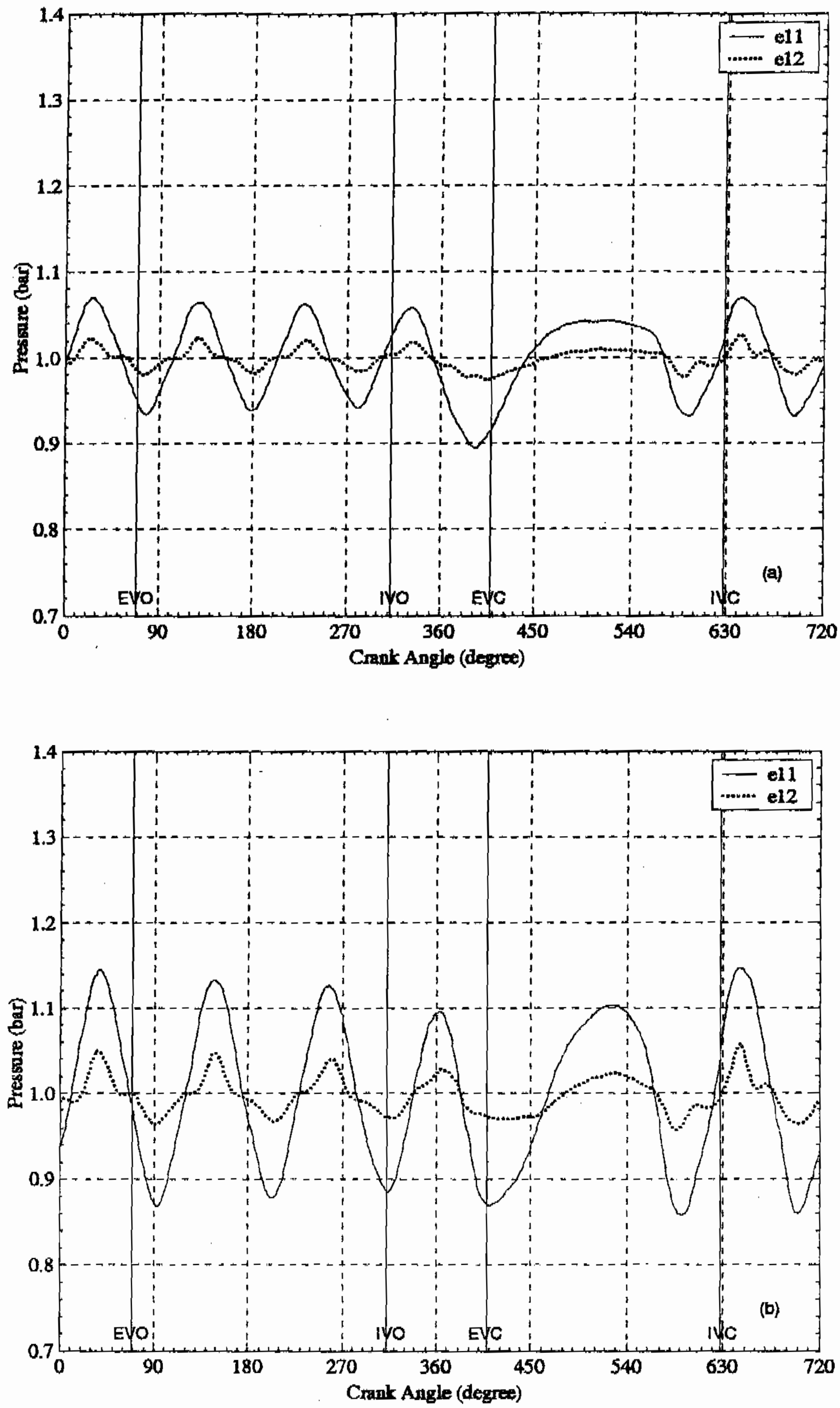

Figure A.24: OSU Dynamometer Experiment: Intake #3 – Pressure versus CAD for Intake Pressure Transducers at (a) 3000 rpm and (b) 3250 rpm

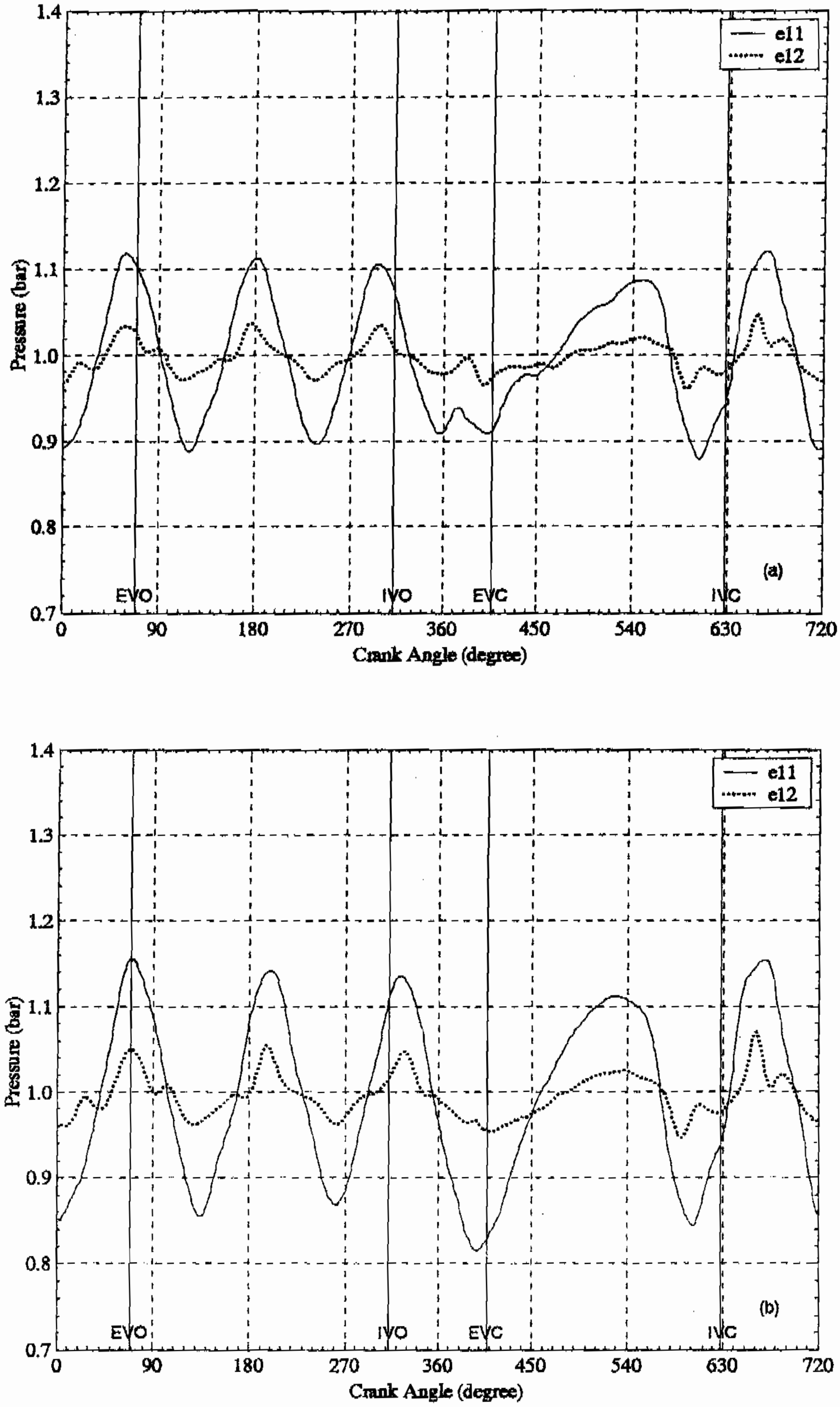

Figure A.25: OSU Dynamometer Experiment: Intake #3 – Pressure versus CAD for Intake Pressure Transducers at (a) 3500 rpm and (b) 3750 rpm

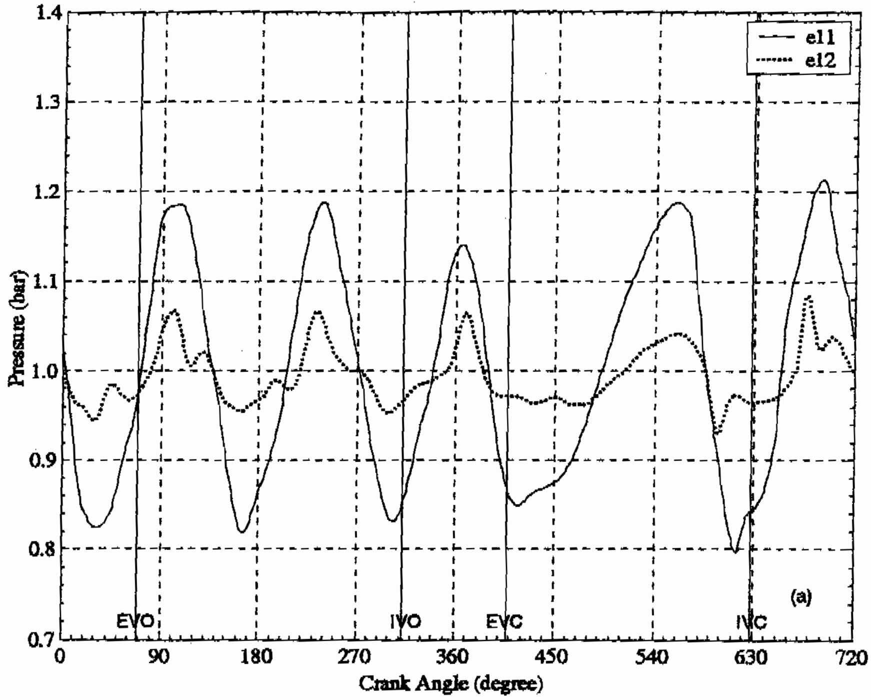

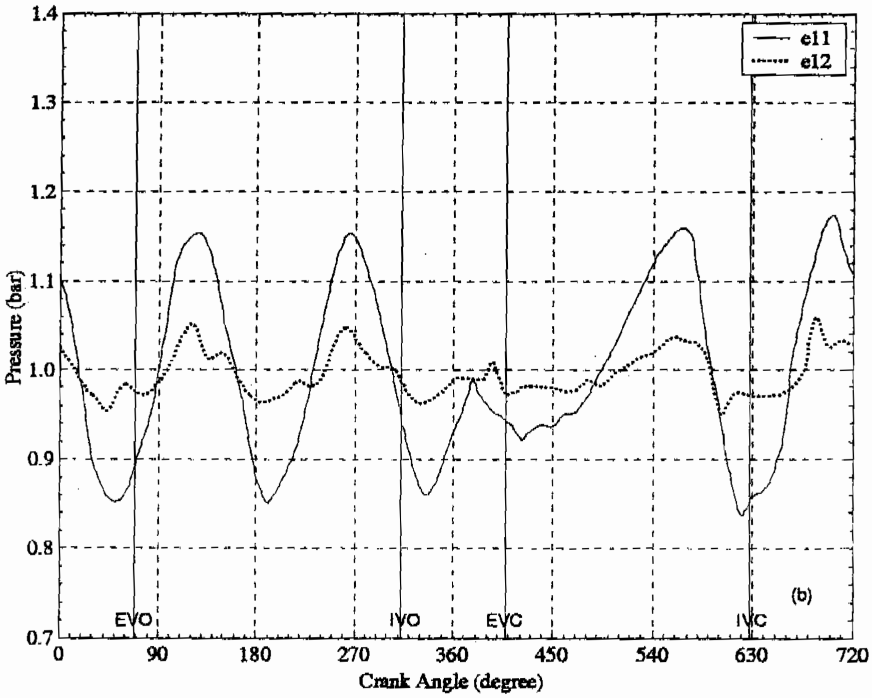

Figure A.26: OSU Dynamometer Experiment: Intake #3 – Pressure versus CAD for Intake Pressure Transducers at (a) 4000 rpm and (b) 4250 rpm

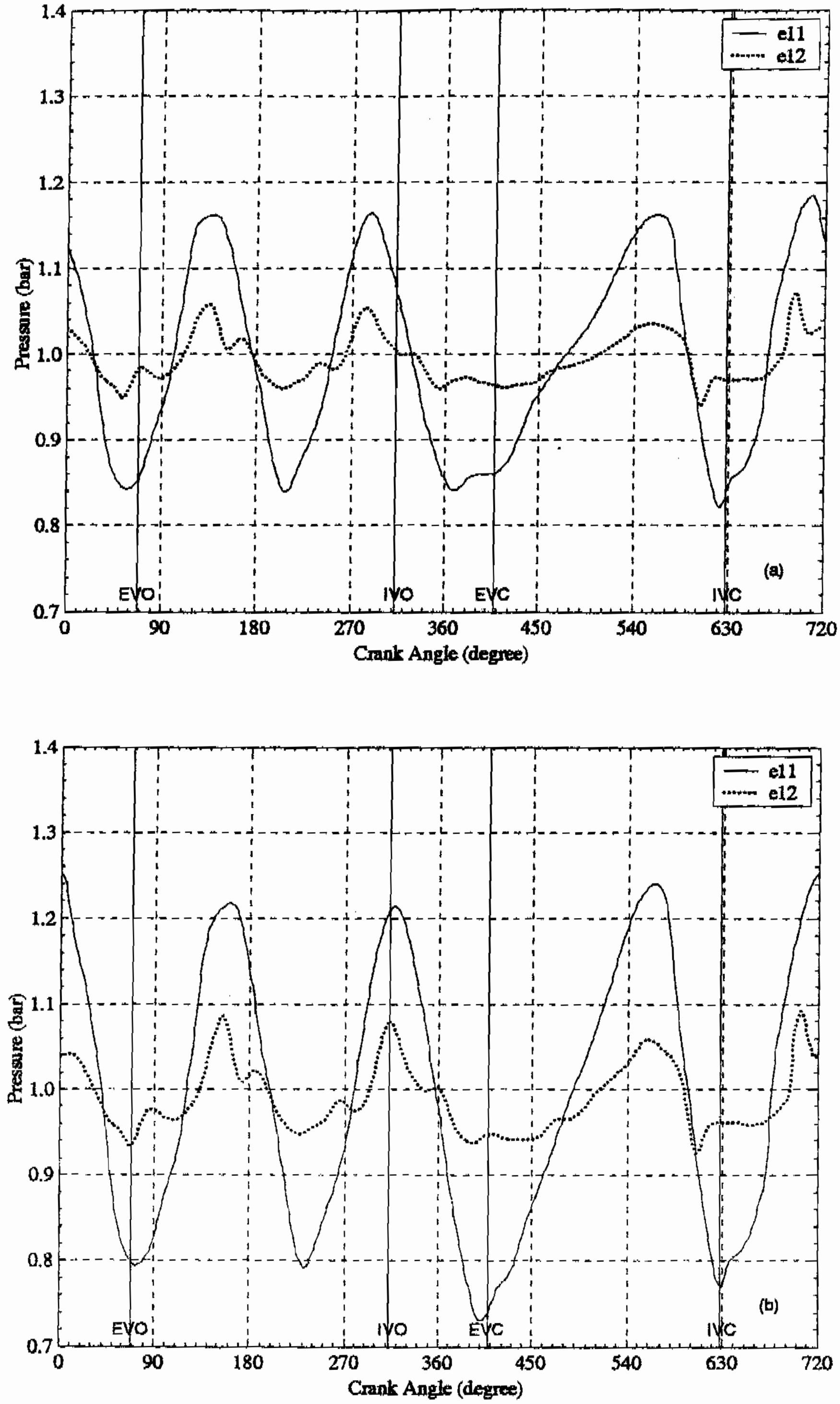

Figure A.27: OSU Dynamometer Experiment: Intake #3 – Pressure versus CAD for Intake Pressure Transducers at (a) 4500 rpm and (b) 4750 rpm

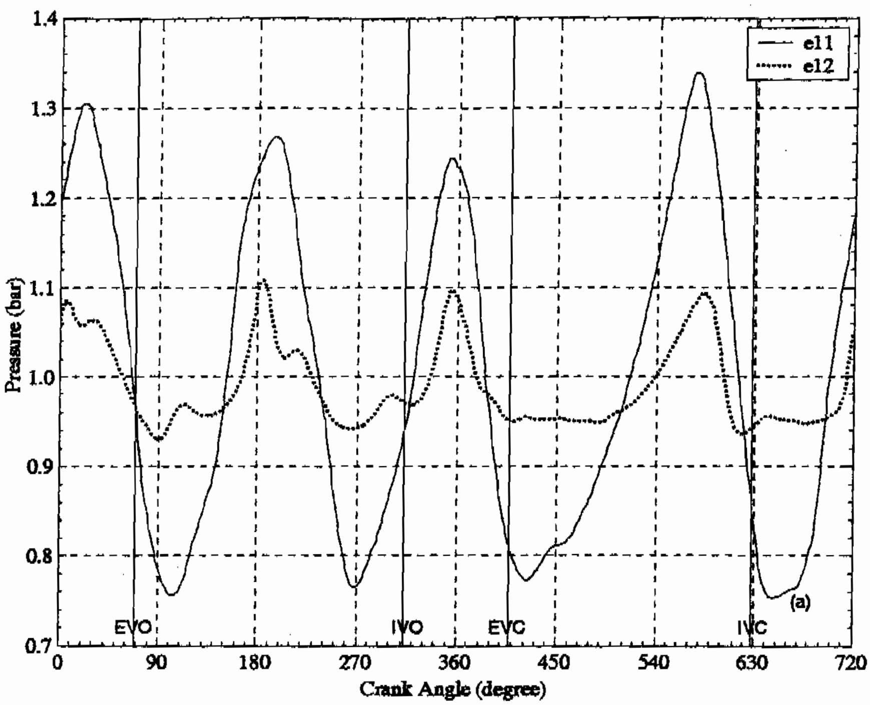

Figure A.28: OSU Dynamometer Experiment: Intake #3 – Pressure versus CAD for Intake Pressure Transducers at (a) 5000 rpm

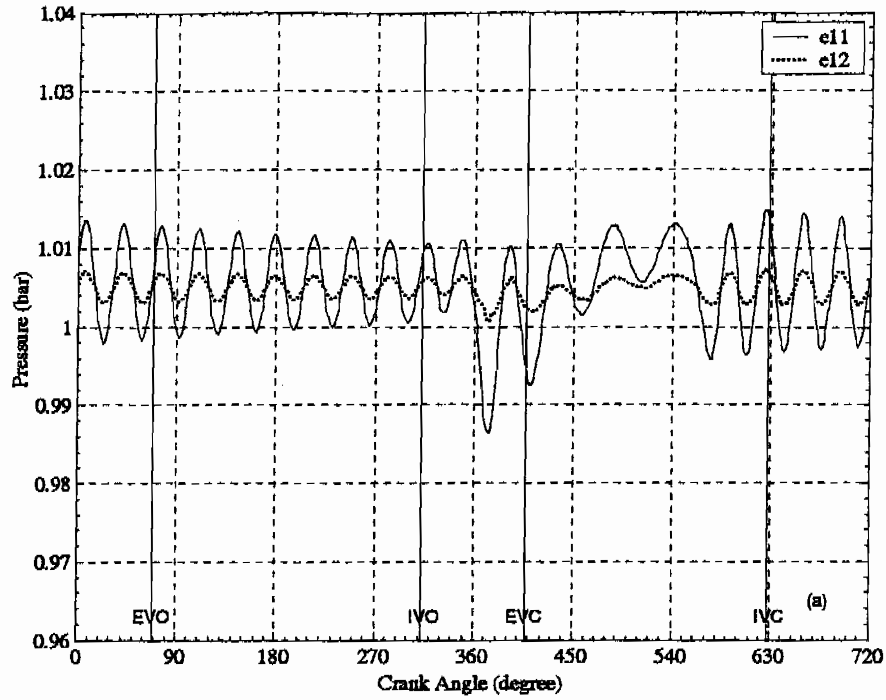

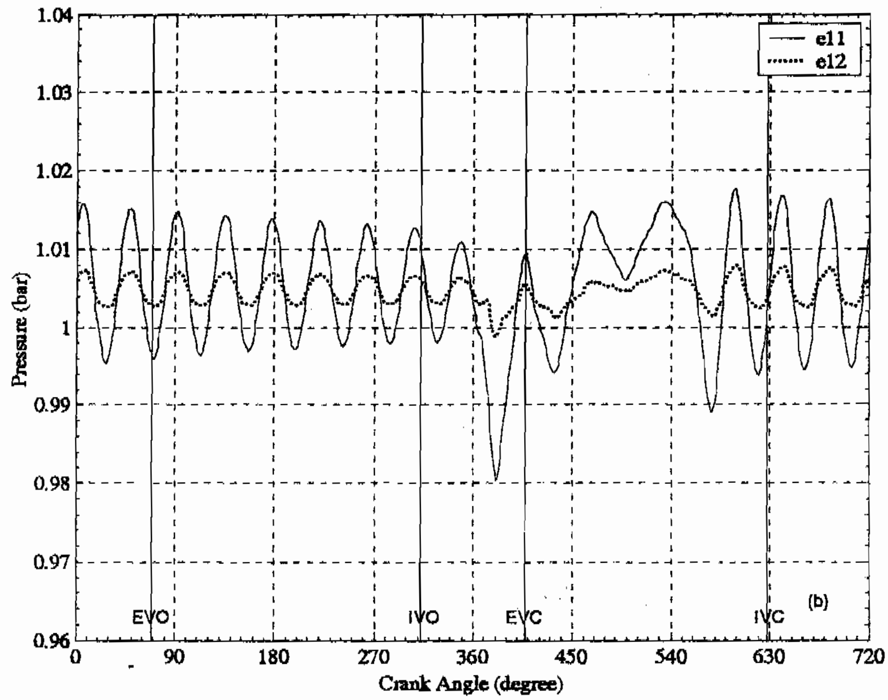

Figure A.29: OSU Dynamometer Experiment: Intake #4 – Pressure versus CAD for Intake Pressure Transducers at (a) 1000 rpm and (b) 1250 rpm

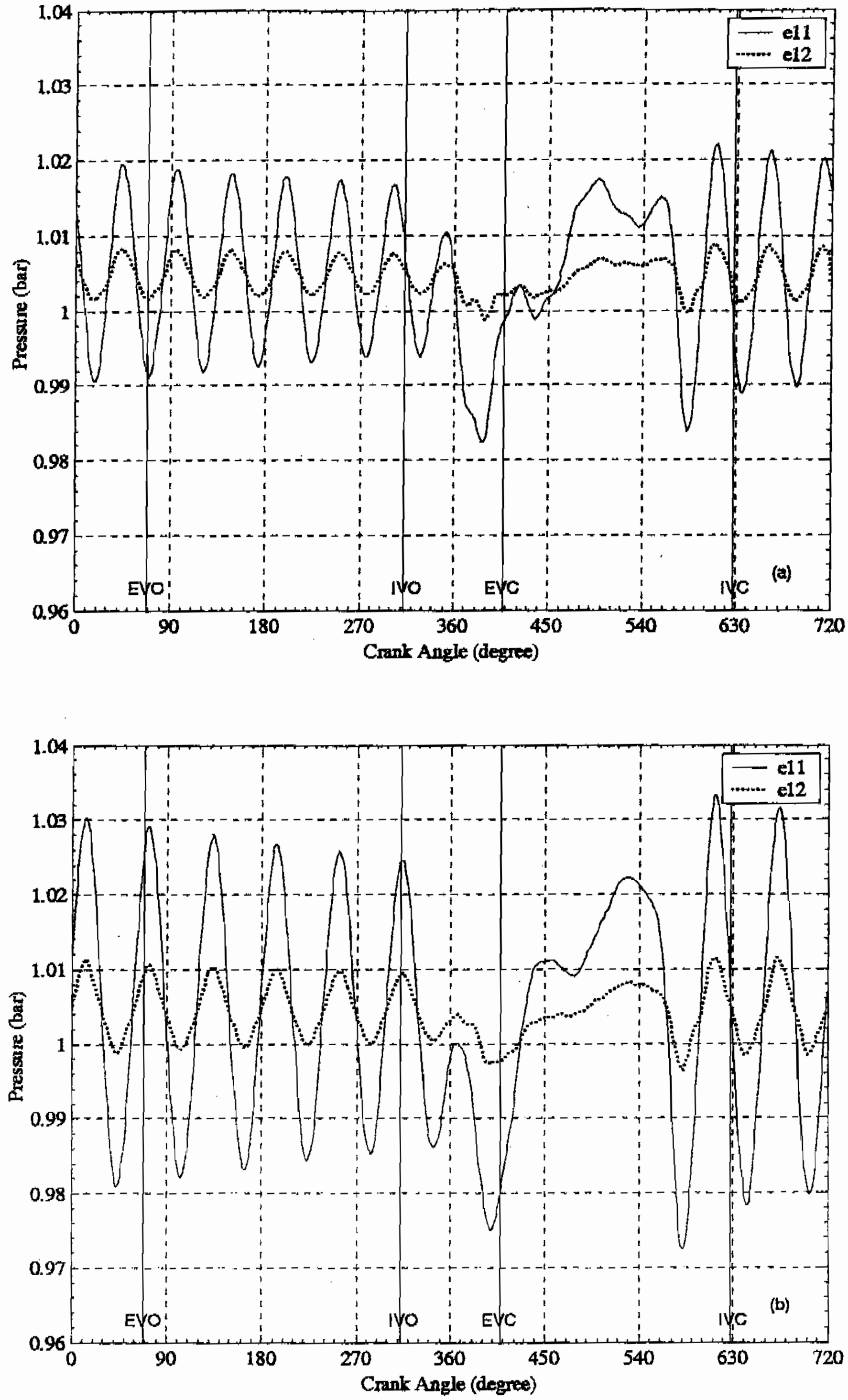

Figure A.30: OSU Dynamometer Experiment: Intake #4 – Pressure versus CAD for Intake Pressure Transducers at (a) 1500 rpm and (b) 1750 rpm

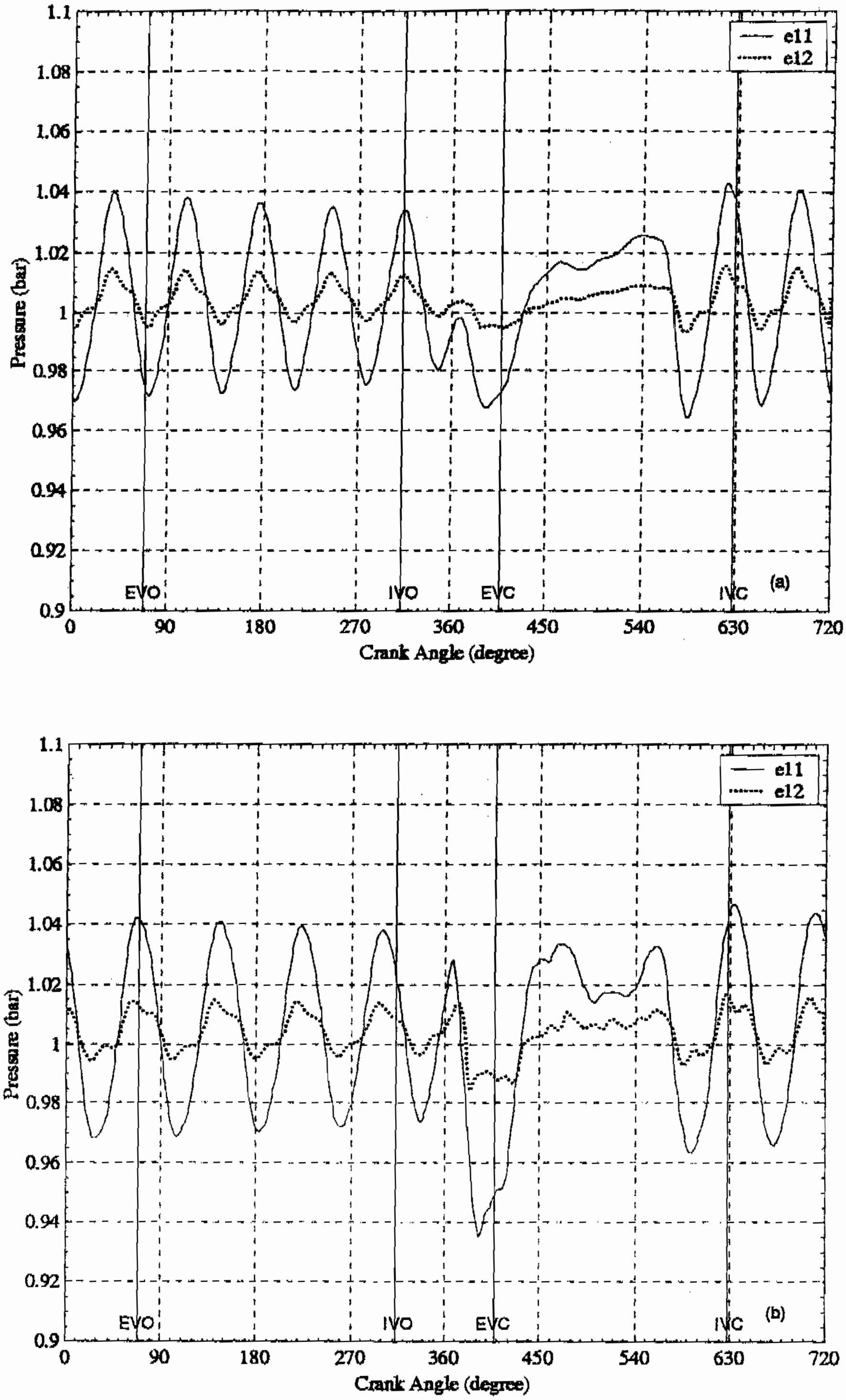

Figure A.31: OSU Dynamometer Experiment: Intake #4 – Pressure versus CAD for Intake Pressure Transducers at (a) 2000 rpm and (b) 2250 rpm

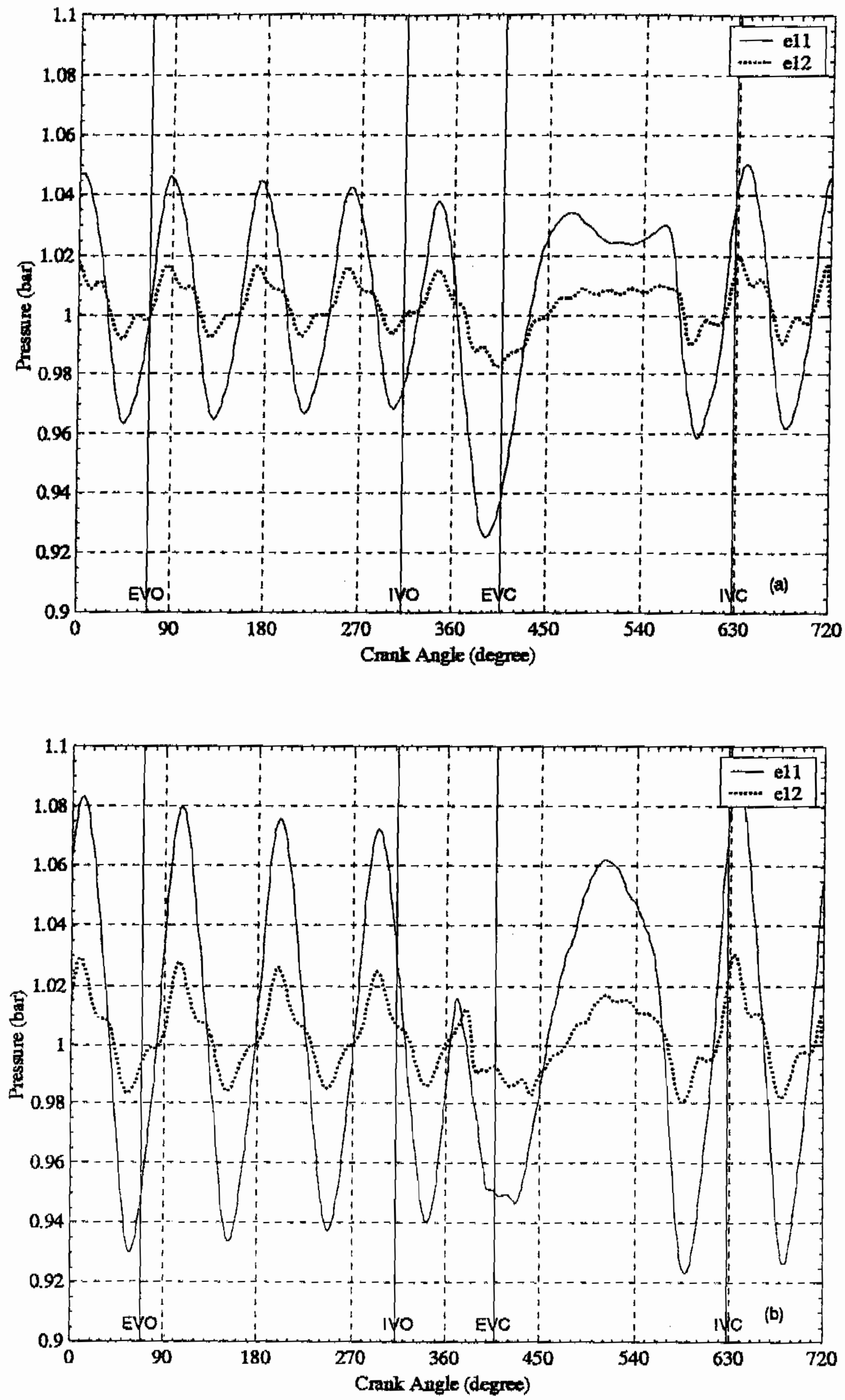

Figure A.32: OSU Dynamometer Experiment: Intake #4 – Pressure versus CAD for Intake Pressure Transducers at (a) 2500 rpm and (b) 2750 rpm

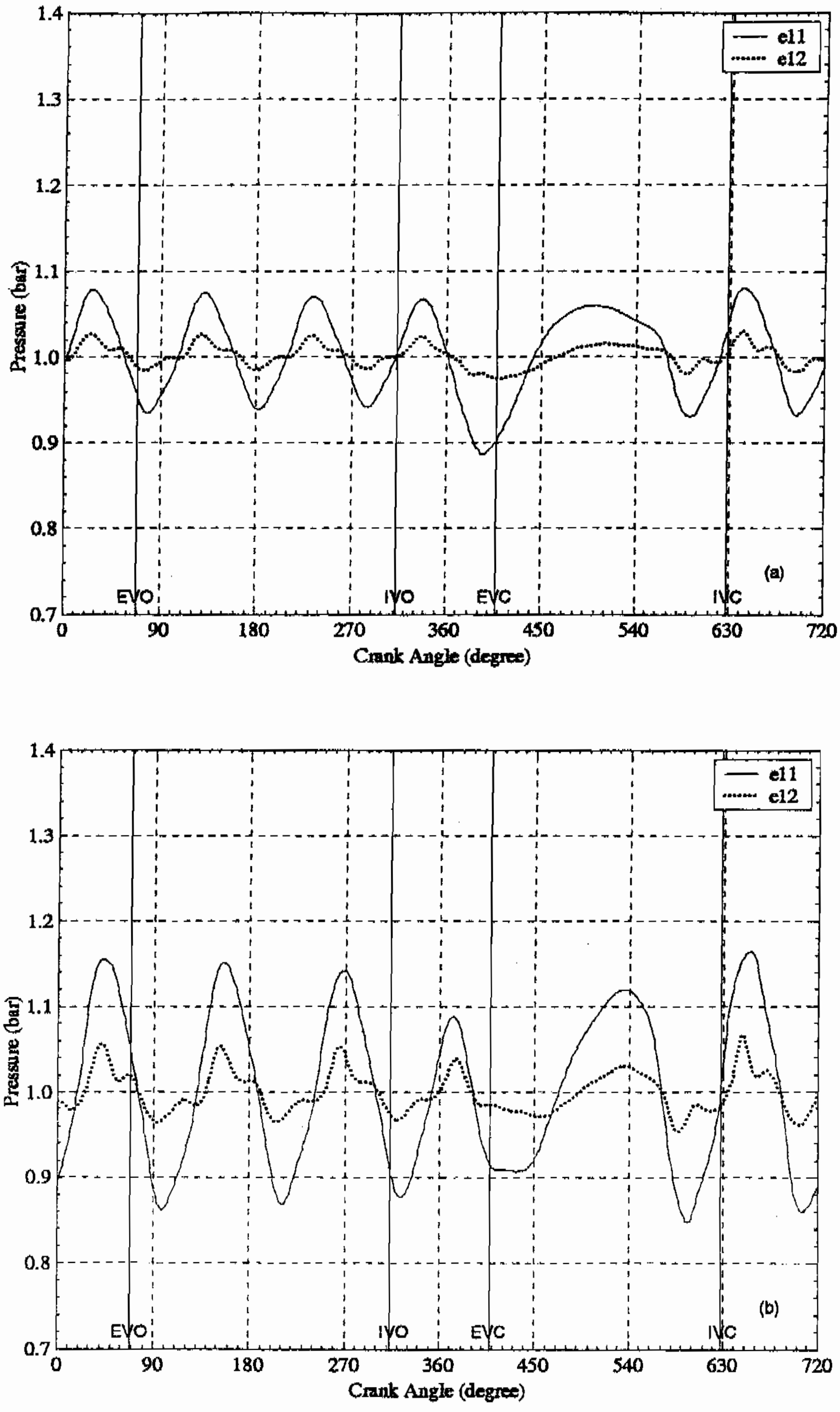

Figure A.33: OSU Dynamometer Experiment: Intake #4 – Pressure versus CAD for Intake Pressure Transducers at (a) 3000 rpm and (b) 3250 rpm

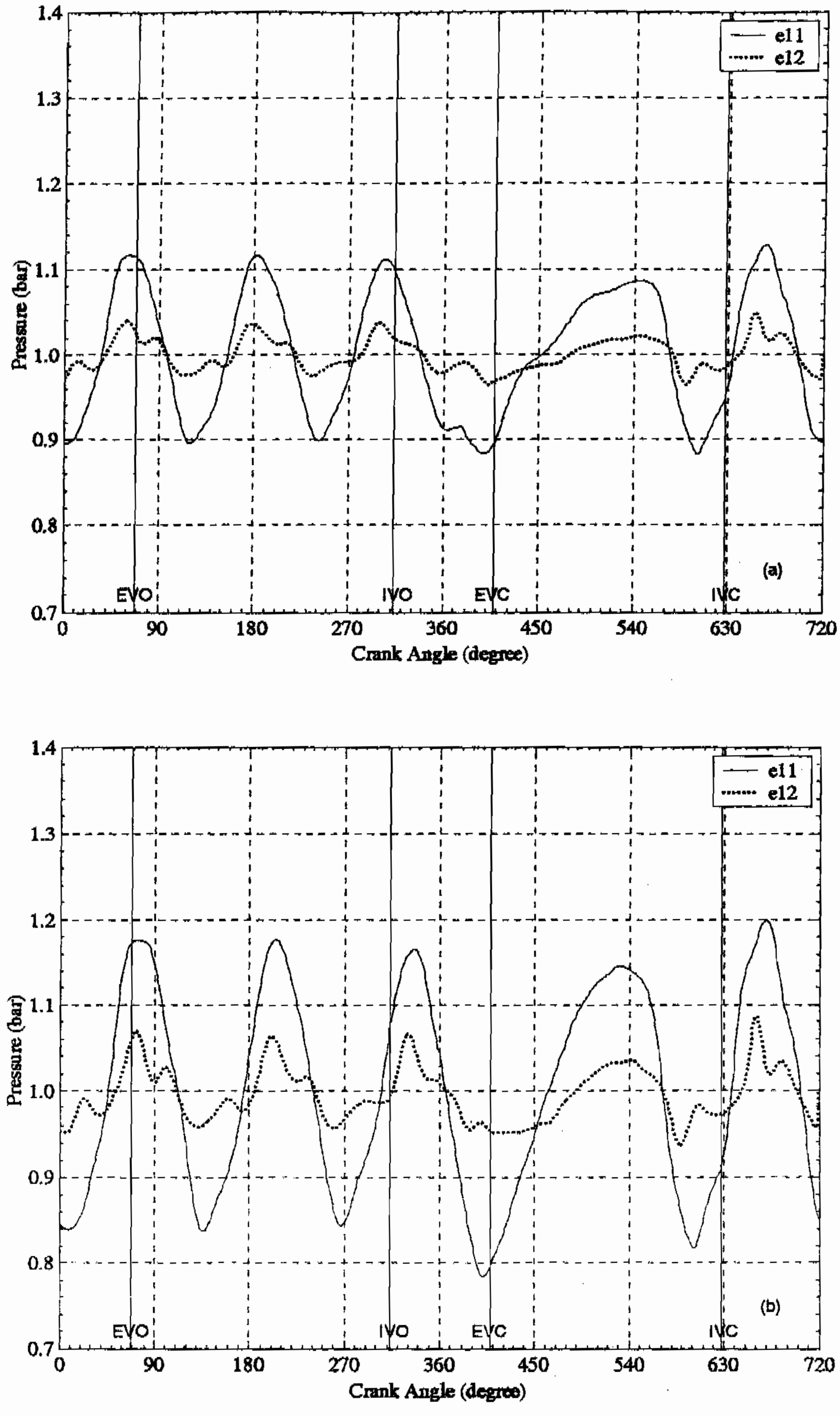

Figure A.34: OSU Dynamometer Experiment: Intake #4 – Pressure versus CAD for Intake Pressure Transducers at (a) 3500 rpm and (b) 3750 rpm

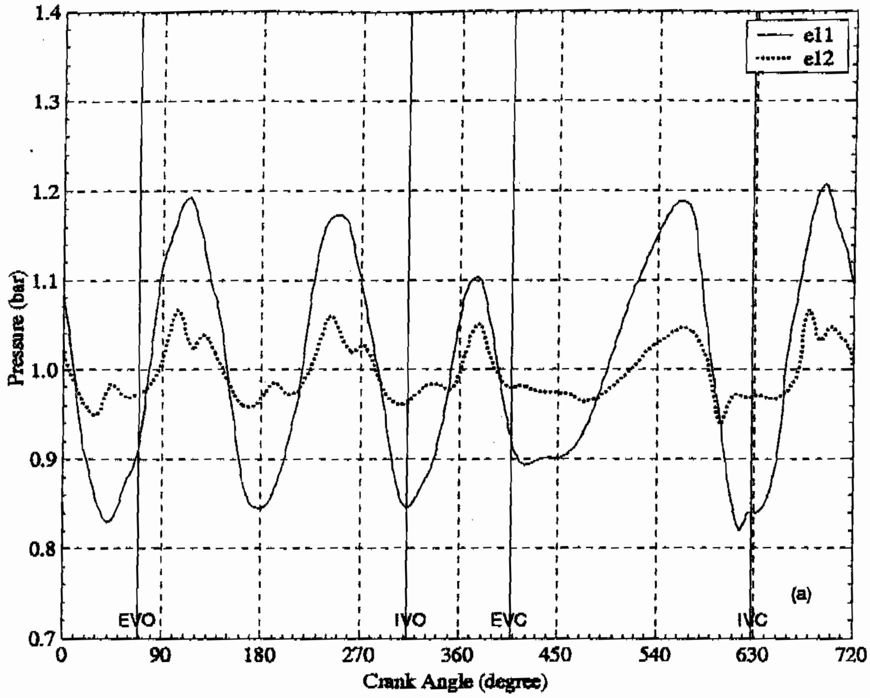

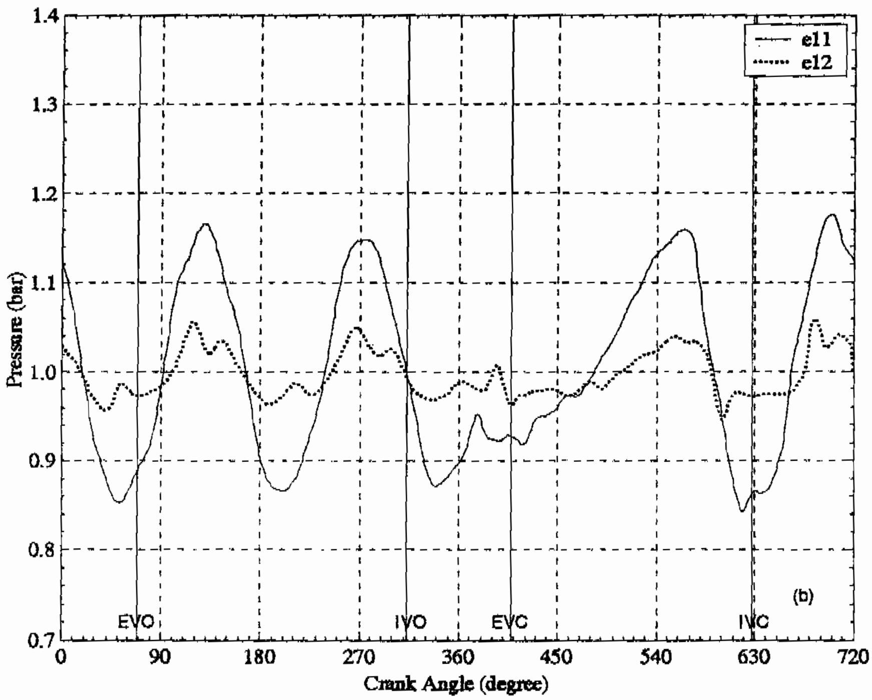

Figure A.35: OSU Dynamometer Experiment: Intake #4 – Pressure versus CAD for Intake Pressure Transducers at (a) 4000 rpm and (b) 4250 rpm

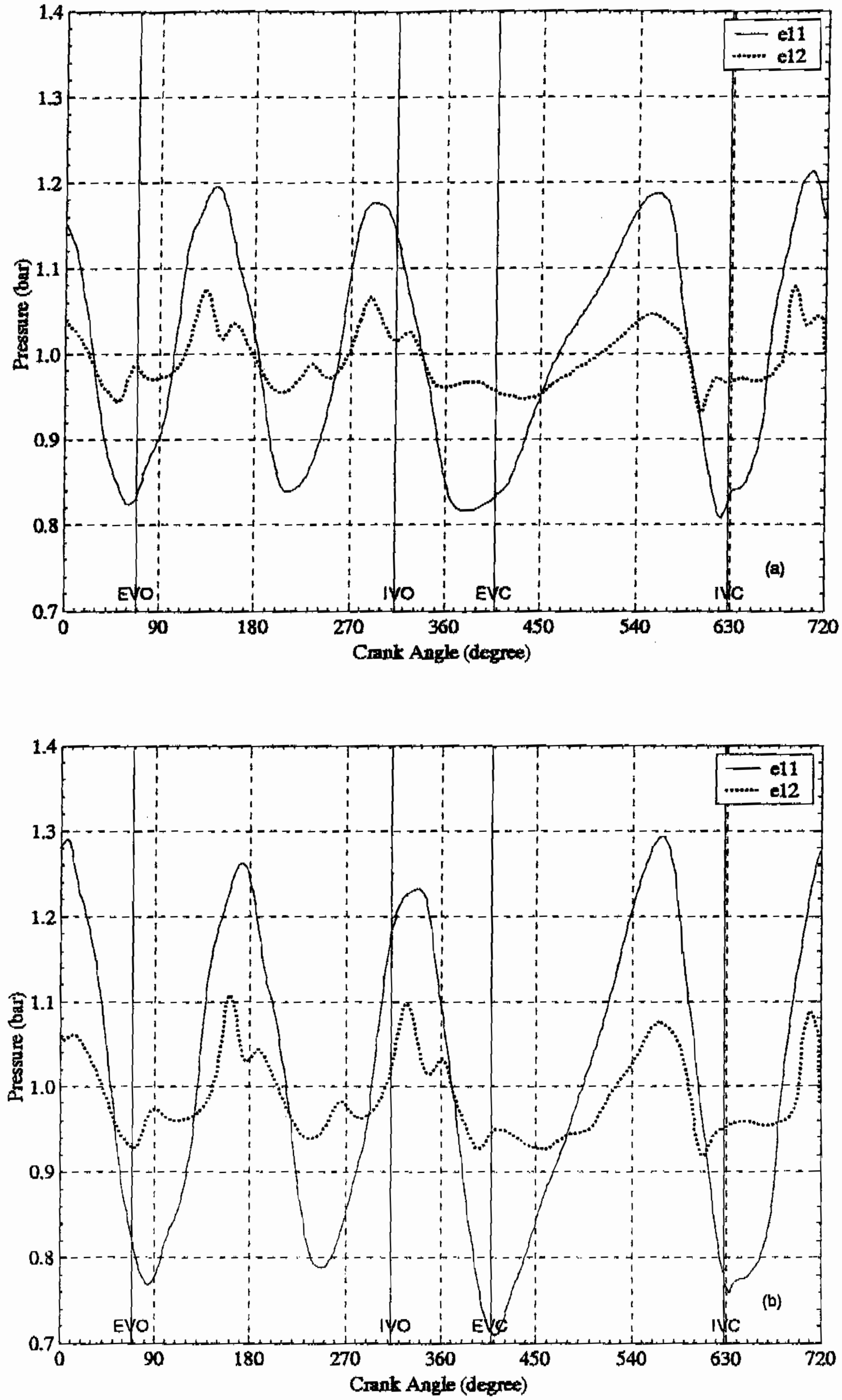

Figure A.36: OSU Dynamometer Experiment: Intake #4 – Pressure versus CAD for Intake Pressure Transducers at (a) 4500 rpm and (b) 4750 rpm

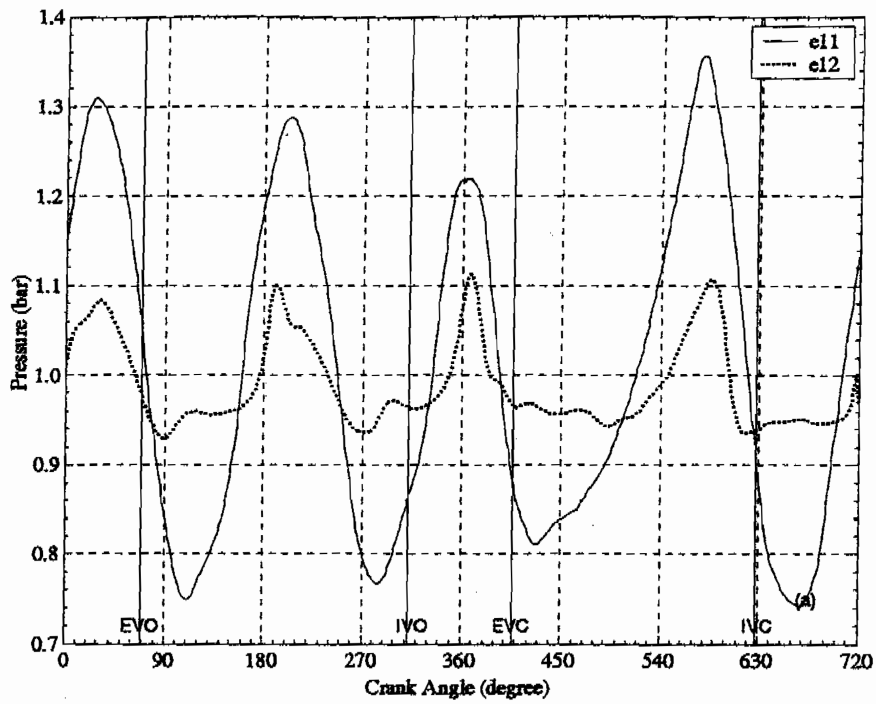

Figure A.37: OSU Dynamometer Experiment: Intake #4 – Pressure versus CAD for Intake Pressure Transducers at (a) 5000 rpm

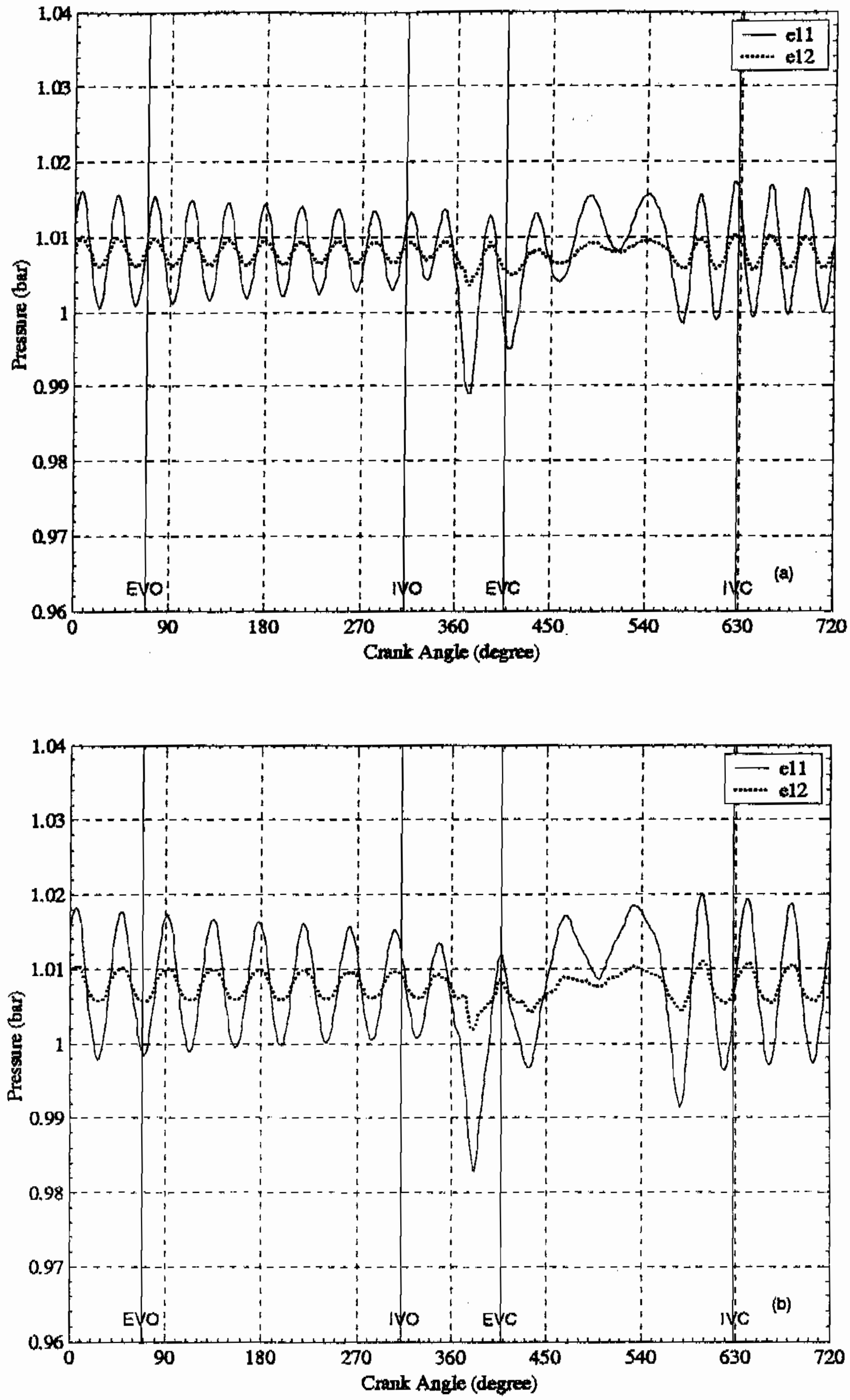

Figure A.38: OSU Dynamometer Experiment: Intake #5 – Pressure versus CAD for Intake Pressure Transducers at (a) 1000 rpm and (b) 1250 rpm

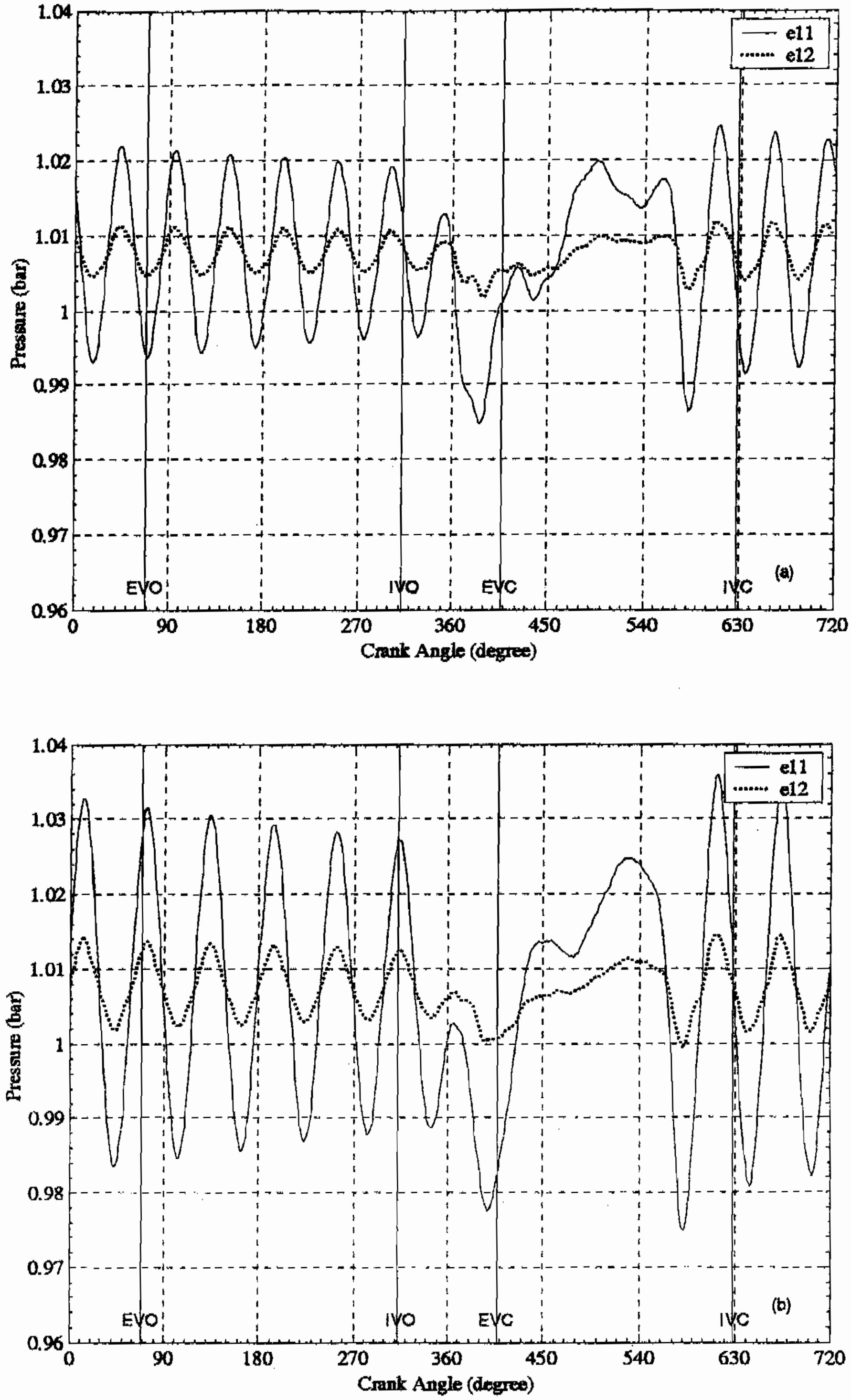

Figure A.39: OSU Dynamometer Experiment: Intake #5 – Pressure versus CAD for Intake Pressure Transducers at (a) 1500 rpm and (b) 1750 rpm

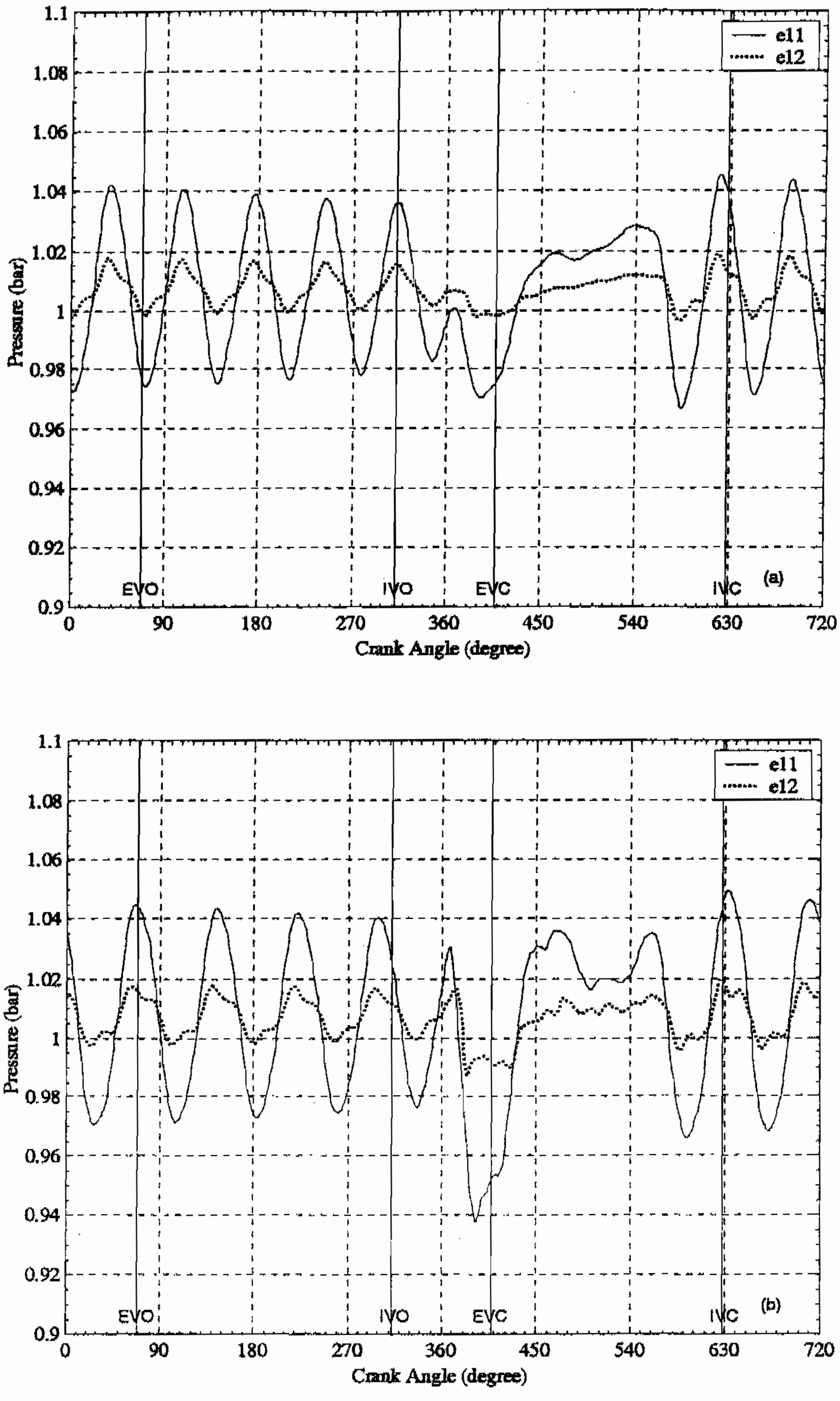

Figure A.40: OSU Dynamometer Experiment: Intake #5 – Pressure versus CAD for Intake Pressure Transducers at (a) 2000 rpm and (b) 2250 rpm

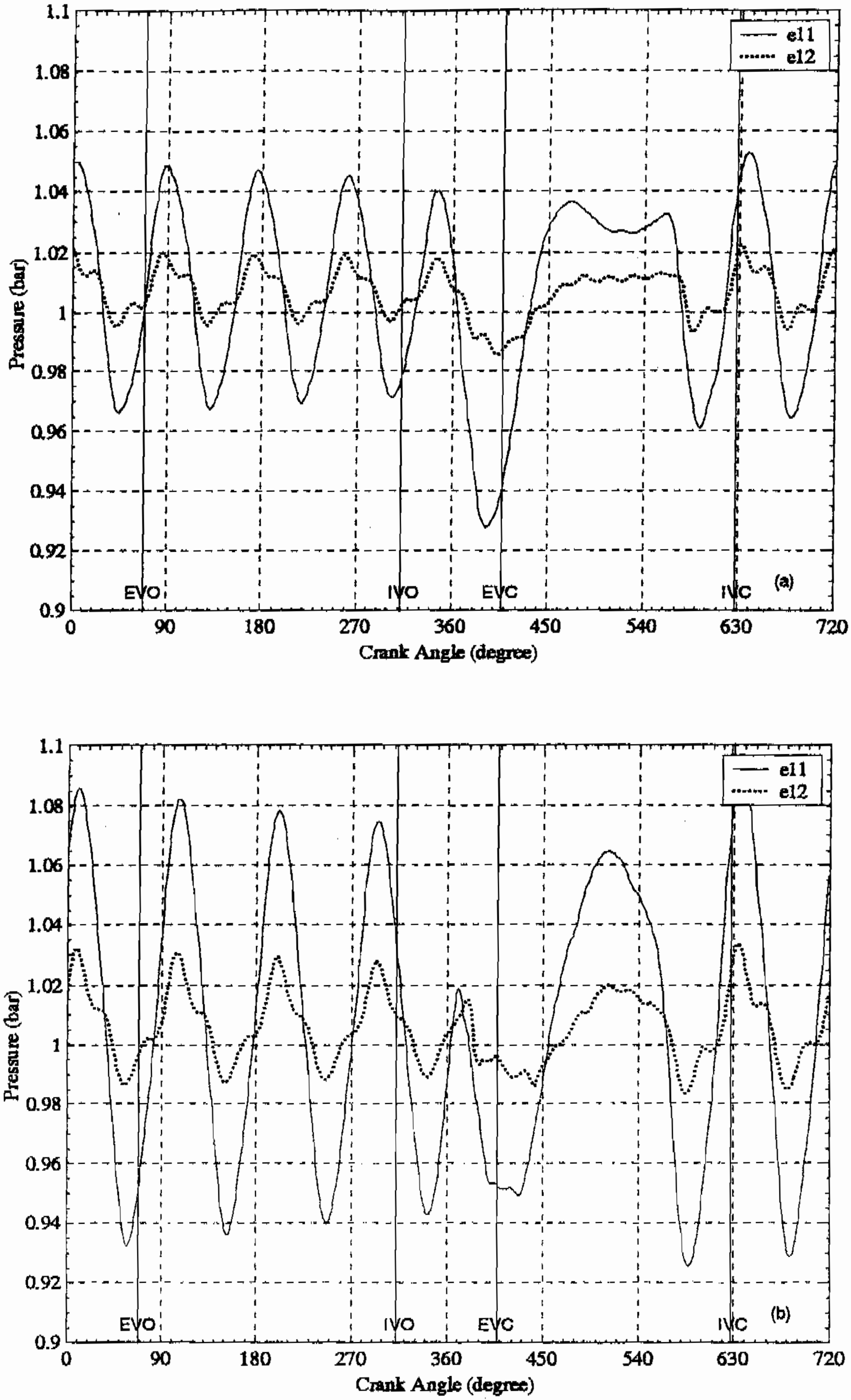

Figure A.41: OSU Dynamometer Experiment: Intake #5 – Pressure versus CAD for Intake Pressure Transducers at (a) 2500 rpm and (b) 2750 rpm

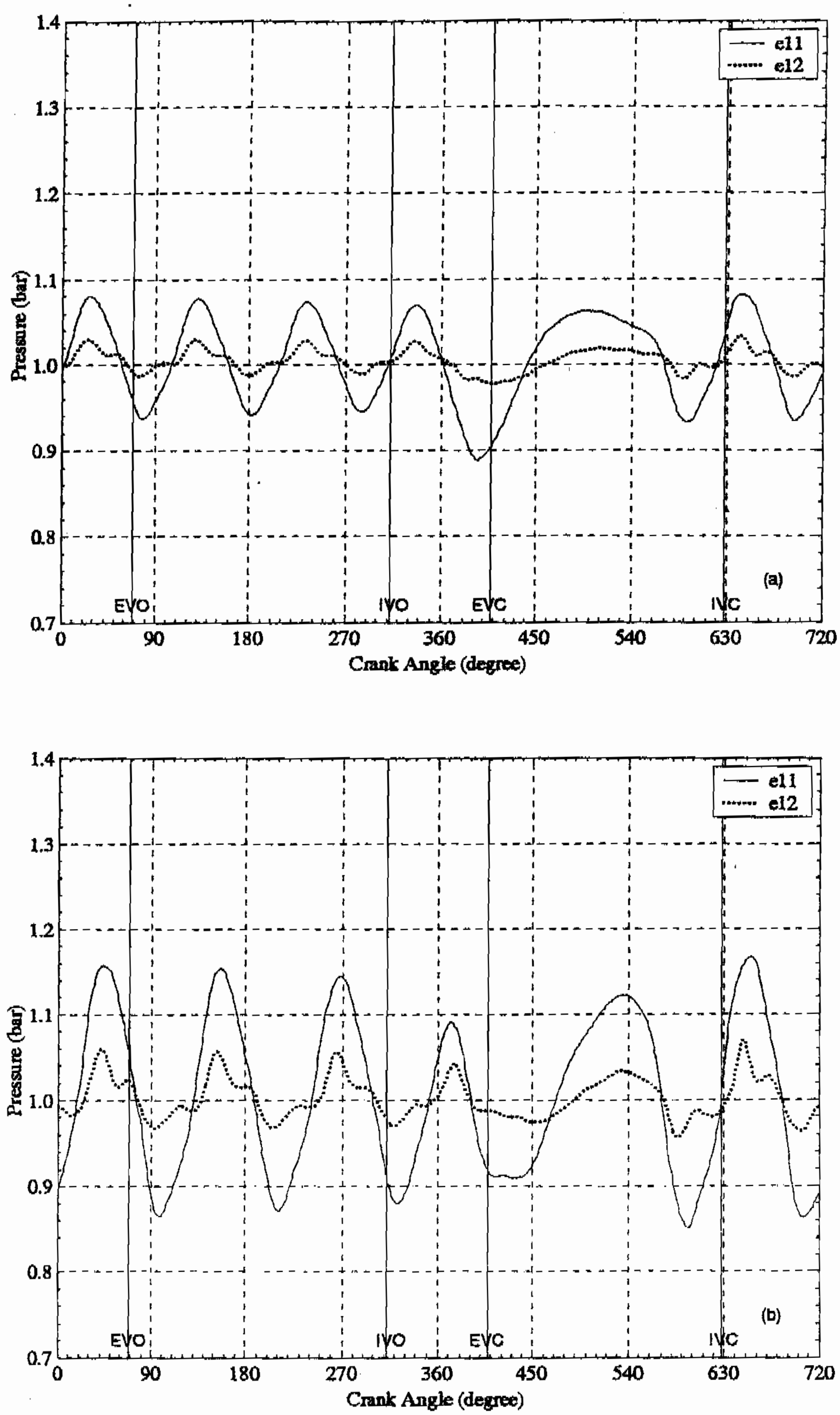

Figure A.42: OSU Dynamometer Experiment: Intake #5 – Pressure versus CAD for Intake Pressure Transducers at (a) 3000 rpm and (b) 3250 rpm

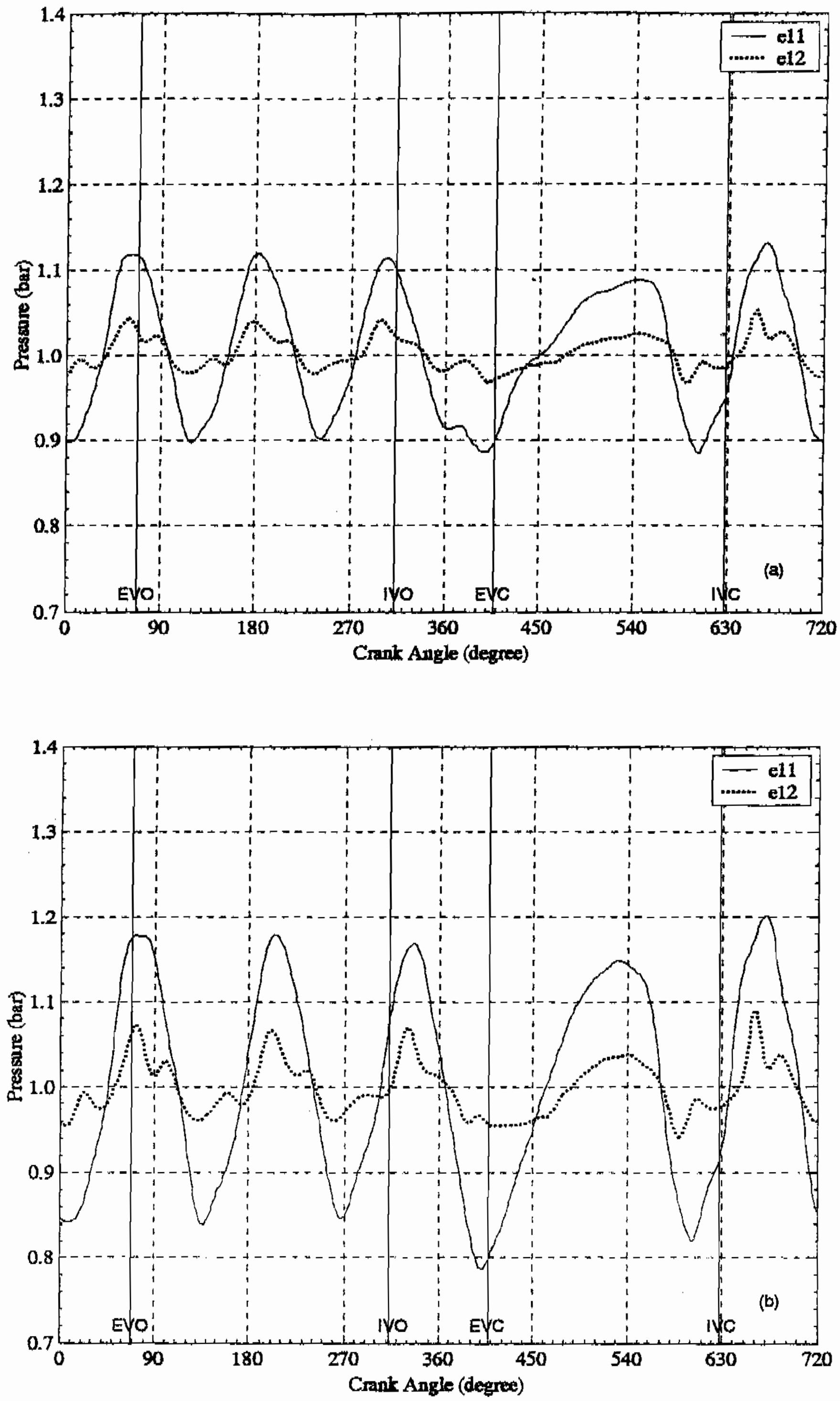

Figure A.43: OSU Dynamometer Experiment: Intake #5 – Pressure versus CAD for Intake Pressure Transducers at (a) 3500 rpm and (b) 3750 rpm

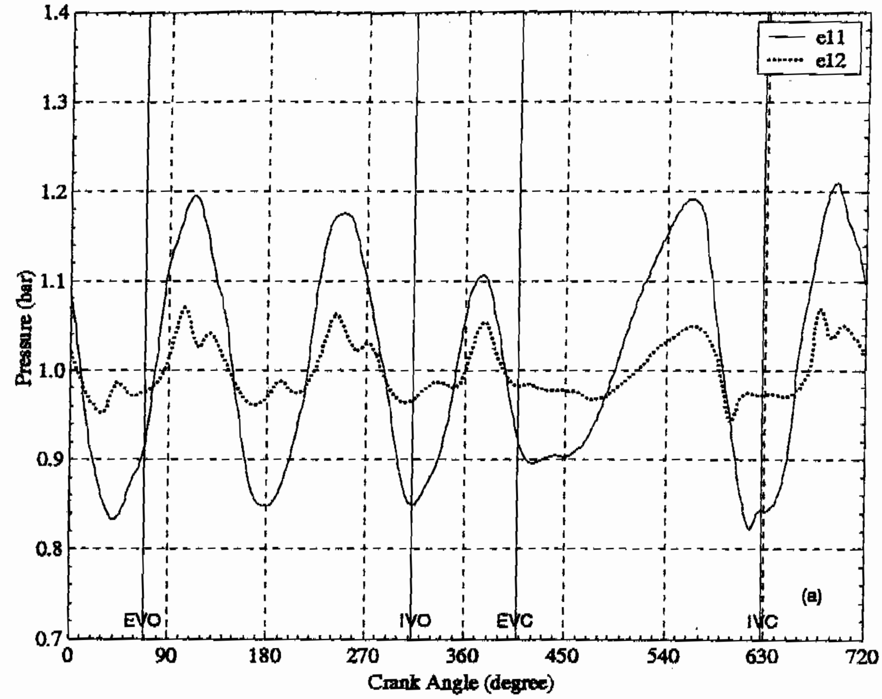

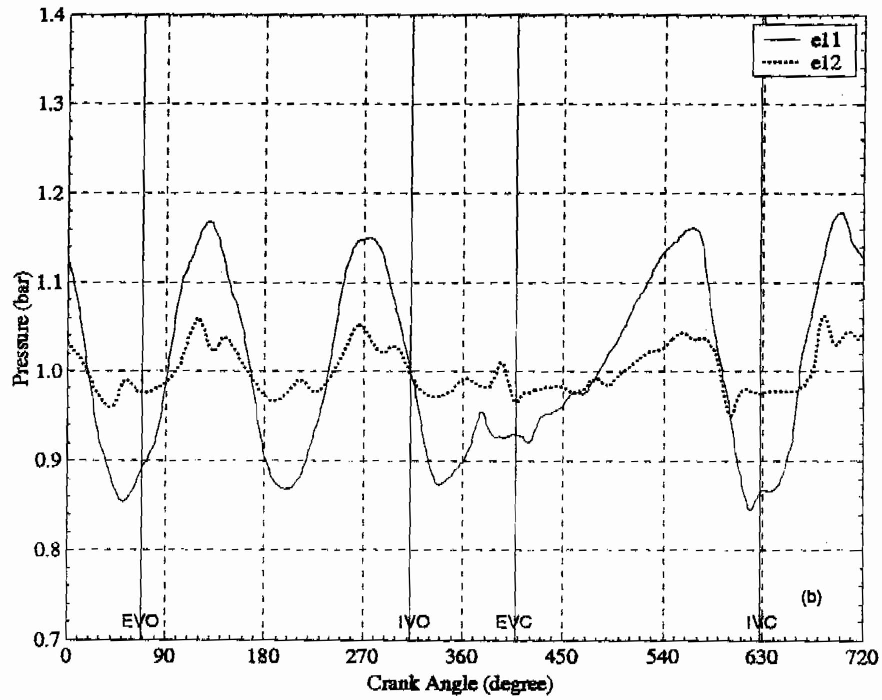

Figure A.44: OSU Dynamometer Experiment: Intake #5 – Pressure versus CAD for Intake Pressure Transducers at (a) 4000 rpm and (b) 4250 rpm

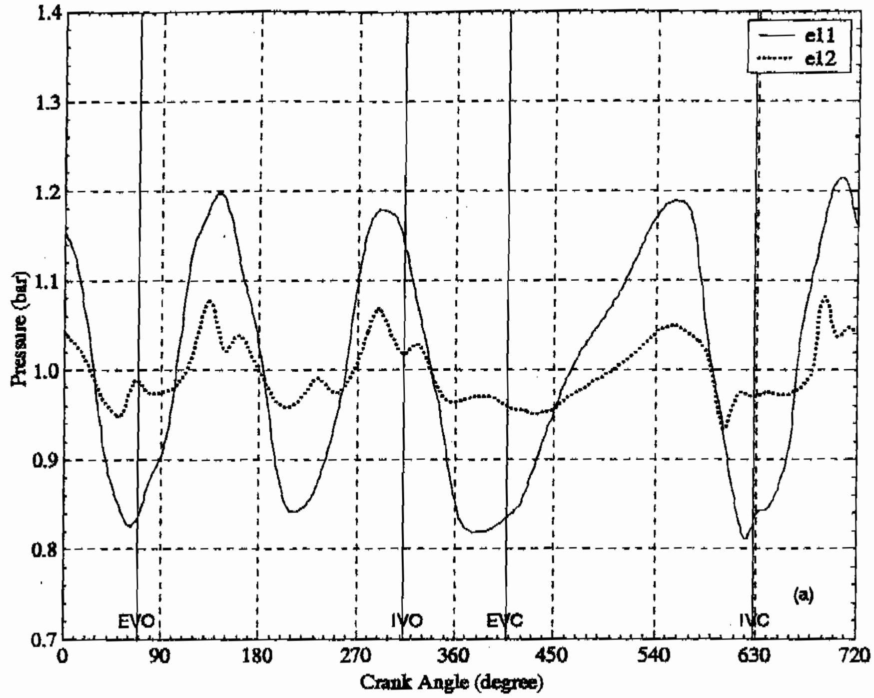

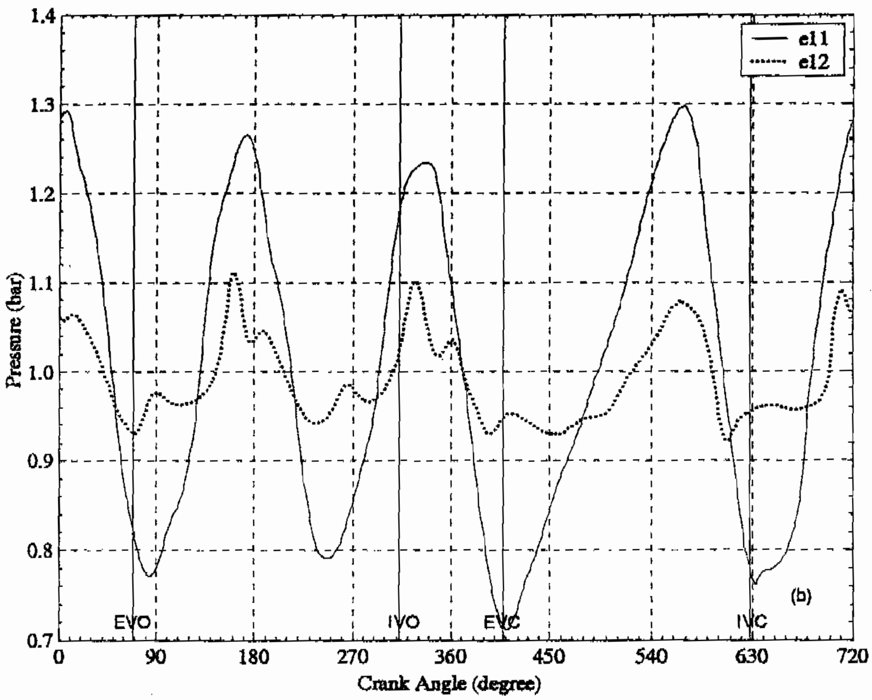

Figure A.45: OSU Dynamometer Experiment: Intake #5 – Pressure versus CAD for Intake Pressure Transducers at (a) 4500 rpm and (b) 4750 rpm

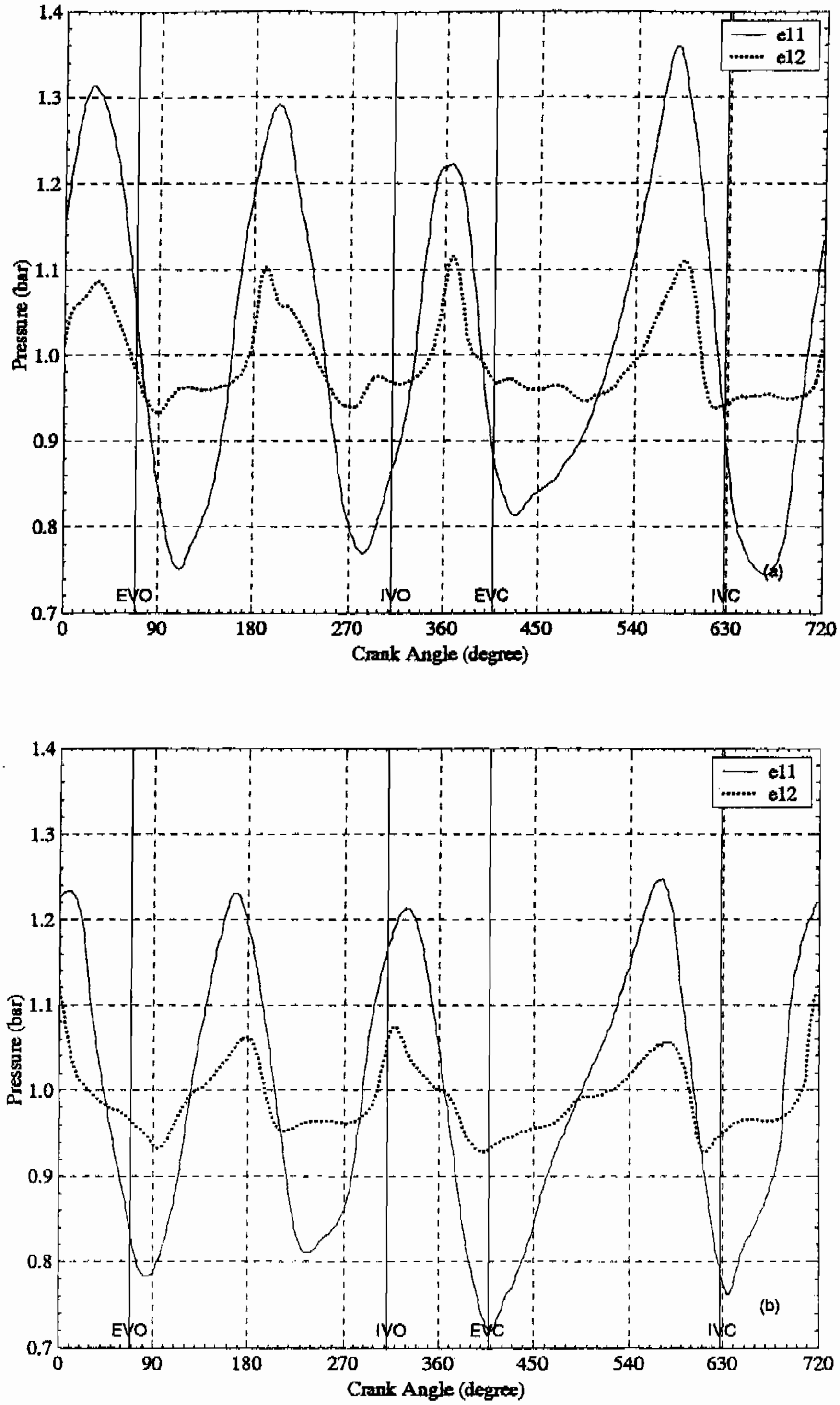

Figure A.46: OSU Dynamometer Experiment: Intake #5 – Pressure versus CAD for Intake Pressure Transducers at (a) 5000 rpm and (b) 5250 rpm

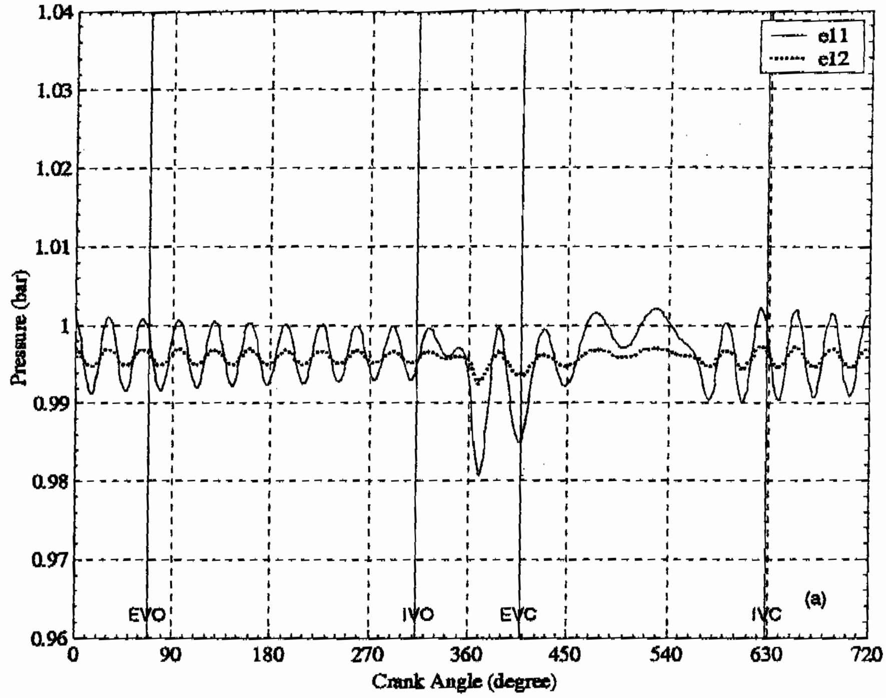

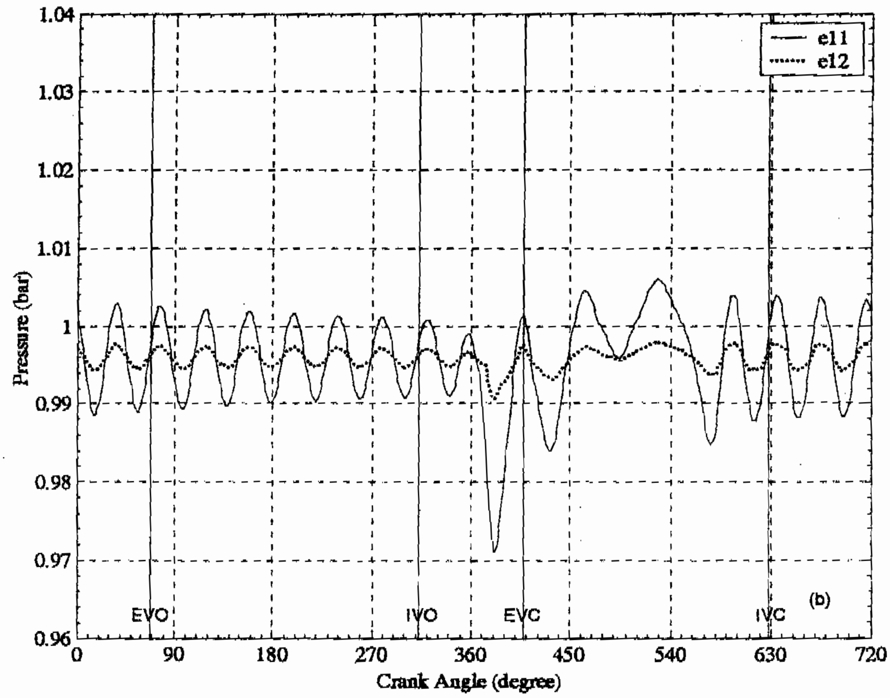

Figure A.47: OSU Dynamometer Experiment: Intake #6 – Pressure versus CAD for Intake Pressure Transducers at (a) 1000 rpm and (b) 1250 rpm

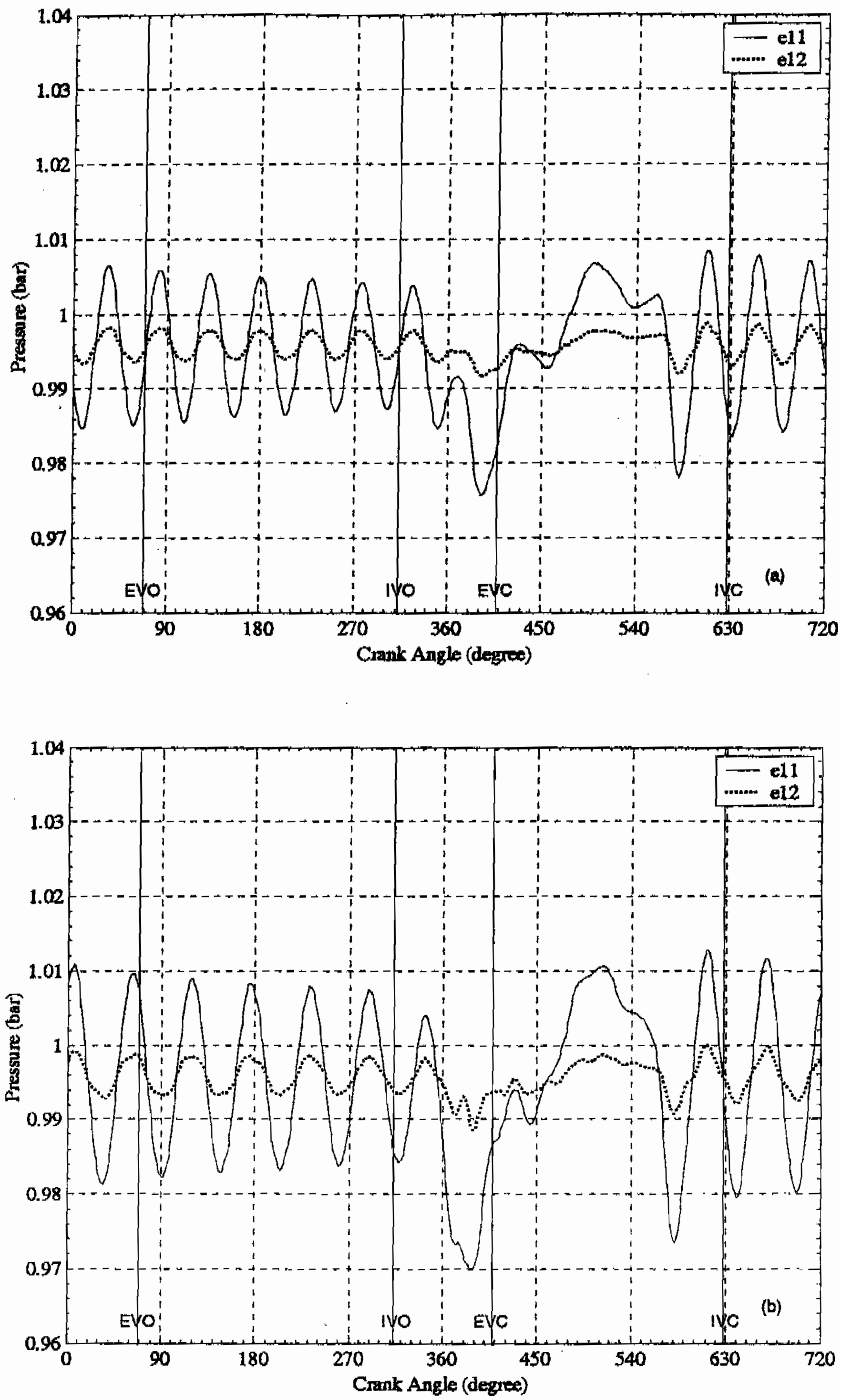

Figure A.47: OSU Dynamometer Experiment: Intake #6 – Pressure versus CAD for Intake Pressure Transducers at (a) 1500 rpm and (b) 1750 rpm

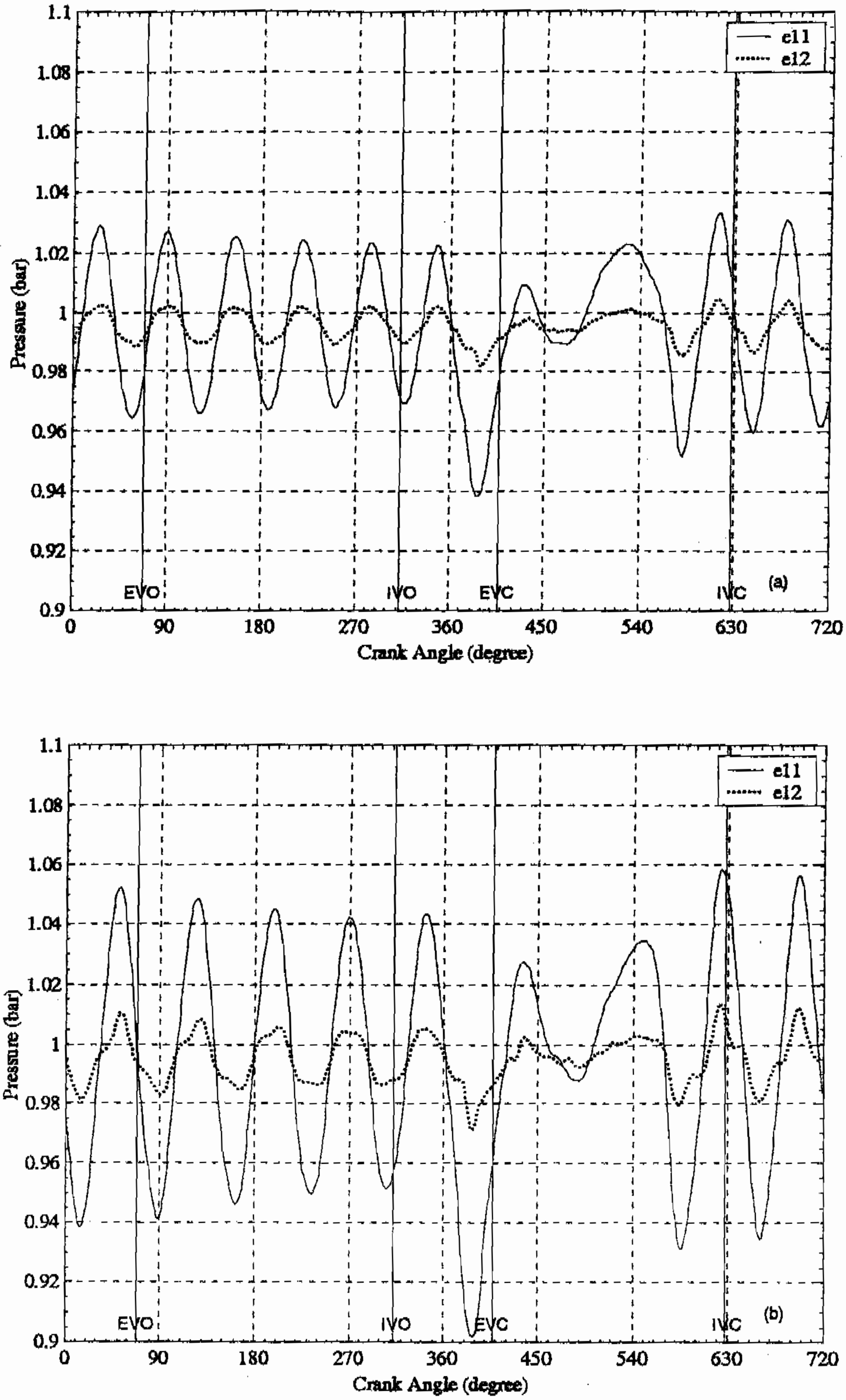

Figure A.49: OSU Dynamometer Experiment: Intake #6 – Pressure versus CAD for Intake Pressure Transducers at (a) 2000 rpm and (b) 2250 rpm

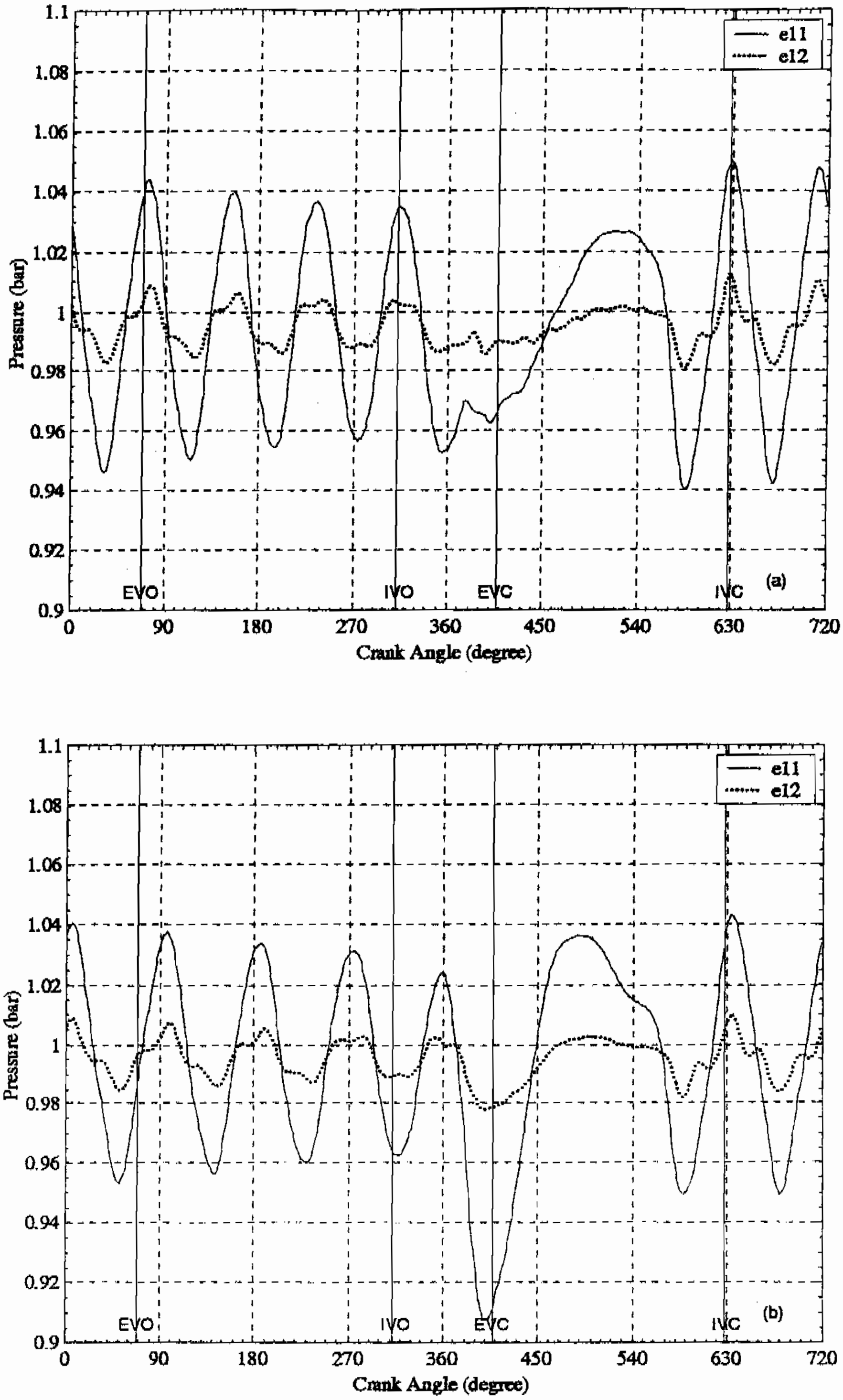

Figure A.50: OSU Dynamometer Experiment: Intake #6 – Pressure versus CAD for Intake Pressure Transducers at (a) 2500 rpm and (b) 2750 rpm

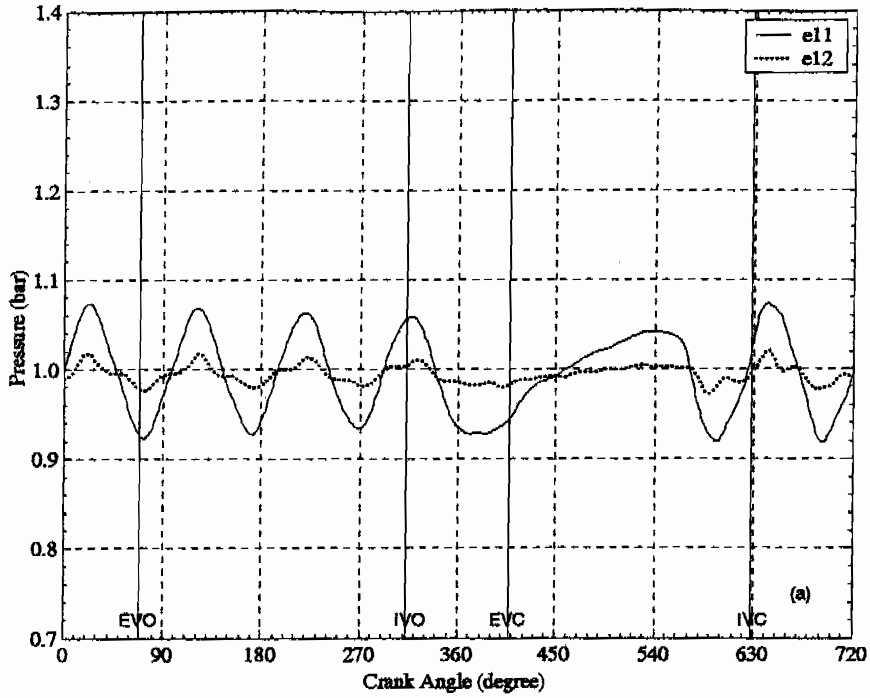

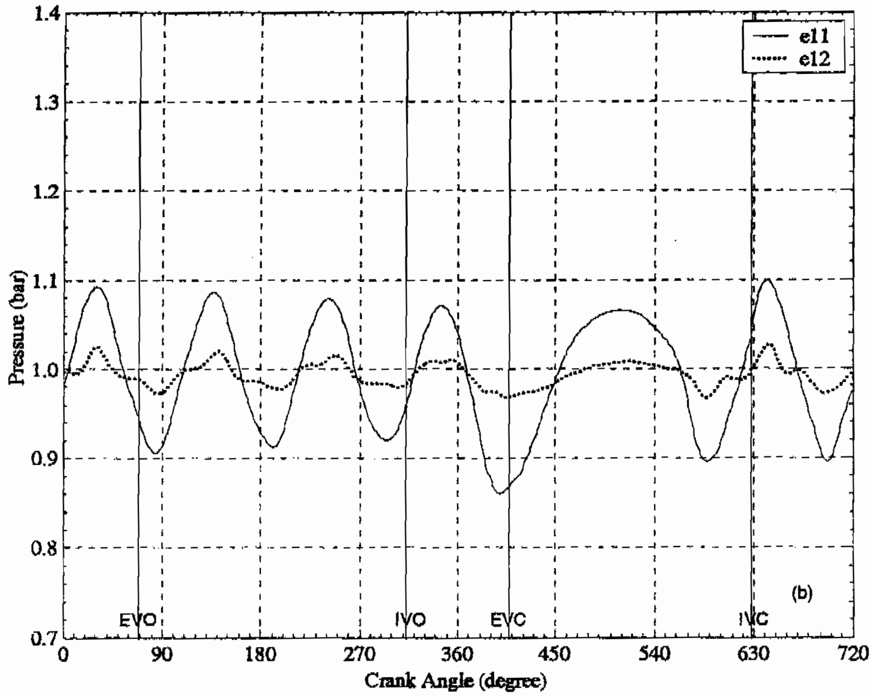

Figure A.51: OSU Dynamometer Experiment: Intake #6 – Pressure versus CAD for Intake Pressure Transducers at (a) 3000 rpm and (b) 3250 rpm

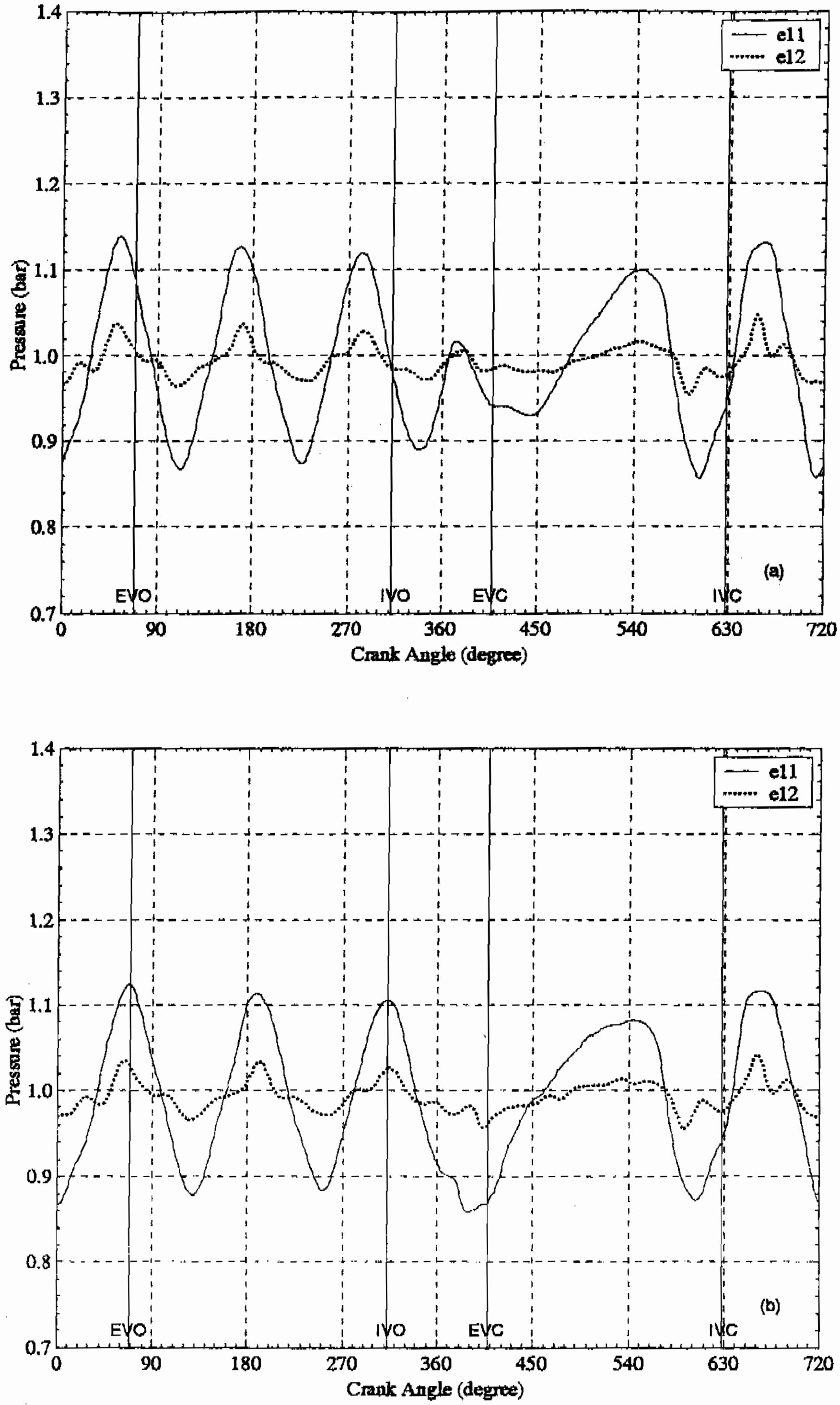

Figure A.52: OSU Dynamometer Experiment: Intake #6 – Pressure versus CAD for Intake Pressure Transducers at (a) 3500 rpm and (b) 3750 rpm

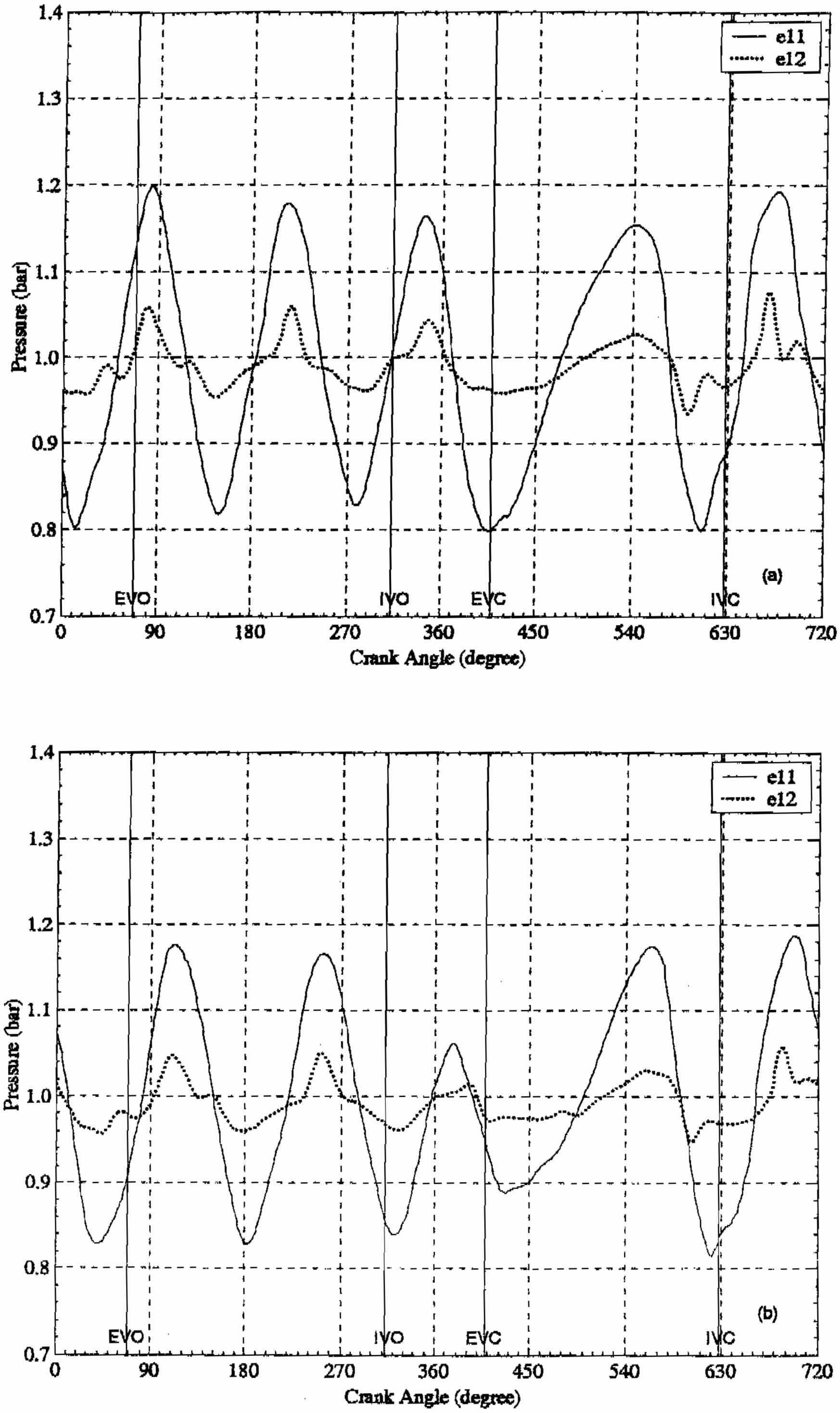

Figure A.53: OSU Dynamometer Experiment: Intake #6 – Pressure versus CAD for Intake Pressure Transducers at (a) 4000 rpm and (b) 4250 rpm

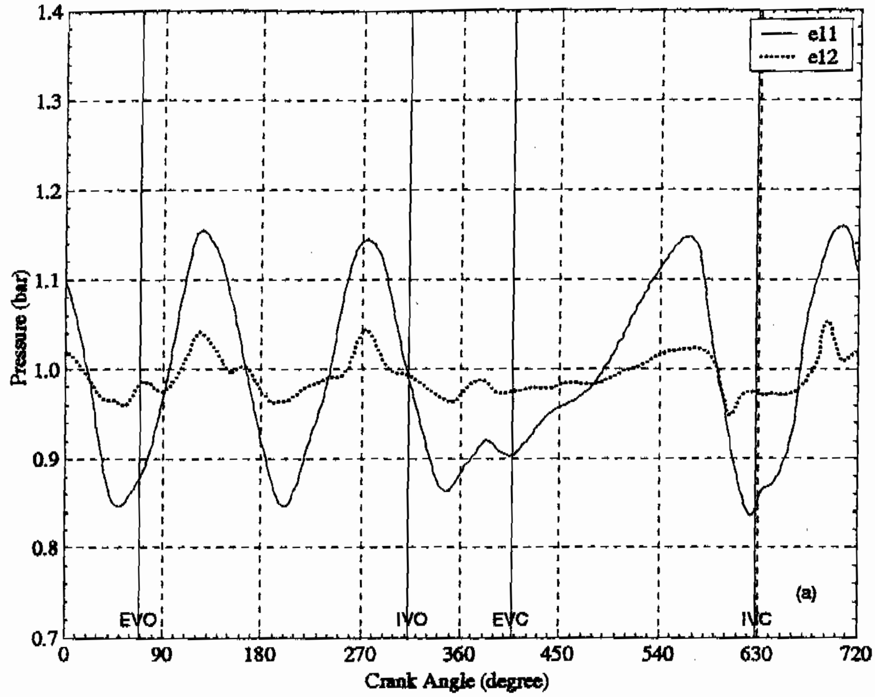

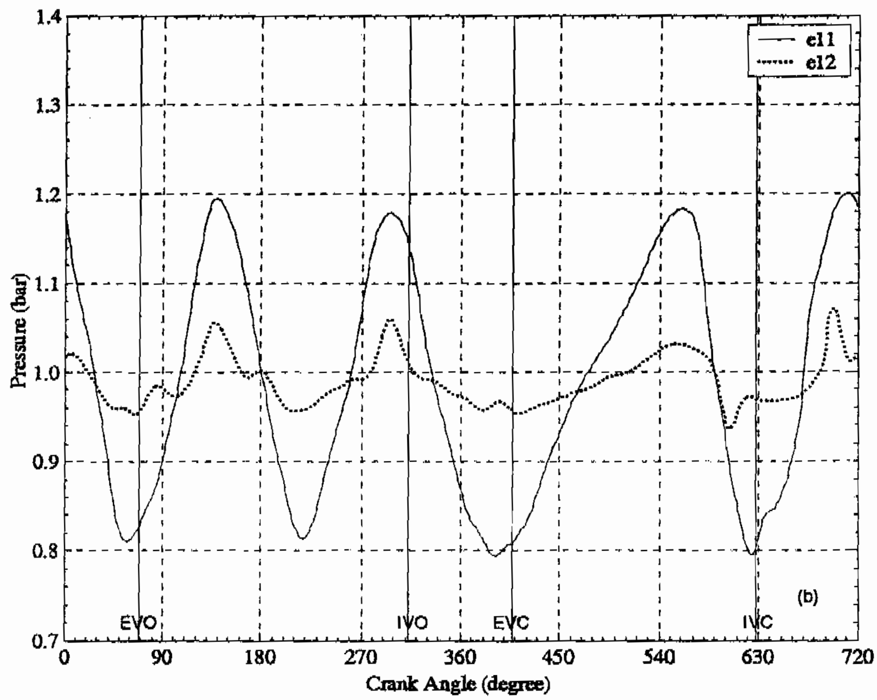

Figure A.54: OSU Dynamometer Experiment: Intake #6 – Pressure versus CAD for Intake Pressure Transducers at (a) 4500 rpm and (b) 4750 rpm

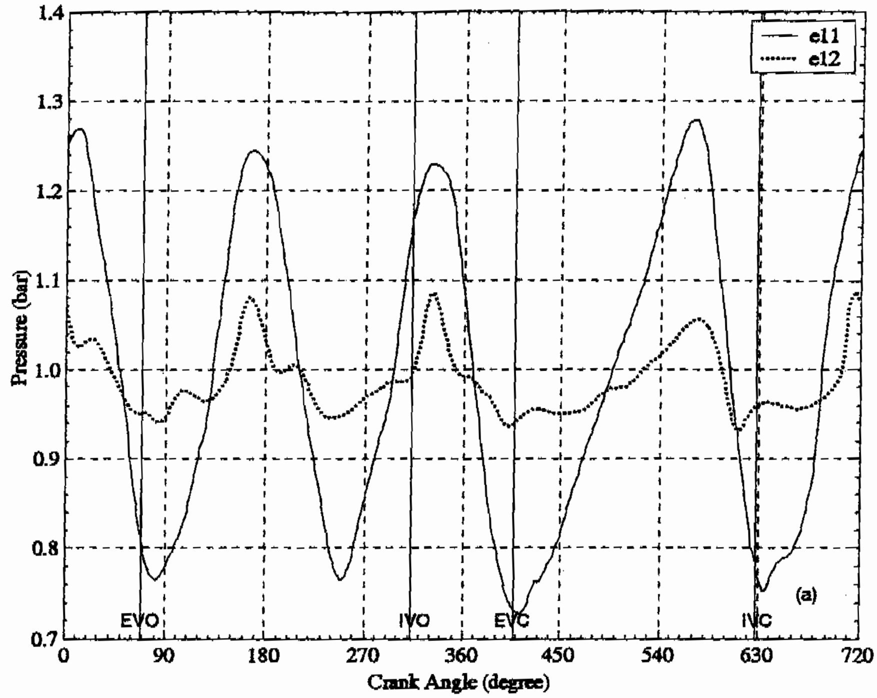

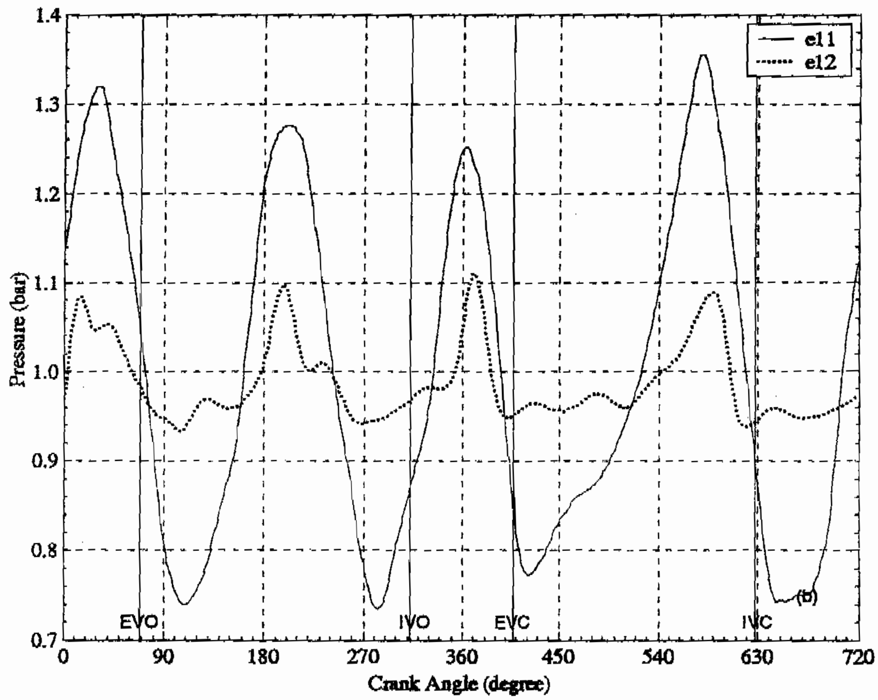

Figure A.55: OSU Dynamometer Experiment: Intake #6 – Pressure versus CAD for Intake Pressure Transducers at (a) 5000 rpm and (b) 5250 rpm

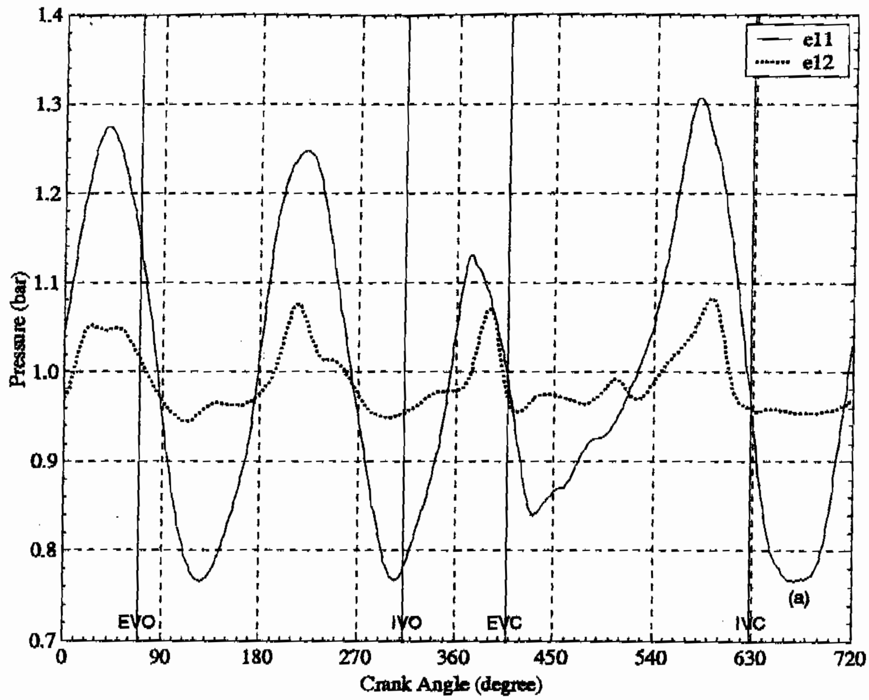

Figure A.56: OSU Dynamometer Experiment: Intake #6 – Pressure versus CAD for Intake Pressure Transducers at (a) 5500 rpm

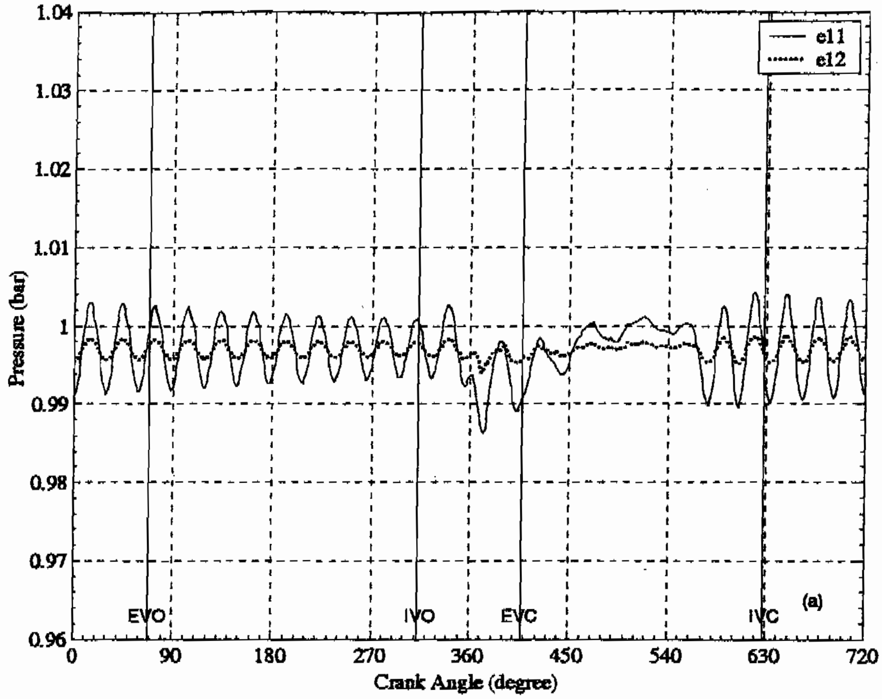

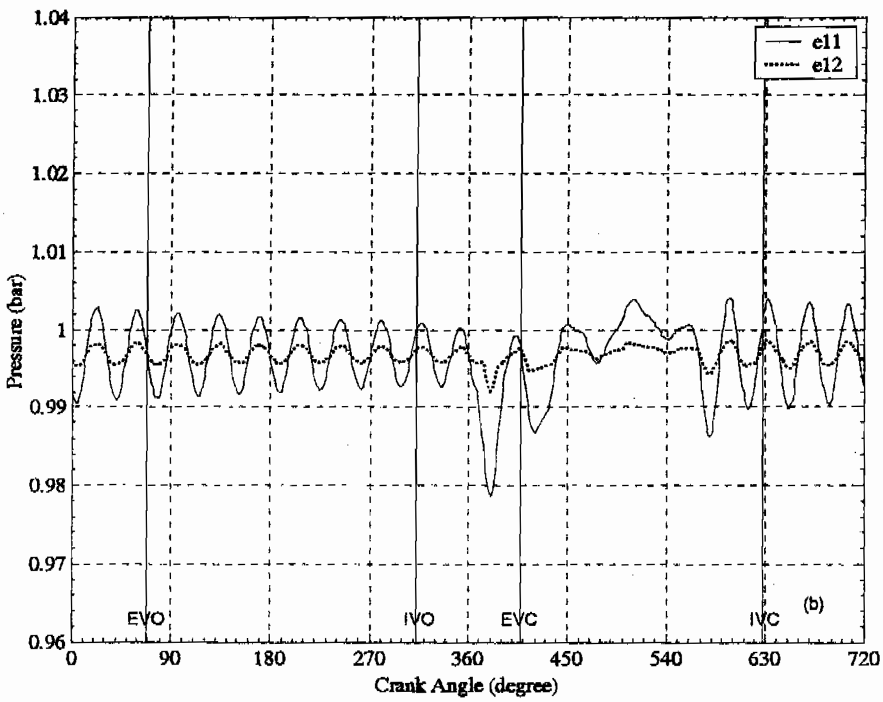

Figure A.57: OSU Dynamometer Experiment: Intake #7 – Pressure versus CAD for Intake Pressure Transducers at (a) 1000 rpm and (b) 1250 rpm

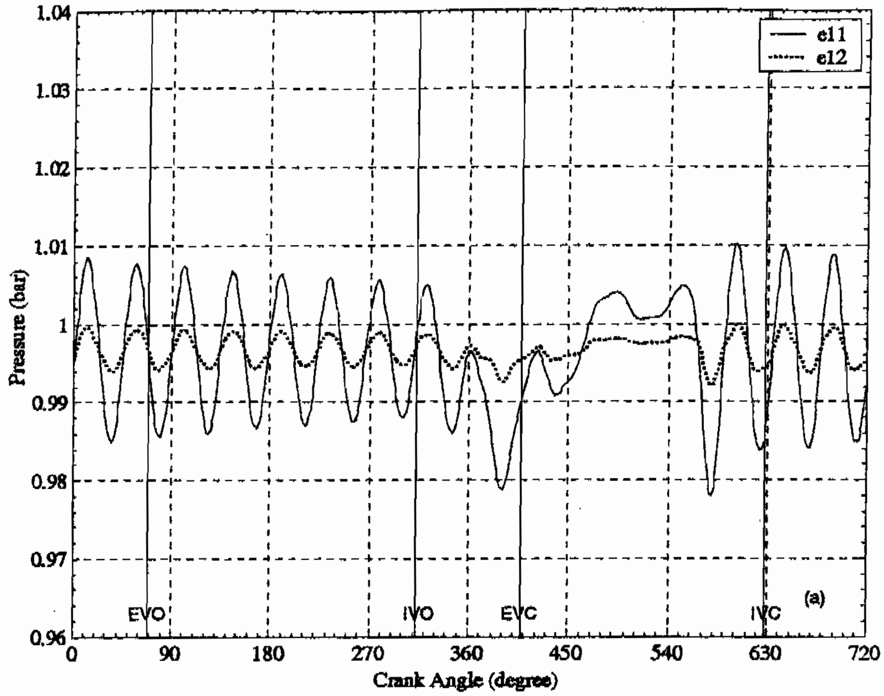

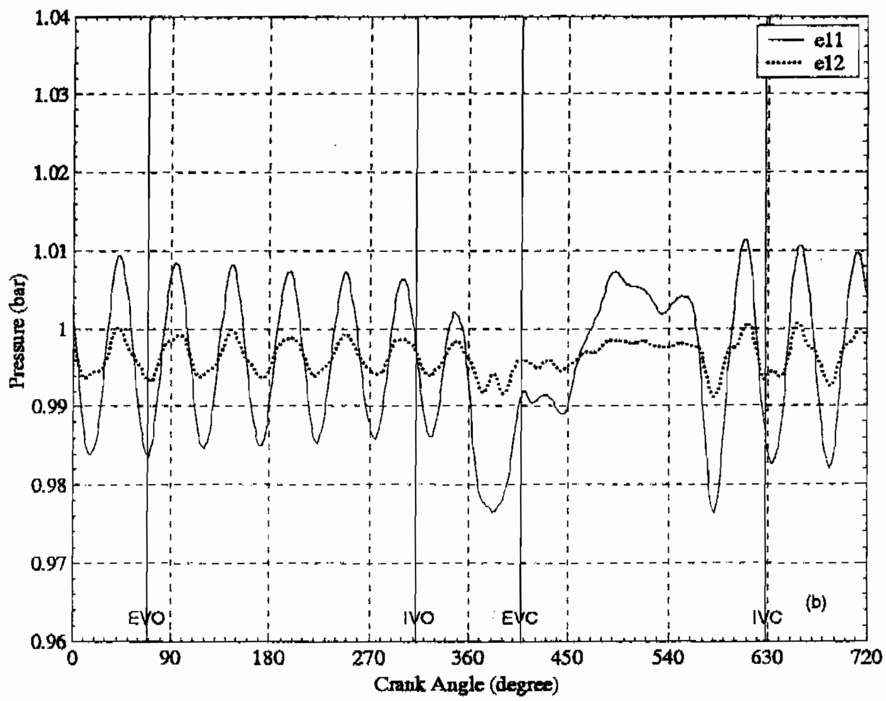

Figure A.58: OSU Dynamometer Experiment: Intake #7 – Pressure versus CAD for Intake Pressure Transducers at (a) 1500 rpm and (b) 1750 rpm

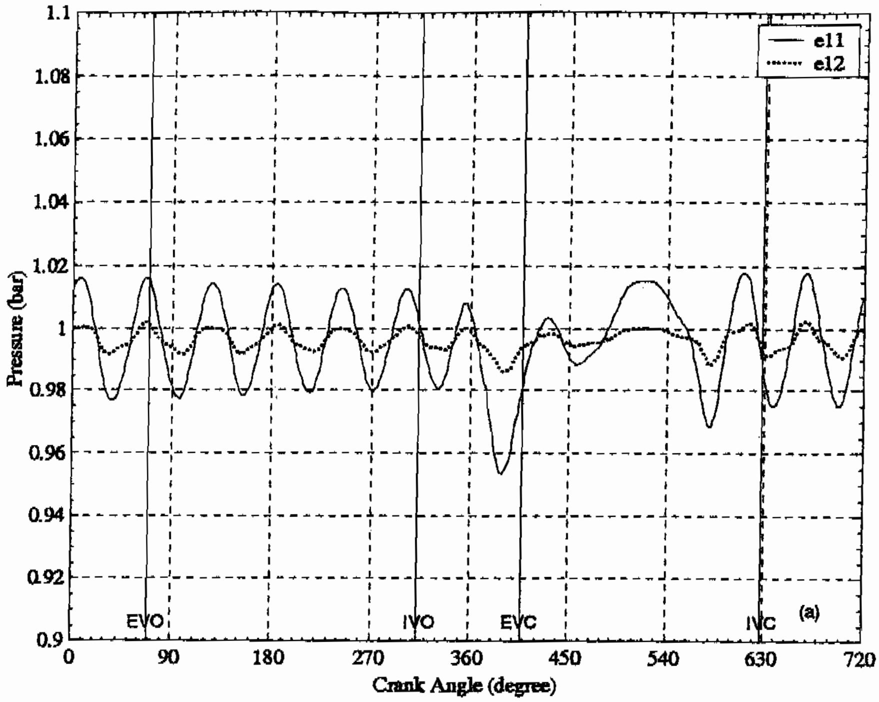

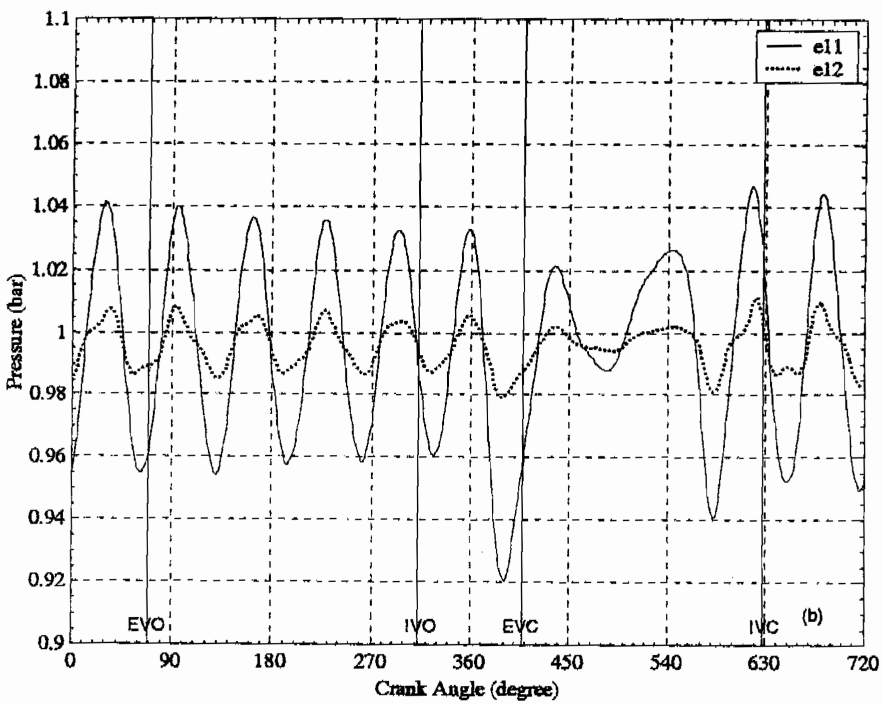

Figure A.59: OSU Dynamometer Experiment: Intake #7 – Pressure versus CAD for Intake Pressure Transducers at (a) 2000 rpm and (b) 2250 rpm

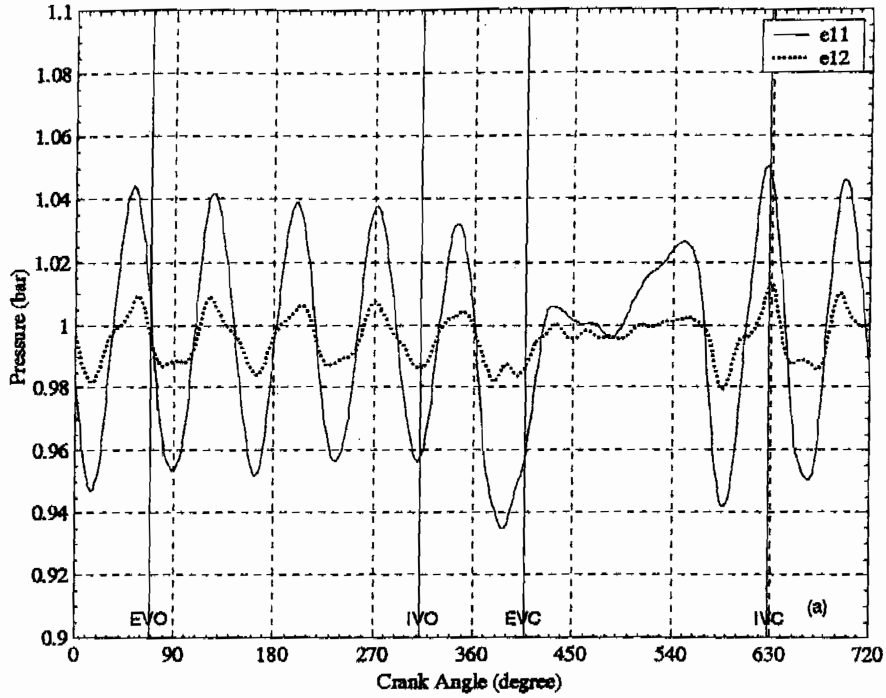

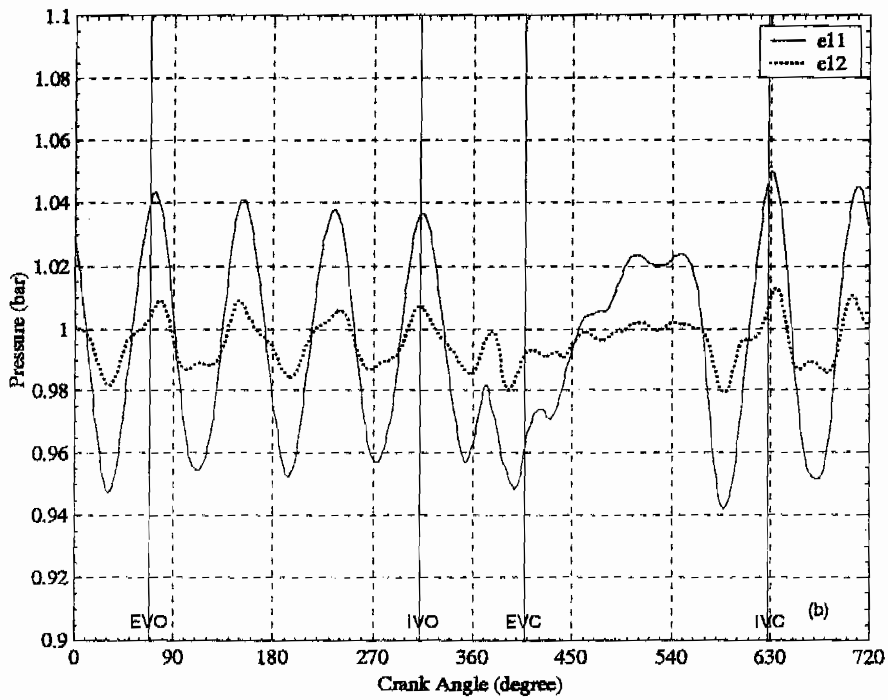

Figure A.60: OSU Dynamometer Experiment: Intake #7 – Pressure versus CAD for Intake Pressure Transducers at (a) 2500 rpm and (b) 2750 rpm

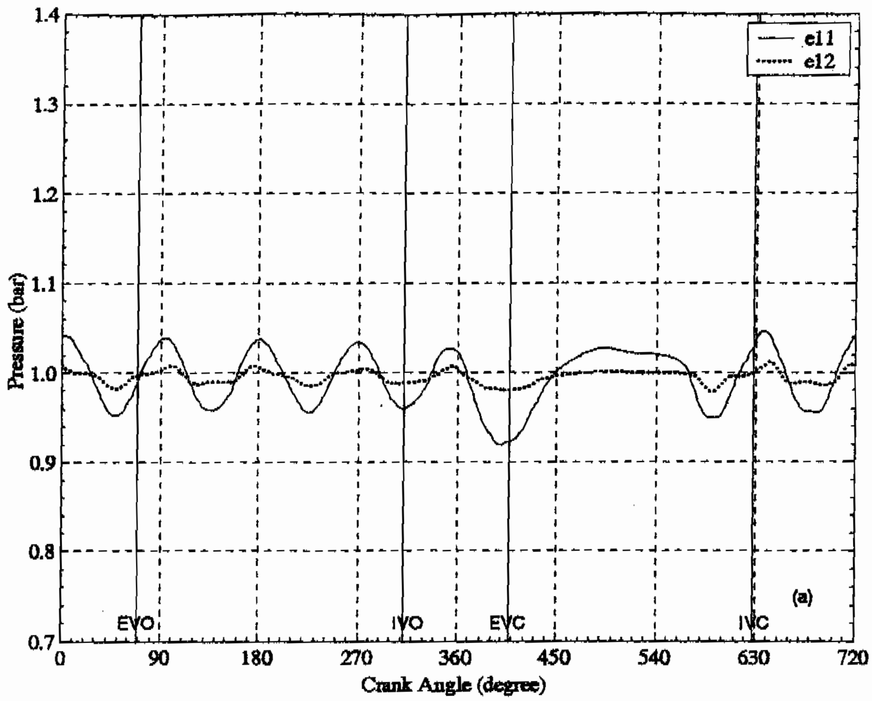

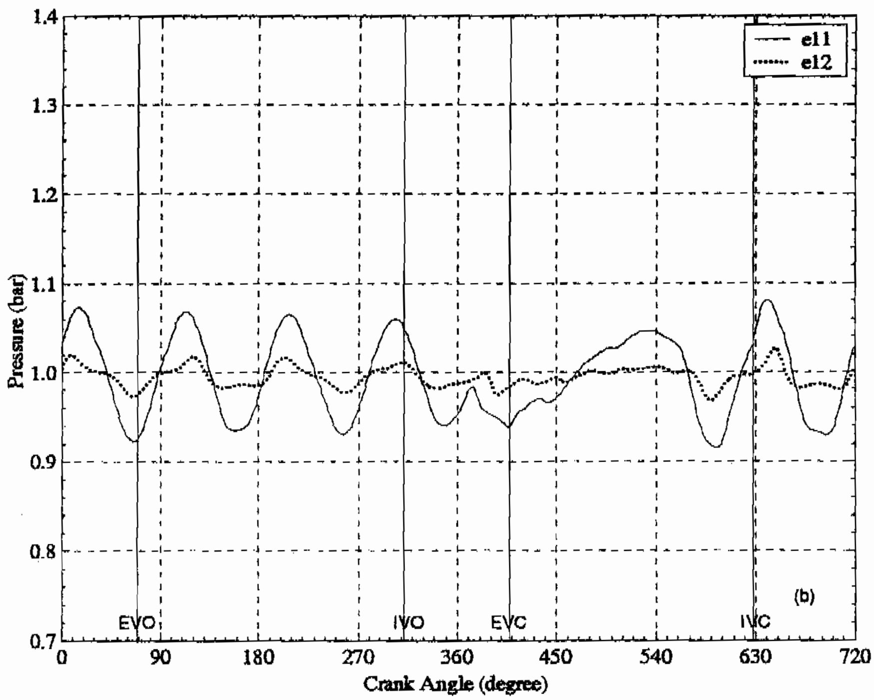

Figure A.61: OSU Dynamometer Experiment: Intake #7 – Pressure versus CAD for Intake Pressure Transducers at (a) 3000 rpm and (b) 3250 rpm

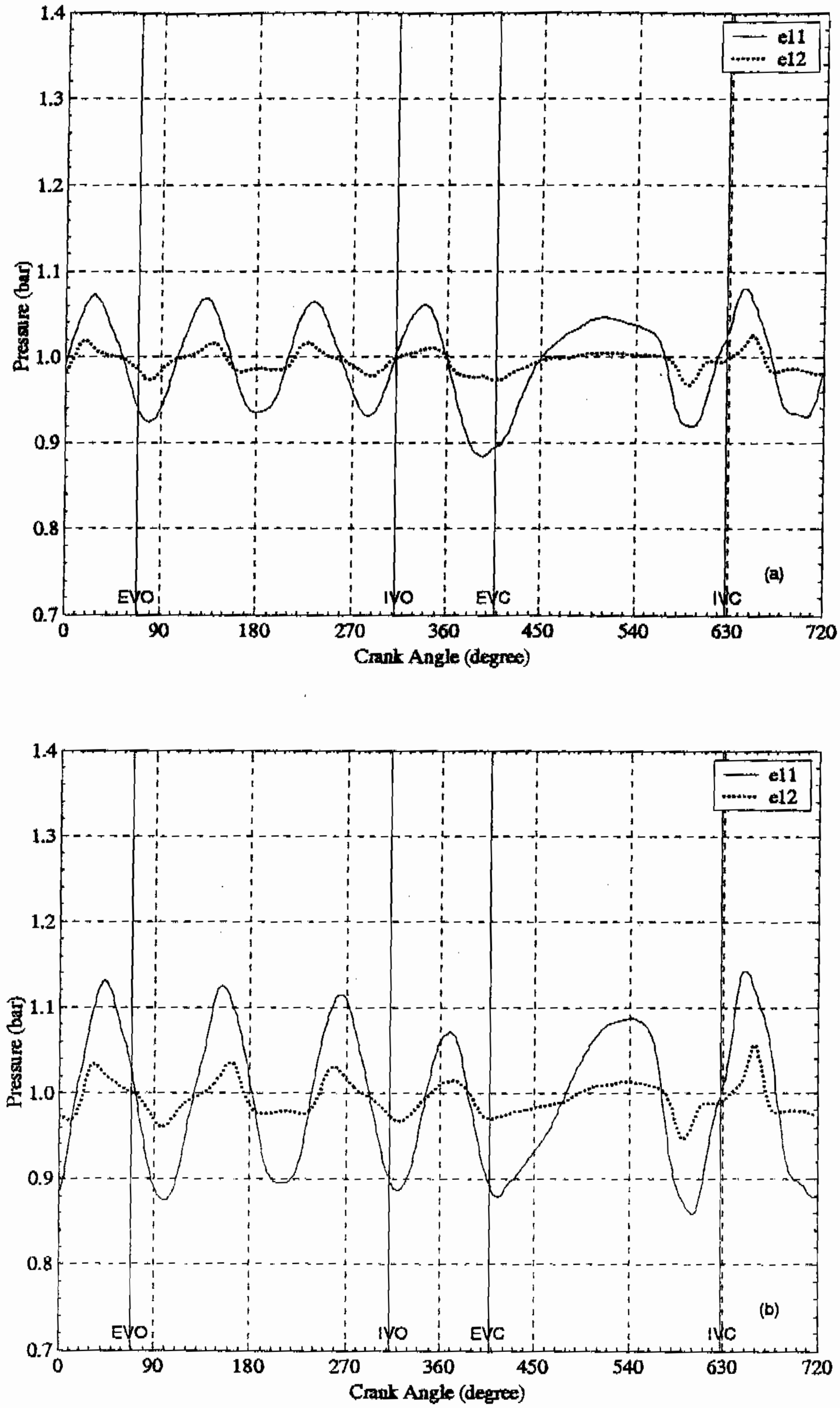

Figure A.62: OSU Dynamometer Experiment: Intake #7 – Pressure versus CAD for Intake Pressure Transducers at (a) 3500 rpm and (b) 3750 rpm

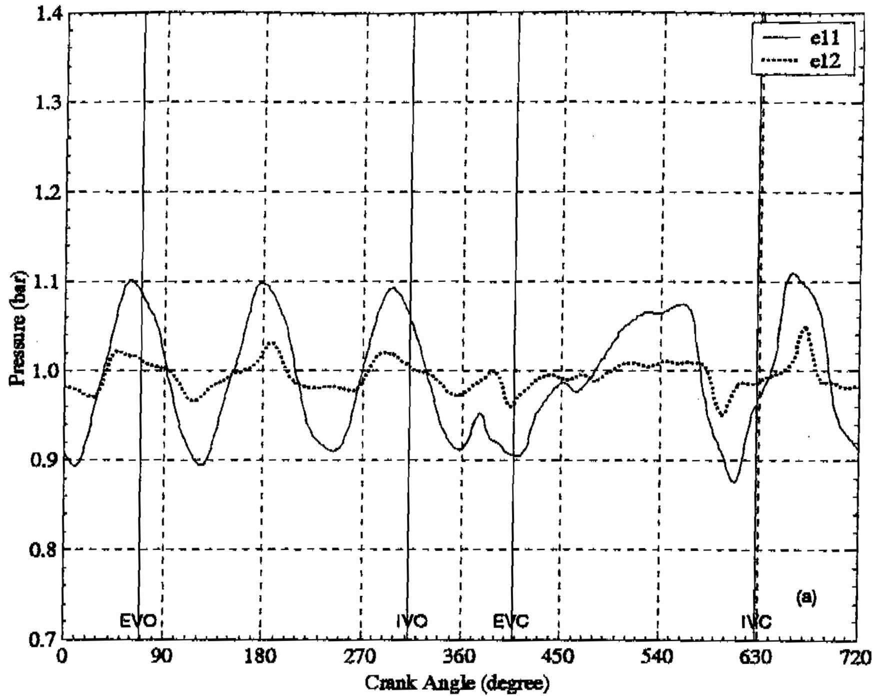

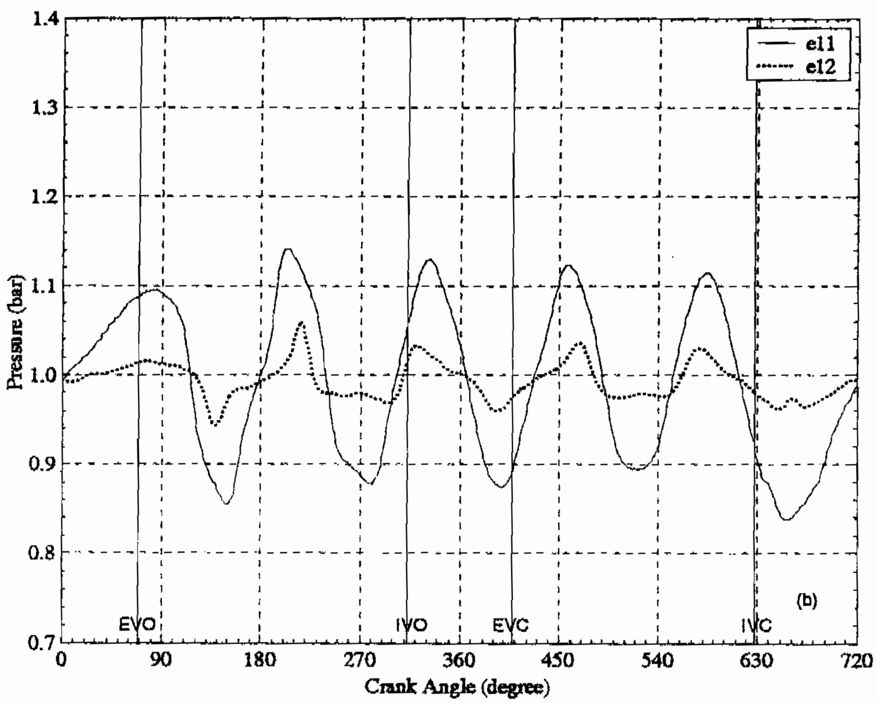

Figure A.63: OSU Dynamometer Experiment: Intake #7 – Pressure versus CAD for Intake Pressure Transducers at (a) 4000 rpm and (b) 4250 rpm

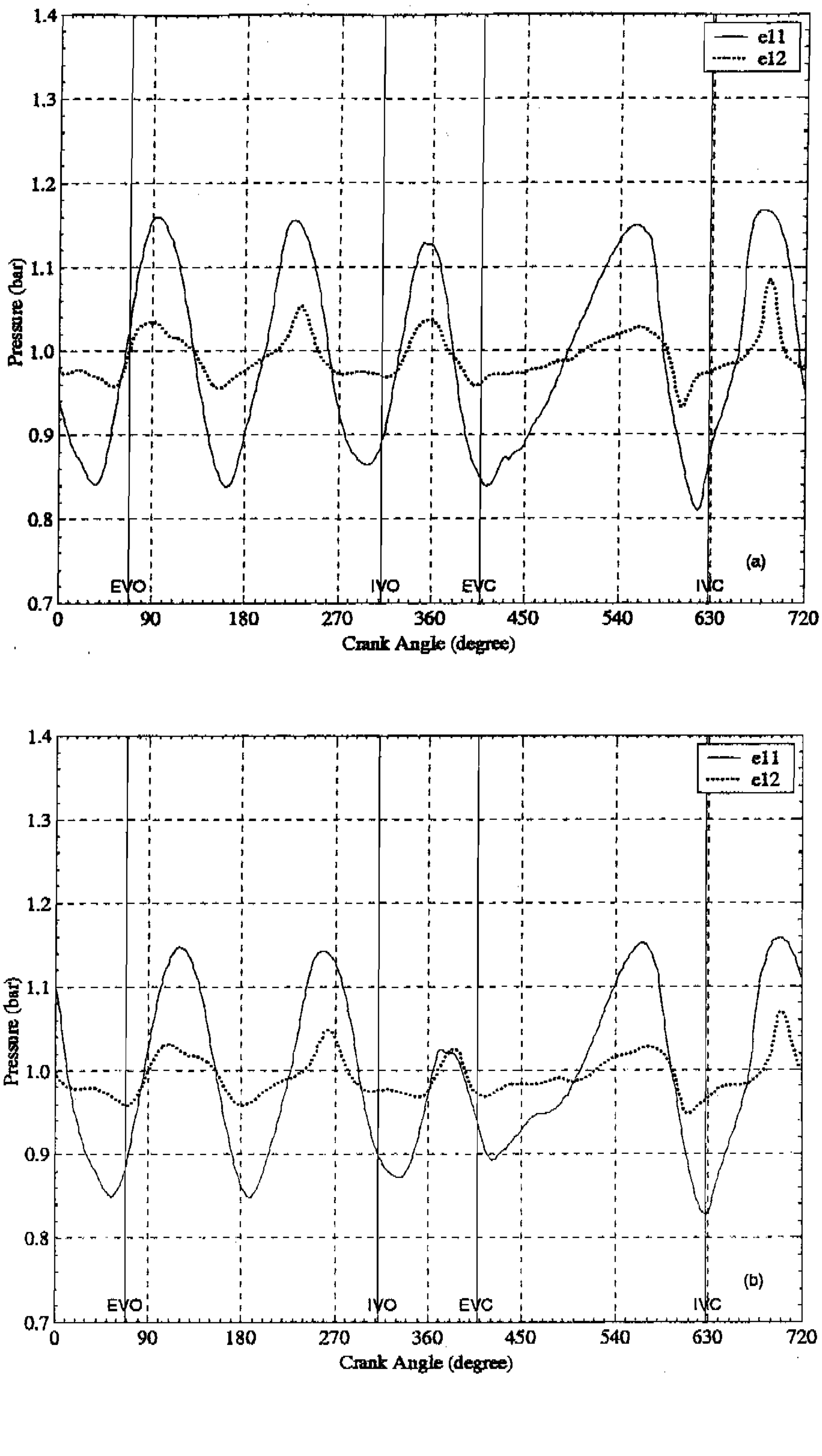

Figure A.64: OSU Dynamometer Experiment: Intake #7 – Pressure versus CAD for Intake Pressure Transducers at (a) 4500 rpm and (b) 4750 rpm

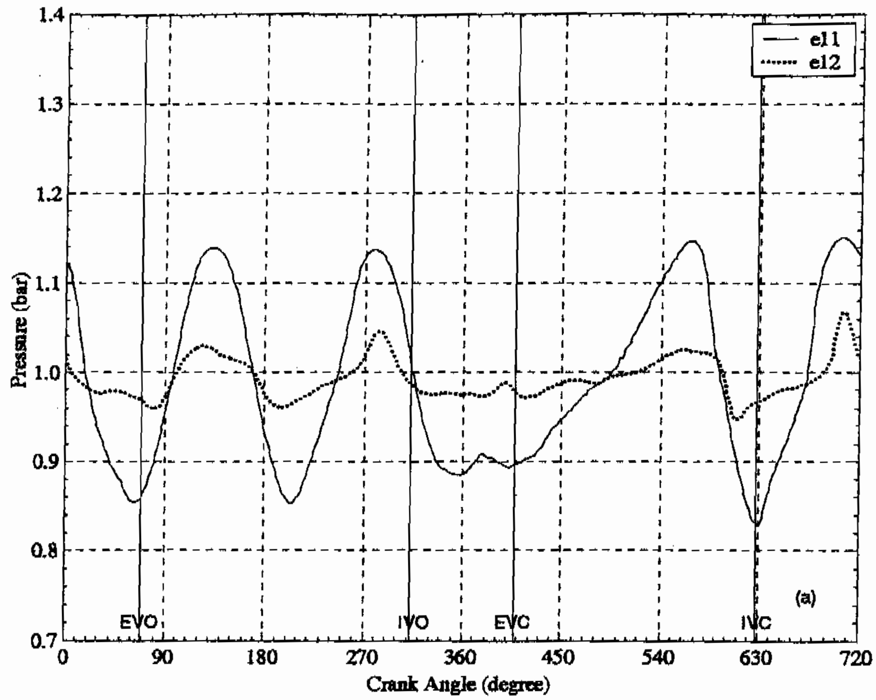

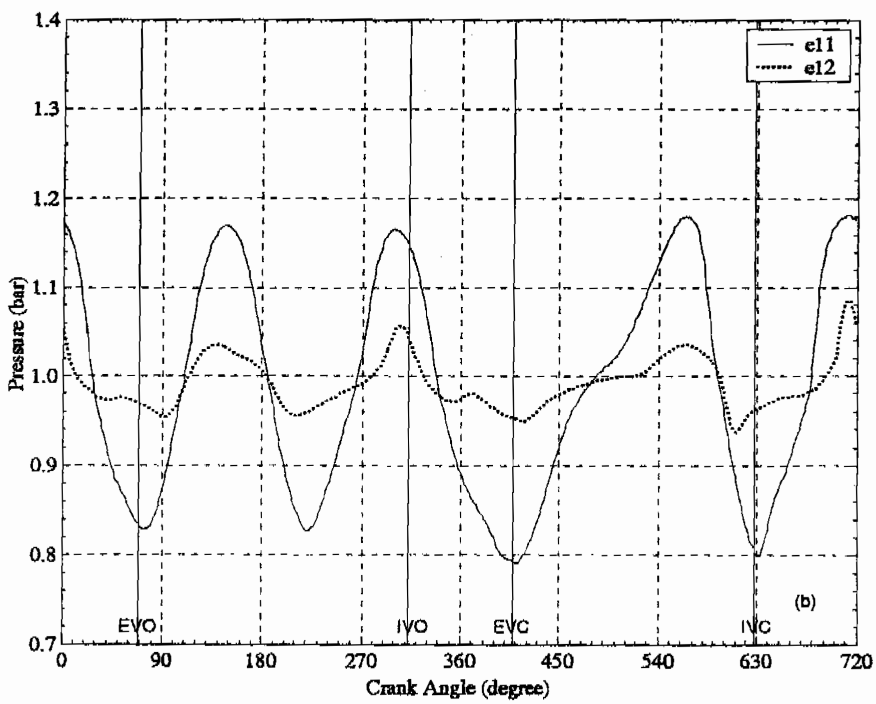

Figure A.65: OSU Dynamometer Experiment: Intake #7 – Pressure versus CAD for Intake Pressure Transducers at (a) 5000 rpm and (b) 5250 rpm

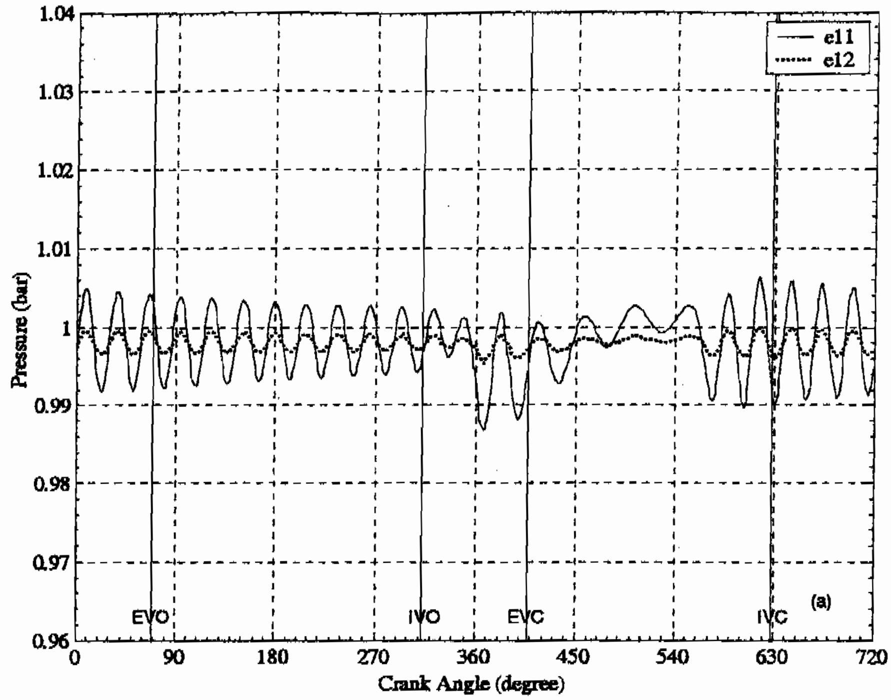

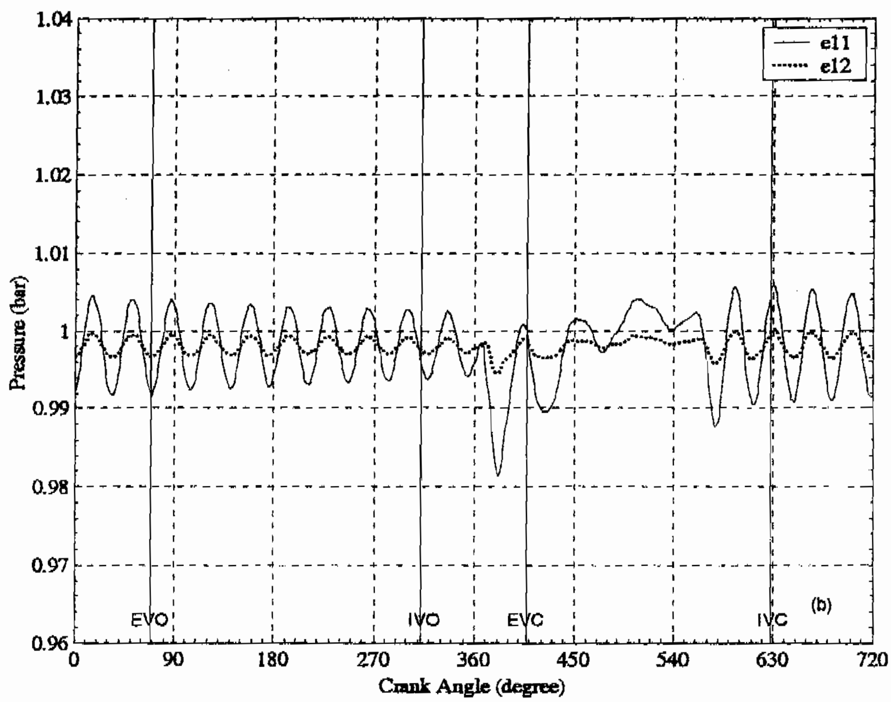

Figure A.66: OSU Dynamometer Experiment: Intake #8 -- Pressure versus CAD for Intake Pressure Transducers at (a) 1000 rpm and (b) 1250 rpm

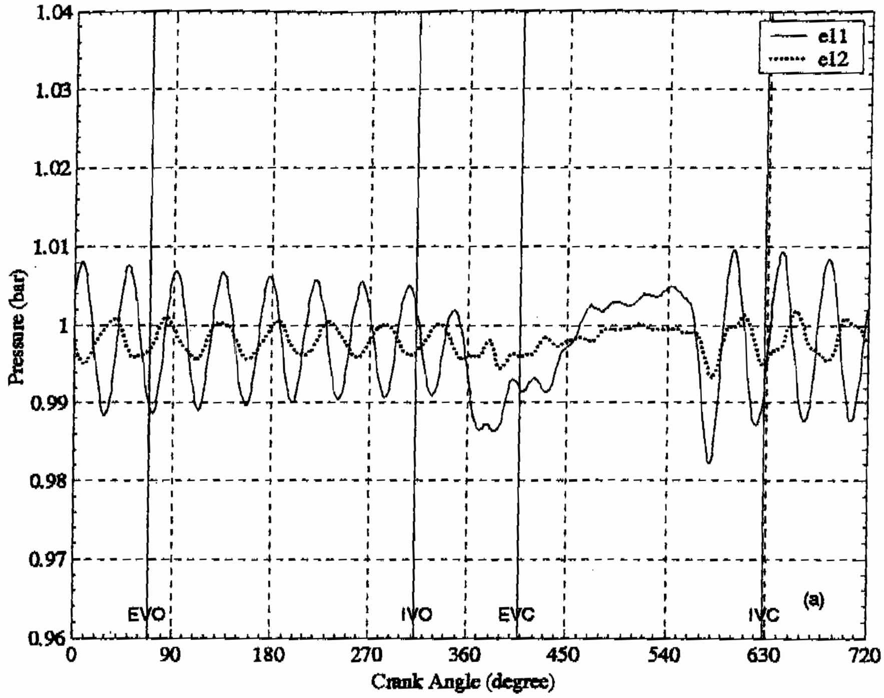

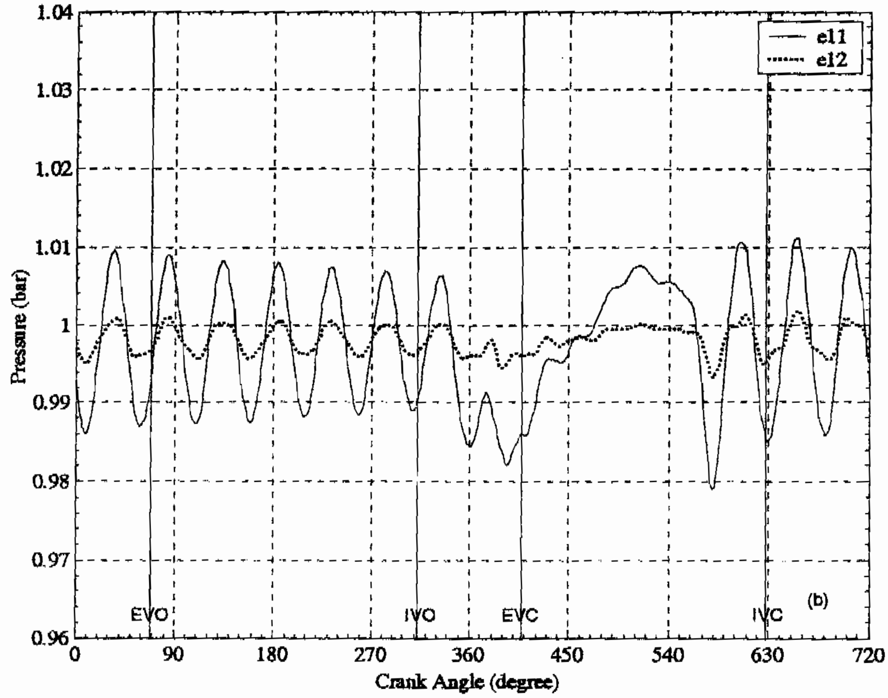

Figure A.67: OSU Dynamometer Experiment: Intake #8 -- Pressure versus CAD for Intake Pressure Transducers at (a) 1500 rpm and (b) 1750 rpm

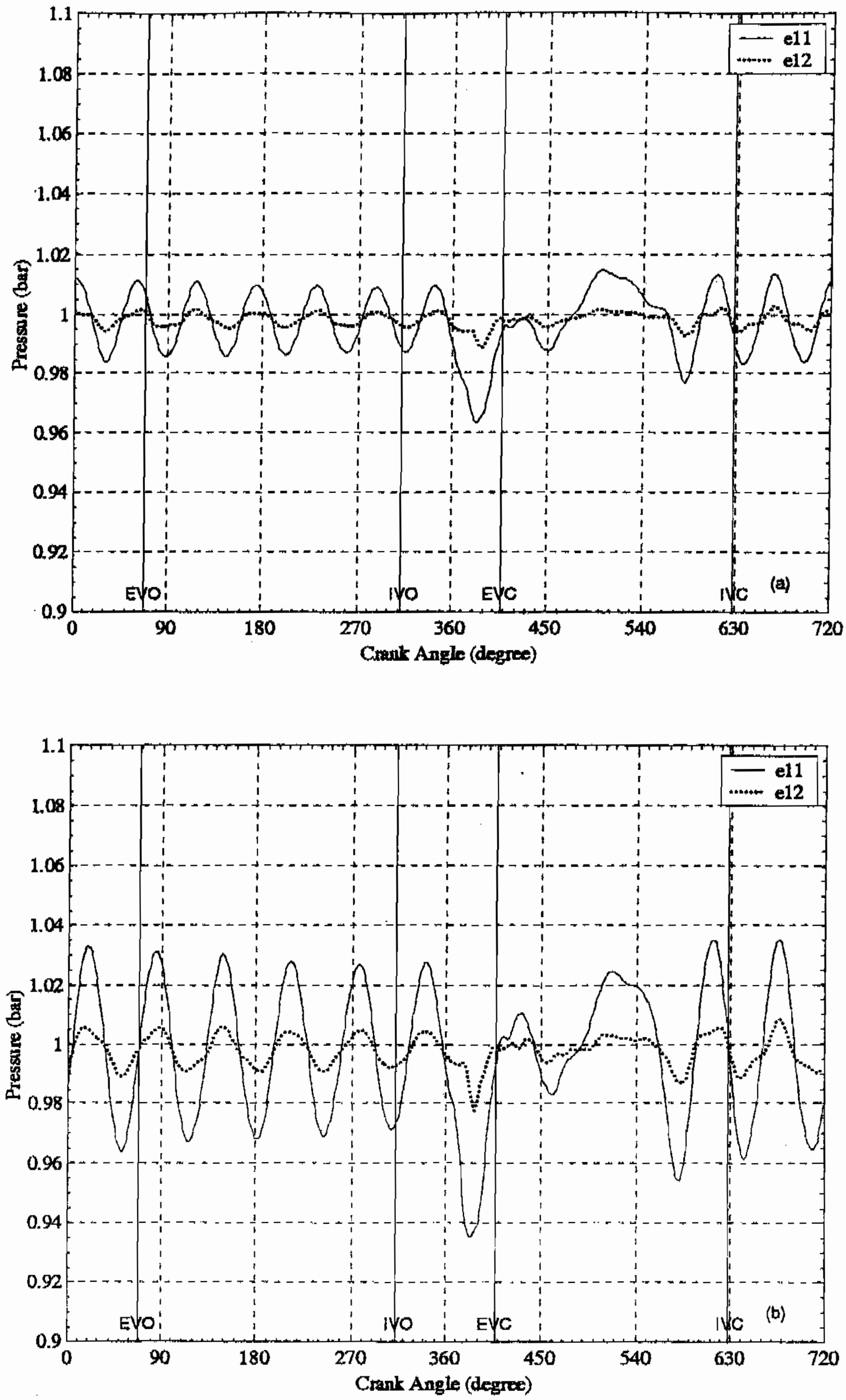

Figure A.68: OSU Dynamometer Experiment: Intake #8 – Pressure versus CAD for Intake Pressure Transducers at (a) 2000 rpm and (b) 2250 rpm

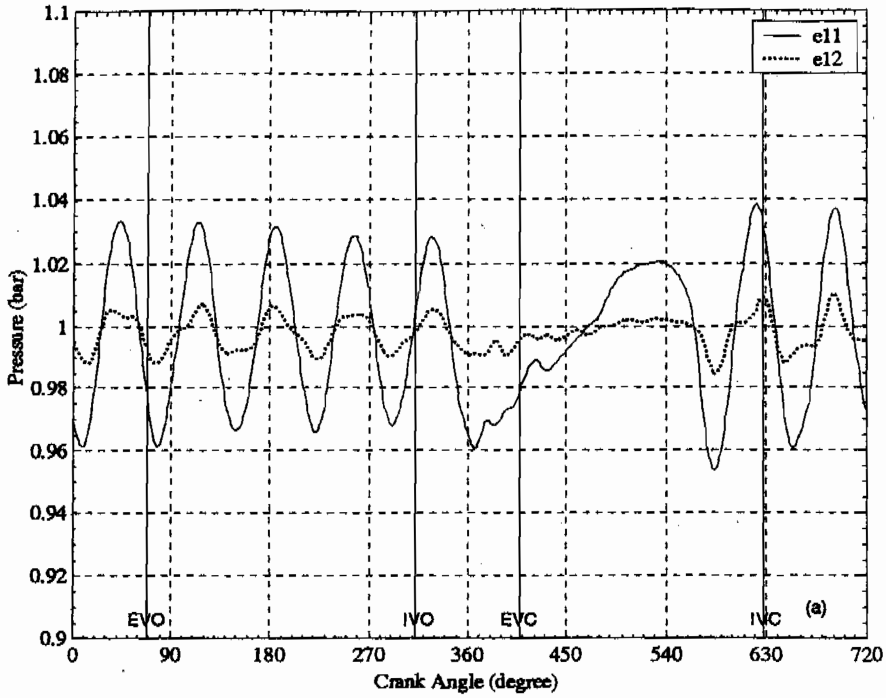

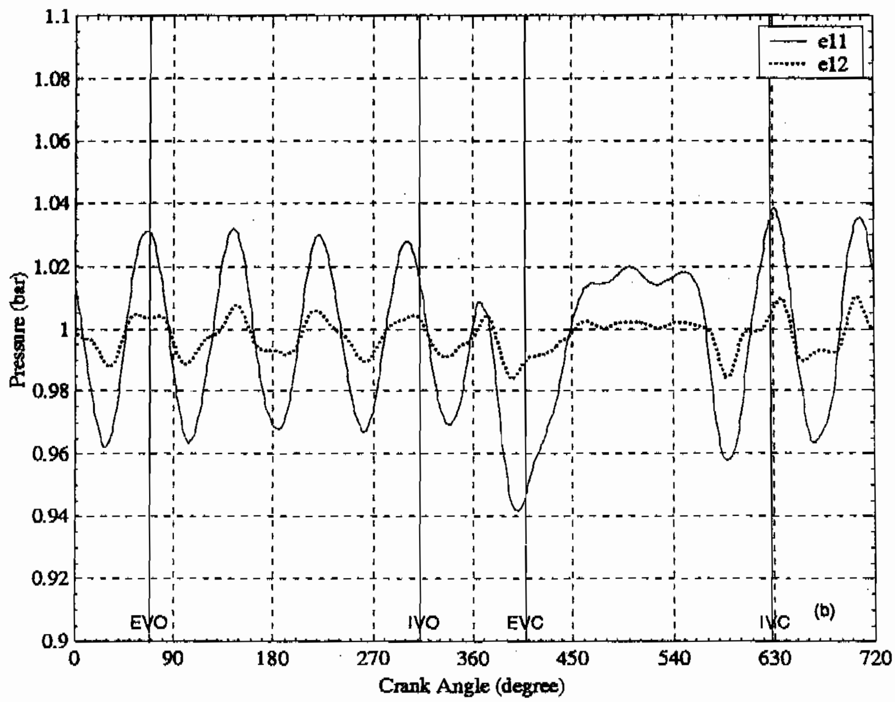

Figure A.69: OSU Dynamometer Experiment: Intake #8 – Pressure versus CAD for Intake Pressure Transducers at (a) 2500 rpm and (b) 2750 rpm

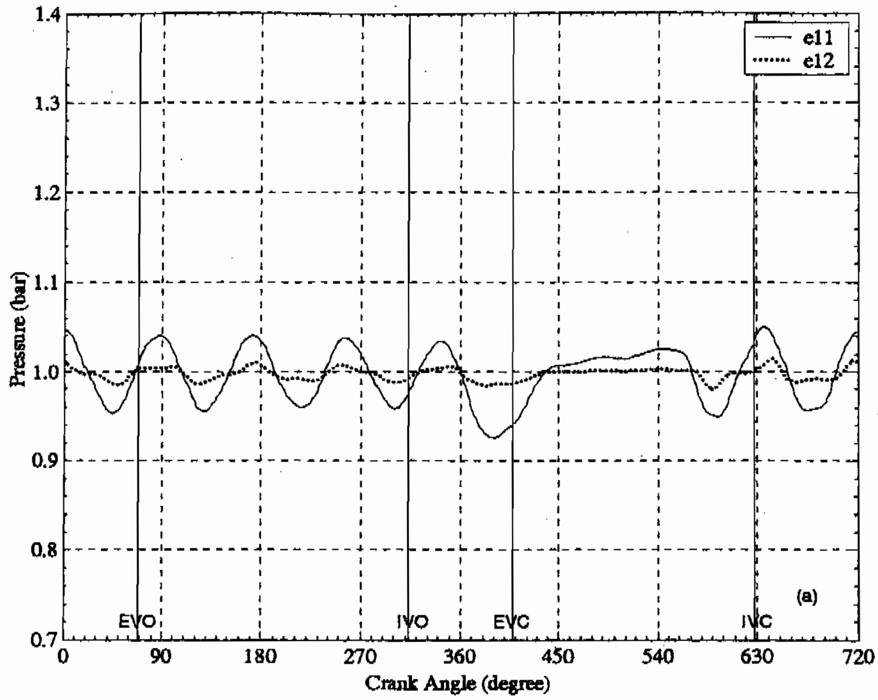

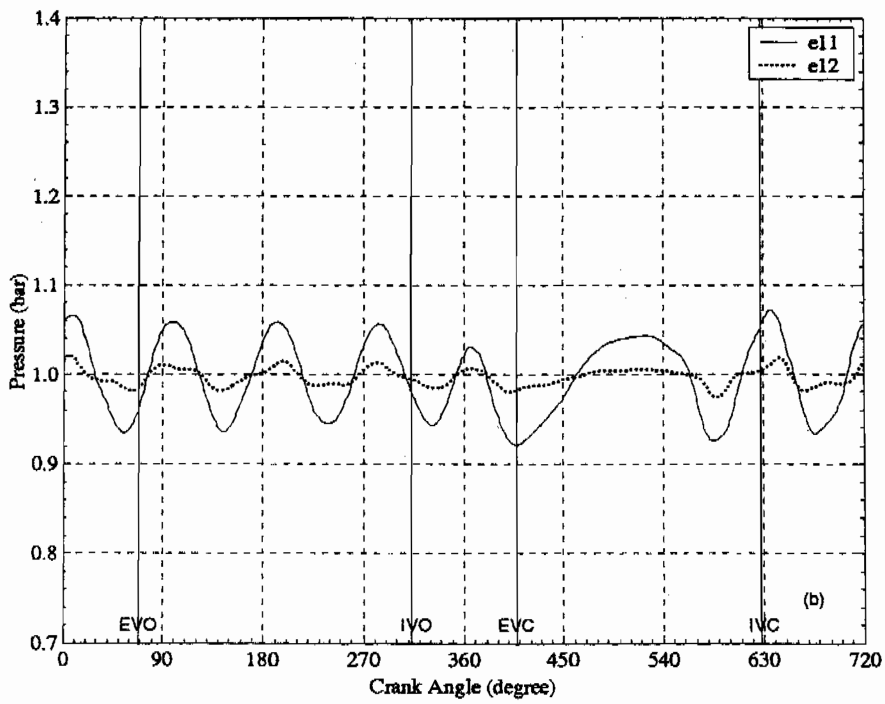

Figure A.70: OSU Dynamometer Experiment: Intake #8 – Pressure versus CAD for Intake Pressure Transducers at (a) 3000 rpm and (b) 3250 rpm

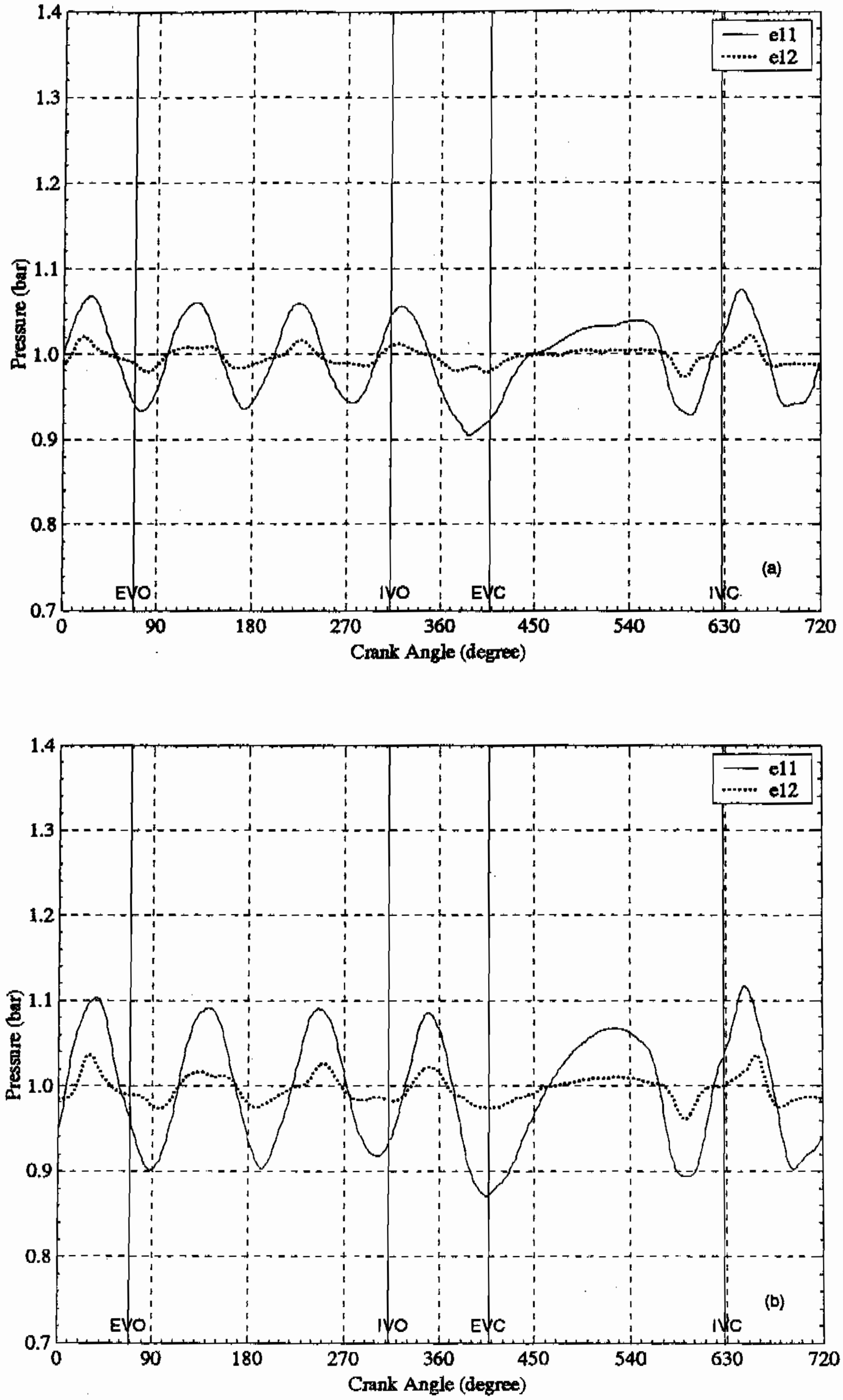

Figure A.71: OSU Dynamometer Experiment: Intake #8 – Pressure versus CAD for Intake Pressure Transducers at (a) 3500 rpm and (b) 3750 rpm

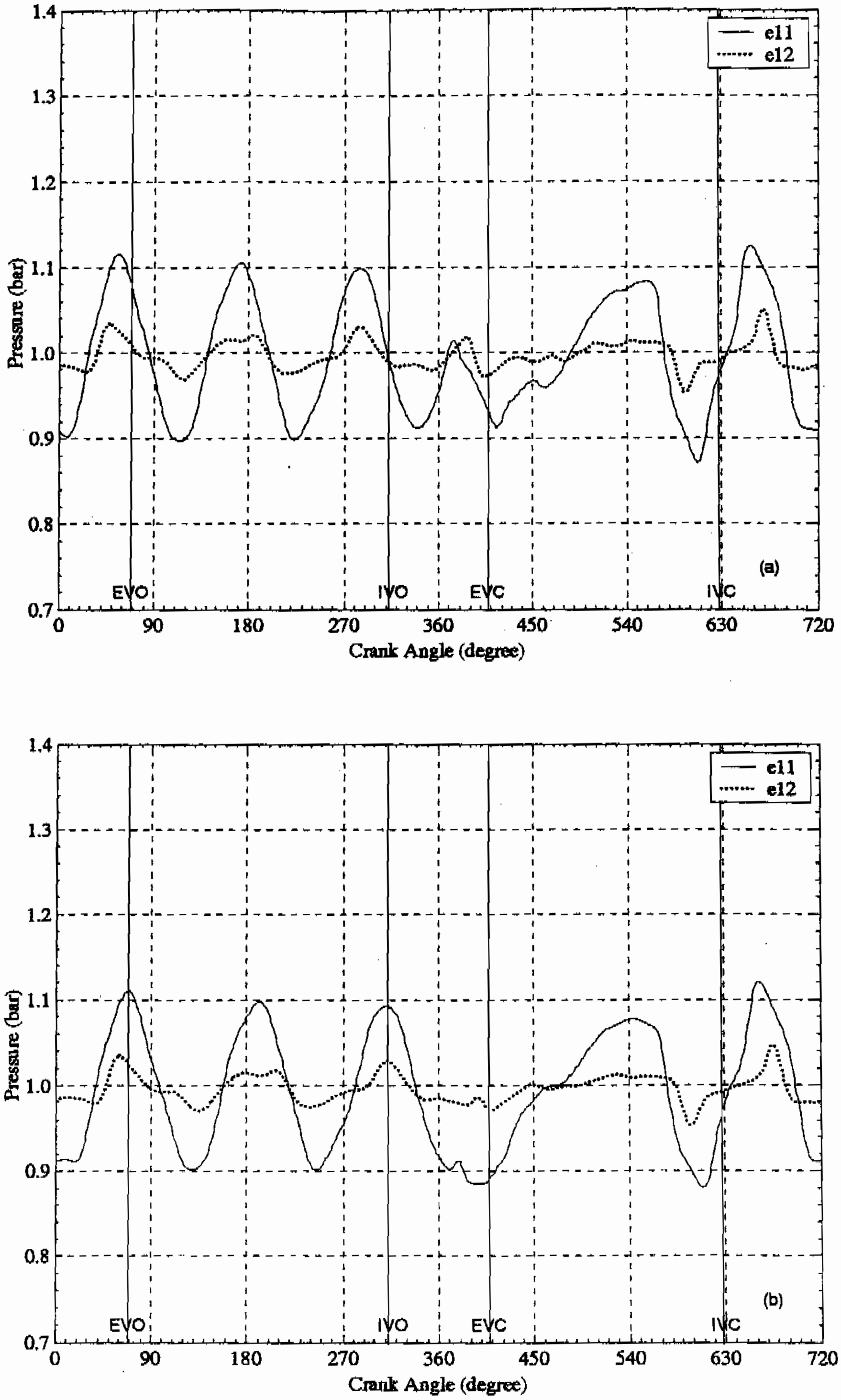

Figure A.72: OSU Dynamometer Experiment: Intake #8 – Pressure versus CAD for Intake Pressure Transducers at (a) 4000 rpm and (b) 4250 rpm

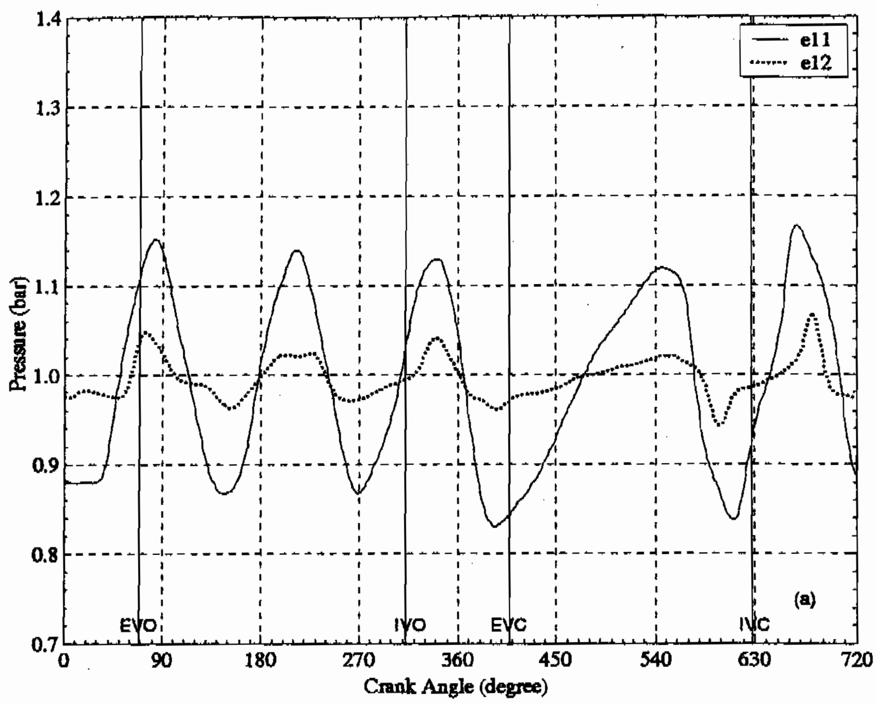

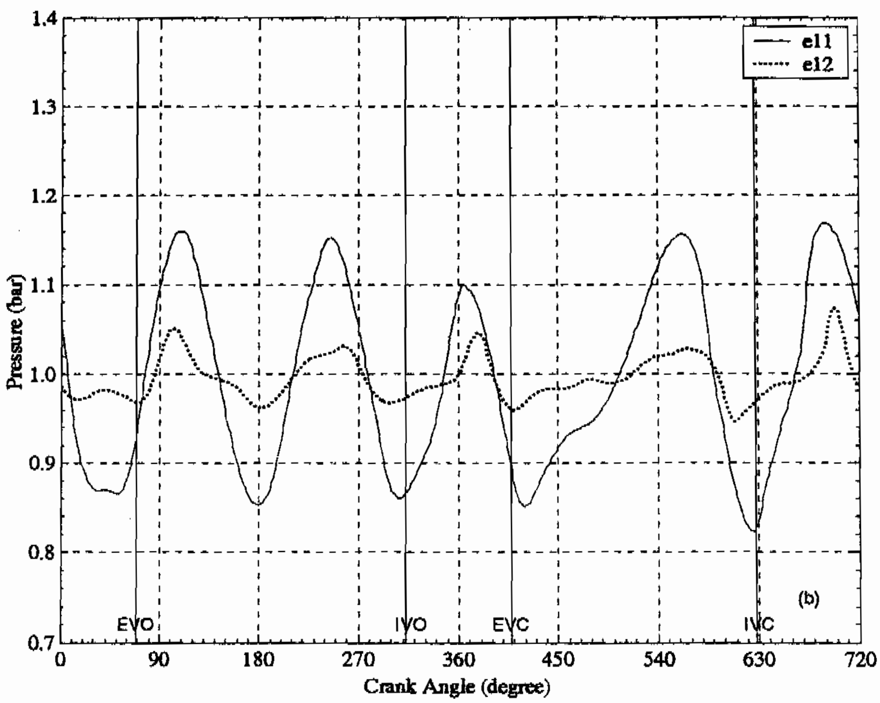

Figure A.73: OSU Dynamometer Experiment: Intake #8 – Pressure versus CAD for Intake Pressure Transducers at (a) 4500 rpm and (b) 4750 rpm

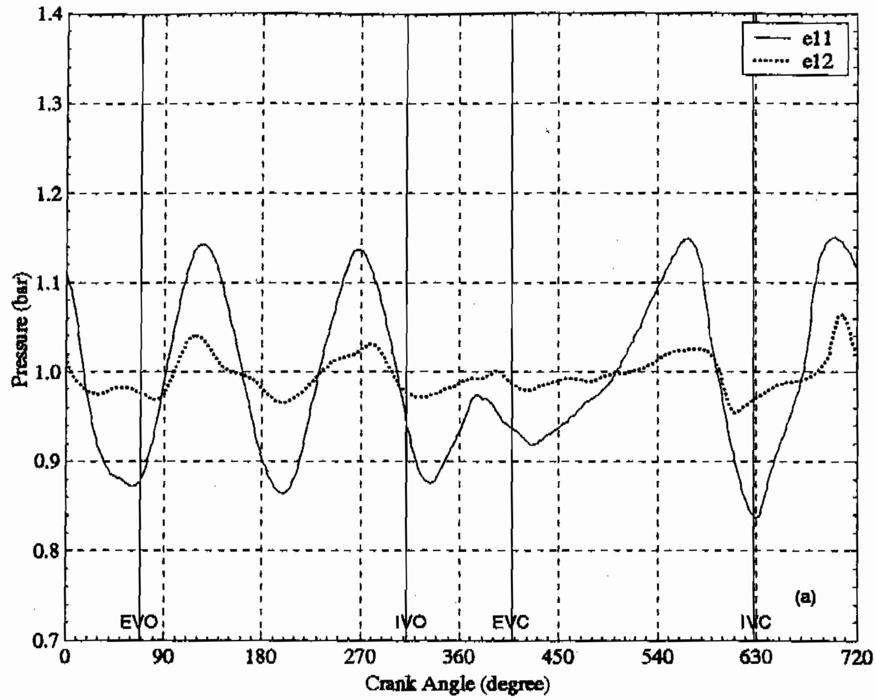

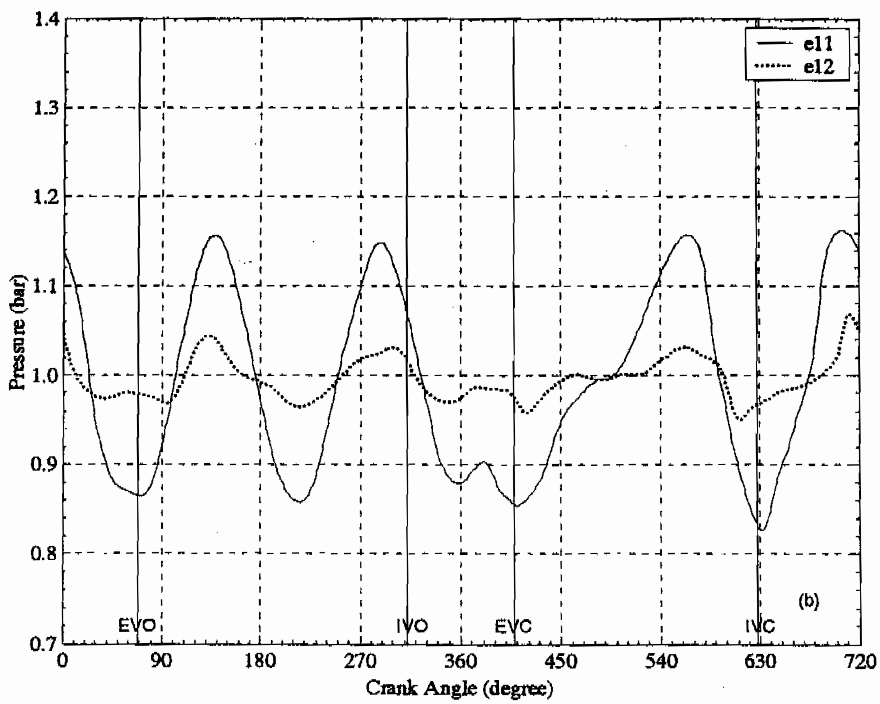

Figure A.74: OSU Dynamometer Experiment: Intake #8 – Pressure versus CAD for Intake Pressure Transducers at (a) 5000 rpm and (b) 5250 rpm

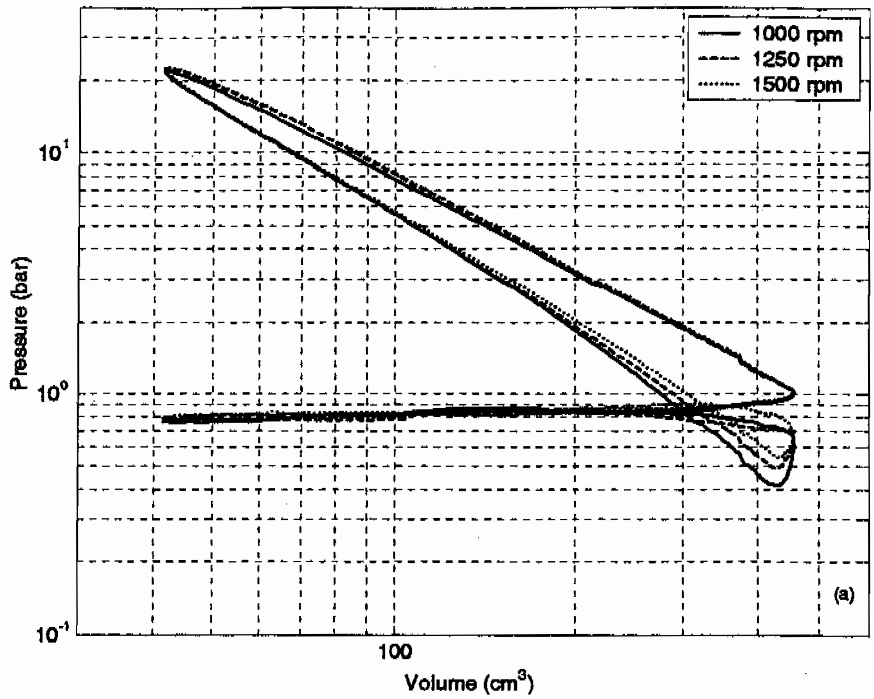

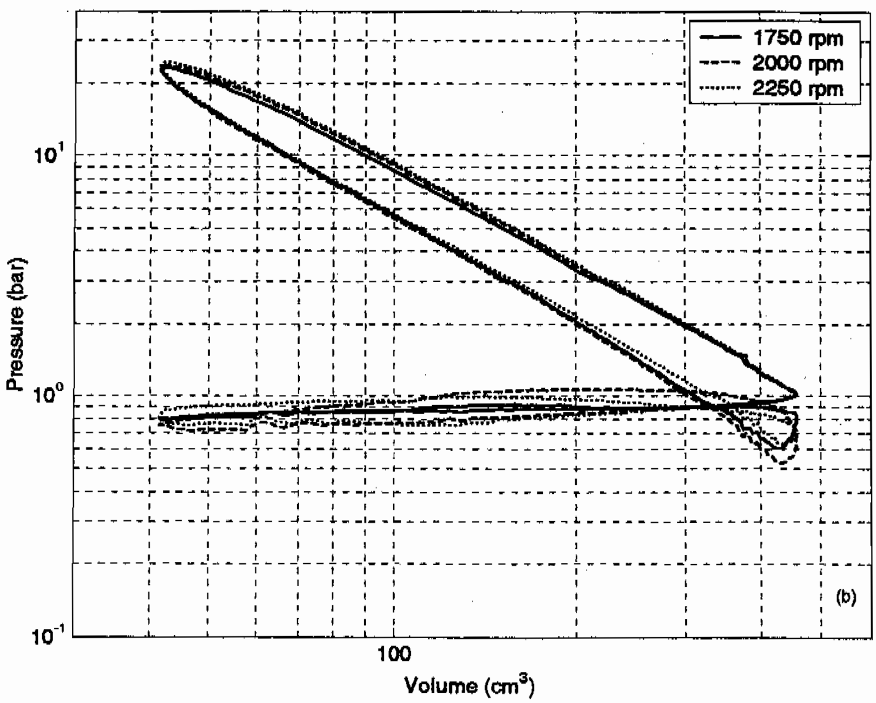

Figure A.75: OSU Dynamometer Experiment: Intake #1 – Pressure versus CAD for In-Cylinder Pressure Transducer at (a) 1000, 1250, and 1500 rpm and (b) 1750, 2000, and 2250 rpm

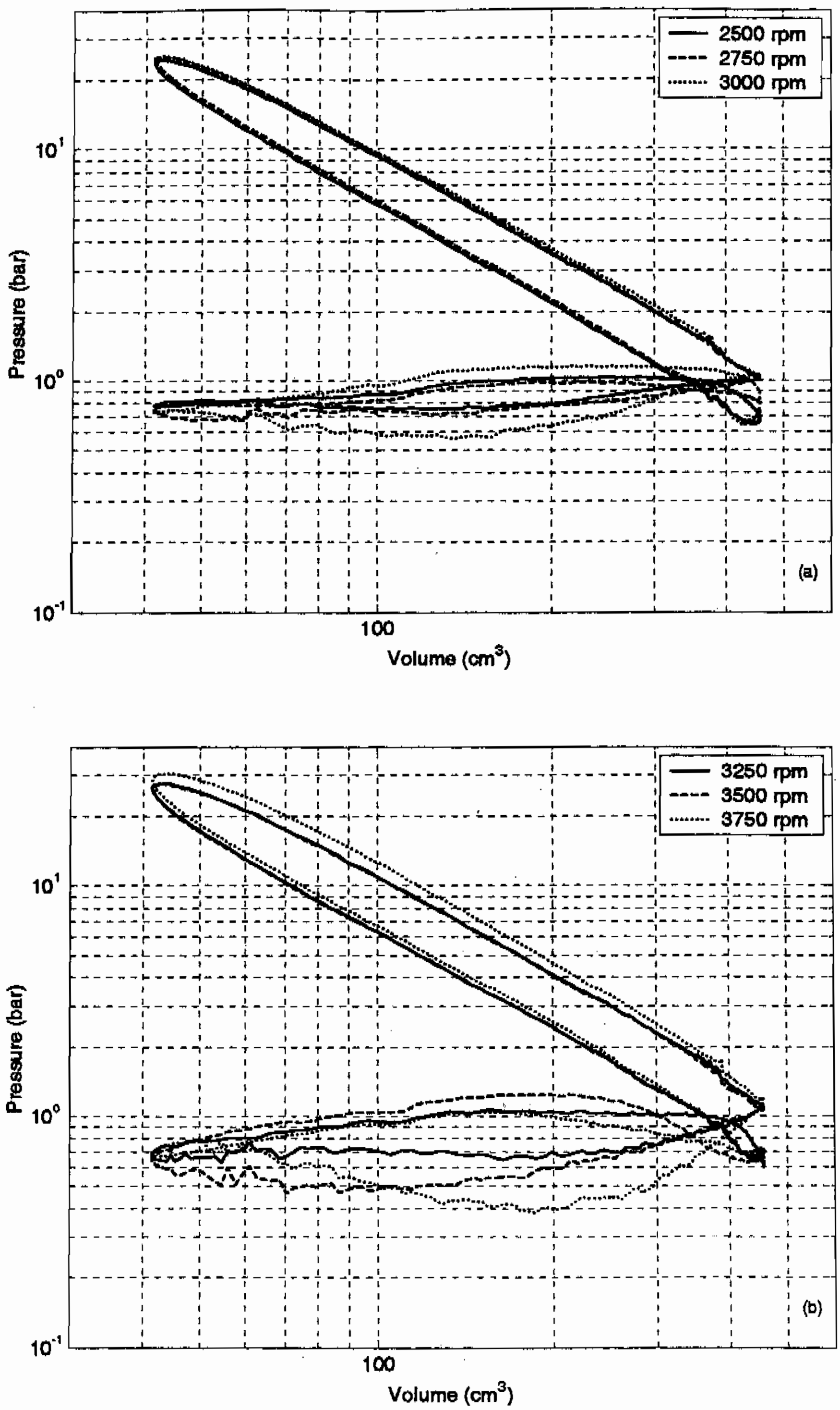

Figure A.76: OSU Dynamometer Experiment: Intake #1 – Pressure versus CAD for In-Cylinder Pressure Transducer at (a) 2500, 2750, and 3000 rpm and (b) 3250, 3500, and 3750 rpm

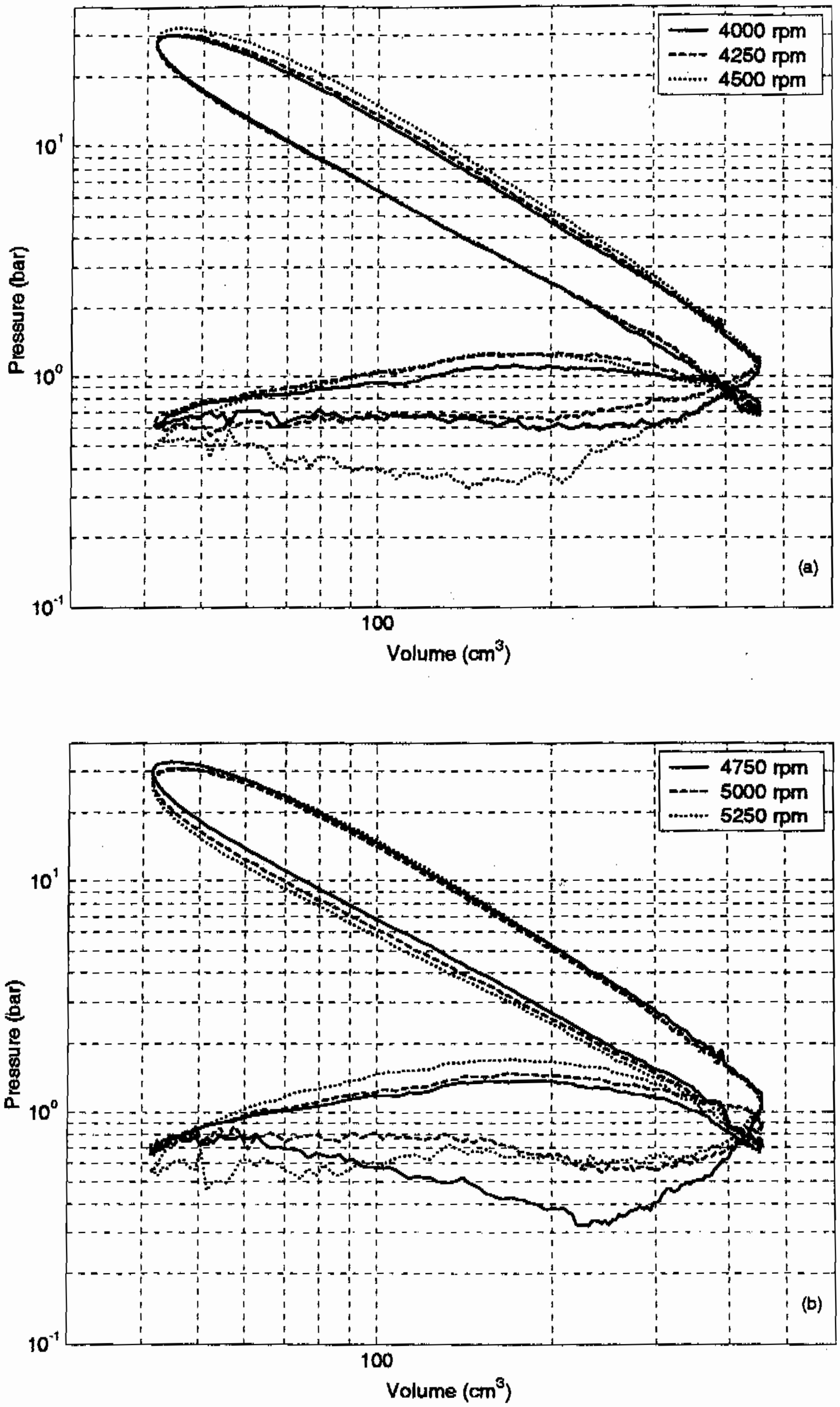

Figure A.77: OSU Dynamometer Experiment: Intake #1 – Pressure versus CAD for In-Cylinder Pressure Transducer at (a) 4000, 4250, and 4500 rpm and (b) 4750, 5000, and 5250 rpm

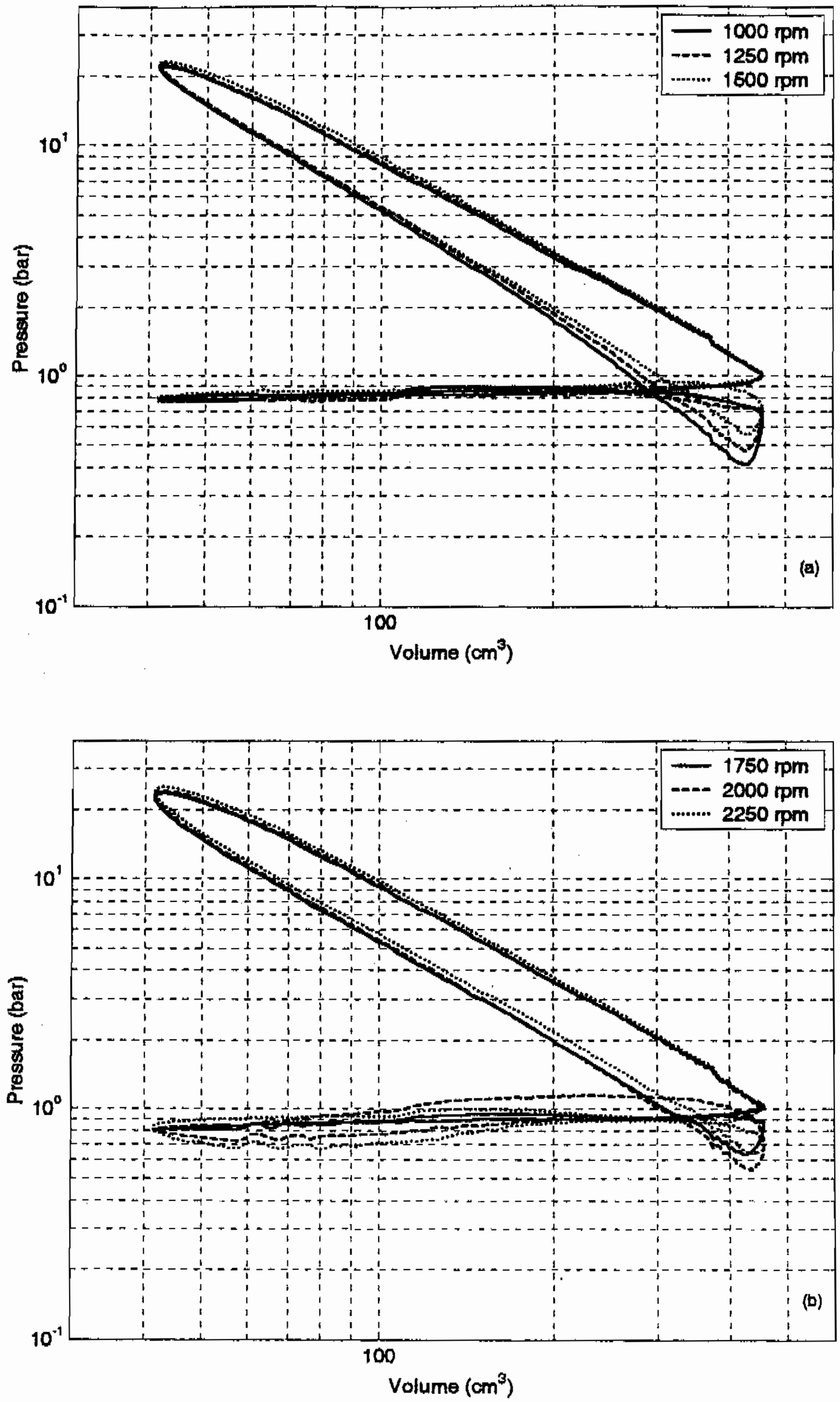

Figure A.78: OSU Dynamometer Experiment: Intake #2 – Pressure versus CAD for In-Cylinder Pressure Transducer at (a) 1000, 1250, and 1500 rpm and (b) 1750, 2000, and 2250 rpm

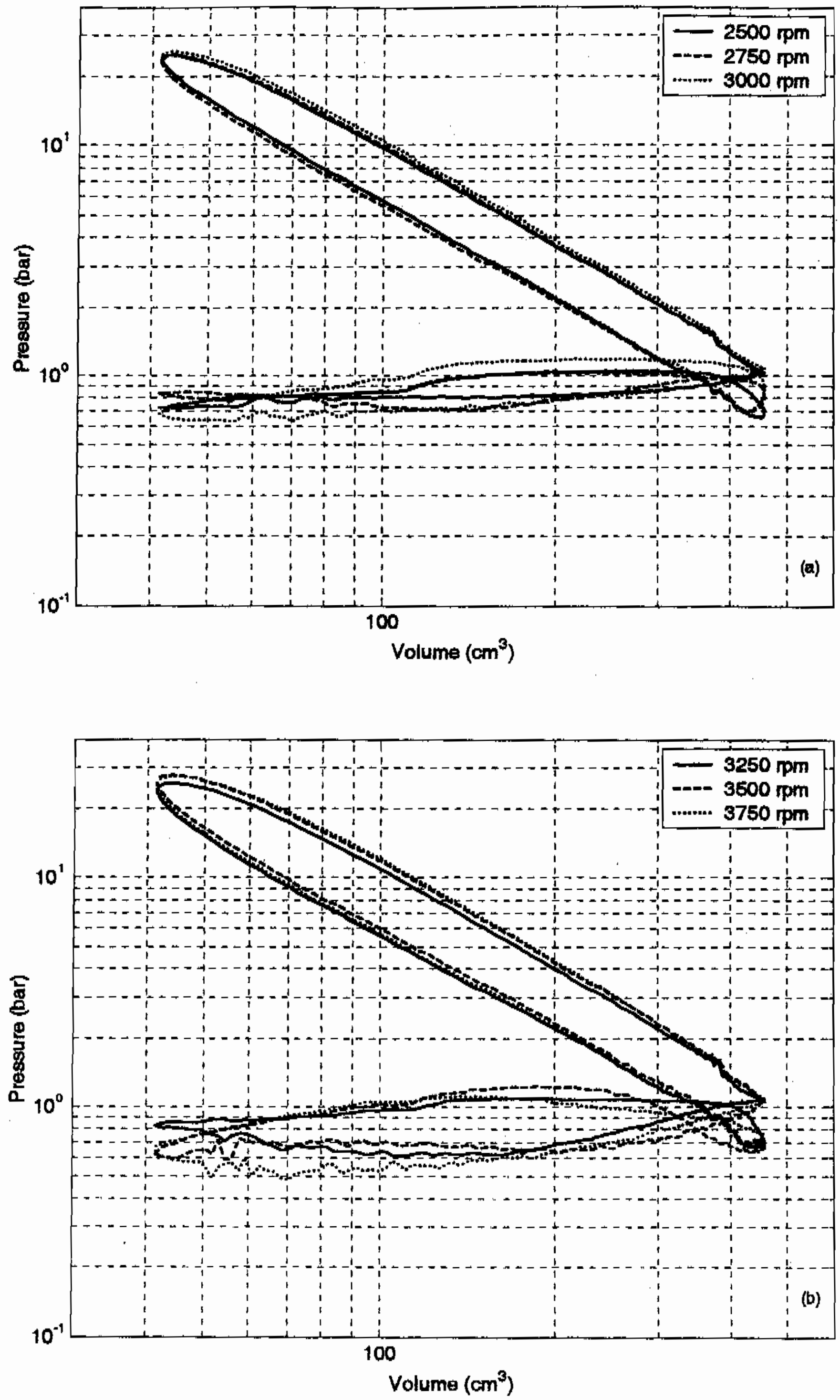

Figure A.79: OSU Dynamometer Experiment: Intake #2 – Pressure versus CAD for In-Cylinder Pressure Transducer at (a) 2500, 2750, and 3000 rpm and (b) 3250, 3500, and 3750 rpm

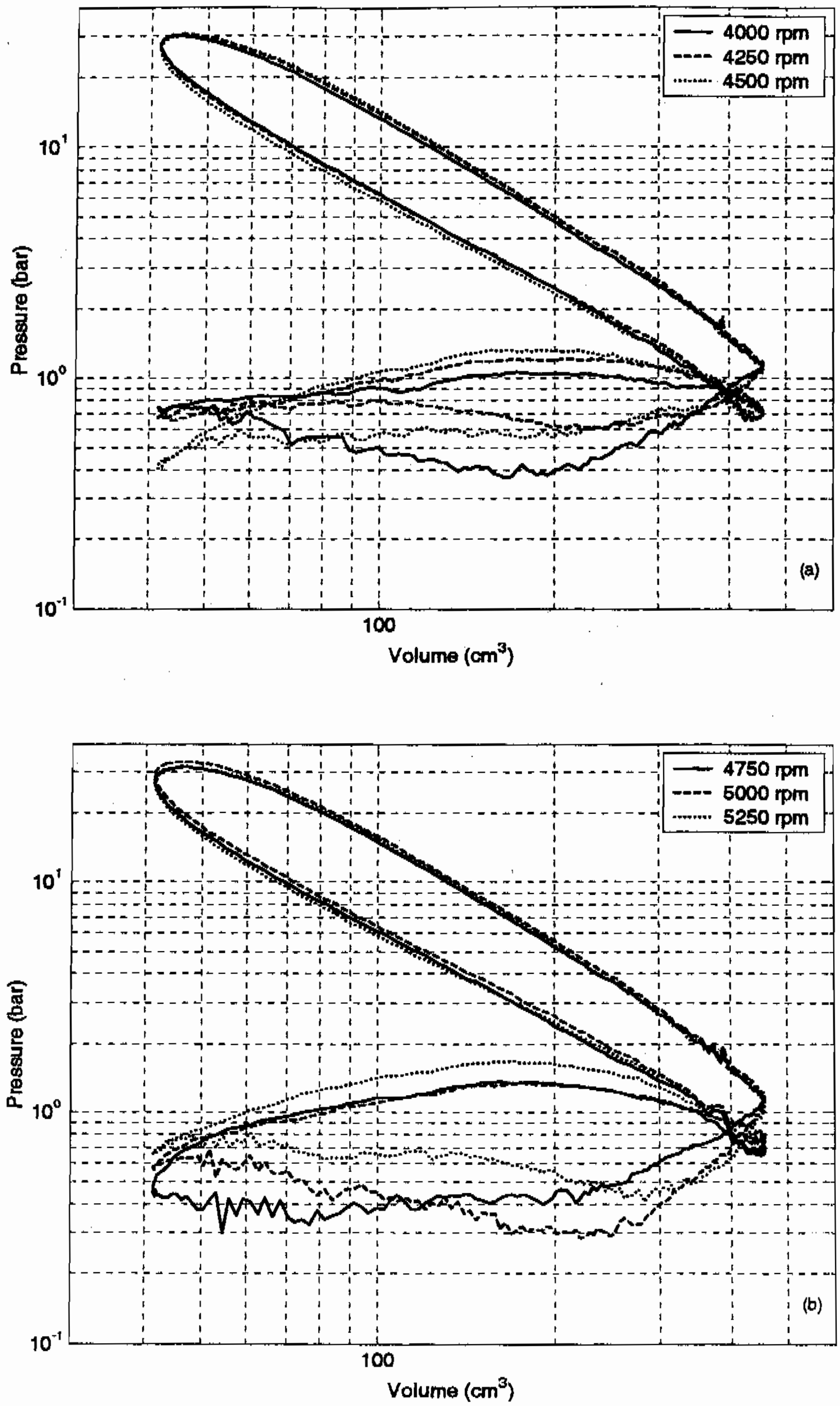

Figure A.80: OSU Dynamometer Experiment: Intake #2 – Pressure versus CAD for In-Cylinder Pressure Transducer at (a) 4000, 4250, and 4500 rpm and (b) 4750, 5000, and 5250 rpm

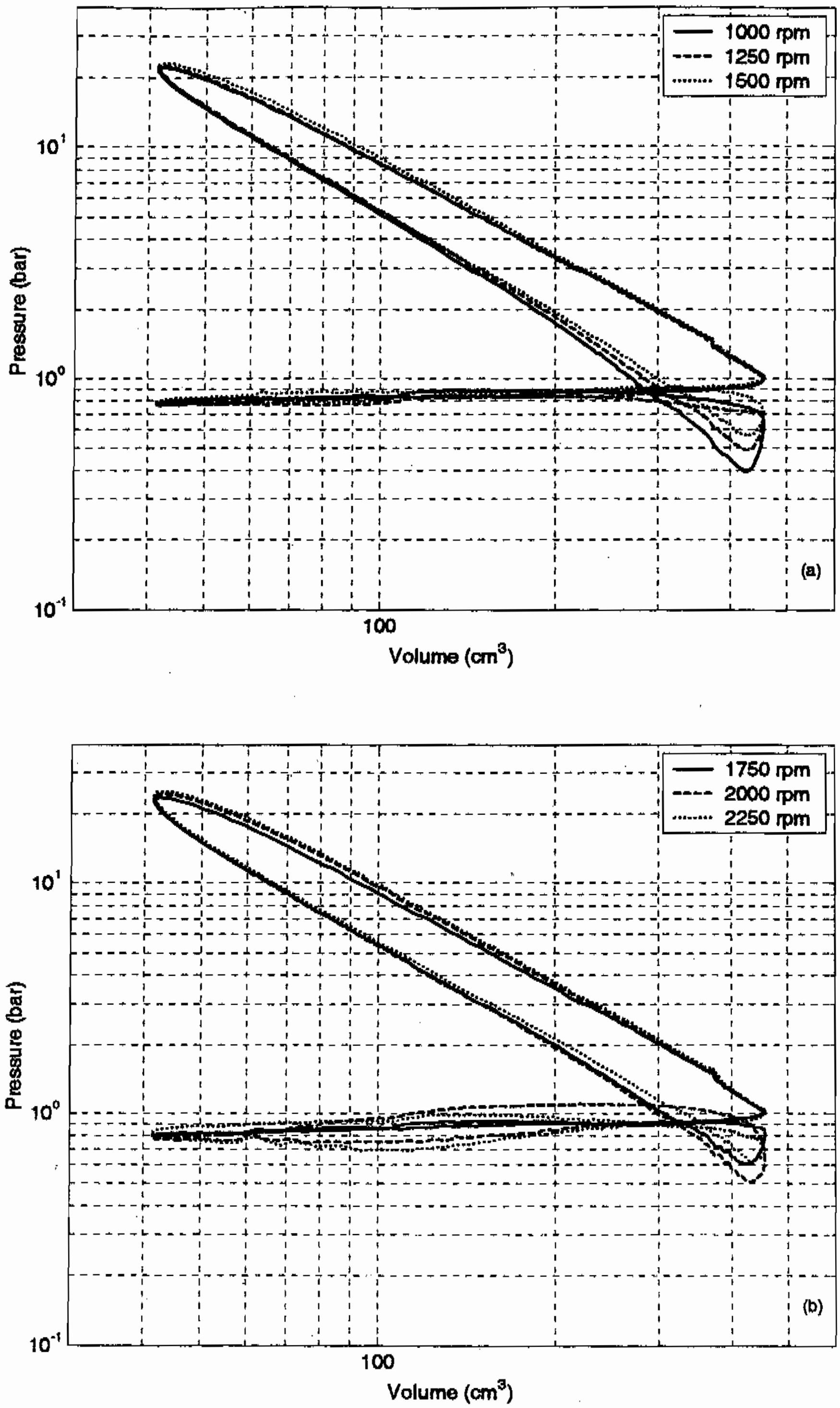

Figure A.81: OSU Dynamometer Experiment: Intake #3 – Pressure versus CAD for In-Cylinder Pressure Transducer at (a) 1000, 1250, and 1500 rpm and (b) 1750, 2000, and 2250 rpm

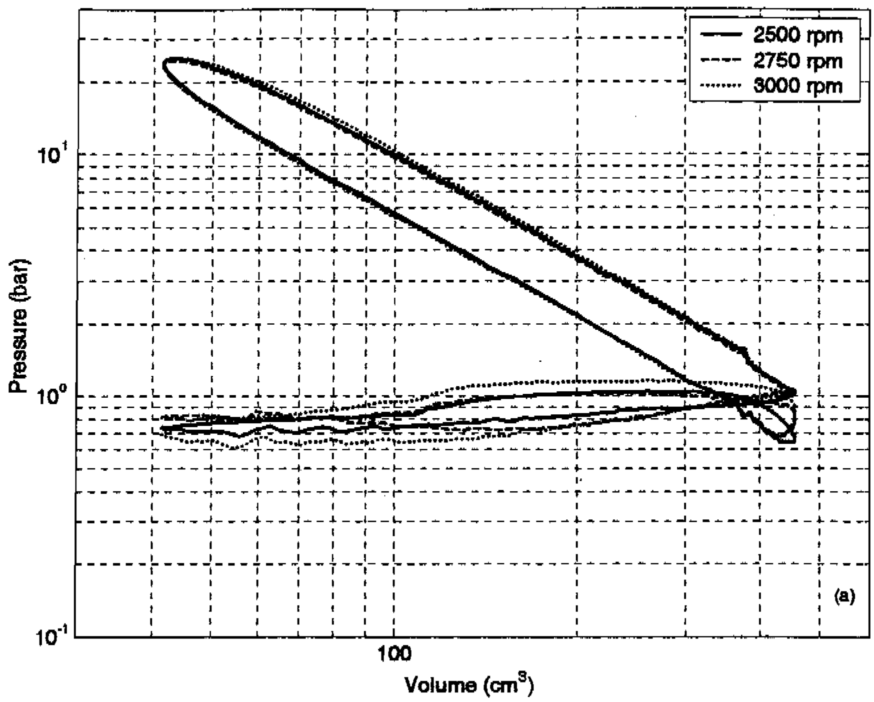

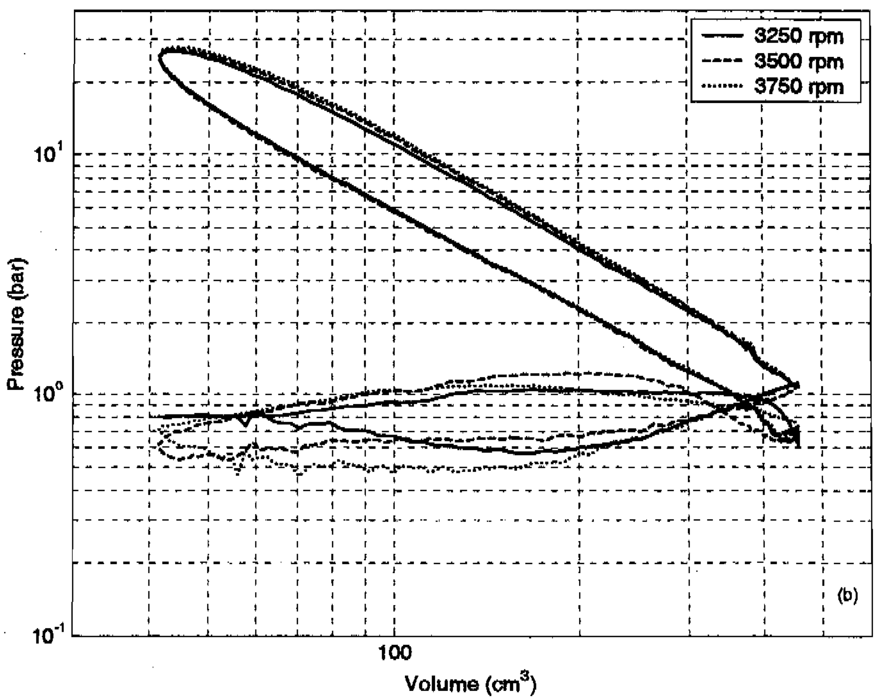

Figure A.82: OSU Dynamometer Experiment: Intake #3 – Pressure versus CAD for In-Cylinder Pressure Transducer at (a) 2500, 2750, and 3000 rpm and (b) 3250, 3500, and 3750 rpm

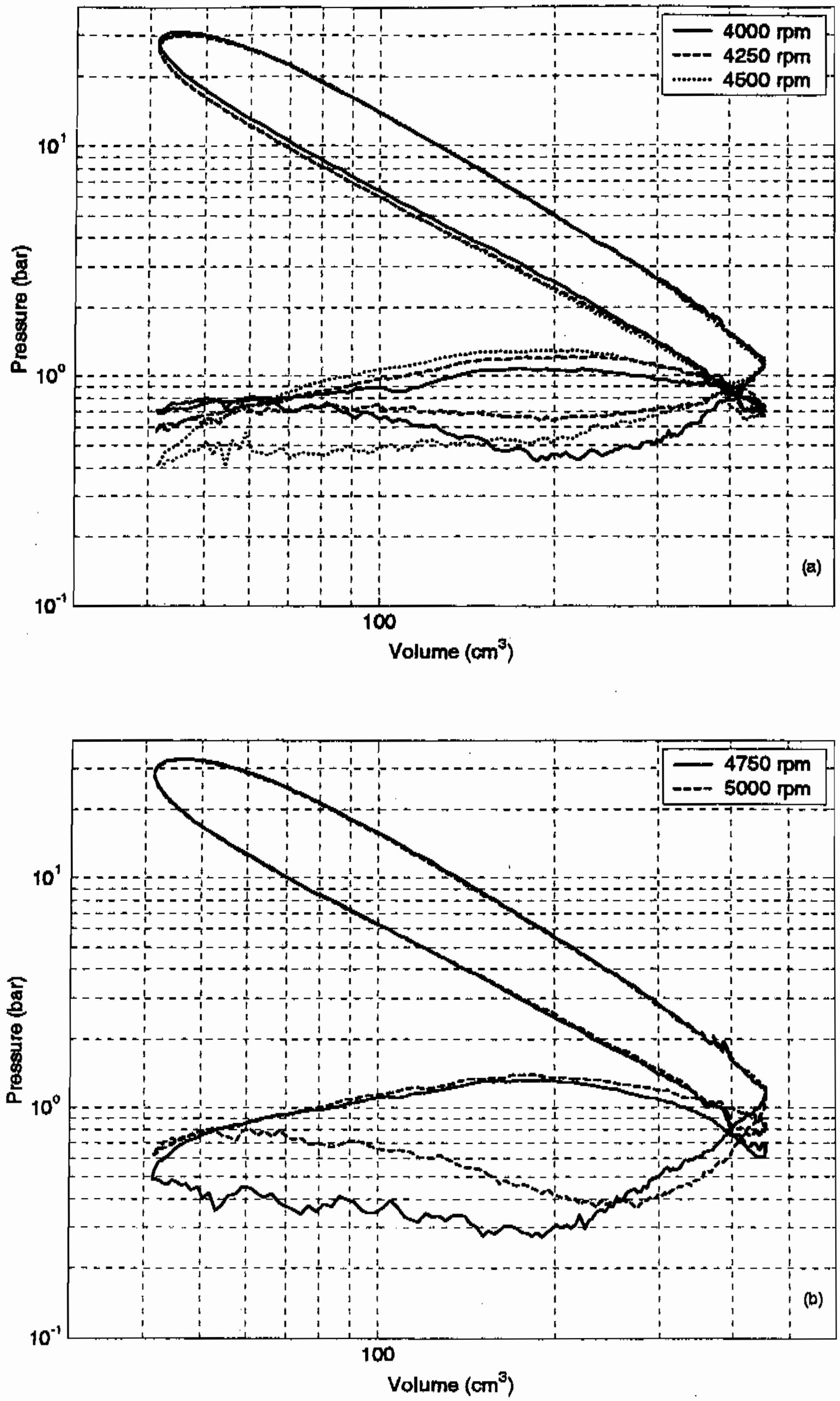

Figure A.83: OSU Dynamometer Experiment: Intake #3 – Pressure versus CAD for In-Cylinder Pressure Transducer at (a) 4000, 4250, and 4500 rpm and (b) 4750 and 5000

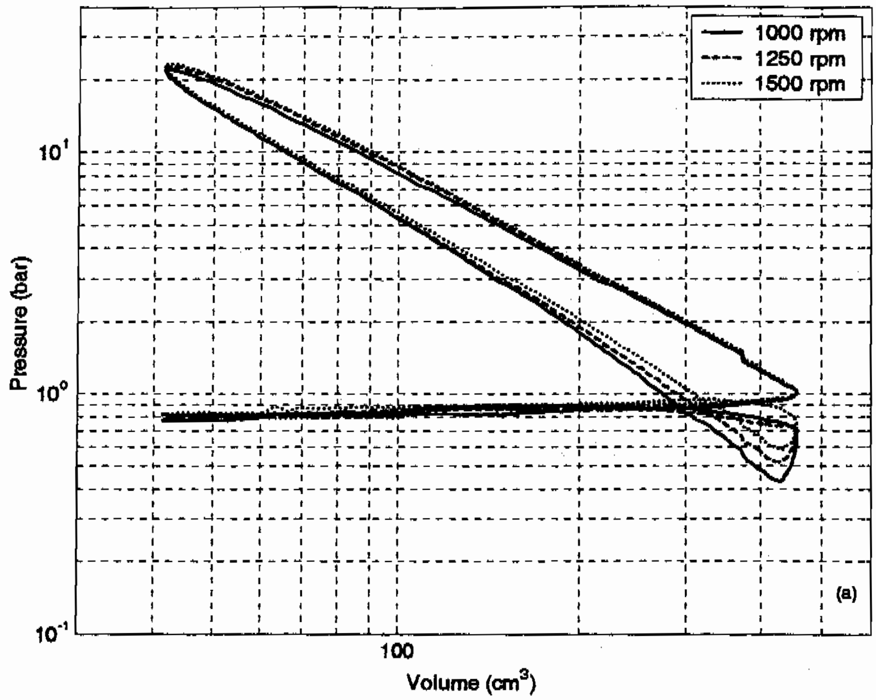

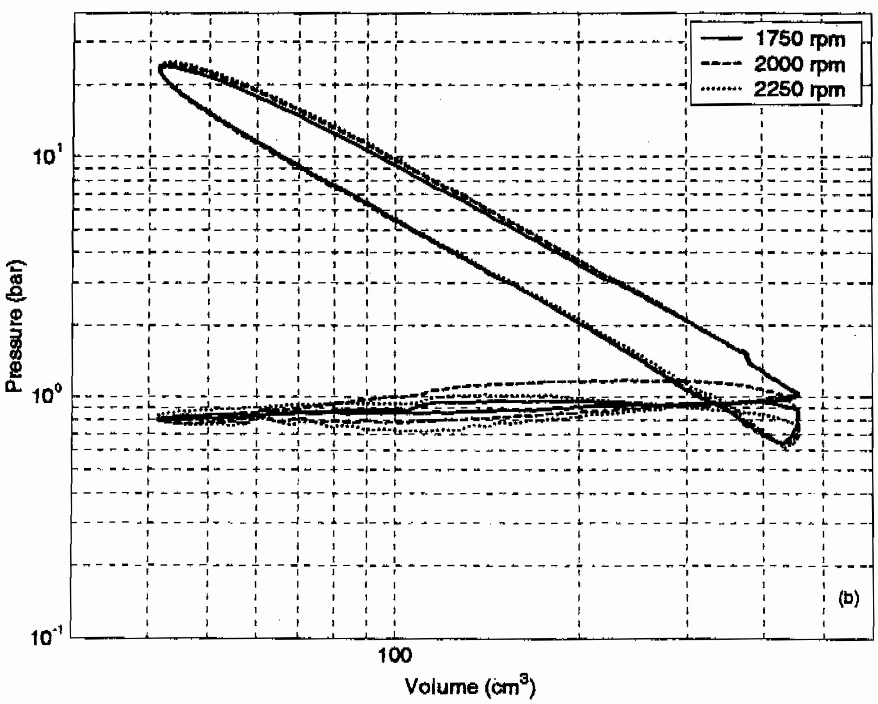

Figure A.84: OSU Dynamometer Experiment: Intake #4 – Pressure versus CAD for In-Cylinder Pressure Transducer at (a) 1000, 1250, and 1500 rpm and (b) 1750, 2000, and 2250 rpm

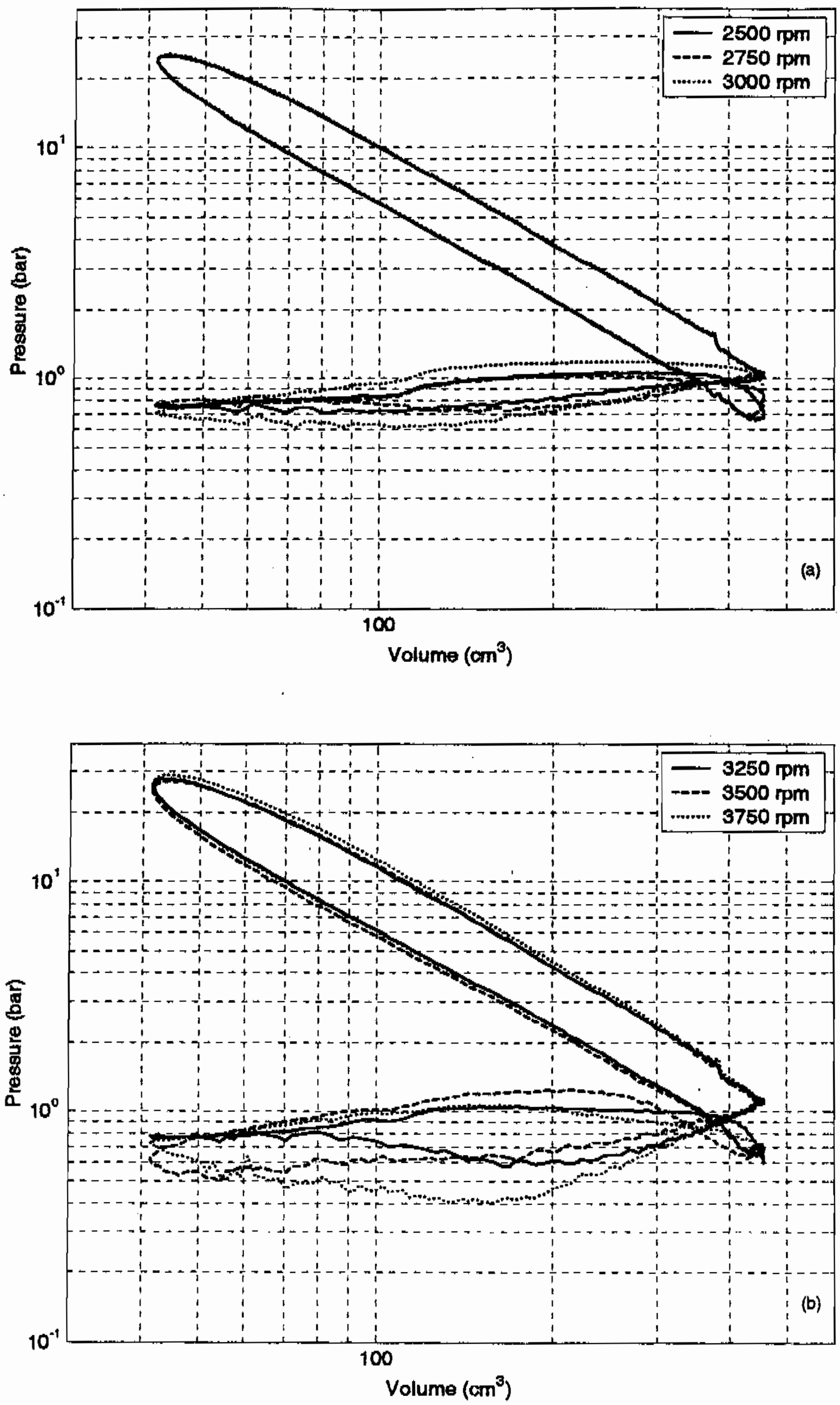

Figure A.85: OSU Dynamometer Experiment: Intake #4 – Pressure versus CAD for In-Cylinder Pressure Transducer at (a) 2500, 2750, and 3000 rpm and (b) 3250, 3500, and 3750 rpm

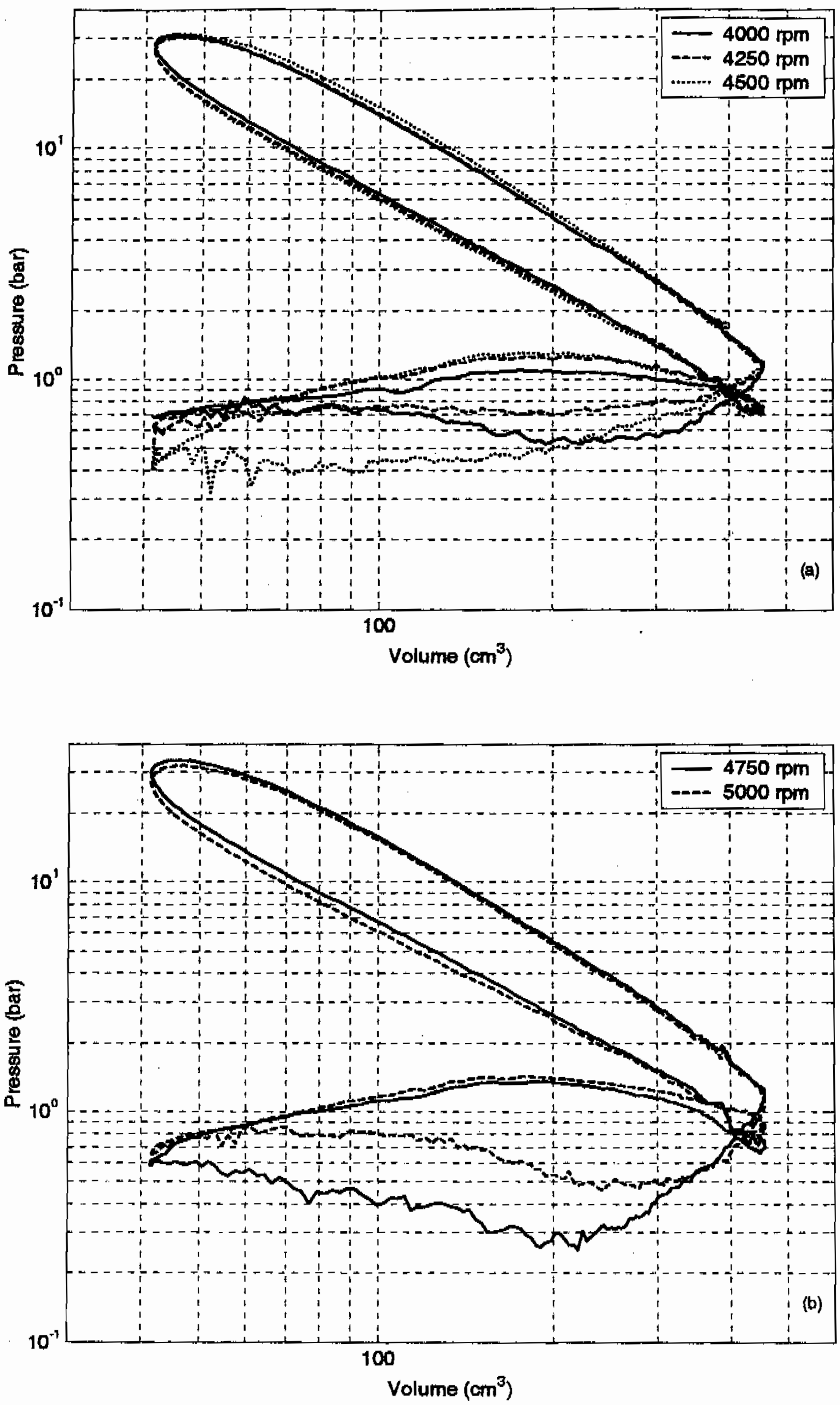

Figure A.86: OSU Dynamometer Experiment: Intake #4 – Pressure versus CAD for In-Cylinder Pressure Transducer at (a) 4000, 4250, and 4500 rpm and (b) 4750 and 5000 rpm

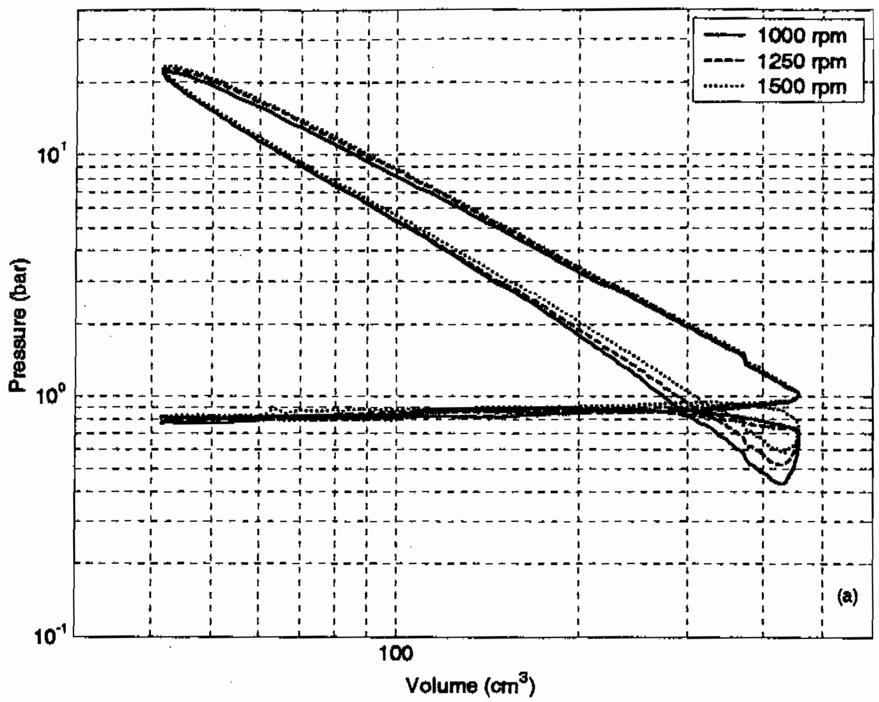

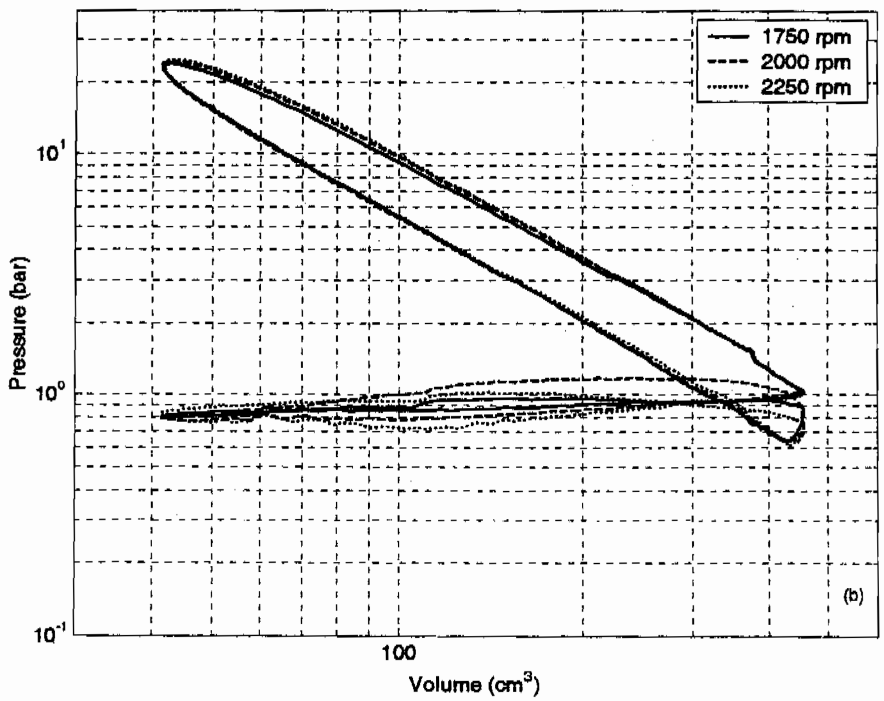

Figure A.87: OSU Dynamometer Experiment: Intake #5 – Pressure versus CAD for In-Cylinder Pressure Transducer at (a) 1000, 1250, and 1500 rpm and (b) 1750, 2000, and 2250 rpm

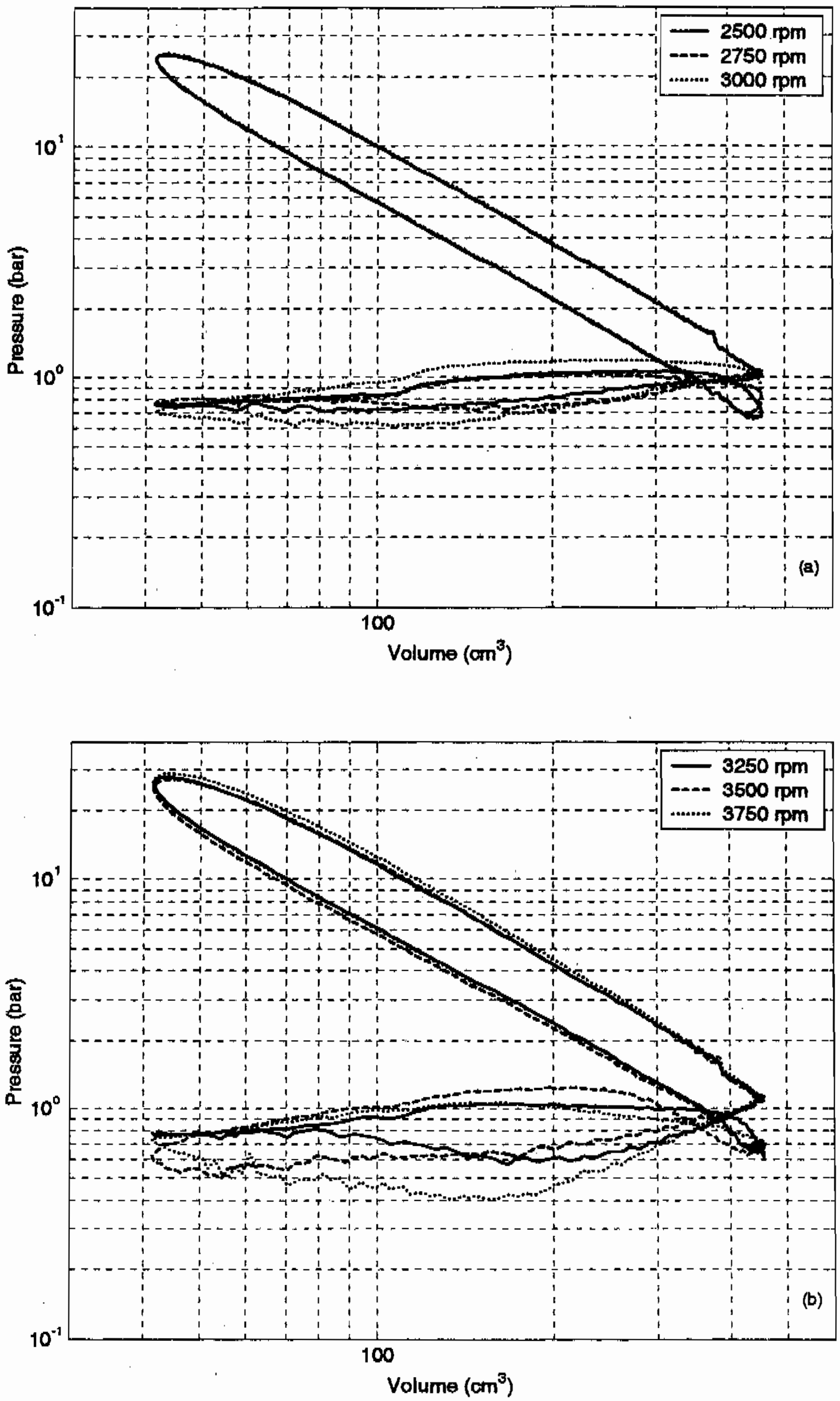

Figure A.88: OSU Dynamometer Experiment: Intake #5 – Pressure versus CAD for In-Cylinder Pressure Transducer at (a) 2500, 2750, and 3000 rpm and (b) 3250, 3500, and 3750 rpm

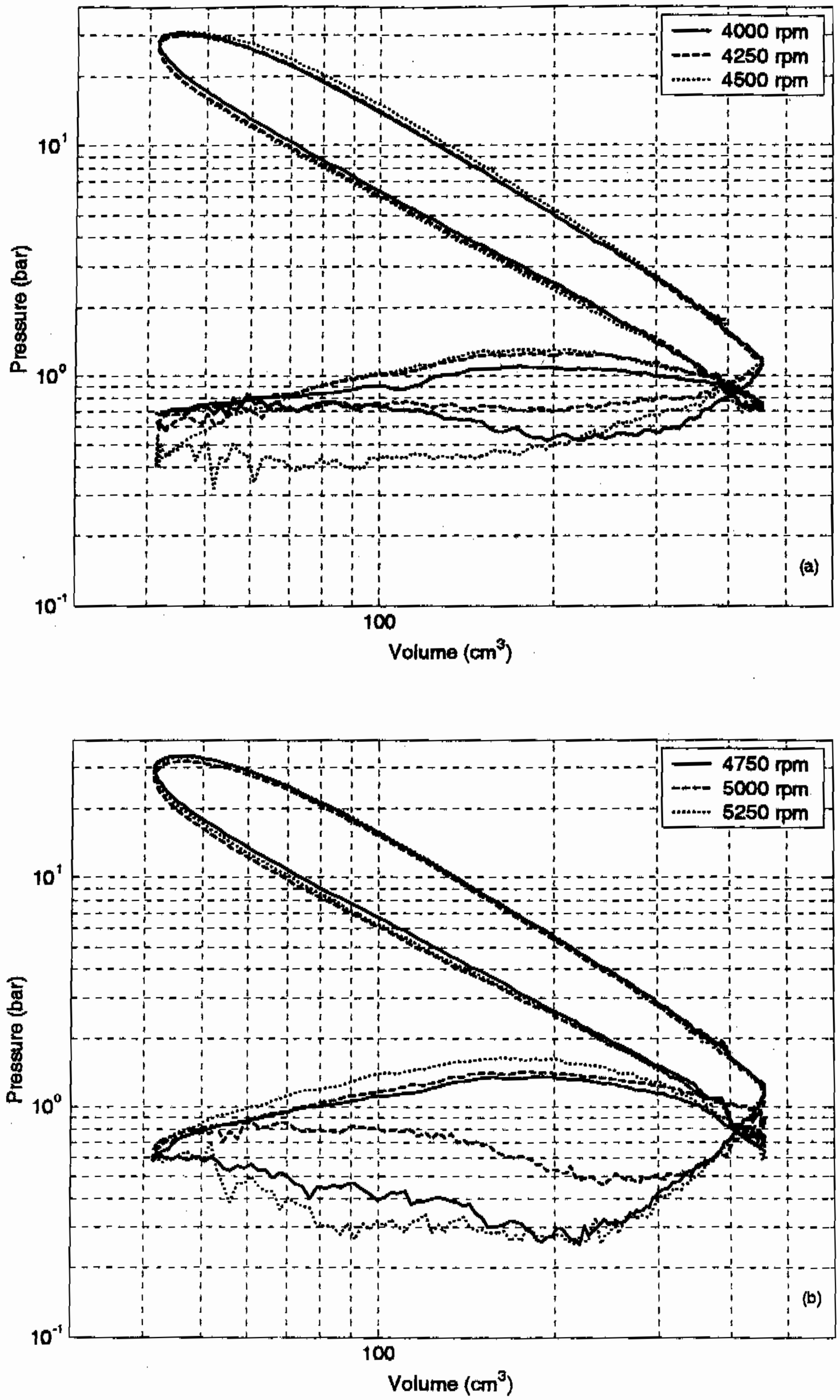

Figure A.89: OSU Dynamometer Experiment: Intake #5 – Pressure versus CAD for In-Cylinder Pressure Transducer at (a) 4000, 4250, and 4500 rpm and (b) 4750, 5000, and 5250 rpm

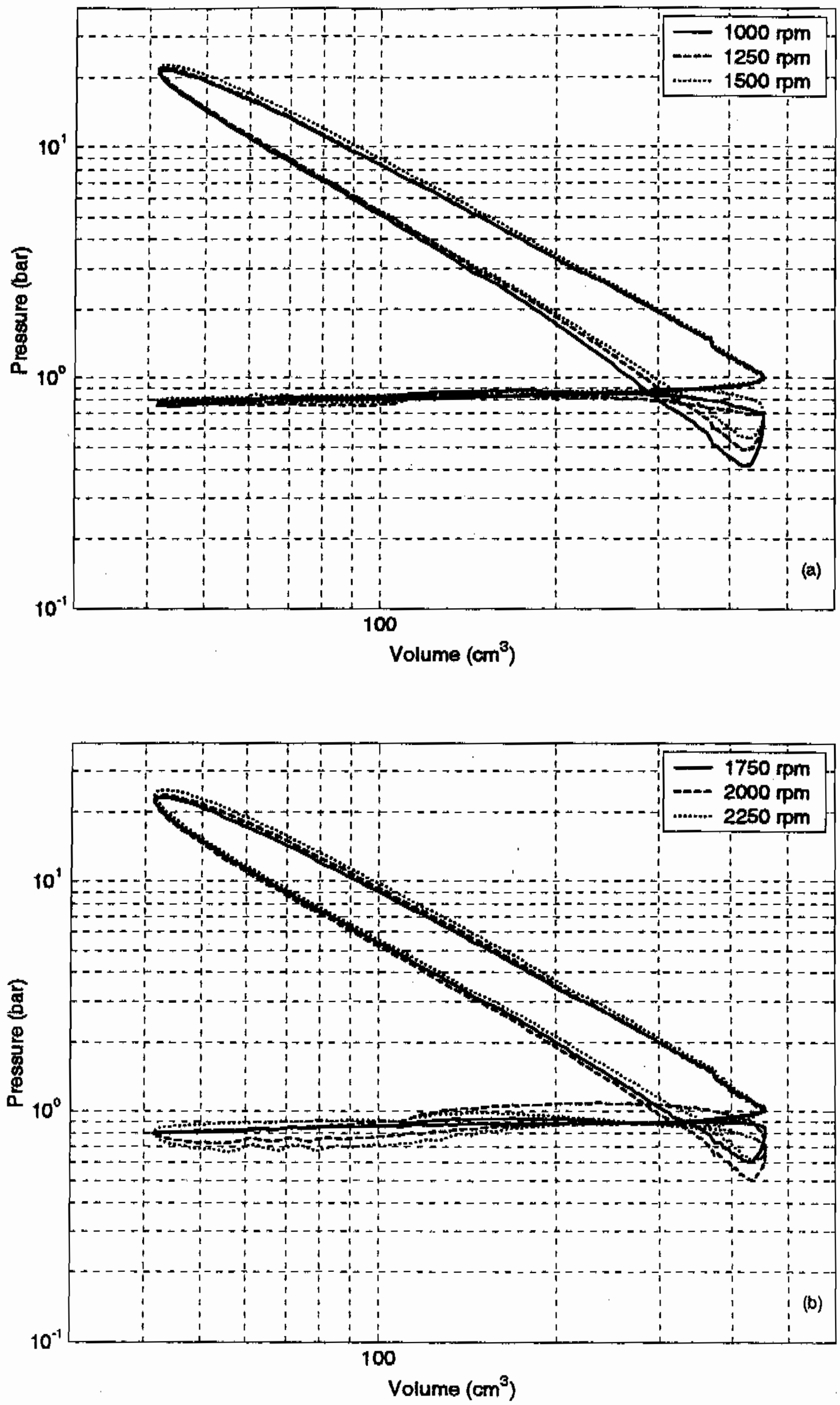

Figure A.90: OSU Dynamometer Experiment: Intake #6 – Pressure versus CAD for In-Cylinder Pressure Transducer at (a) 1000, 1250, and 1500 rpm and (b) 1750, 2000, and 2250 rpm

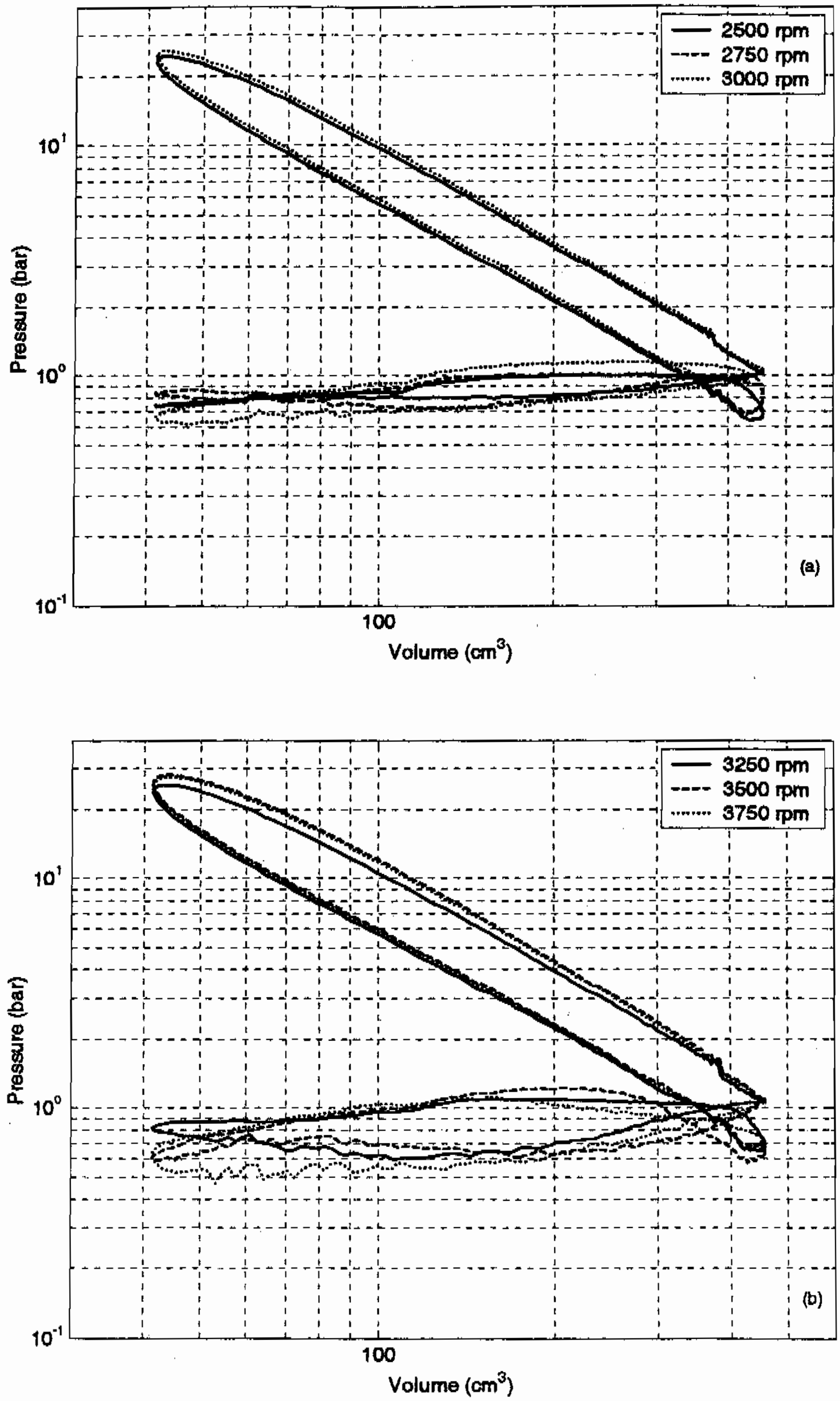

Figure A.76: OSU Dynamometer Experiment: Intake #6 – Pressure versus CAD for In-Cylinder Pressure Transducer at (a) 2500, 2750, and 3000 rpm and (b) 3250, 3500, and 3750 rpm

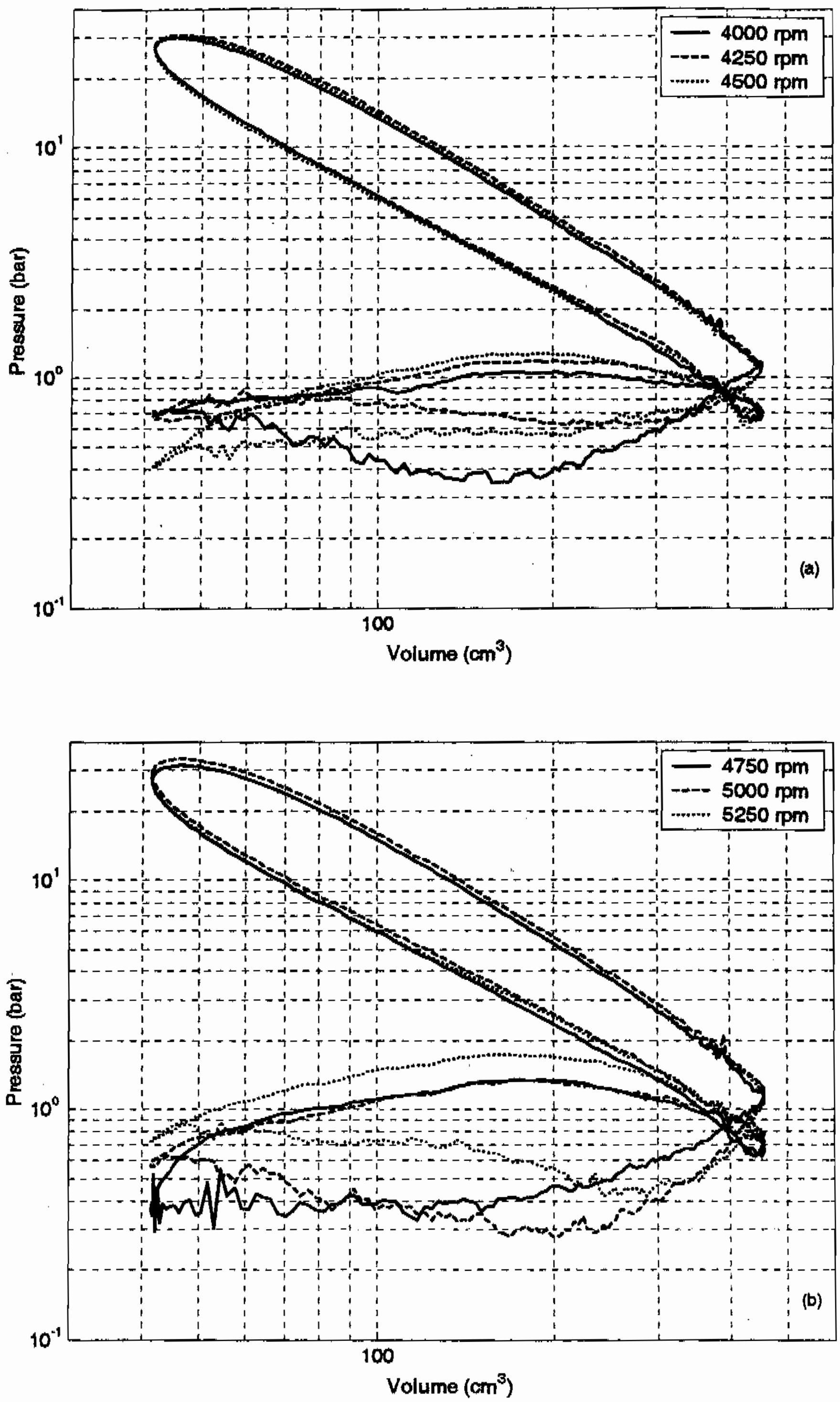

Figure A.92: OSU Dynamometer Experiment: Intake #6 – Pressure versus CAD for In-Cylinder Pressure Transducer at (a) 4000, 4250, and 4500 rpm and (b) 4750, 5000, and 5250 rpm

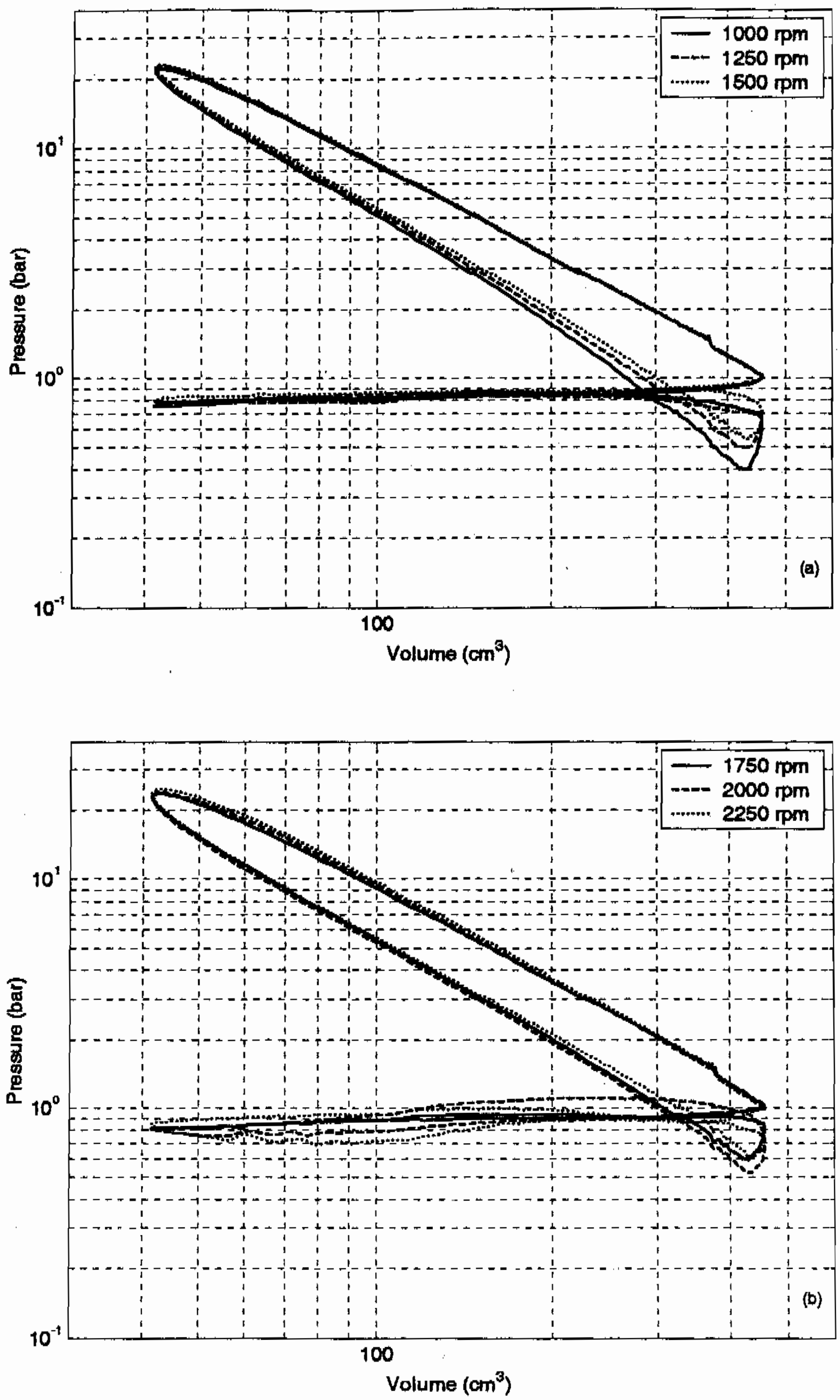

Figure A.93: OSU Dynamometer Experiment: Intake #7 – Pressure versus CAD for In-Cylinder Pressure Transducer at (a) 1000, 1250, and 1500 rpm and (b) 1750, 2000, and 2250 rpm

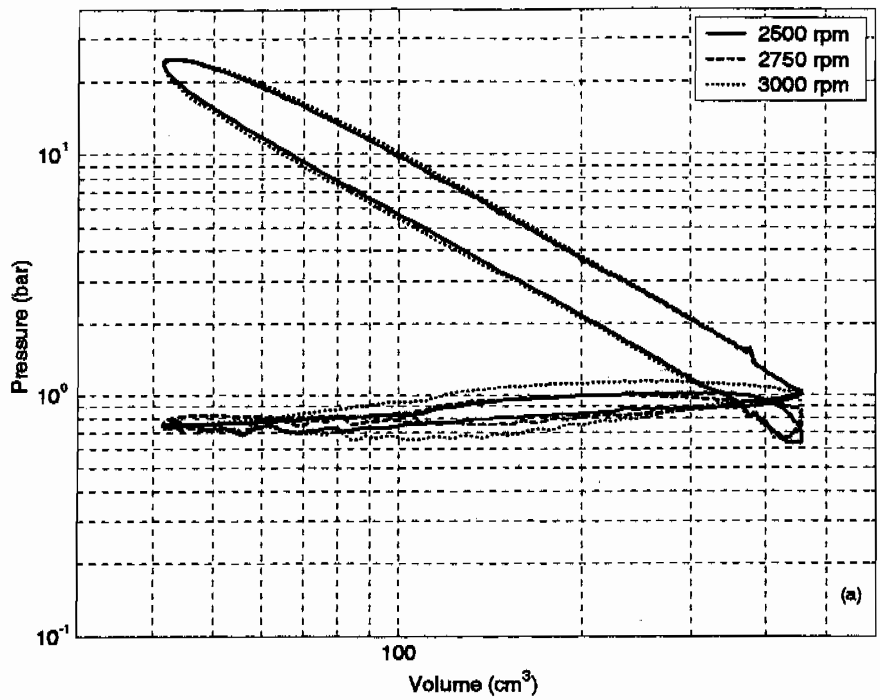

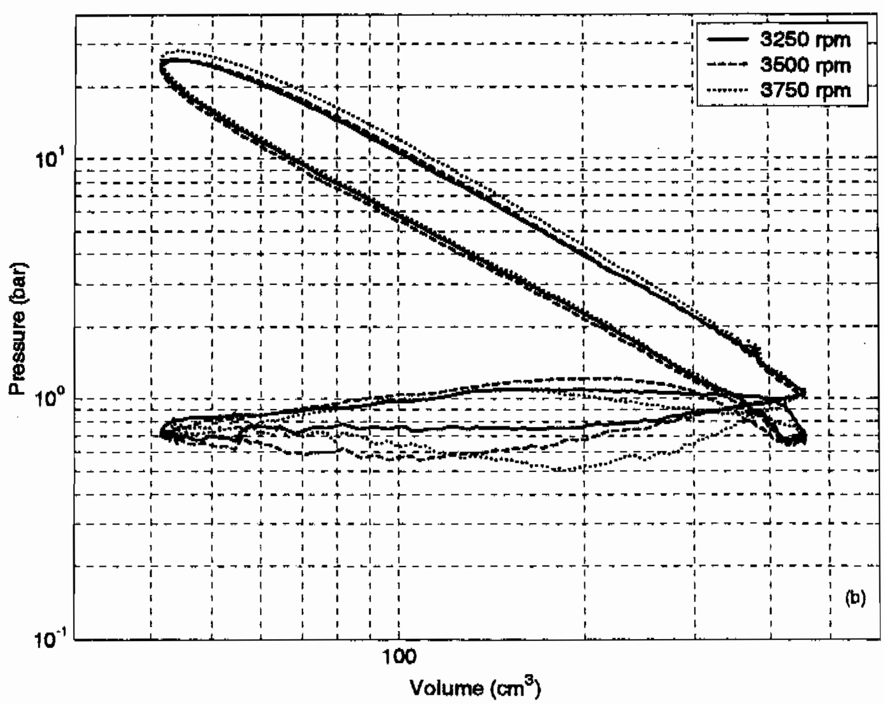

Figure A.94: OSU Dynamometer Experiment: Intake #7 – Pressure versus CAD for In-Cylinder Pressure Transducer at (a) 2500, 2750, and 3000 rpm and (b) 3250, 3500, and 3750 rpm

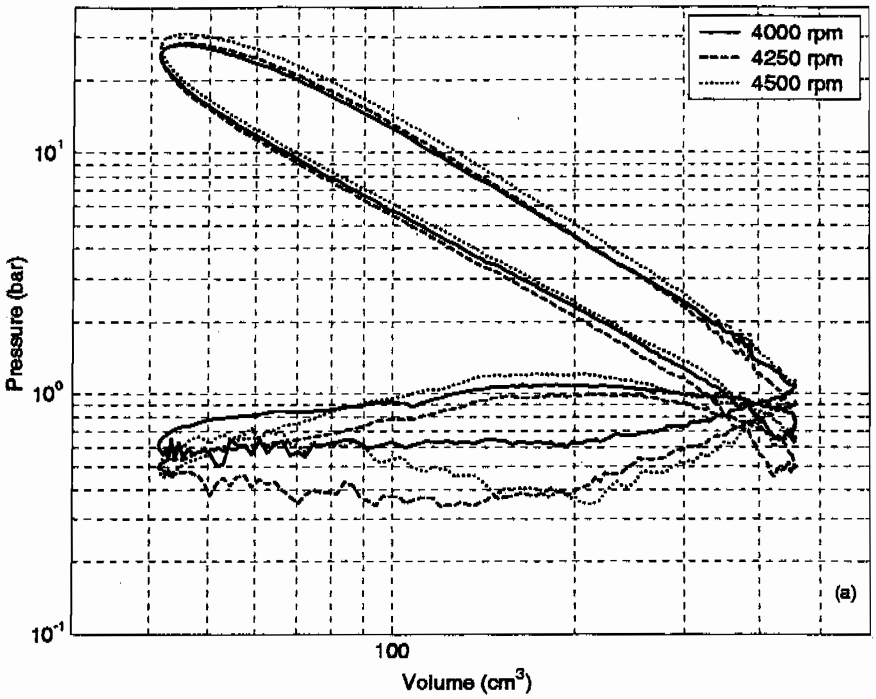

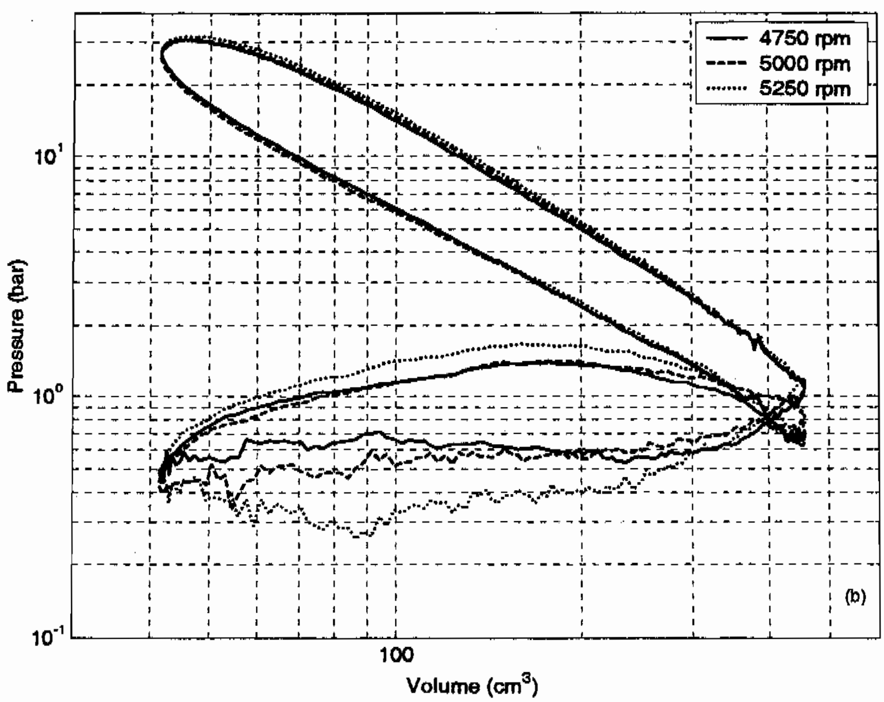

Figure A.95: OSU Dynamometer Experiment: Intake #7 – Pressure versus CAD for In-Cylinder Pressure Transducer at (a) 4000, 4250, and 4500 rpm and (b) 4750, 5000, and 5250 rpm

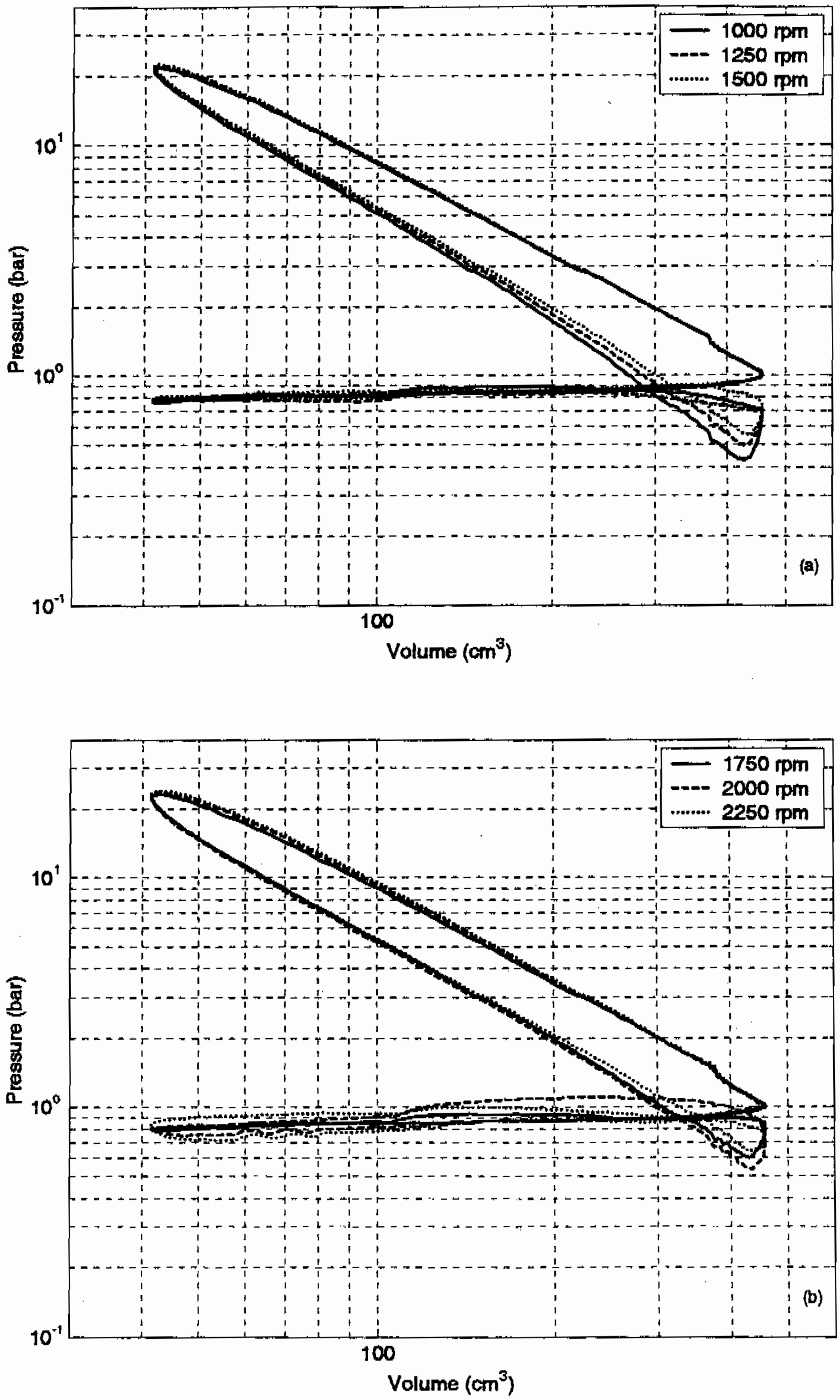

Figure A.96: OSU Dynamometer Experiment: Intake #8 – Pressure versus CAD for In-Cylinder Pressure Transducer at (a) 1000, 1250, and 1500 rpm and (b) 1750, 2000, and 2250 rpm

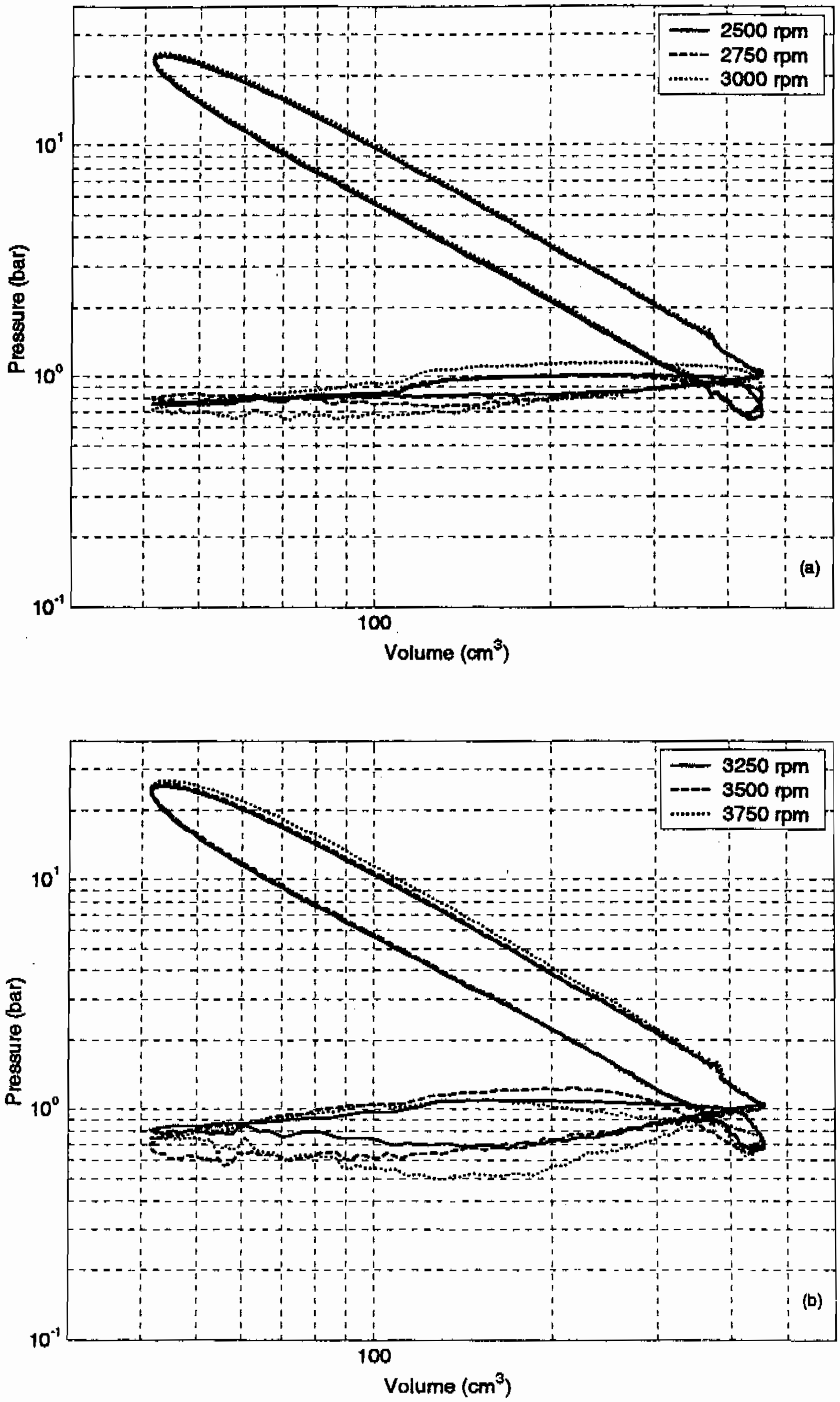

Figure A.97: OSU Dynamometer Experiment: Intake #8 – Pressure versus CAD for In-Cylinder Pressure Transducer at (a) 2500, 2750, and 3000 rpm and (b) 3250, 3500, and 3750 rpm

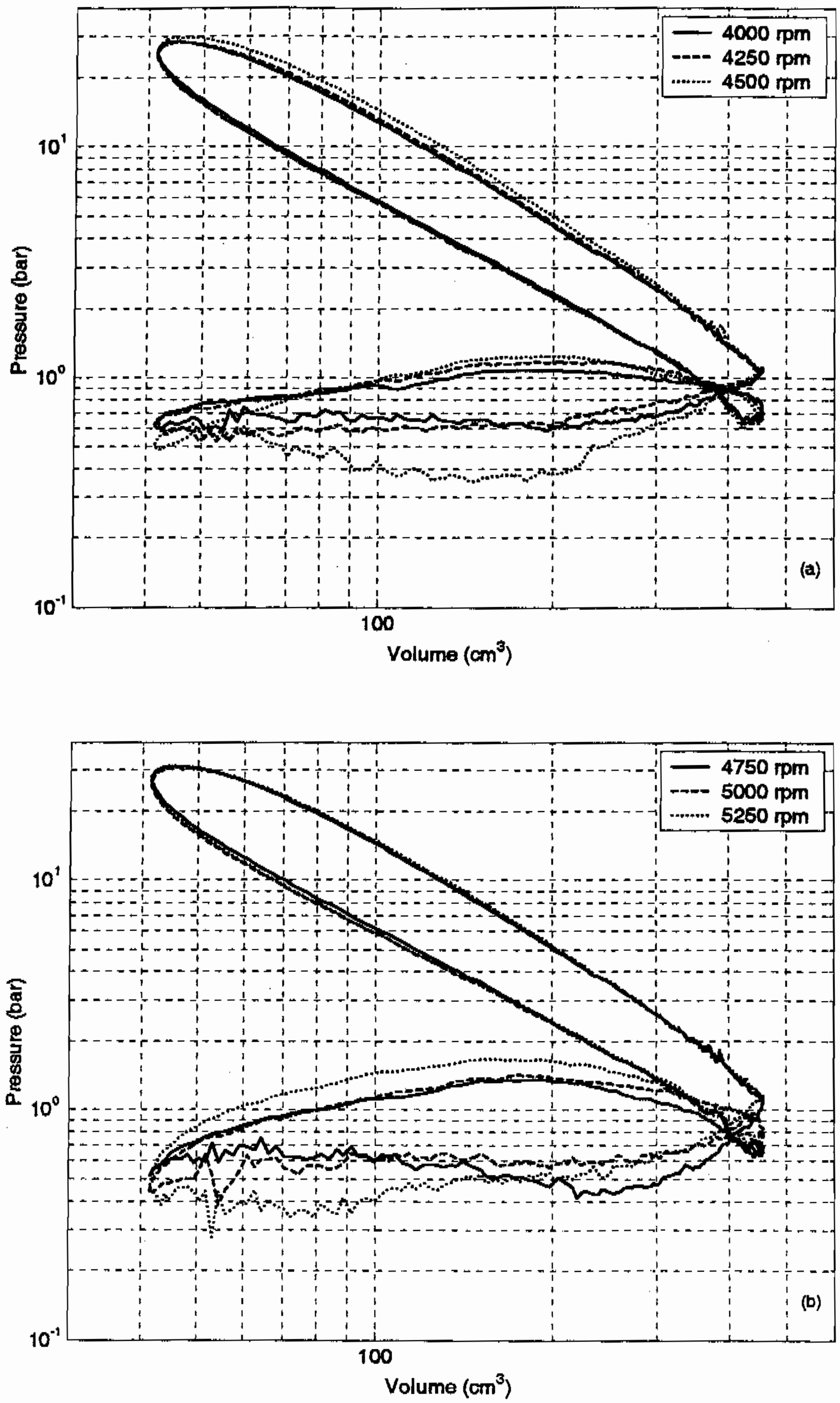

Figure A.98: OSU Dynamometer Experiment: Intake #8 – Pressure versus CAD for In-Cylinder Pressure Transducer at (a) 4000, 4250, and 4500 rpm and (b) 4750, 5000, and 5250 rpm

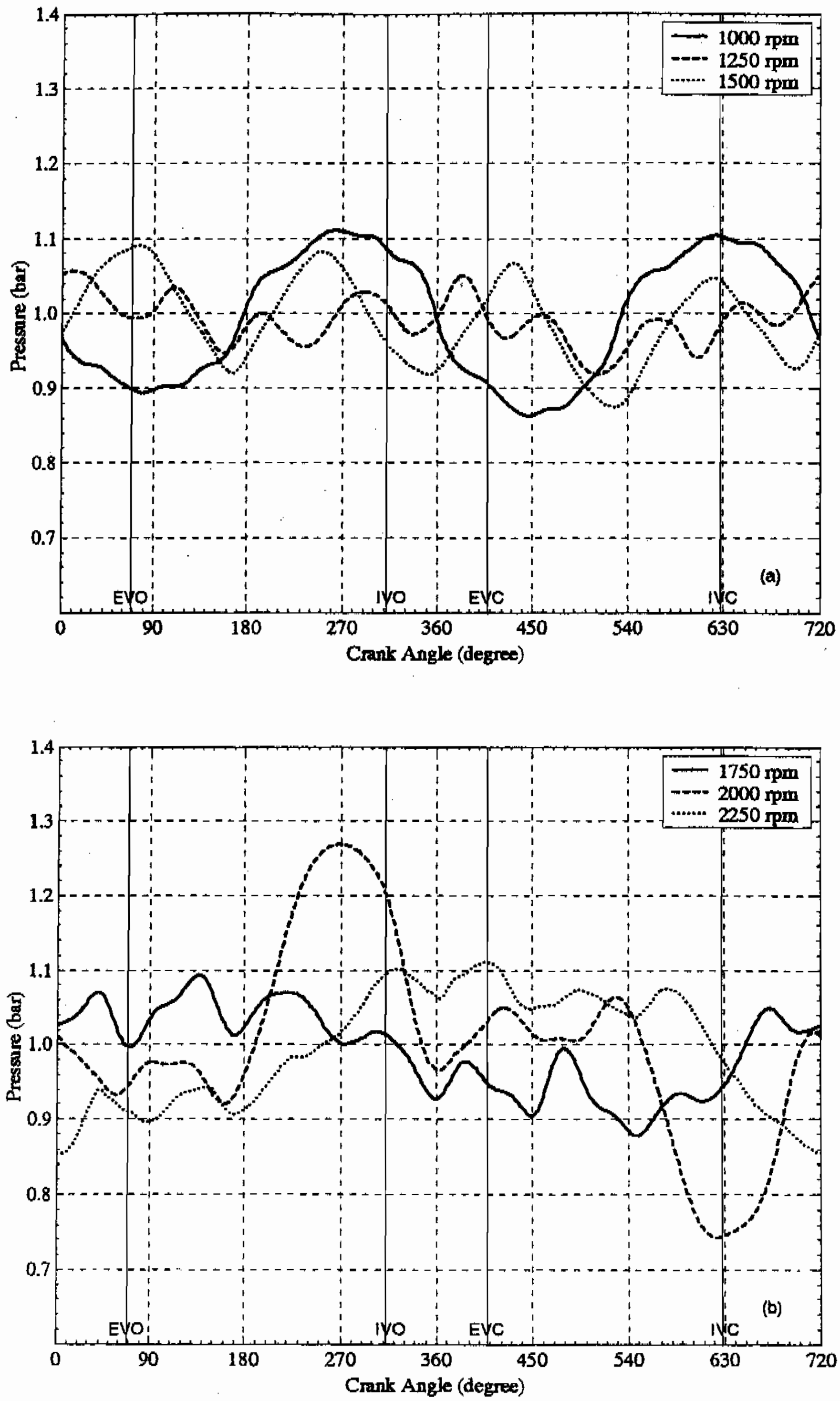

Figure A.99: OSU Dynamometer Experiment: Intake #1 – Pressure versus CAD for Exhaust Pressure Transducer at (a) 1000, 1250, and 1500 rpm and (b) 1750, 2000, and 2250 rpm

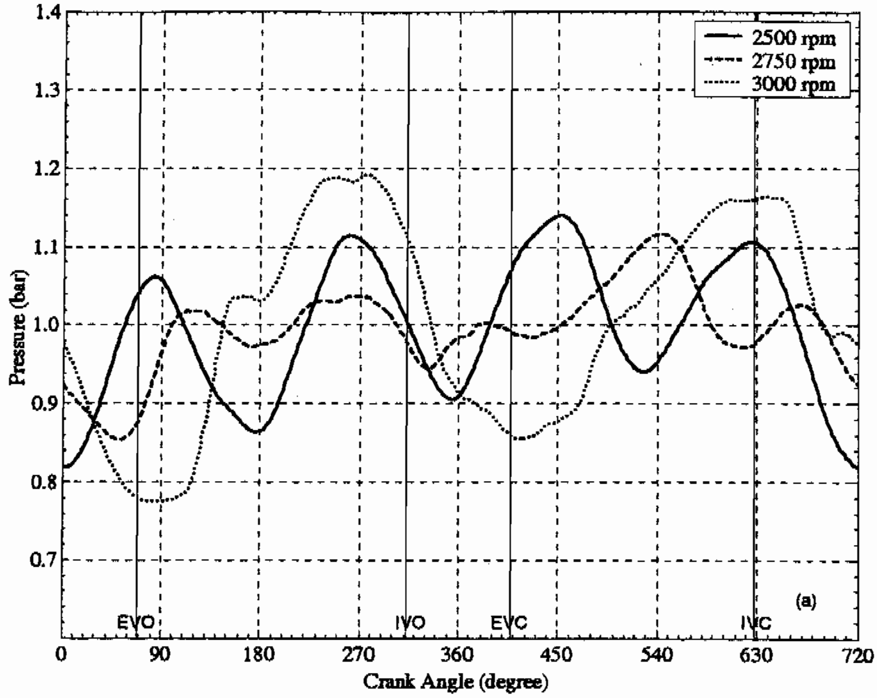

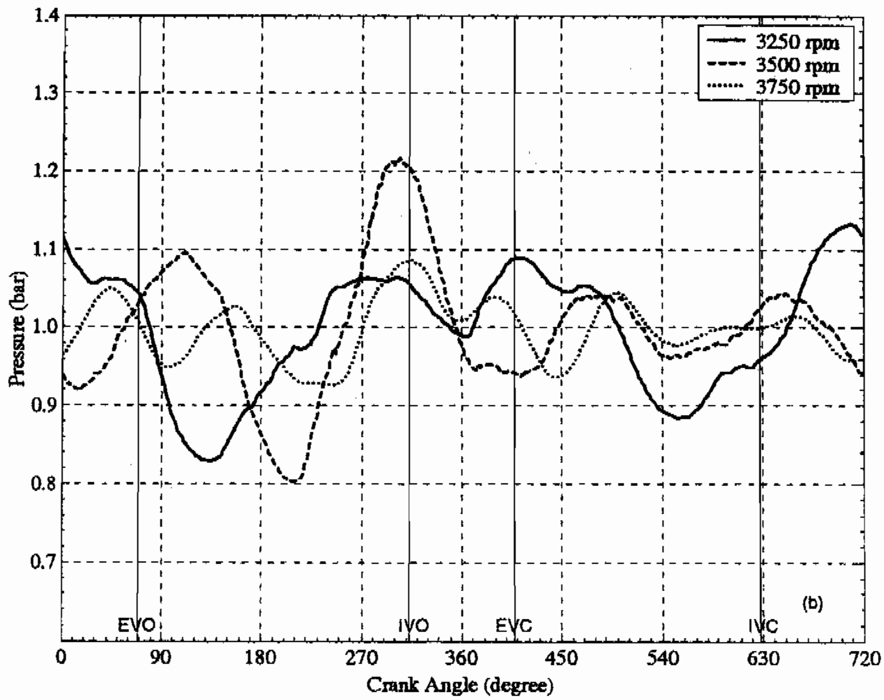

Figure A.100: OSU Dynamometer Experiment: Intake #1 – Pressure versus CAD for Exhaust Pressure Transducer at (a) 2500, 2750, and 3000 rpm and (b) 3250, 3500, and 3750 rpm

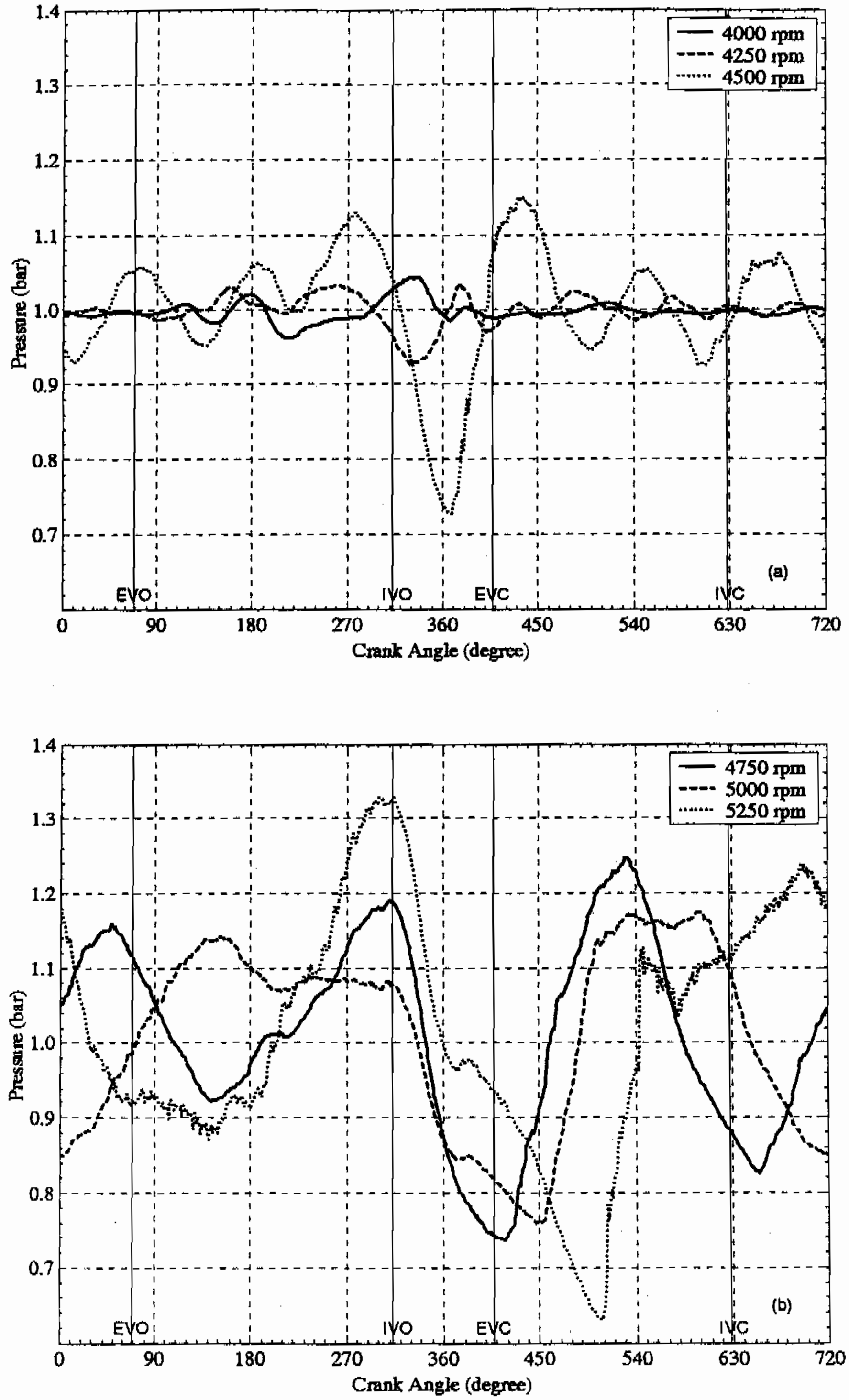

Figure A.101: OSU Dynamometer Experiment: Intake #1 – Pressure versus CAD for Exhaust Pressure Transducer at (a) 4000, 4250, and 4500 rpm and (b) 4750, 5000, and 5250 rpm

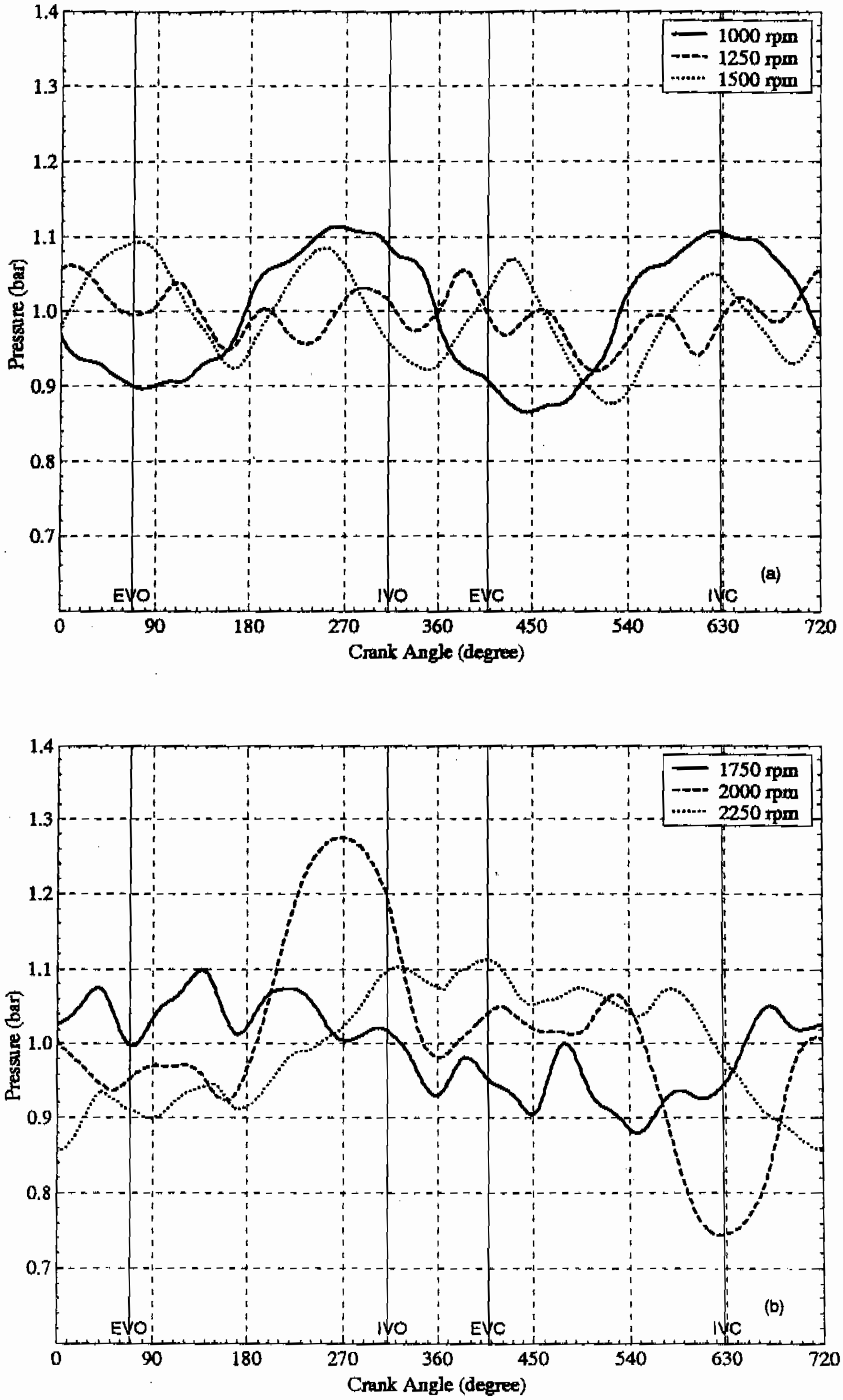

Figure A.102: OSU Dynamometer Experiment: Intake #2 – Pressure versus CAD for Exhaust Pressure Transducer at (a) 1000, 1250, and 1500 rpm and (b) 1750, 2000, and 2250 rpm

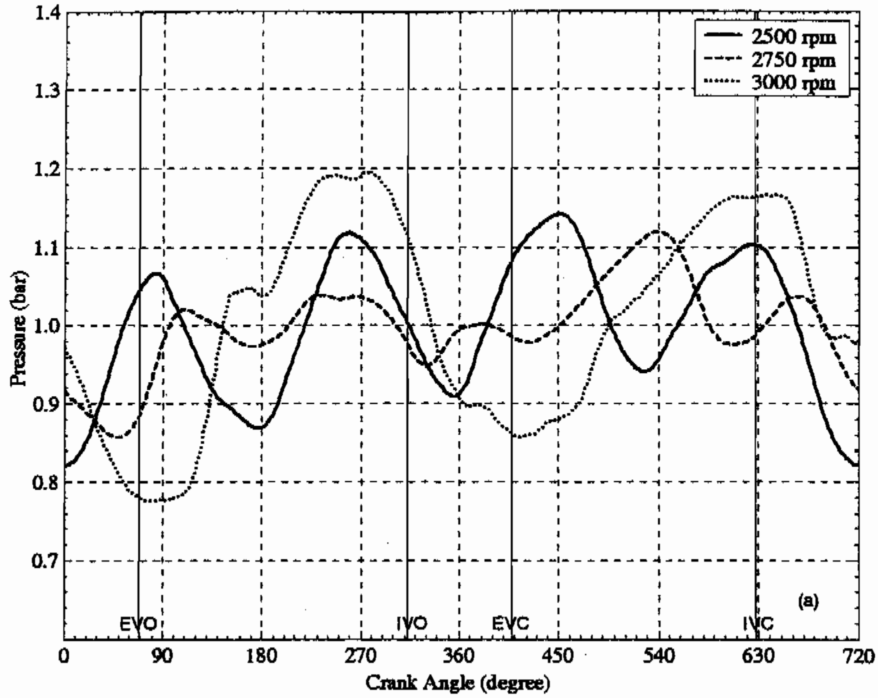

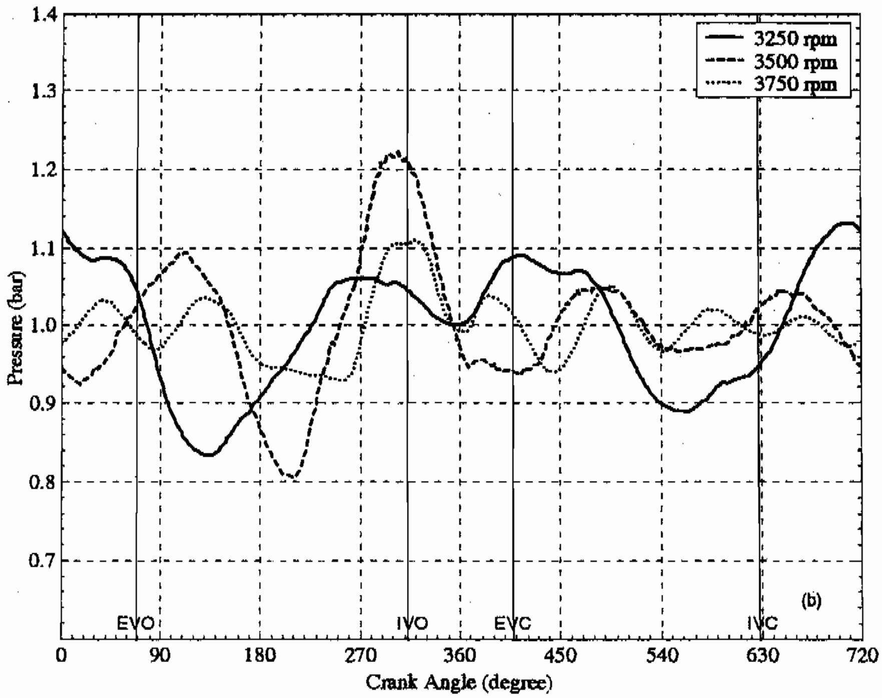

Figure A.103: OSU Dynamometer Experiment: Intake #2 – Pressure versus CAD for Exhaust Pressure Transducer at (a) 2500, 2750, and 3000 rpm and (b) 3250, 3500, and 3750 rpm

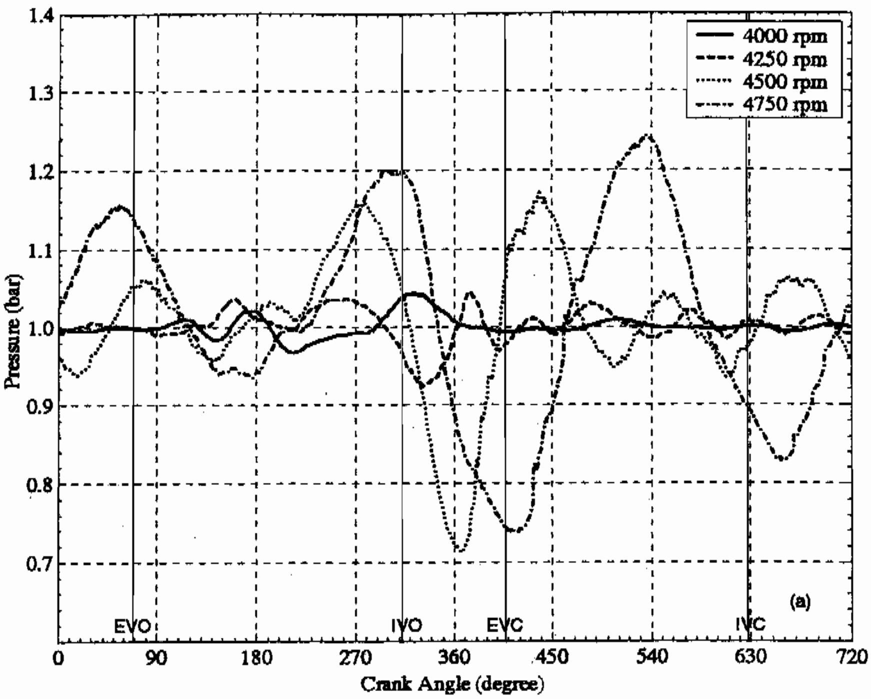

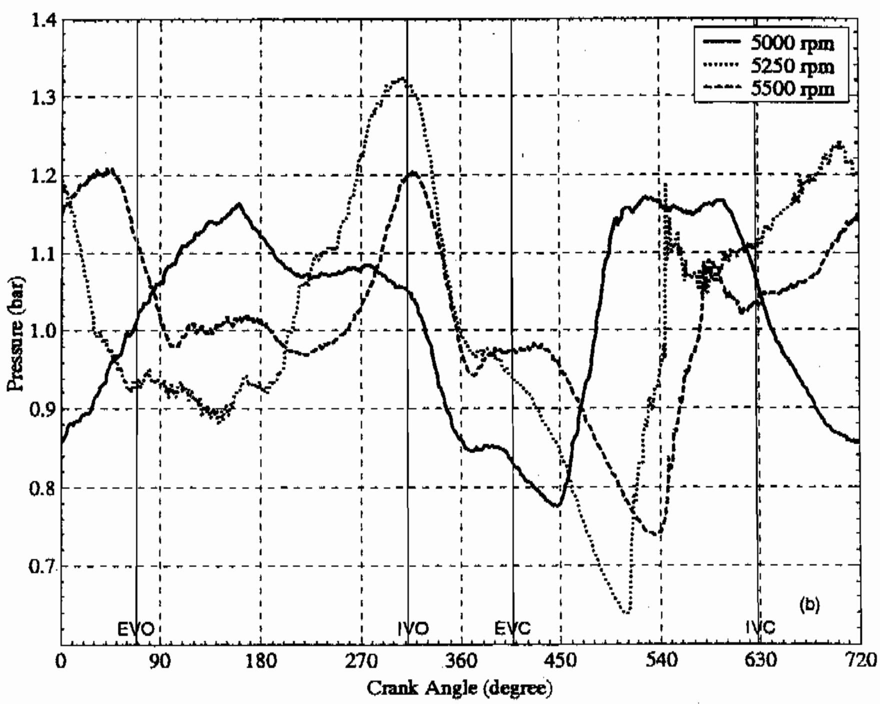

Figure A.104: OSU Dynamometer Experiment: Intake #2 – Pressure versus CAD for Exhaust Pressure Transducer at (a) 4000, 4250, 4500, and 4750 rpm and (b) 5000, 5250, and 5500 rpm

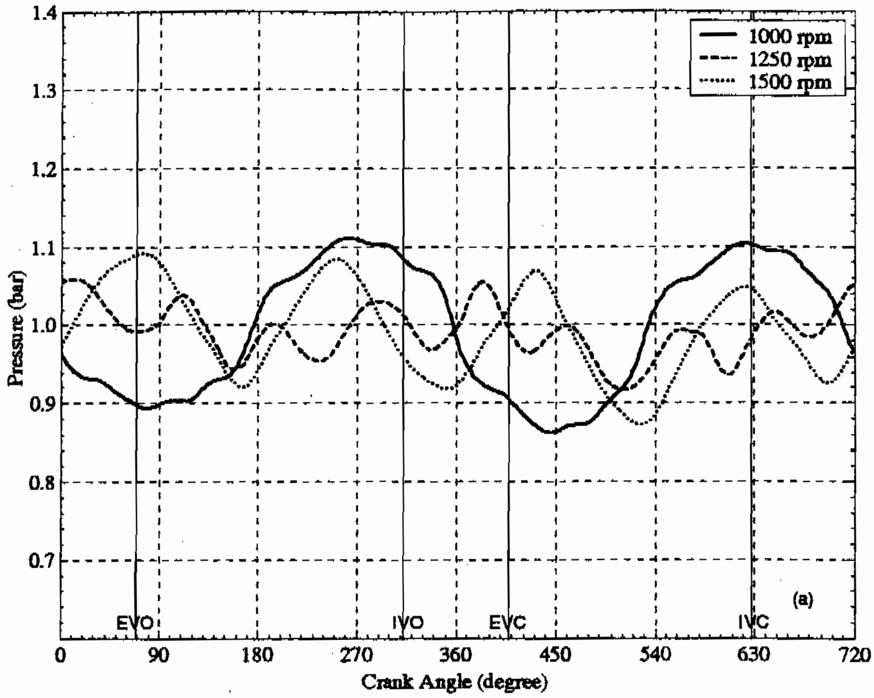

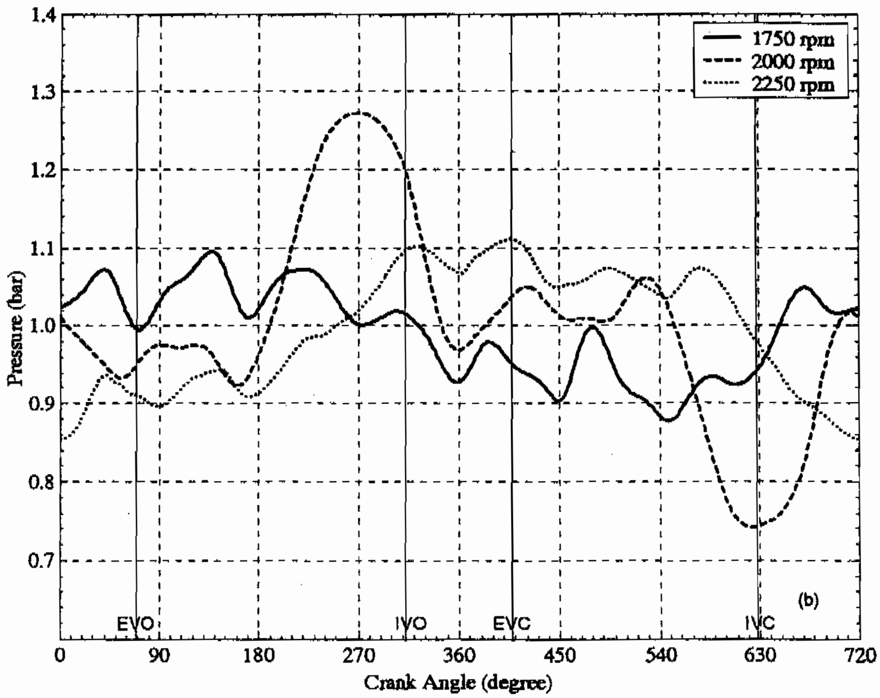

Figure A.105: OSU Dynamometer Experiment: Intake #3 – Pressure versus CAD for Exhaust Pressure Transducer at (a) 1000, 1250, and 1500 rpm and (b) 1750, 2000, and 2250 rpm

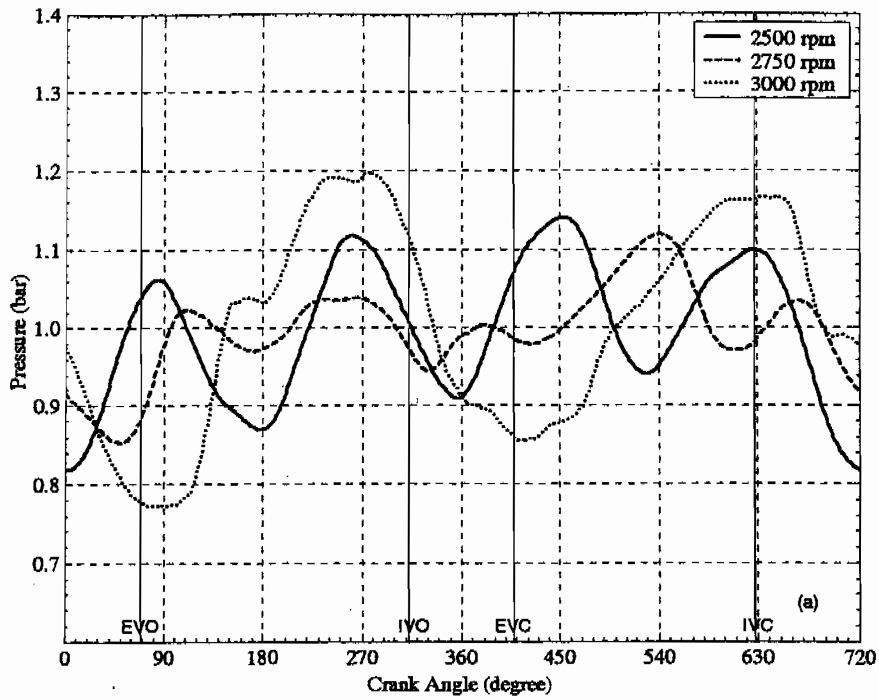

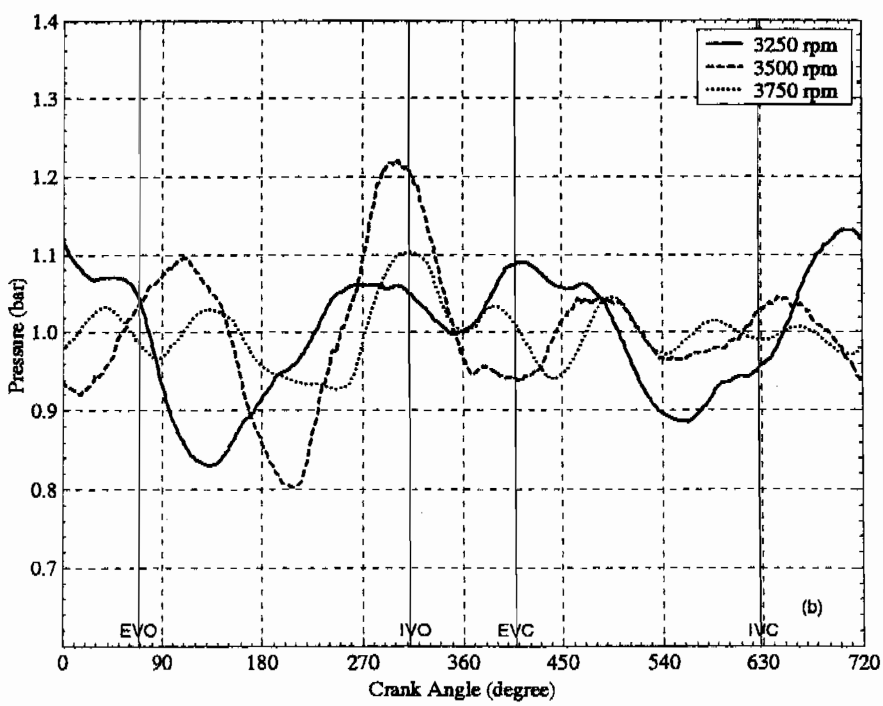

Figure A.106: OSU Dynamometer Experiment: Intake #3 – Pressure versus CAD for Exhaust Pressure Transducer at (a) 2500, 2750, and 3000 rpm and (b) 3250, 3500, and 3750 rpm

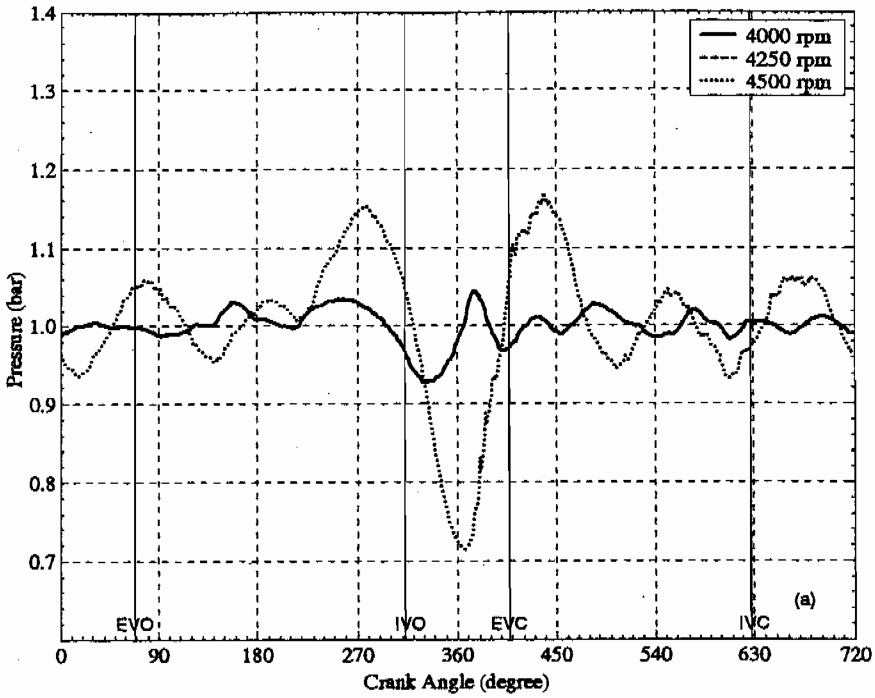

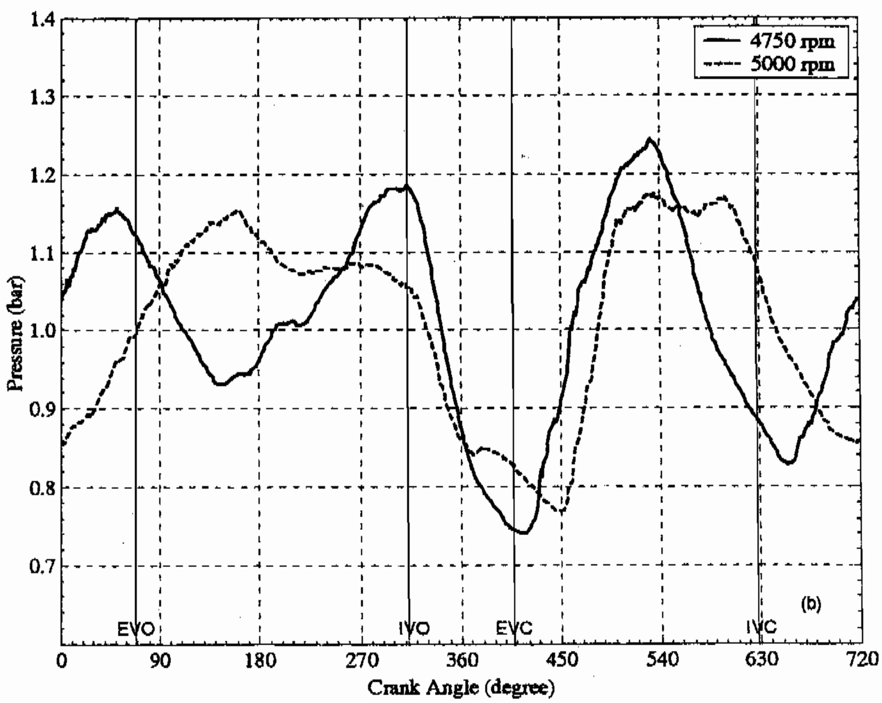

Figure A.107: OSU Dynamometer Experiment: Intake #3 – Pressure versus CAD for Exhaust Pressure Transducer at (a) 4000, 4250, and 4500 rpm and (b) 4750, 5000, and 5250 rpm

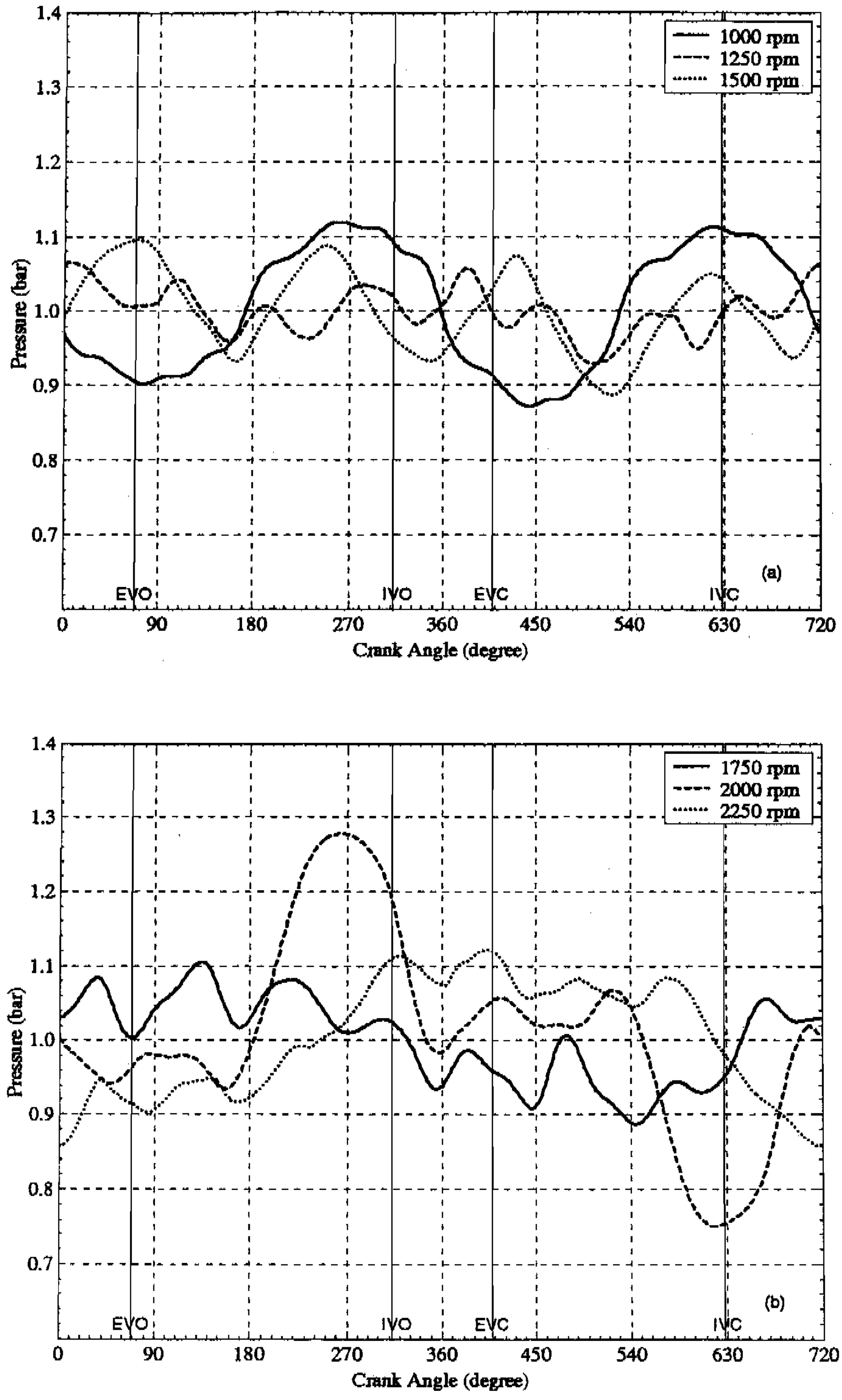

Figure A.108: OSU Dynamometer Experiment: Intake #4 – Pressure versus CAD for Exhaust Pressure Transducer at (a) 1000, 1250, and 1500 rpm and (b) 1750, 2000, and 2250 rpm

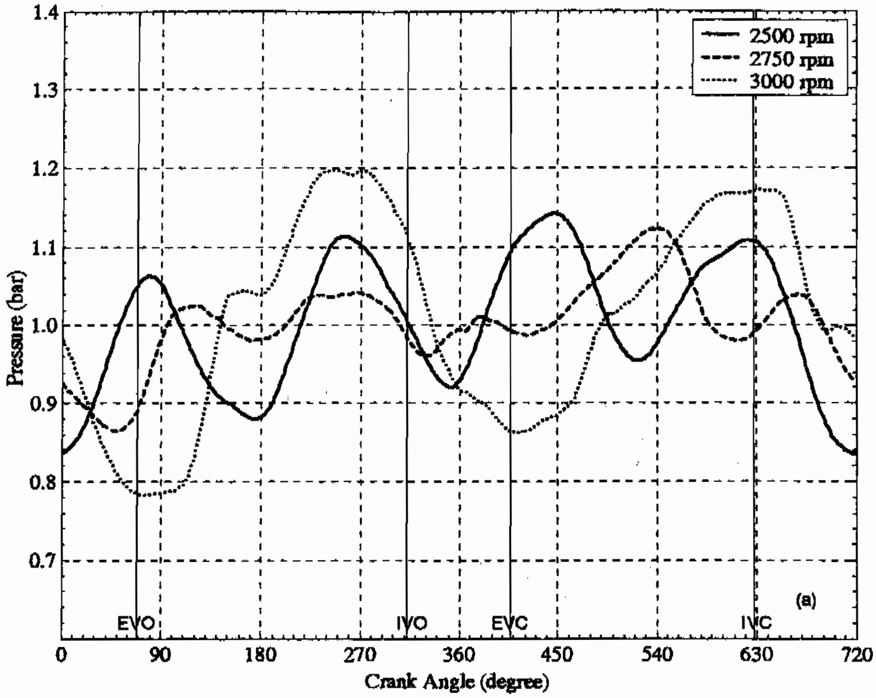

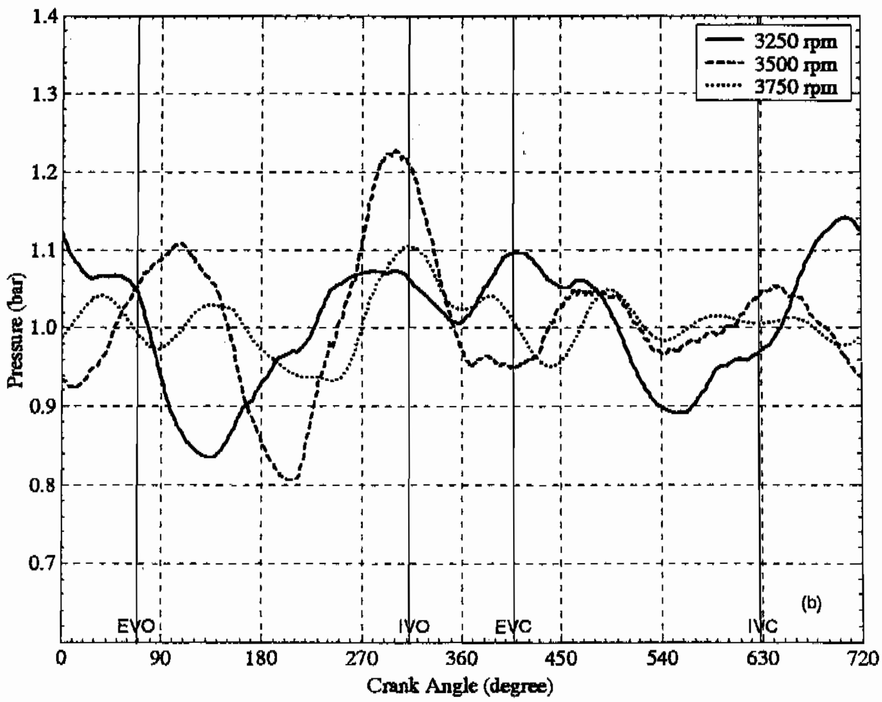

Figure A.109: OSU Dynamometer Experiment: Intake #4 – Pressure versus CAD for Exhaust Pressure Transducer at (a) 2500, 2750, and 3000 rpm and (b) 3250, 3500, and 3750 rpm

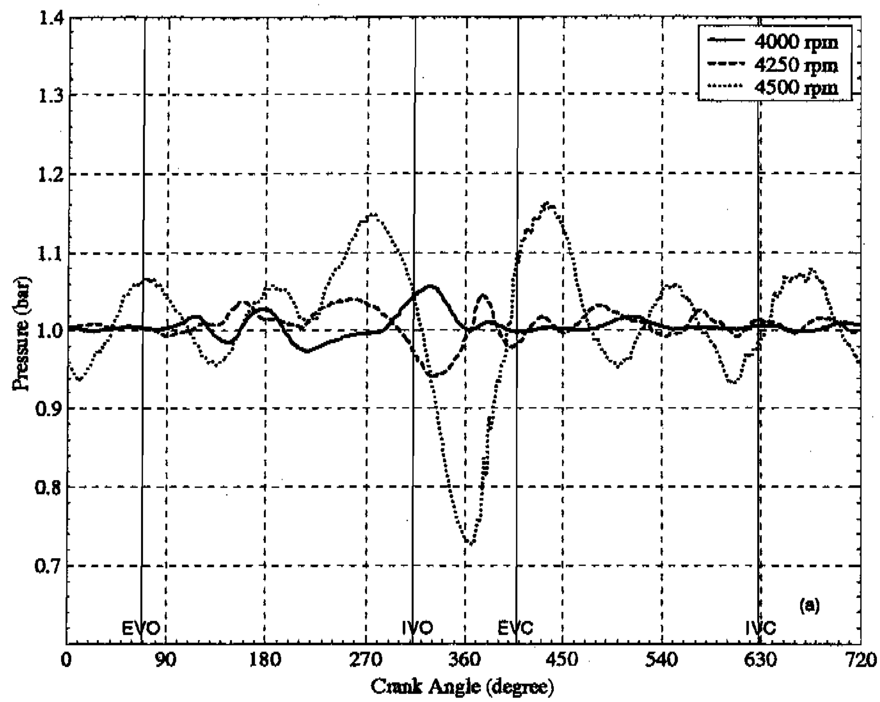

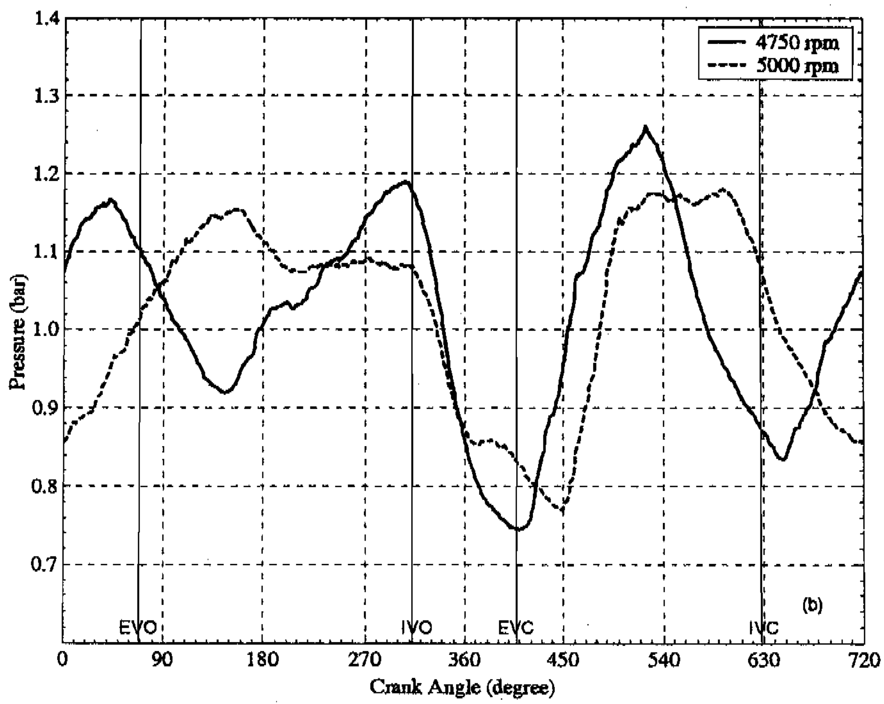

Figure A.110: OSU Dynamometer Experiment: Intake #4 – Pressure versus CAD for Exhaust Pressure Transducer at (a) 4000, 4250, and 4500 rpm and (b) 4750 and 5000

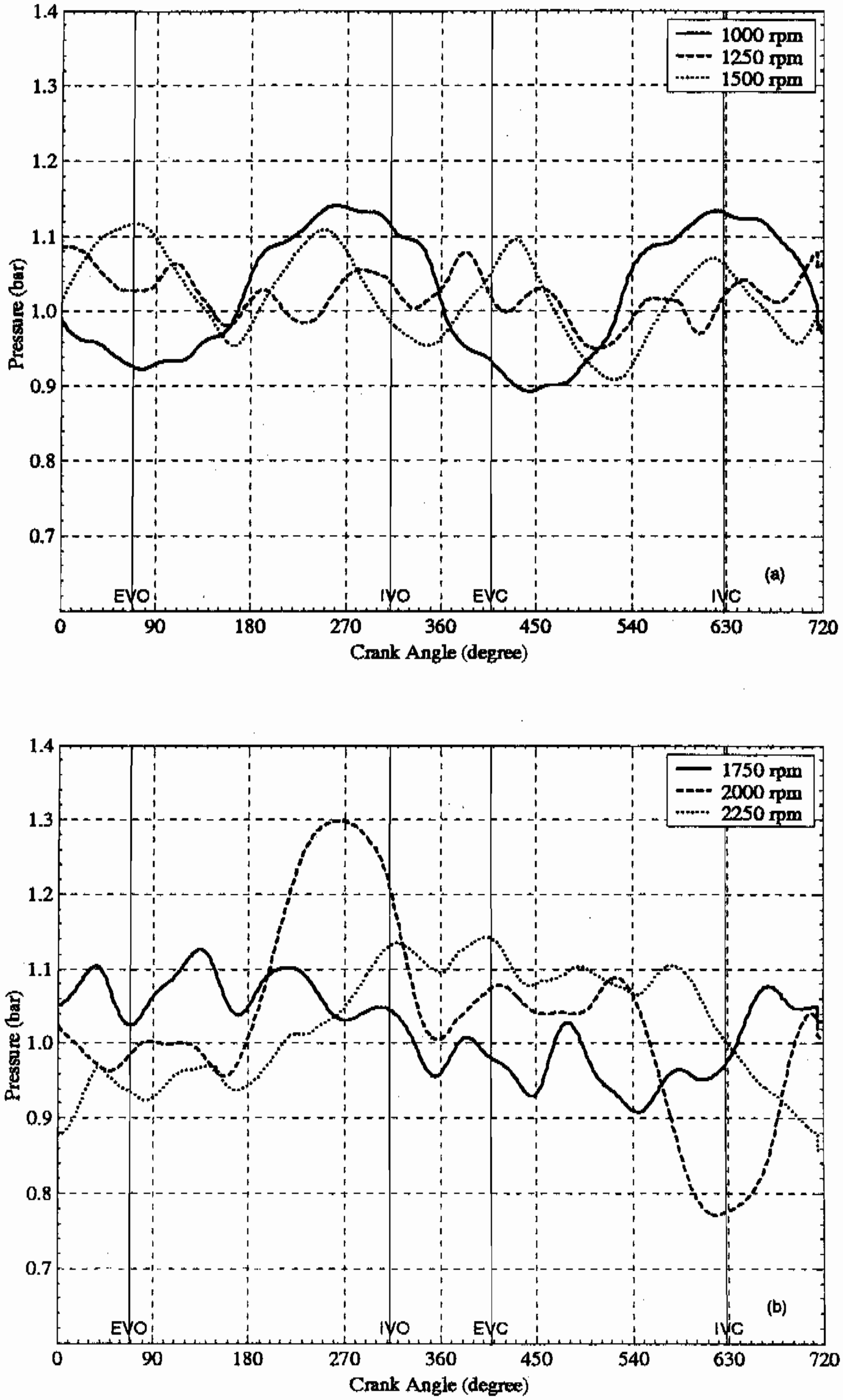

Figure A.111: OSU Dynamometer Experiment: Intake #5 – Pressure versus CAD for Exhaust Pressure Transducer at (a) 1000, 1250, and 1500 rpm and (b) 1750, 2000, and 2250 rpm

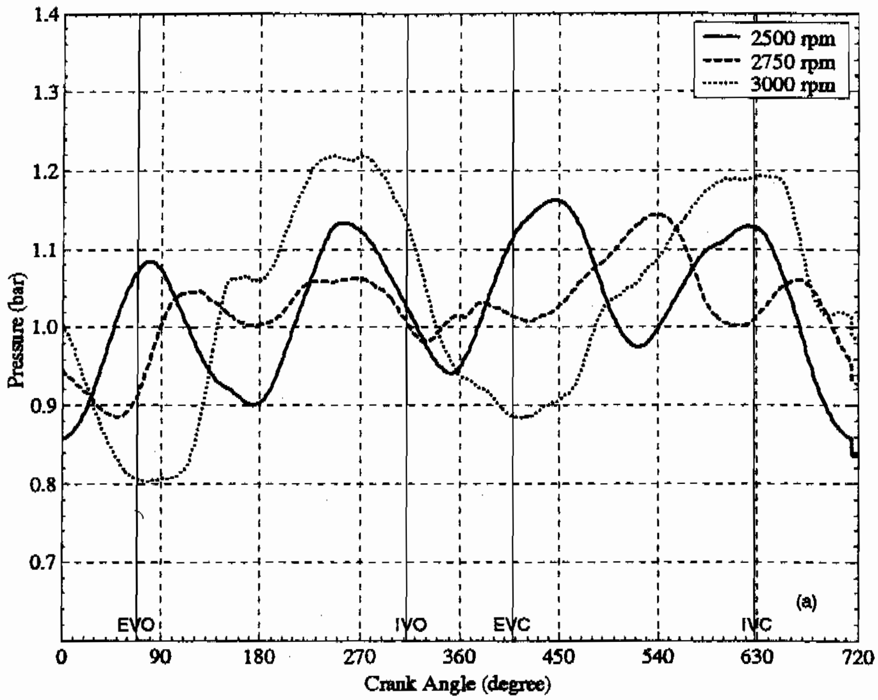

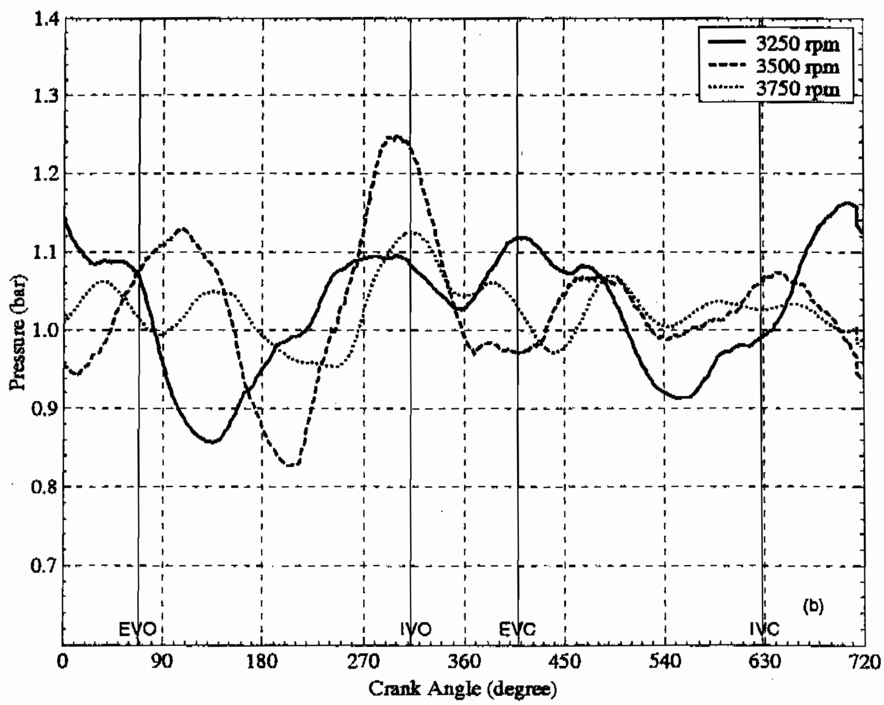

Figure A.112: OSU Dynamometer Experiment: Intake #5 – Pressure versus CAD for Exhaust Pressure Transducer at (a) 2500, 2750, and 3000 rpm and (b) 3250, 3500, and 3750 rpm

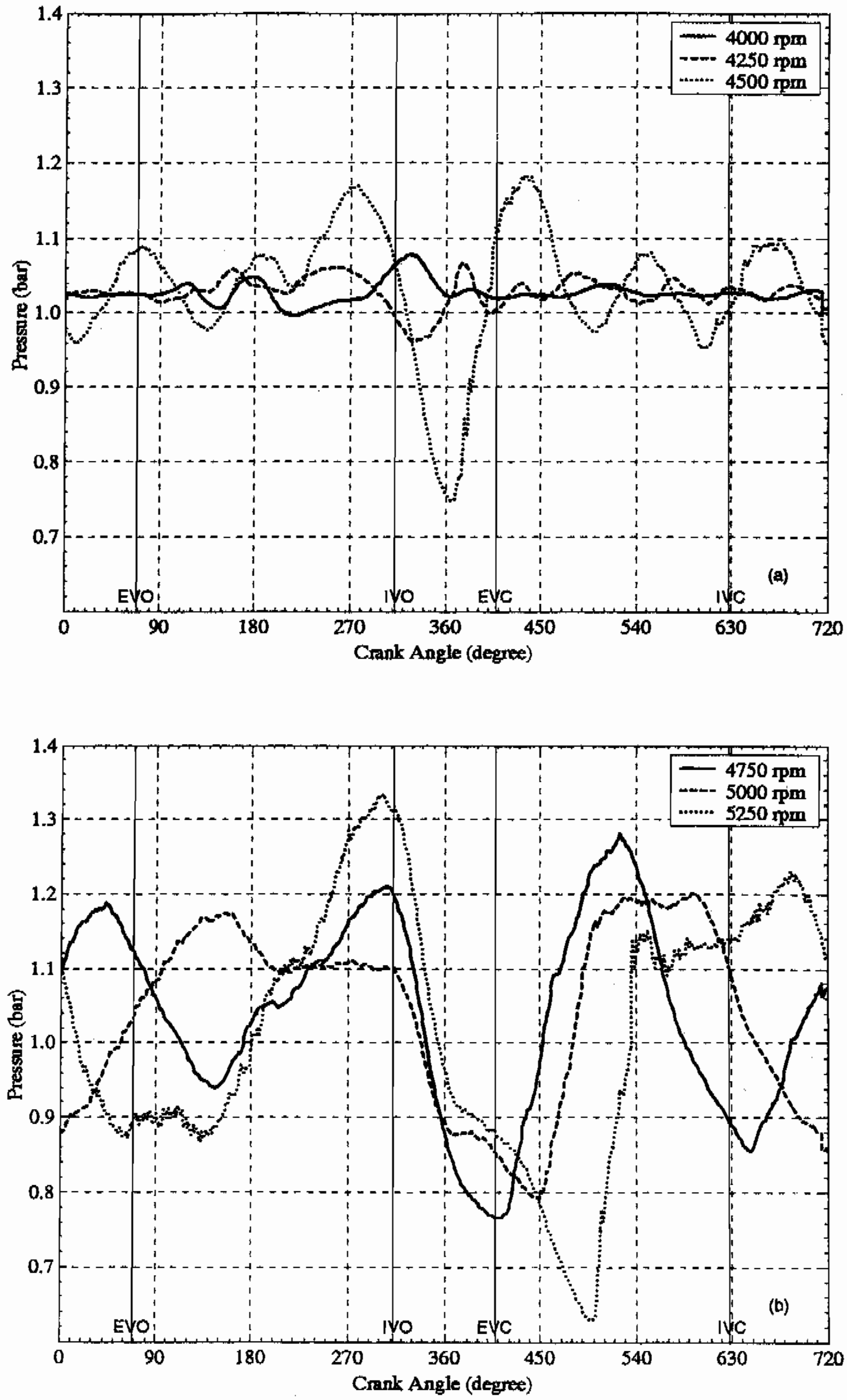

Figure A.113: OSU Dynamometer Experiment: Intake #5 – Pressure versus CAD for Exhaust Pressure Transducer at (a) 4000, 4250, and 4500 rpm and (b) 4750, 5000, and 5250 rpm

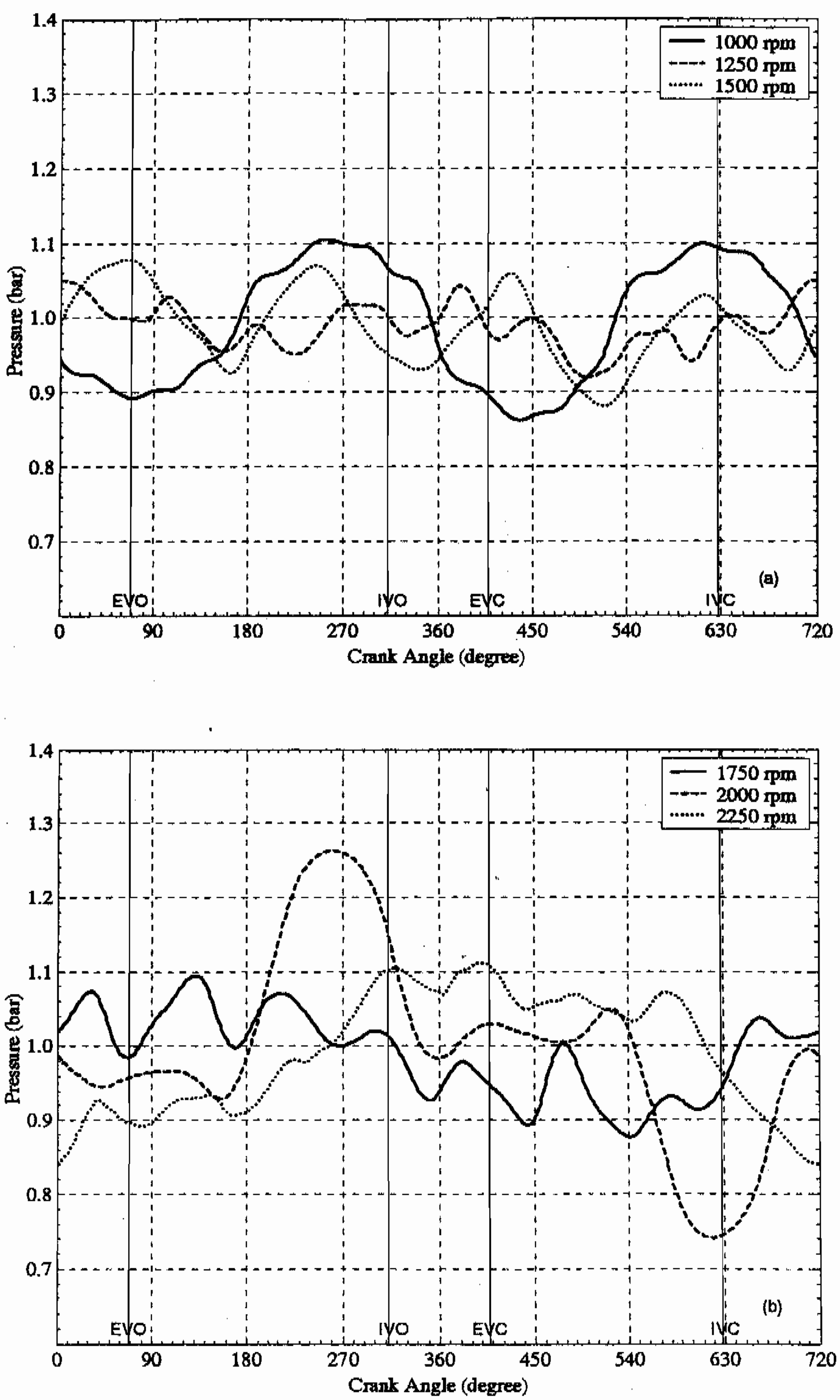

Figure A.114: OSU Dynamometer Experiment: Intake #6 – Pressure versus CAD for Exhaust Pressure Transducer at (a) 1000, 1250, and 1500 rpm and (b) 1750, 2000, and 2250 rpm

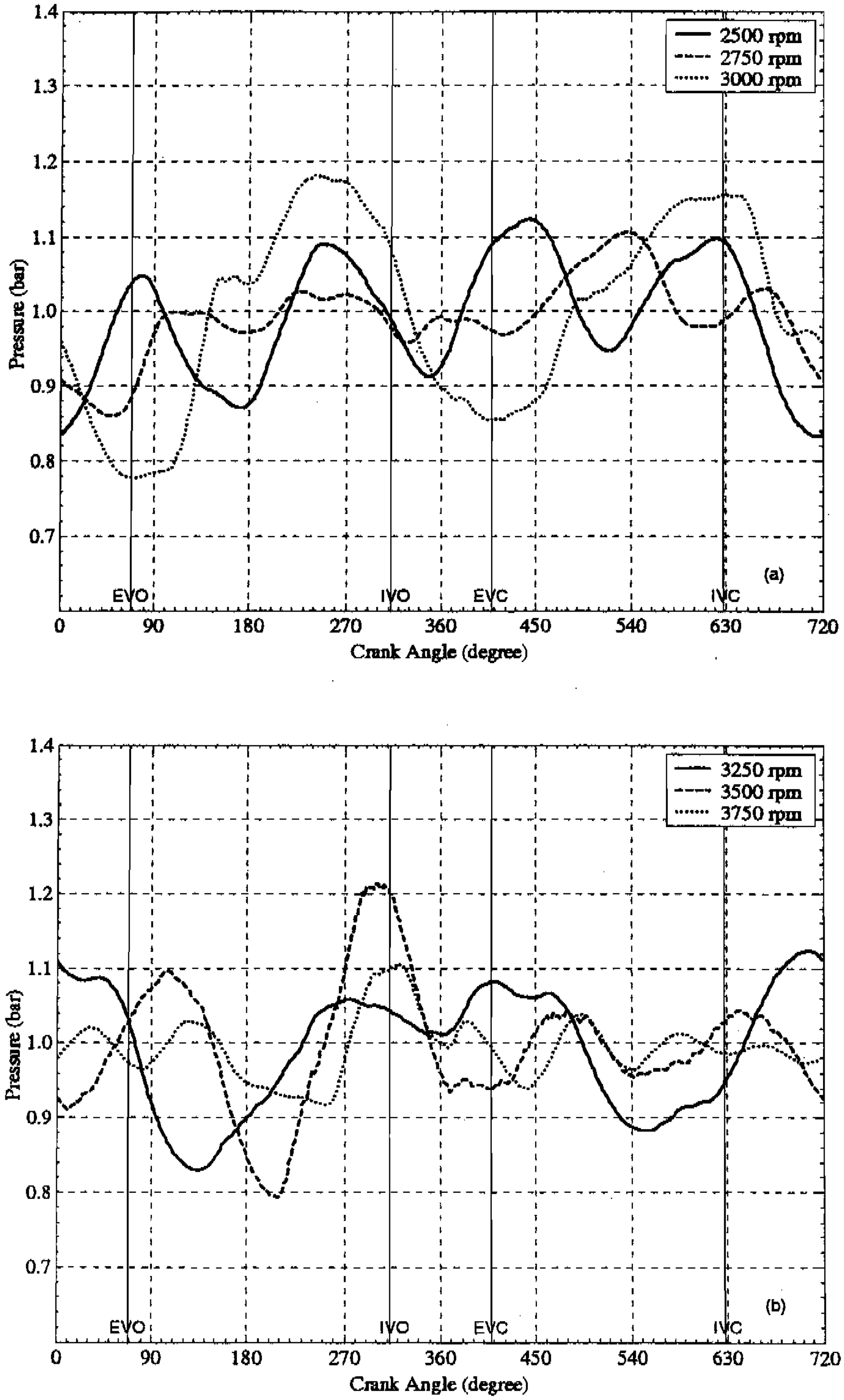

Figure A.115: OSU Dynamometer Experiment: Intake #6 – Pressure versus CAD for Exhaust Pressure Transducer at (a) 2500, 2750, and 3000 rpm and (b) 3250, 3500, and 3750 rpm

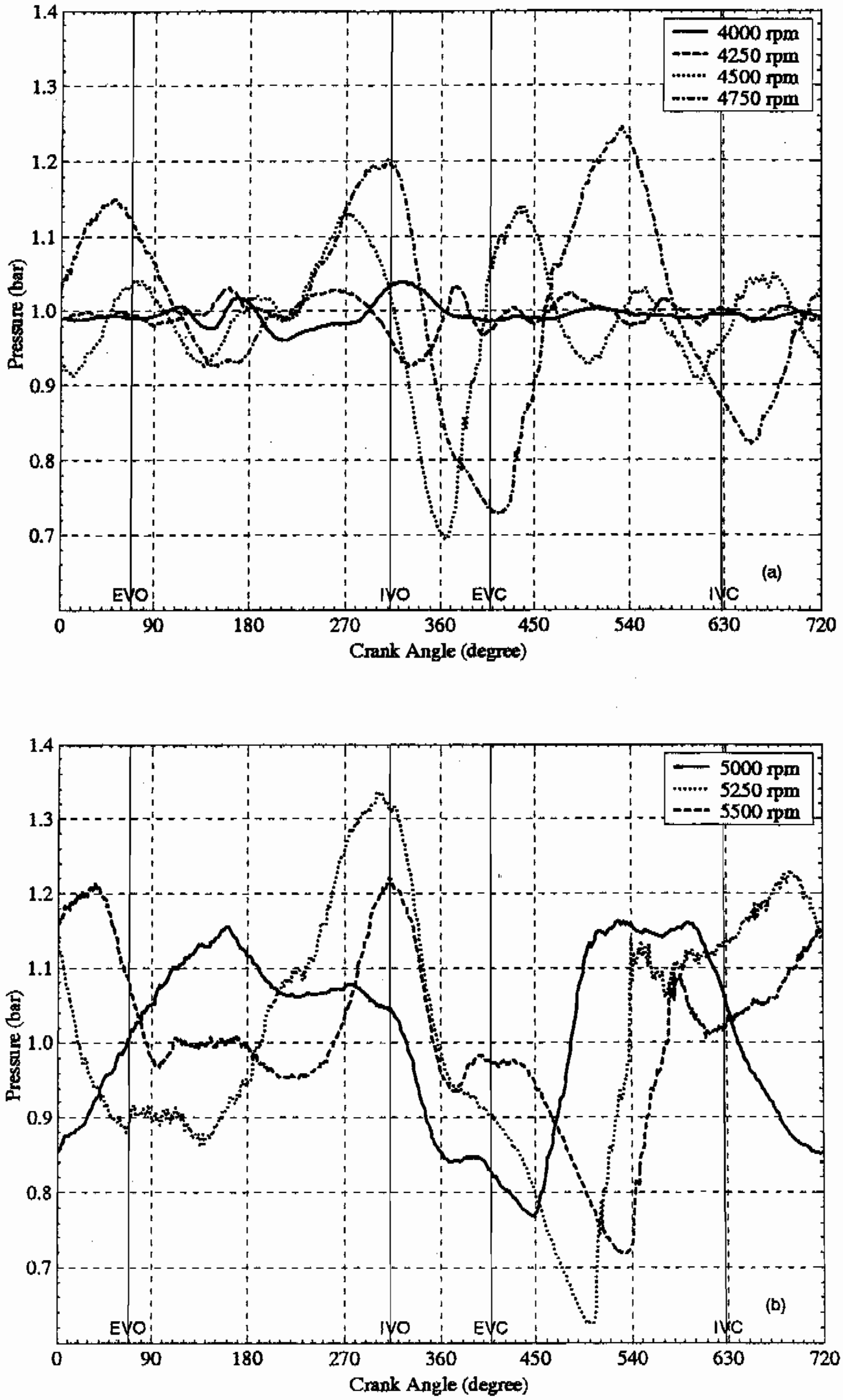

Figure A.116: OSU Dynamometer Experiment: Intake #6 – Pressure versus CAD for Exhaust Pressure Transducer at (a) 4000, 4250, 4500, and 4750 rpm and (b) 5000, 5250, and 5500 rpm

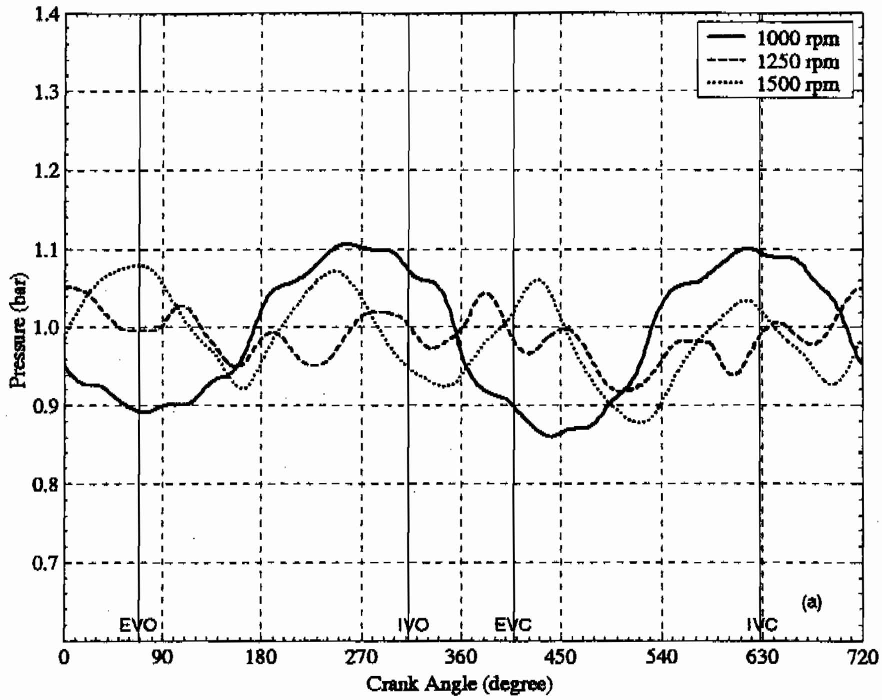

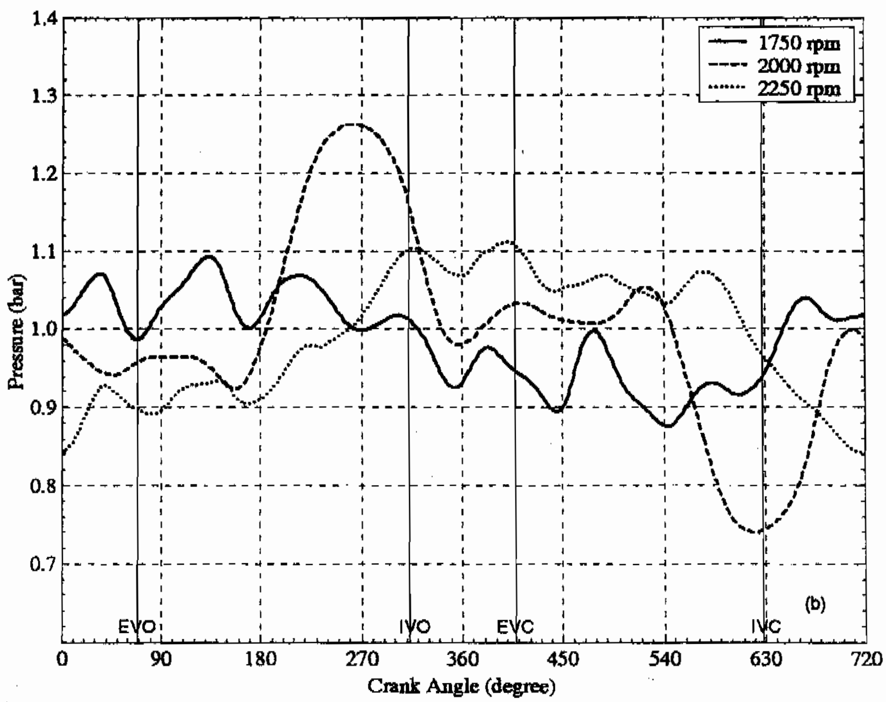

Figure A.117: OSU Dynamometer Experiment: Intake #7 – Pressure versus CAD for Exhaust Pressure Transducer at (a) 1000, 1250, and 1500 rpm and (b) 1750, 2000, and 2250 rpm

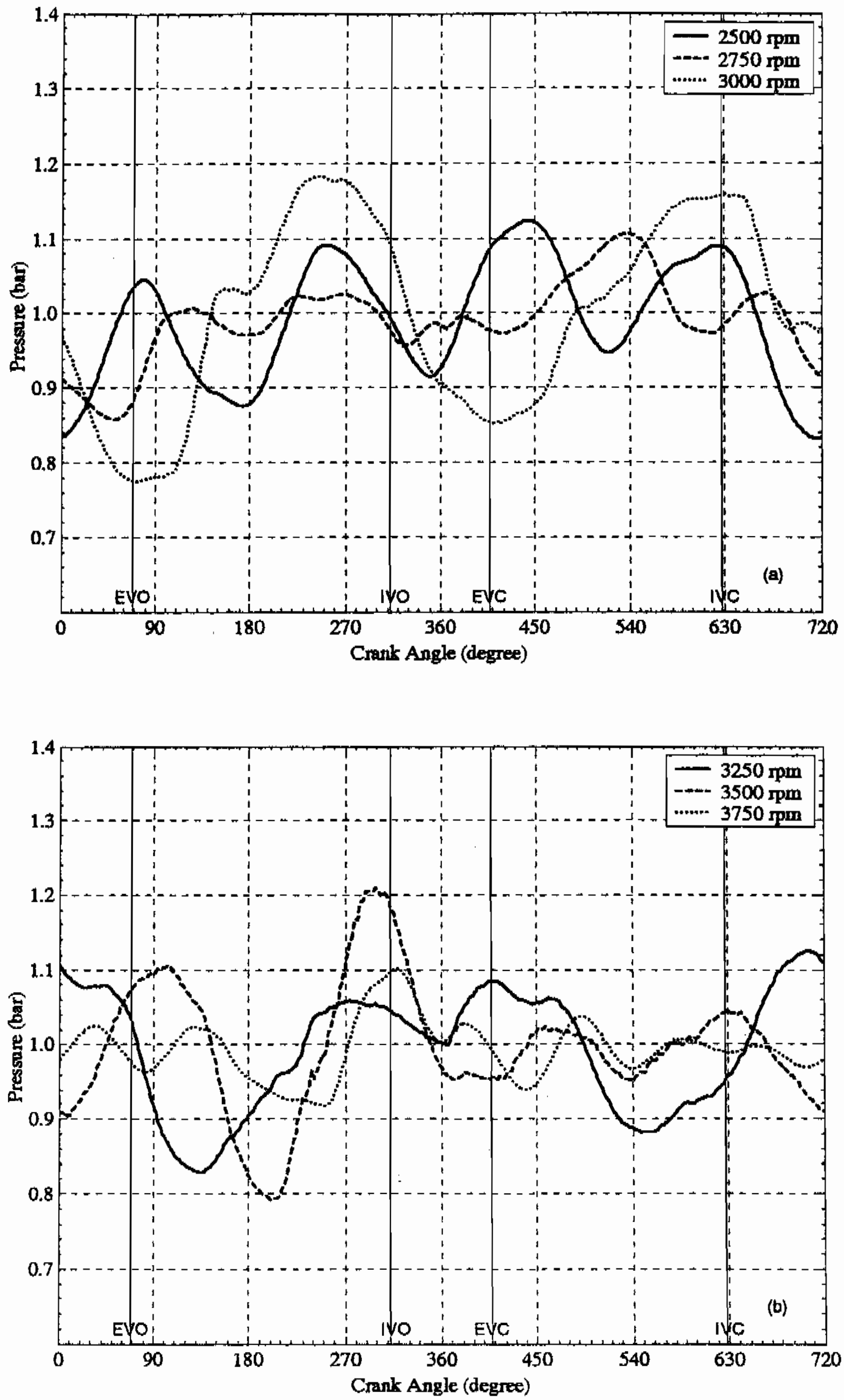

Figure A.118: OSU Dynamometer Experiment: Intake #7 – Pressure versus CAD for Exhaust Pressure Transducer at (a) 2500, 2750, and 3000 rpm and (b) 3250, 3500, and 3750 rpm

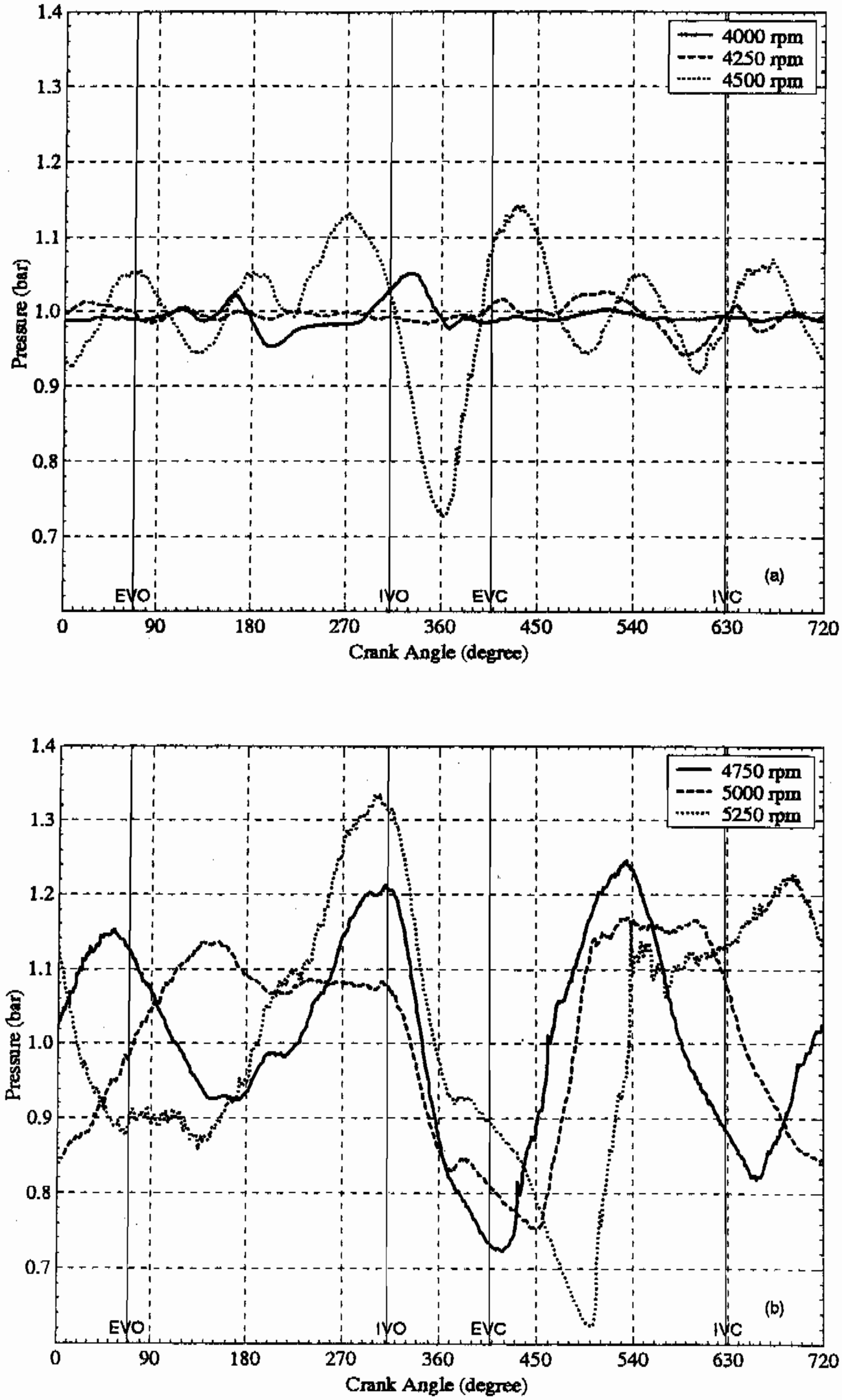

Figure A.119: OSU Dynamometer Experiment: Intake #7 – Pressure versus CAD for Exhaust Pressure Transducer at (a) 4000, 4250, and 4500 rpm and (b) 4750, 5000, and 5250 rpm

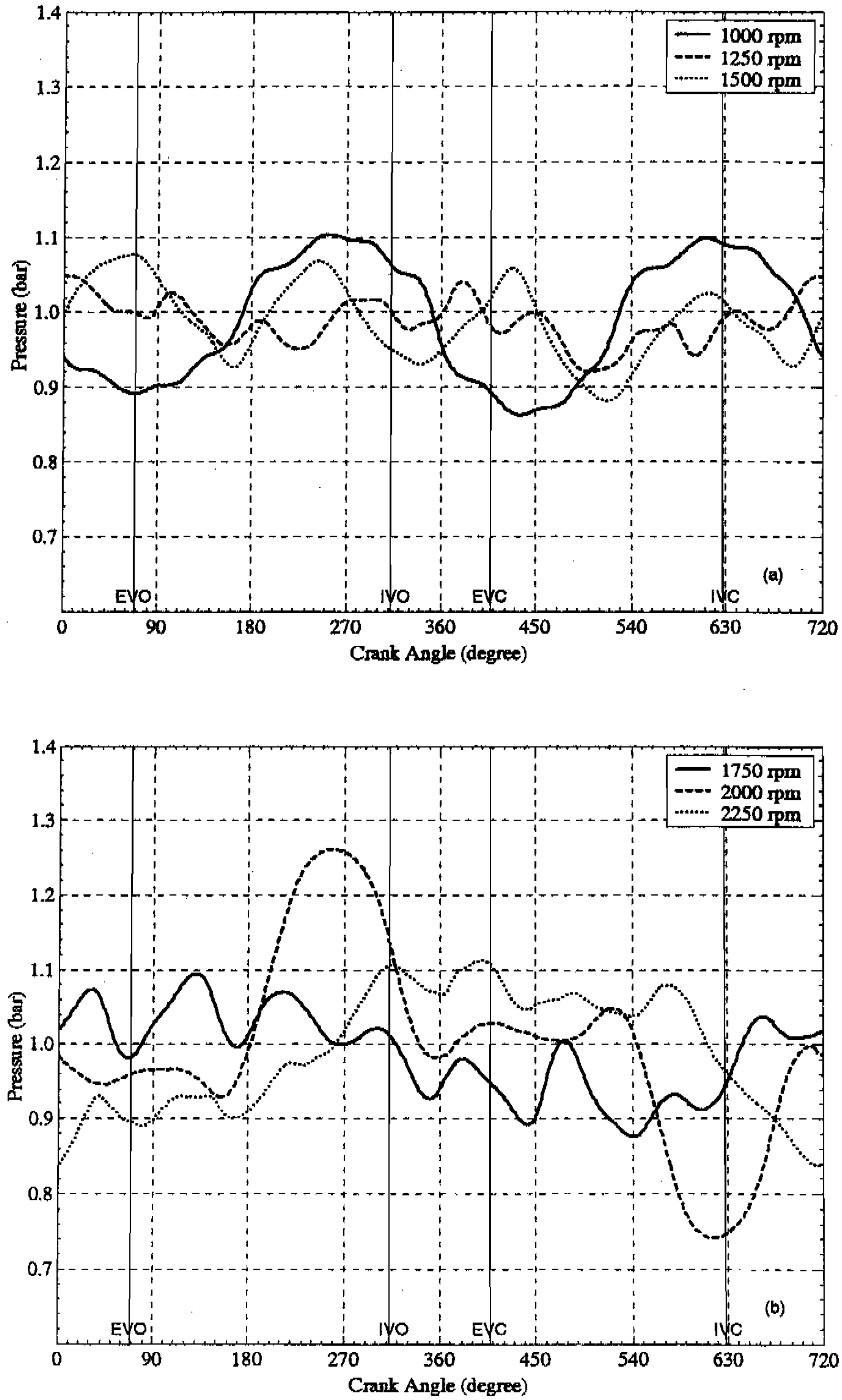

Figure A.120: OSU Dynamometer Experiment: Intake #8 – Pressure versus CAD for Exhaust Pressure Transducer at (a) 1000, 1250, and 1500 rpm and (b) 1750, 2000, and 2250 rpm

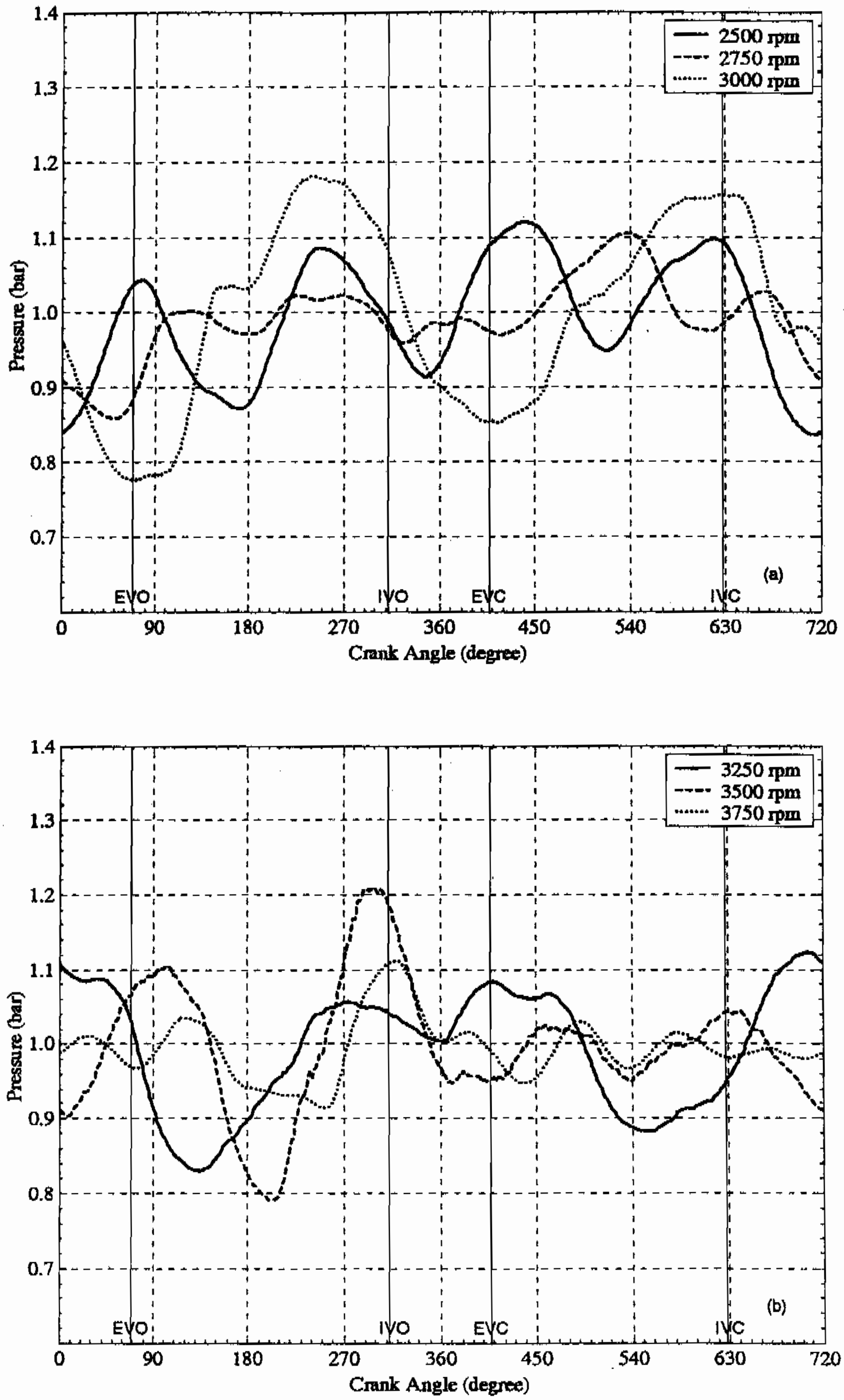

Figure A.121: OSU Dynamometer Experiment: Intake #8 – Pressure versus CAD for Exhaust Pressure Transducer at (a) 2500, 2750, and 3000 rpm and (b) 3250, 3500, and 3750 rpm

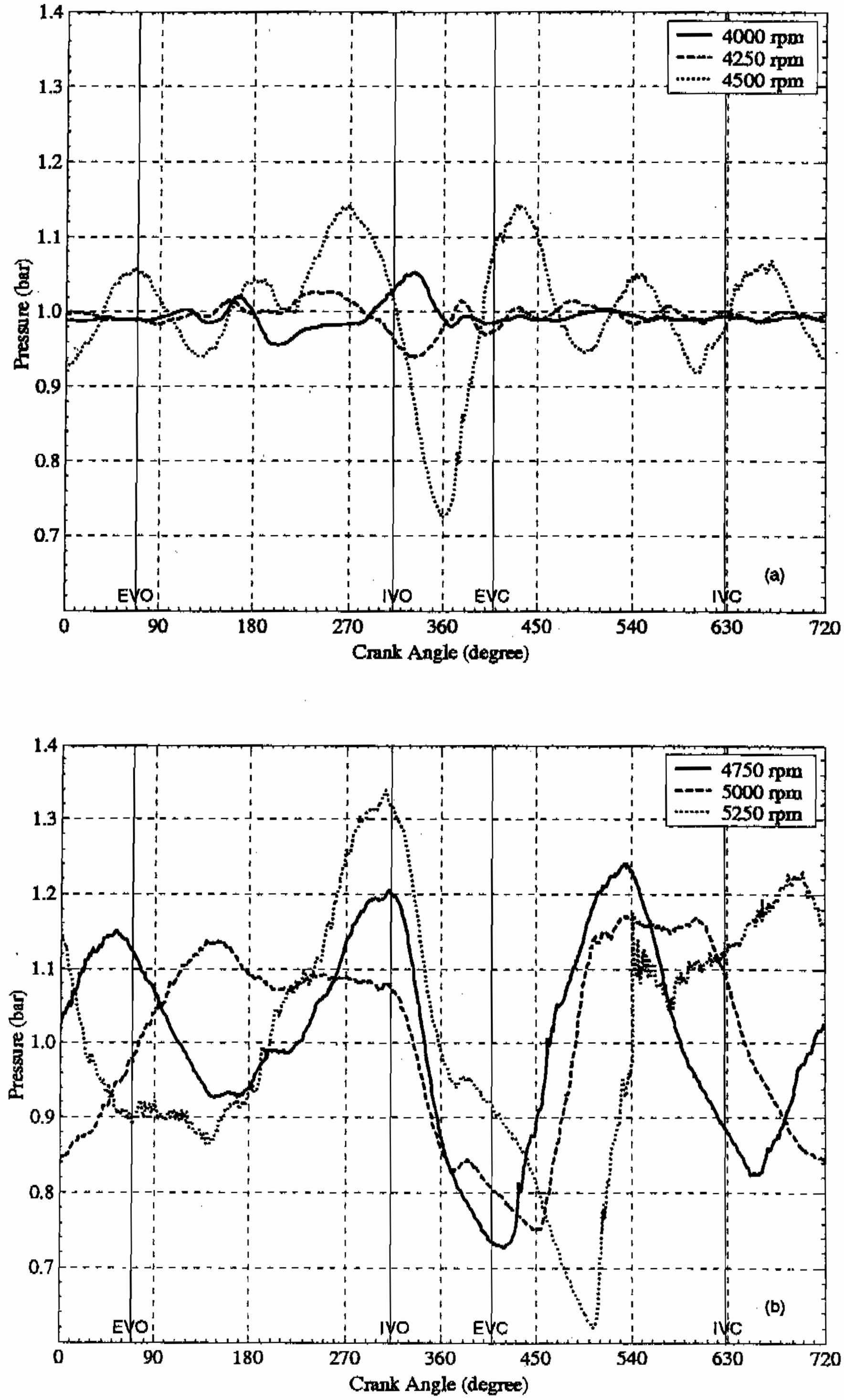

Figure A.122: OSU Dynamometer Experiment: Intake #8 – Pressure versus CAD for Exhaust Pressure Transducer at (a) 4000, 4250, and 4500 rpm and (b) 4750, 5000, and 5250 rpm

BIBLIOGRAPHY

Benajes, J., Reyes, E., Bermudez, V., and Serrano, J.R., 1998. "Pre-design Criteria for Exhaust Manifolds in I.C. Automotive Engines." SAE Paper 980783.

Benson, R.S., Gary, R.D., and Woollatt, D., 1964. "A Numerical Solution of Unsteady Flow Problems." *International Journal of Mechanical Sciences*; 6:117-144.

Chapman, M., Novak, J.M. and Stein, R.A., 1982. "Numerical Modeling of Inlet and Exhaust Flows in Multi-Cylinder Internal Combustion Engines." *Flows in Internal Combustion Engines,* T. Uzkan, editor. ASME WAM.

Chapman, M., Novak, J.M. and Stein, R.A., 1983. "A Nonlinear Acoustic Model of Inlet and Exhaust Flow in Multi-Cylinder Internal Combustion Engines." ASME 83-WA/DSC-14.

Dickey, N.S., Selamet, A. and Tallio, K.V., 2003. "Effects of Numerical Dissipation and Dispersion on Acoustic Predictions from a Time-Domain Finite Difference Technique for Non-Linear Wave Dynamics." *Journal of Sound and Vibration*; 259(1):193-208.

Driels, M.R., 1975. "Dynamics of I.C. Engine Induction Systems." *Journal of Sound and Vibration*; 43(3):499-510.

Engleman, Helmuth W., 1973. "Design of a Tuned Intake Manifold." ASME 73-WA/DGP-2.

Koester, E.W., 1904. "Luftkompressoran." *ZVDI*, 48, 109-118.

Kothamasu, V., 1998. "Effect of Intake and Exhaust Elements on Sound Attenuation and Engine Performance: An Experimental and Computational Investigation." Master's Thesis, The Ohio State University.

Lakshminarayanan, P.A., Janakiraman, P.A., Babu, M.K., and Murthy, B.S., 1979. "Prediction of Gas Exchange Processes in a Single Cylinder Internal Combustion Engine." SAE Paper 790359.

Matsumoto, I. and Ohata, A., 1986. "Variable Induction Systems to Improve Volumetric Efficiency at Low and/or Medium Engine Speeds." SAE Paper 860111.

Meisner, S., and Sorenson, S.C., 1986. "Computer Simulation of Intake and Exhaust Manifold Flow and Heat Transfer." SAE Paper 860242.

Morel, T., Flemming, M.F., and Lapointe, L.A., 1990. "Characterization of Manifold Dynamics in the Chrysler 2.2 S.I. Engine by Measurement and Simulation." SAE Paper 900679.

Morse, P.M., Boden, R.H., and Schecter, H., 1938. "Acoustic Vibrations and Internal Combustion Engine Performance. I. Standing Waves in the Intake Pipe system." *Journal of Applied Physics*; 9:16-23.

Novak, J., and Kach, R.A., 1996. "Computer Optimization of Camshaft Lift Profiles for a NASCAR V-8 Engine with Restrictor Plate." SAE Paper 962514.

Ohata, A. and Isida, Y., 1982. "Dynamic Inlet Pressure and Volumetric Efficiency of Four Cycle Cylinder Engine." SAE Paper 820407.

Selamet, A., Dickey, N.S., and Novak, J.M., 1994. "The Herschel-Quincke Tube:A Theoretical, Computational, and Experimental Investigation." *Journal of Acoustical Society of America* 95(5):3177-3185.

Selamet, A., Dickey, N.S., and Novak, J.M., 1995. "Theoretical, Computational and Experimental Investigation of Helmholtz Resonators with Fixed Volume: Lumped Versus Distributed Analysis." *Journal of Sound and Vibration*; 187(2):358-367.

Selamet, A., Kothamasu, V., and Novak, J.M., 2001. "Insertion Loss of a Helmholtz Resonator in the Intake System of Internal Combustion Engines: an Experimental and Computational Investigation." *Applied Acoustics* 62, 381-409.

Selamet,A., Ji, Z.L., and Kach, R.A., 2001. "Wave Reflections from Duct Terminations." *Journal of Acoustical Society of America*, 109(4):1304-1311.

Silvestri, J.J., Morel, T. and Costello, M., 1994. "Study of Intake Wave Dynamics and Acoustics by Simulation and Experiment." SAE Paper 940206.

Tabaczynski, R.J., 1982. "Effects of Inlet and Exhaust System Design on Engine Performance." SAE Paper 821577, pp.71-81.

Takizawa, M., Uno, T., Oue, T., and Yura, T., 1982. "A Study of Gas Exchange Process Simulation of an Automotive Multi-Cylinder Internal Combustion Engine." SAE

Paper 820410.

Thompson, Michael P., 1968. "Non-Mechanical Supercharging of a Four-stroke Diesel Engine." Master's Thesis, The Ohio State University.

Thompson, Michael P. and Engleman, Helmuth W., 1969. "The Two Types of Resonance in Intake Tuning." ASME 69-DGP-11.

Winterbone, D.E. and Pearson, R.J., 1990. "A Rapid Wave Action Simulation Technique for Intake Manifold Design." SAE Paper 900676.

Winterbone, D.E. and Yoshitomi, M., 1990. "The Accuracy of Calculating Wave Action in Engine Intake Manifolds." SAE Paper 900677.

Winterbone, D.E. and Pearson, R.J., 1999. *Design Techniques for Engine Manifolds*. SAE Book R-274.